

Blokelv-1 core Well, GGU 511101, Upper Jurassic Hareelv Formation in Jameson Land, East Greenland - Final Well Report. Volume 1(3)

Contribution to Petroleum Geological Studies,
Services and Data in East and
Northeast Greenland

Morten Bjerager, Peter Alsen,
Jørgen Bojesen-Koefoed, Peter Japsen,
Claus Kjøller, Lotte Melchior Larsen,
Hans Peter Nytoft, Mette Olivarius,
Dan Olsen, Henrik Ingermann Petersen,
Stefan Piasecki & Niels Schovsbo



Blokelv-1 Core Well, GGU 511101, Upper Jurassic Hareelv Formation in Jameson Land, East Greenland – Final Well Report. Volume 1(3)

Contribution to Petroleum Geological Studies,
Services and Data in East and
Northeast Greenland

Morten Bjerager, Peter Alsen,
Jørgen Bojesen-Koefoed, Peter Japsen,
Claus Kjøller, Lotte Melchior Larsen,
Hans Peter Nytoft, Mette Olivarius,
Dan Olsen, Henrik Ingermann Petersen,
Stefan Piasecki & Niels Schovsbo

Confidential report

Copy No.

Released 01-07-2025

© De Nationale Geologiske Undersøgelser for Danmark og Grønland (GEUS), 2009 (Geological Survey of Denmark and Greenland)

No part of this publication may be reproduced or utilised in any form or by any means, electronic or mechanical, including photocopying, recording or by any information storage and retrieval system, without prior written permission from the publisher, GEUS. Disputes on copyright and other intellectual property rights shall be governed by Danish law and subject to Danish jurisdiction.

1.	Executive summary	7
1.1	Objectives	8
1.2	Main conclusions	8
1.3	Implications for exploration	12
2.	Introduction	14
2.1	Objectives	15
2.2	Well data, general information	16
2.3	Sampling programme at drill site	17
3.	Stratigraphy	21
3.1	Lithostratigraphy	21
3.2	Biostratigraphy	24
3.2.1	Dinoflagellate stratigraphy	24
3.2.2	Ammonite stratigraphy	30
3.3	Chemostratigraphy	47
3.3.1	Methods	47
3.3.2	Chemical trends	48
3.3.3	Chemostratigraphical highlights	49
3.3.4	Conclusions	50
3.4	Petrophysical core log stratigraphy	59
3.4.1	Methods	59
3.4.2	Results	61
3.5	Stratigraphic conclusions	64
3.6	References	65
4.	Sedimentology	68
4.1	Sedimentary facies.	69
4.2	Discussion and conclusions	72
4.3	References	73
5.	Mineralogy and Diagenesis	79
5.1	Data	79
5.2	Methods	79
5.2.1	X-Ray Diffraction	79
5.2.2	Thin sections and point counts	80
5.2.3	Scanning Electron Microscopy	81
5.3	Results	81
5.3.1	Mineralogy	81
5.3.2	Burial induced diagenesis	83
5.3.3	Basalt sill induced diagenesis	86
5.3.4	Exhumation induced diagenesis	87
5.3.5	Diagenetic causes and effects	87
5.4	Conclusions	89
5.5	References	90

6.	Porosity, Permeability and Grain Density	108
6.1	Methods	108
6.2	Results	109
6.3	Discussion and conclusions.....	110
6.4	References.....	111
7.	Petroleum Geology	117
7.1	Screening data and vitrinite reflectance - Source rock quality and thermal maturity.....	117
7.1.1	Methods	117
7.1.2	Kerogen composition	118
7.1.3	Source rock quality	118
7.1.4	Thermal maturity and the oil window	119
7.1.5	Conclusions	120
7.1.6	References.....	121
7.2	Biomarker analysis – Extraction, MPLC-separation, GC, GC-MS and GC-MS-MS	142
7.2.1	Methods	142
7.2.2	Organic matter	145
7.2.3	Maturity	147
7.2.4	Conclusions	147
7.2.5	References.....	147
7.3	Stable Carbon isotope analyses	175
7.3.1	References.....	176
7.4	Headspace gas analysis.....	183
8.	Sandstone Provenance	185
8.1	Data.....	185
8.2	Methods	185
8.2.1	Heavy mineral analysis.....	185
8.2.2	Zircon age dating	186
8.3	Results and Discussion	187
8.3.1	Heavy mineral assemblage	187
8.3.2	Age distributions	188
8.4	Conclusions.....	191
8.5	References.....	191
9.	Igneous Intrusions	204
9.1	Lithology	204
9.2	Petrography.....	204
9.3	Chemical compositions	205
9.4	Discussion.....	206
9.5	Conclusions.....	206
9.6	References.....	206
10.	Apatite Fission Track Analysis (AFTA)	213

10.1	Thermal history reconstruction	213
10.1.1	Thermal history interpretation of AFTA data	213
10.1.2	Thermal history interpretation of VR data	215
10.1.3	Integration of AFTA and VR data, palaeotemperature profiles and mechanisms of heating and cooling.....	215
10.1.4	Thermal history synthesis.....	216
10.1.5	Thermal history reconstruction	217
10.2	References.....	218
11.	Appendix	223
11.1	Sedimentological profiles.....	
11.2	Core photographs	
11.3	Thin sections.....	
11.4	Geochemistry data.....	
11.5	Headspace gas analysis.....	
11.6	Biomarker data.....	
11.7	Thermal History reconstruction in the Blokely Borehole, East Greenland, based on AFTA® and VR data, GEOTRACK report.	
11.8	Spectral Core Gamma Log for Blokely Well GGU 511101, data report.....	

1. Executive summary

This report presents the core data package of the Upper Jurassic Blokelv core (GGU 511101) drilled in central Jameson Land, East Greenland. The report is delivered to the participating sponsoring companies of the specific analytical programme of the Blokelv core and which is described in appendix B1 in the collaboration agreement between GEUS and sponsoring Oil Companies regarding Petroleum Geological Studies, Services and Data in East and Northeast Greenland.

The analytical programme is very extensive and includes many different methods. All descriptions, data and results are systematically presented in this report. By far the most of the descriptions, analytical work and interpretation have been carried out at GEUS; in a few cases consultants have been used for specific analyses (AFTA, isotopes, headspace gas).

Blokelv GGU 511101 was drilled in central Jameson Land during the summer of 2008 app. 35 km west of Constable Pynt, and is situated in the central and, conceivably, deepest part of the Jameson Land Basin. Blokelv is the first core hole in an onshore drilling program in East and Northeast Greenland starting in 2008. It was drilled to a total depth of 233.8 m; the core diameter is 56 mm, and the core recovery was 100% from 1.72–233.8 m. The core probably represents the most extensively sampled and analysed Upper Jurassic succession in the North Atlantic region.

The Blokelv core recovered fractured homogenous gravity flow sandstones of the Sjøelandselv Member (Hareelv Formation, Upper Jurassic) from 0–10 m; very dark grey to black mudstones with grey homogenous gravity flow sandstones and heterolithic sandstone and mudstones of the Katedralen Member (Hareelv Formation) from 10 m–TD. The base of the Hareelv Formation was not reached. Mudstones comprise 57% and sandstones comprise 41% of the cored Katedralen Mb. Possible bentonite beds are present at 25.8 m, 79.9 m, 83.2 m and 216 m.

Igneous intrusions represented by one dyke, (0.30 m thick) at 7 m depth, and three sills (0.72 m, 1.07 m and 1.98 m thick) were recorded at 27, 55 and 102 meters, respectively.

Bitumen/oil stains occur on the faces of a fracture within the sill at 55.4 m and in a belemnite at 105.25 m. The mudstones in general release a scent of oil. Sandstones are commonly brownish-grey stained towards the boundaries with the mudstones.

A suite of well log runs was planned in the field, including gamma spectral log, sonic log and conductivity log. Logging in the field included a complete conductivity log and a gamma log from 232–184 m. Logging programme in the field was hereafter terminated due to bore-hole collapse. A spectral gamma log and density log of the entire core were later measured in GEUS Core Laboratory.

1.1 Objectives

The primary objectives of the Blokelv well were to core the Upper Jurassic Katedralen Member of the Hareelv Formation in the central and deepest part of the Jameson Land Basin in order to gain insight into the thickness, composition and stratigraphy of this combined mudstone source rock and sandstone reservoir rock succession, *i.e.*:

- Improve the stratigraphic control of the extent of the Katedralen Member and to constrain the upper and lower boundaries.
- Develop an improved depositional model of the Katedralen Member on basis of the core material.
- Acquire lithological data on the Katedralen Member in order to obtain quantitative data on the distribution of sandstone and mudstone intervals and individual bed thicknesses.
- Acquire fresh unweathered samples for modern analyses of source rock potential and reservoir quality within the Katedralen Mb.

1.2 Main conclusions

Lithostratigraphically the Blokelv core encounters the Sjøellandselv Member in the top 10 m and the Katedralen Member from 10 to 233.8 m TD, both of the Hareelv Formation. The base of the Katedralen Member was not reached by the core-well suggesting that the thickness of the Katedralen Member exceeds 225 m in the area.

The biostratigraphy of the Blokelv core is based on 50 samples prepared for dinoflagellate analyses and 42 levels with ammonites that have been assigned to biostratigraphic zones

and correlated to chronostratigraphic zones. The flora and fauna belongs to the Boreal Realm with correlation to SubBoreal/Tethys realms. The interval represented by Katedralen Member biostratigraphically spans Middle Oxfordian – Kimmeridgian based on dinoflagellates and constrained by 8 ammonite zones thus probably spanning about 9 my of continuous sedimentation. The Sjøellandselv Member is dated to early Volgian by dinoflagellates.

Deposition of the Katedralen Member occurred in an anoxic environment with dark grey to black laminated mudstones in central part of the Jameson Land Basin. The organic content of the mudstones is predominantly of marine origin, however with an increasing terrestrial proportion in the deeper part, i.e. the interval 100–233.8 m. Massive fine to medium grained sandstones were deposited by gravity flows in the deeper part of the basin during episodic collapse of the sandy shelf margin. After deposition the sandstones were later fluidised and remobilised to form complex geometrical sandstone bodies in the mudstone dominated succession. Some sandstone injectites were formed during early burial and were later folded during continuous compaction and burial. Remobilisation of sandstone occurred locally and shows transitions from sandstone with local water escape structures to completely remobilised massive sandstones. Sandstone injectites commonly carry irregular mudstone clasts scavenged from the hostrock during injection, occasionally forming mudstone conglomerates with a sandstone matrix. Heterolithic intervals are present in the lower, middle and upper part of the cored Katedralen Member and are interpreted as deposited from low density turbidite currents, that may have been associated with relative sea-level falls. The medium to coarse grained sandstones of the Sjøellandselv Member represent mass flow to high density turbidite sandstones deposited from collapse of the prograding shelf margin during relative lowering of sea-level.

Bulk geochemical analysis of sandstones in the core shows that they can be classified as quartz arenites with a few levels rich in ankerite. Sandstones mainly consist of quartz averaging 66 wt%, with feldspar (mainly albite and K-feldspar) averaging 8 wt%. Mica (predominantly muscovite) and clay minerals comprises on average 14 wt%. Ankerite is diagenetically precipitated, and in general, ankerite amounts to 5 wt% or less, but locally up to 41 wt% is observed, resulting in a marked reduction in porosity. The sandstones are considered as relatively immature due to abundant angular grains, high mica content and generally high feldspar content.

Mudstone mineralogy is dominated by clay minerals and mica with an average of 69 wt%. Among the clay minerals kaolinite predominate, with minor proportions of illite, vermiculite and smectite. Quartz averages 17%. Pyrite is rather abundant, 6 wt% on average.

The degree of diagenesis is characterised as medium with early dissolution of plagioclase and precipitation of microquartz, as well as ankerite-replacement of plagioclase, and formation of mixed-layer clays, and framboidal pyrite. Later diagenesis includes precipitation of macroquartz, commonly as overgrowth, rare apatite, pyrite and Ti-oxides. Diagenesis influenced by igneous intrusions includes precipitation of microquartz, ankerite, mixed-layer clay, local baryte and dissolution of K-feldspar. Precipitation of ankerite is also associated with dissolution of smectite and degradation of bioclasts. Later diagenesis includes precipitation of kaolinite and formation of secondary porosity created by dissolution of K-feldspar.

Reservoir quality of sandstone units is measured by conventional core analysis on 27 sandstone plugs. Porosity measurements show that the majority of the massive sandstone units, 2–10 m thick, in the cored succession record porosities from 15–25% and permeabilities from 20–200 mD. Fieldwork on outcrops shows that these massive sandstone units may attain vertical thicknesses up to 50 m.

Source rock evaluation of the Blokely core is based on 139 samples that were analysed for the content of total carbon (TC, wt%), total organic carbon (TOC, wt%) and total sulphur (TS, wt%). Moreover the samples were subjected to Rock-Eval type pyrolysis. The analyses show that the marine black mudstones of the Hareelv Formation are rich source rocks composed of sapropelic Type II kerogen. The average TOC amounts to 7 wt% and HI reaches 363 mg HC/g TOC, averaging 265 mg HC/g TOC. Overall the mudstones are oil-prone to gas-/oil-prone and the source rock quality can be classified as good to excellent. Calculation of the generation potential of the reactive part of the kerogen yields a HI_{live} of 303 mg HC/g TOC, indicating an oil-generative potential. Igneous intrusions have locally deteriorated the remaining source rock potential due to local maturation of the mudstones. VR, T_{max} and PI increase with depth through the well and it appears that the mudstones in the lower part of the drilled section have entered the earliest part of the oil window. Around the igneous intrusions the mudstones are well within or beyond the oil window and oil has been generated.

Biomarker analysis was conducted on a subset of the same samples that were used for the source rock evaluation, and 40 of the 139 mudstone samples were selected for solvent extraction, MPLC-separation, gas chromatography (GC) and gas chromatography-mass spectrometry (GC-MS and GC-MS-MS) of the saturated fraction. Two samples of oil/bitumen found near the igneous intrusions around 55 and 104 m were also analysed. Extracts of the Blokely mudstones show the typical characteristics of a marine source rock

but with an increasing proportion of terrestrial-influenced kerogen below ~120 m. The deeper parts of the core are within the oil window.

Stable carbon isotope analyses were conducted on saturated, aromatic polar and asphalthe fractions of 20 solvent extracts and 2 oil/bitumen samples from the Blokelyv core. The crossplot of $\delta^{13}\text{C}_{(\text{saturates})}$ versus $\delta^{13}\text{C}_{(\text{aromatics})}$ shows that extract samples generally plot very close to the line between “waxy” (*i.e.* terrestrially dominated, above line) and “non-waxy” (*i.e.* marine, below line) oils or extracts. Both oil/bitumen samples plot well within the “non-waxy”, marine field.

Headspace gas analyses were conducted on 21 core pieces evenly spaced throughout the drilled section. Hydrocarbon gas concentrations are very variable but generally low, dominated by methane. Only six samples allowed carbon and hydrogen isotope analysis to be carried out. Out of these five show compositions conformable with a thermogenic origin.

Provenance studies include mineral CCSEM (Computer Controlled Scanning Electron Microscopy) analyses and zircon LA-ICP-MS (Laser Ablation - Inductively Coupled Plasma - Mass Spectroscopy) age datings and were carried out on sandstones at six different levels in the Blokelyv core. The provenance of the sandstones is assumed to have been located in the hinterland close to the Jurassic coast of East Greenland, where the complex geology accounts for the diverse age distributions. The upland of the supplying rivers has primarily been local, as seen by the poorly sorted heavy mineral assemblages, but with some contributions from more distant sources. The provenance area has changed steadily but slowly during the deposition, except for an interruption in the middle of the core resulting in changing dominance of the major age peaks. In the upper part of the core there is a weak upward trend of decreasing transport distance for the deposited sediments, as represented by the progradation of shelf margin sandstone wedges of the Raukelv Formation in the Late Jurassic.

Intrusive igneous rocks cut the sedimentary succession in the Blokelyv core at four levels: 7.05–7.35 m (thickness 0.3 m), 26.4–27.1 m (thickness 0.7 m), 55.2–56.4 m (thickness 1.2 m) and 100.1–102.0 m (thickness 1.9 m). The uppermost intrusion is classified as a dyke while the three lower intrusions are classified as sills. The two thickest sills have caused alteration of the surrounding sediments. The dyke and sills are lithologically similar and consist of fine-grained, sparsely plagioclase-olivine-phyric basalt, and are compositionally similar to the main type of sills and dykes in the Jameson Land Basin. These are dated at 52–53 Ma, and the Blokelyv sills most probably have the same age.

Thermal History Reconstruction study of the Blokelyv borehole is based on new Apatite Fission Track Analysis (AFTA®) data in two core samples from the borehole, together with vitrinite reflectance (VR) and other organic maturity data. Key aspects of this reconstruction are: 1) Surface temperature of 20°C at 30 Ma and earlier, decreasing to 10°C at 12 Ma and to the present-day value of 4°C over the last 12 Myr. 2) Palaeogeothermal gradient of 30°C/km, constant to the present day. 3) Localised heating within the vicinity of sample GC1052-2 to a palaeotemperature around 120°C, shown at ~53 Ma but any time between 56 and 45 Ma is allowed by the regional timing constraints on this episode. 4) An additional 2750 metres of section deposited above the Late Jurassic section intersected in the borehole, between 146 and 36 Ma. 5) Subsequent removal of 1150 metres of section between 36 and 30 Ma, followed by deposition of a further 600 metres of section between 30 and 12 Ma. 6) Removal of the remaining 2200 metres of additional section between 12 Ma and the present day.

1.3 Implications for exploration

This report demonstrates clearly that the concept of shallow-core drilling followed by an extensive analytical programme is very important and cost-effective for evaluation of exploration possibilities and critical risk factors in frontier areas like East Greenland.

The Data package of the Blokelyv core from Jameson Land will – together with other future packages – be of essential value for understanding and predicting source and reservoir rocks, and may provide many other details of relevance for correlation to offshore areas.

The Blokelyv core is a major step forward in the understanding of the distribution, potential and character of Upper Jurassic source rocks in East Greenland. The source rocks found in the core have been characterized systematically with focus on generative potential and detailed organic geochemistry.

Good to excellent marine oil-prone source rocks are found throughout the Kimmeridgian succession which is anoxic in character. The cumulative thickness of the Kimmeridgian source rock interval is more than 65 metres. The top of the source rock in the Blokelyv core is placed at the Kimmeridgian/Volgian boundary, but in other parts of the basin the source rock may extent stratigraphically upward.

In addition the Oxfordian succession contains good source rocks that are oil/gas-prone. The Oxfordian source rocks were deposited under less anoxic conditions. The cumulative thickness of the Oxfordian source rock is more than 65 metres. The base of the source rock has not been penetrated.

The Blokely core also contains good reservoir rocks. With the documentation of a number of 2–10 metres thick sandstone units with high porosities (15–25% range) and moderate to good permeabilities (20–200 mD range). The cumulative succession of massive sandstones with potential high porosities attains more than 72 m in the core. The possibility of such reservoir sandstones within an excellent source rock and seal may suggest additional exploration targets. This play-type should be considered in more detail during future exploration. The sandstones, which are partly injective by nature, may also be of great importance as migration conduits.

2. Introduction

This report presents the core data package of the Upper Jurassic Blokelyv core (GGU 511101) drilled in central Jameson Land, East Greenland. The report is delivered to the participating sponsoring companies of the specific analytical programme of the Blokelyv core as described in appendix B1 in the collaboration agreement between GEUS and sponsoring oil companies regarding petroleum geological studies, services and data in East and Northeast Greenland.

Blokelyv borehole was drilled in central Jameson Land in the summer of 2008 app. 35 km west of Constable Pynt (Figs. 2.1, 2.2). Blokelyv is the first core hole of an onshore drilling programme in East and Northeast Greenland starting in 2008.

The Blokelyv borehole was spudded on August 7th 2008 and completed on August 15th 2008 at a total depth of 233.8 m. The core diameter is 56 mm, and the core recovery was 100% from 1.72–233.8 m.

The Blokelyv borehole is located in the central and deepest part of the Jameson Land Basin. The terrain plateaus in this area consist of sandstones of the Upper Jurassic Sjøællandselv Member (Hareelv Formation) underlain by alternating black mudstones and grey – yellowish grey sandstones of the Katedralen Member (Hareelv Formation). The lower part of the Katedralen Member is generally poorly exposed in the region, but passes into silty mudstones of the Fossilbjerget Formation (Fig. 3.1.1).

The Blokelyv core recovered fractured homogenous sandstones of the Sjøællandselv Member (Hareelv Formation) from 0–10 m and very dark grey to black mudstones with grey homogenous gravity flow sandstones and heterolithic sandstones and mudstones of the Katedralen Member (Hareelv Formation) from 10–233.8 m (TD). The base of the Hareelv Formation was not reached. Mudstones comprise 57% and sandstones comprise 41% of the cored Katedralen Member. Possible bentonite beds are present at 25.8 m, 79.9 m, 83.2 m and 216 m.

Igneous intrusions represented by one dyke, (0.30 m thick) at 7.05–7.35 m depth, and three sills (0.70 m, 1.2 m and 1.9 m thick) were recorded at 26.4–27.1 m, 55.2–56.4 m and 100.1–102.0 m depth, respectively.

Bitumen/oil stains occur in a fracture within the sill at 55.4 m and in a belemnite at 105.25 m. The mudstones in general release a scent of oil. Sandstones are commonly stained brownish-grey towards the boundaries with the mudstones.

A suite of well log applications was planned in the field, including gamma spectral log, sonic log and conductivity log. Logging in the field included a complete conductivity log and a gamma log from 184–232 m. Logging programme in the field was hereafter terminated due to borehole collapse. A spectral gamma log and density log for the complete core were later measured in the core-lab at GEUS.

2.1 Objectives

The primary objectives of the Blokely well were to drill the Upper Jurassic Katedralen Member of the Hareelv Formation in the central and deepest part of the Jameson Land Basin in order to gain insight into the thickness, composition and stratigraphy of this combined mudstone source rock and sandstone reservoir rock succession, *et.*:

- Improve the stratigraphic control of the extent of the Katedralen Member and to constrain the upper and lower boundaries.
- Develop an improved depositional model of the Katedralen Member on basis of the core material.
- Acquire lithological data on the Katedralen Member in order to obtain quantitative data on the distribution of sandstone and mudstone intervals and individual bed thicknesses.
- Acquire fresh unweathered samples for modern analyses of source rock quality and reservoir quality within the Katedralen Member.

2.2 Well data, general information

Country	Greenland / Denmark
Borehole number	GGU 511101
Borehole name	Blokelv
Area	Central East Greenland, Jameson Land
Operator	GEUS
Drilling operator	GEUS
Borehole Location	
Altitude:	181 m above mean sea level.
Coordinates WGS 84:	Latitude: 70°45.305' N, Longitude: 23°40.430' W
UTM Zone:	27W 0401666 N - 7852249 E
Drill rig	
Drill rig	Diamant Board 747
Drilling contractor	Faxe Kalk A/S
Casing diameter	85 mm
Casing depth	20 m
Borehole diameter	76 mm
Core diameter	56 mm
Total depth	233.8 m
Core recovery	100% from 1.72–233.8 m
Status	Abandoned open hole, top of casing closed with a steel cap.
Logistic history:	
Rig arrival East Greenland, Constable Pynt	August 4 th 2008
Rig arrival at drill location Blokelv	August 5 th 2008
Spud	August 7 th 2008
Drilling completed	August 15 th 2008
Drill rig back at Constable Pynt	August 16 th 2008
Effective drilling	8 days
Total days on drill location	12 days

Permafrost was present from a few decimetres below terrain surface and down to about 100 m.

2.3 Sampling programme at drill site

A total of 79 whole round core samples for gas analyses were collected immediately from the bottom of each recovered core at every 3 m. Samples have lengths up to about 10 cm and they were stored in sealed metal cans.

Samples collected for preliminary biostratigraphic age identification based on dinoflagellates include three mudstone samples from the top part of the cored Katedralen Member at 10.10 m (511201), 15.0 m (511202) and 18.80 m (511203); and four mudstone samples from the lowermost part of the cored Katedralen Member at 201.90 m (511209), 216.6 m (511210), 224.68 m (511211) and 233.80 m (511212).

Bitumen and oil samples were collected at 55.4 m (511206) and 105.47 m (gas-can; bel-emnite with oil), respectively. In addition gas and water samples were collected at 162.5 m (511207, 511208), where a gas and oil film was observed in the drill water.

One surface sample (511204) of weathered mudstone (Sjællandselv Member) was collected at the drill site (0 m drilling / 181 m a.s.l.).

An extensive sampling programme of the Blokelyv cores was later conducted at GEUS laboratories.

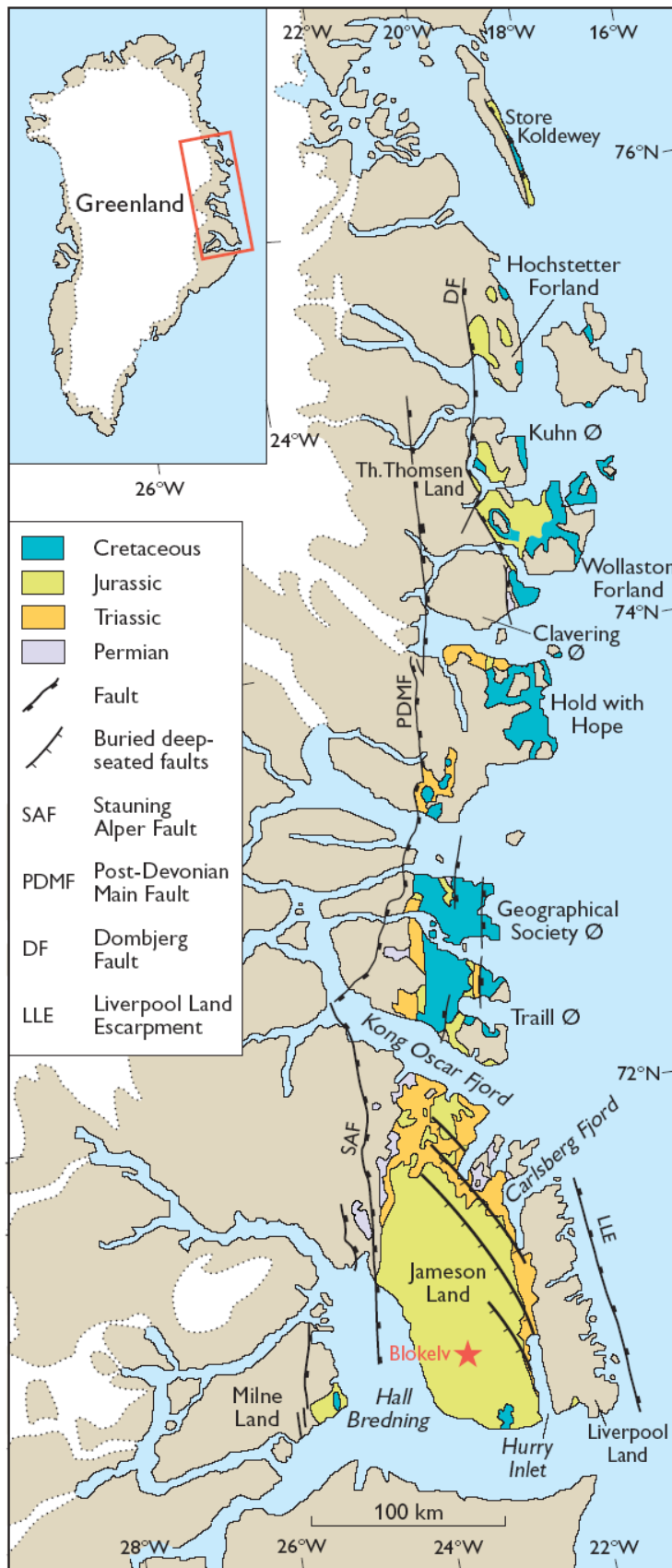
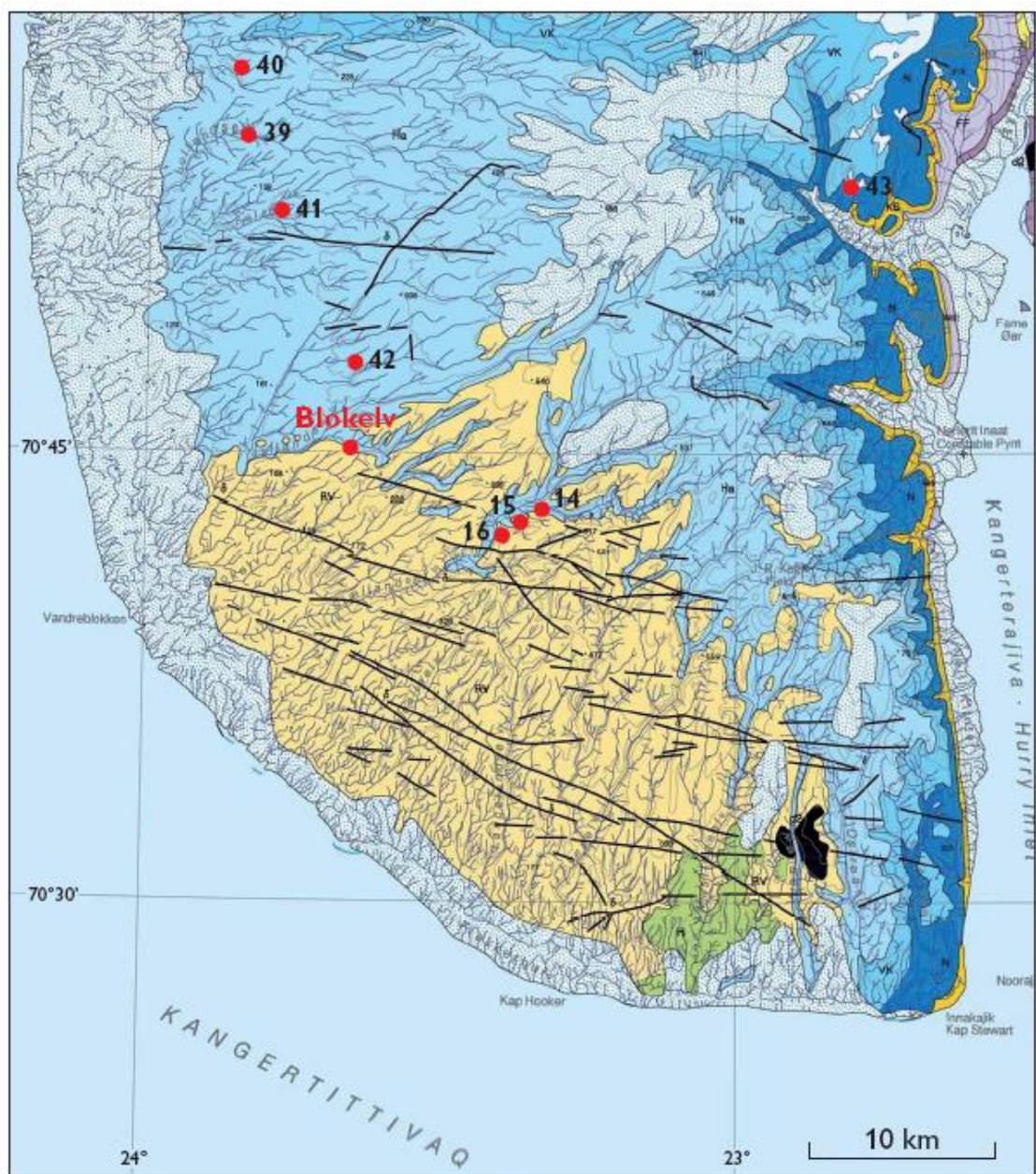


Fig. 2.1 Geological map of East Greenland with indication of the Blokelyv borehole site.



- Sjællandselv Member (Hareelv Formation), Raukelv Formation
- Katedralen Member (Hareelv Formation)
- Vardekløft Group
- Neil Klintor Group
- Boreholes

Fig 2.2 Geological map of the southern part of Jameson Land showing the Blokelyv borehole location and other boreholes in the area.

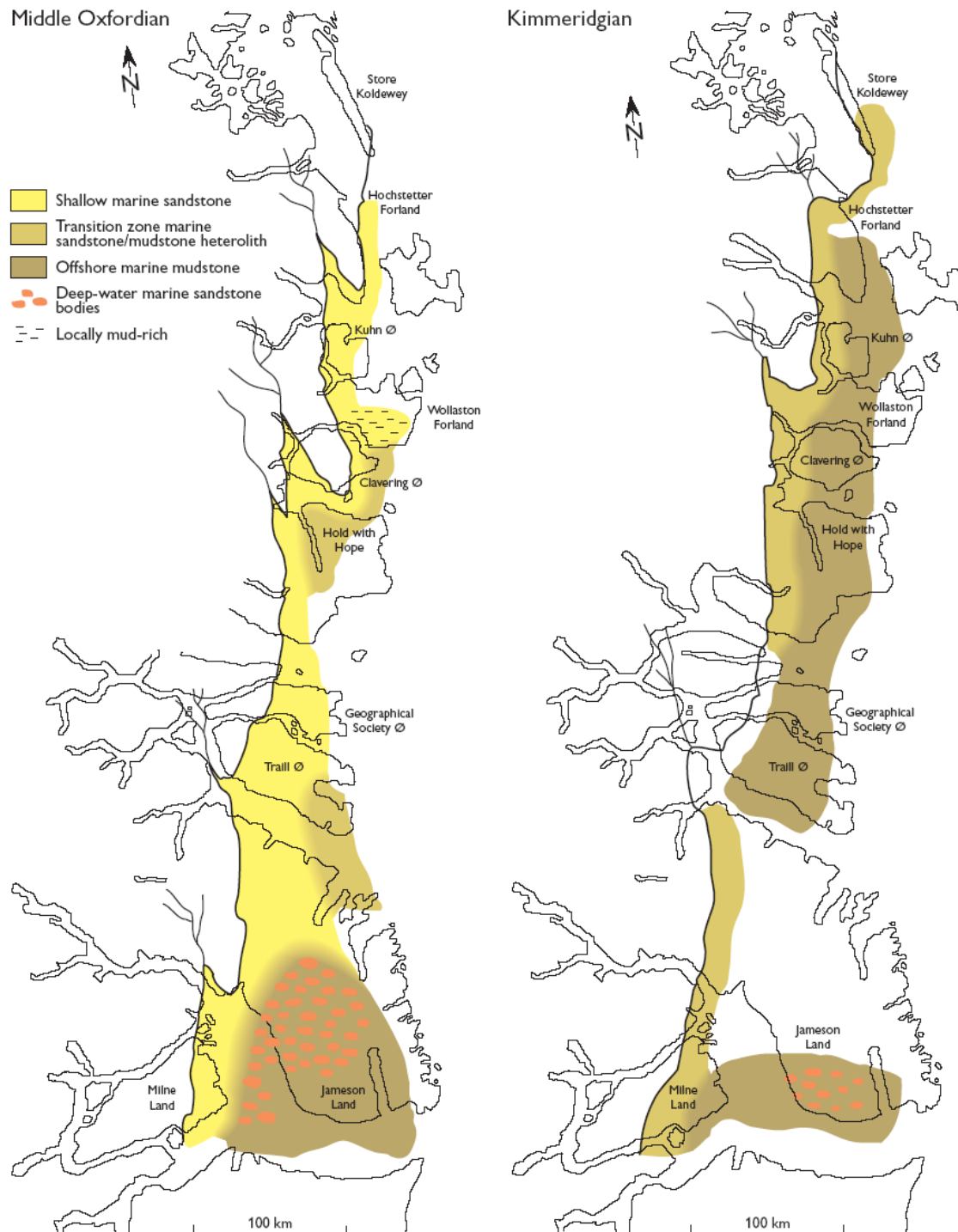


Fig. 2.3 Palaeogeographic maps of East and Northeast Greenland in Middle Oxfordian and Kimmeridgian times (From Surlyk 2003).

3. Stratigraphy

3.1 Lithostratigraphy

Jurassic lithostratigraphy in Jameson Land, East Greenland is defined by Surlyk *et al.* (1973) and Surlyk (2003) (Fig. 3.1.1). Upper Jurassic in the Jameson Land Basin comprises the offshore to basinal mudstone and sandstone dominated Hareelv Formation with the Katedralen and Sjøllandselv Members. The base of the formation is defined by a flooding surface overlying Middle Jurassic offshore sandy mudstones of the Fossilbjerget Formation in the central part of the basin and shows a transition landwards (towards the north and west) into the mainly shallow marine sandstones of the Olympen Formation with the Athene, Hades and Zeus Members (Fig. 3.1.1, Surlyk 2003). The Hareelv Formation represents a general deepening upward succession and ending with a shallowing in the uppermost part as represented by the sandstone dominated Sjøllandselv Member. The upper boundary of the Hareelv Formation is overlain by a stepwise eastward progradation of the shelf-margin wedges of sandstones of the Raukelv Formation (Volgian).

The primary objective of the Blokelv borehole was to recover Upper Jurassic black organic-rich basinal mudstones of the Katedralen Member of the Hareelv Formation (Bojesen-Koefoed *et al.* 2009).

The Blokelv core recovered fractured homogenous sandstones of the Sjøllandselv Member (Hareelv Formation) from 0–10 m and very dark grey to black mudstones with grey homogenous gravity flow sandstones and heterolithic sandstones and mudstones of the Katedralen Member (Hareelv Formation) from 10–233.8 m (TD) (Fig 3.1.2). The base of the Hareelv Formation was not reached. Mudstones comprise 57% and sandstones comprise 41% of the cored Katedralen Member. Possible bentonite beds are present at 25.8 m, 79.9 m, 83.2 m and 216 m.

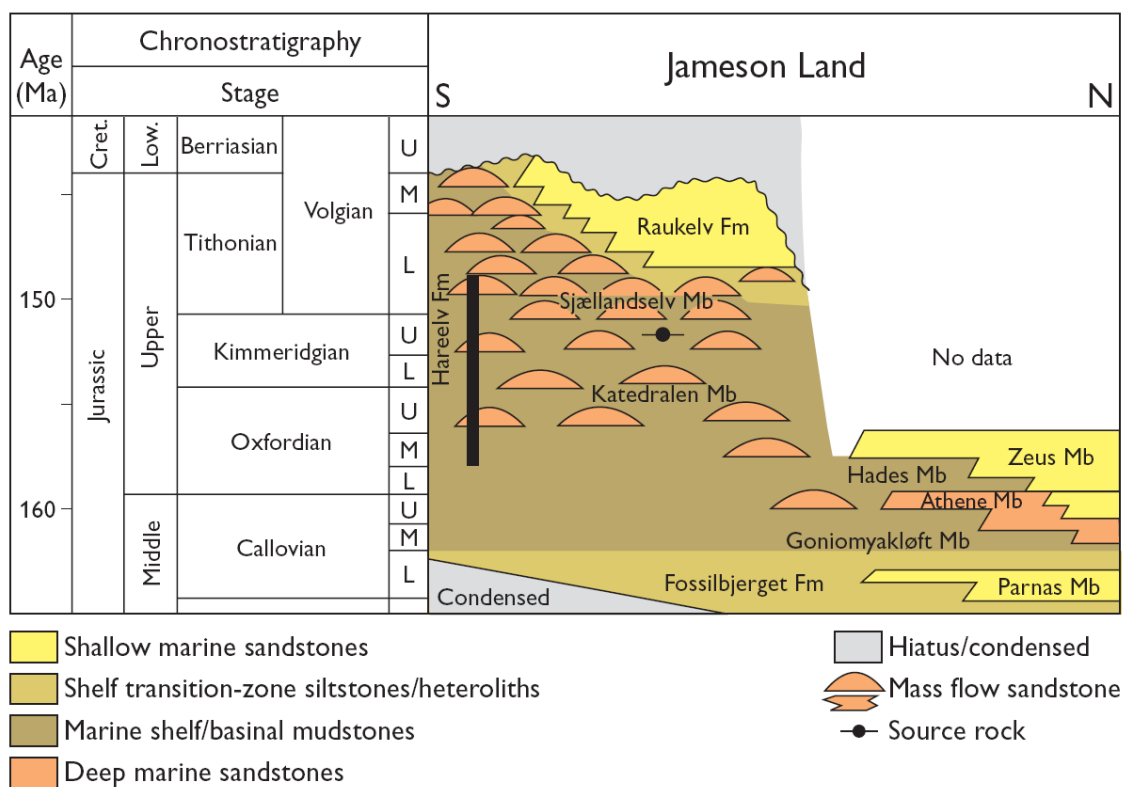
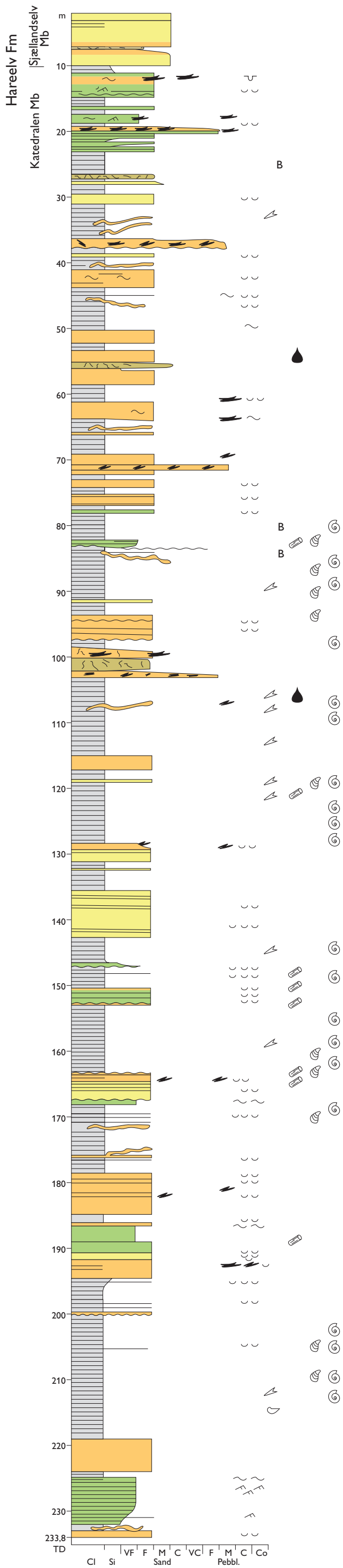


Figure 3.1.1 Upper Jurassic stratigraphical scheme. The cored succession at Blokelyv is indicated with black line.



Legend

- Sandstone, intrusive
- Sandstone, low density turbidite
- Sandstone, high density turbidite
- Mudstone
- Igneous intrusion
- Planar lamination/bedding
- Cross-lamination
- Wavy bedding
- Slump
- Sandstone intrusion
- Burrow
- Mudstone intra clast
- Large mudstone clast
- B Bentonite
- Coal
- Belemnite
- Bitumen
- Ammonite
- Bivalve
- Brachiopod

Figure 3.1.2 Lithological log of the Blokely core.

3.2 Biostratigraphy

Jurassic stratigraphy is based on ammonite biostratigraphy. Standard chronozones are established for the Jurassic based on ammonite zonations. The ammonite zonation in East Greenland is boreal and the boreal ammonite zonation is established on material from Milne Land and Jameson Land, central East Greenland (Callomon & Birkelund 1982; Birkelund & Callomon 1985; Callomon 1993).

In NW Europe, Jurassic dinoflagellate stratigraphy is correlated to subboreal–boreal ammonite zonation (Woollam & Riding 1983; Riding & Thomas 1992). However, the North–South extension of the Jurassic sea-way (Ziegler 1982) from warm Tethys to boreal and possible arctic environments induce stratigraphic variations in first and last occurrences of the dinoflagellates across the latitudes.

In central East Greenland, dinoflagellate stratigraphy is correlated with the ammonite stratigraphy zone by zone in successions on Milne Land and Jameson Land (Piasecki 1981; Smelror 1988; Milner & Piasecki 1996; Piasecki 1996; Larsen *et al.* 2003). This “boreal” correlation is used for dating of the Blokely core and the recorded dinoflagellate events in the present core are therefore correlated with corresponding events and their stratigraphic relation to ammonite fauna horizons reported from these successions in Jameson Land and Milne land.

3.2.1 Dinoflagellate stratigraphy

Material and methods

Eight samples were handpicked from the core together with one surface sample at the drill site for early preparation. Fifty samples were subsequently collected from mudstones in the Blokely core for palynological analysis and prepared by standard preparation techniques in the Stratigraphic Laboratory at GEUS.

The preparation includes treatment with acids (HCl, HF, HNO₃) and filtering at 20 µm filters. This treatment removes carbonates and silicates (clay, silt and sand) from the samples. The remaining organic sedimentary material is resistant to the acids. The present

material is highly resistant to preparation and repeated oxidations, extended ultrasonic treatments, washing in potassium hydroxide and filtering were necessary to recover at least some identifiable dinoflagellate cysts.

The remaining organic material is mounted in glycerine-gelatine on preparation glasses for visual analysis by microscopy.

Dinoflagellate stratigraphy

C. densiplicatum Zone (233.80–216.80 m): The last occurrence of *Trichodinium scharburghense* (232,80 m), *Rigaudella aemula* (224,80 m) and the maximum in occurrence of *Kalyptea* spp. (218,40 m) are all reported in the upper *C. densiplicatum* Zone between ammonite fauna horizon M6 and M7 (Figure 3.2.6) at Milne Land (Piasecki 1996).

Assemblage: A poor assemblage characterised by the last occurrences of generally Lower Oxfordian species; *Kalyptea* spp., *Nannoceratopsis pellucida*, *Pareodinia* spp., *Rigaudella aemula*, *Trichodinium scharburghense* and *Wanaea* spp. is recorded.

Age: Middle Oxfordian, Late Jurassic.

C. tenuiserratum Zone (216.8–209.8 m) is not identified by dinoflagellates but its presence is confirmed by ammonites (see below; chapter 3.2.2).

Assemblage: A poor assemblage with *Kalyptea* spp., *Pareodinia* spp. and *Rhyncodiniopsis cladophora*.

Age: Middle Oxfordian, Late Jurassic.

A. glosense – A. serratum Zones (209.8–167.93 m): The first occurrences of *Leptodinium subtile* and *Systematophora* spp. are reported in upper *C. tenuiserratum* to lower *A. glosense* Zones between ammonite fauna horizons M8 and M9 (Figure 3.2.6) at Milne Land (Piasecki 1996). The upper limit of the zone is confirmed by ammonites (see below; chapter 3.2.2).

Assemblage: A poor assemblage of *Gonyaulacysta jurassica*, *Pareodinia* spp., *Rhynchodiniopsis cladophora* and *Sirmiodinium grossii*. *Kalyptea* spp., *Evansia* spp. and *Chytroisphaeridia hyalina* are not recorded higher in the succession.

Age: Late Oxfordian, Late Jurassic.

A. regulare – A. rosenkrantzi Zones (167.93–121.0 m): The maximum occurrence of *Adnathosphaerium “hartzi”* (120.06 m) occurs above the *A. regulare* – *A. rosenkrantzi* Zones in the overlying *P. baylei* Zone (Piasecki 1996) and therefore the zones are confined to the succession below this event. The stratigraphic extent of the *A. regulare* – *A. rosenkrantzi* Zones is confirmed by ammonites (see chapter 3.2.2).

Assemblage: A poor assemblage of *Cribroperidinium* spp., *Gonyaulacysta jurassica*, *Pareodinia* spp. and *Rhynchodiniopsis cladophora*.

Age: Late Oxfordian, Late Jurassic.

P. baylei Zone (121.0–109.25 m): The maximum occurrence of *Adnathosphaerium “hartzi”* (120.06 m) is reported in lower *P. baylei* Zone below ammonite fauna horizon M14 at Milne land (Piasecki 1996). The presence and stratigraphic extension of the *P. baylei* Zone in the Blokely core is confirmed by ammonites (see chapter 3.2.2).

Assemblage: A poor assemblage of *Adnathosphaeridium “hartzi”* (Figure 3.2.1D) and *Gonyaulacysta jurassica* (Figure 3.2.1B)

Age: Earliest Kimmeridgian, Late Jurassic.

R. cymodoce Zone (109.25–91.25 m) is not clearly identified on the basis of dinoflagellates but the presence and stratigraphic range is indicated by ammonites (see chapter 3.2.2).

Assemblage: A poor assemblage not well documented in this study but with *Glossodinium dimorphum*, *Gonyaulacysta jurassica* and *Sirmiodinium grossii*.

Age: Kimmeridgian, Late Jurassic.

A. mutabilis Zone (91.25–82.0 m): The lower boundary of this zone is not demarcated by dinoflagellate events in the Blokely core. The zone is, however, limited upwards by the first occurrence of abundant *Perisseiasphaeridium pannosum* (82.14 m), which is recorded in the lowermost *A. eudoxus* Zone, ammonite fauna horizon M20 at Milne Land (Piasecki 1996).

Assemblage: A poor assemblage of *Glossodinium dimorphum*, *Gonyaulacysta jurassica*, *Sirmiodinium grossii* and *Systematophora* spp.

Age: Kimmeridgian, Late Jurassic.

A. eudoxus Zone (82.0–59.39 m): The first occurrence of abundant *Perisseiasphaeridium pannosum* (82,14m) is recorded in the lowermost *A. eudoxus* Zone, ammonite fauna horizon M20 at Milne Land (Piasecki 1996). The presence of the zone is confirmed by the highest ammonite in the Blokely core (see later). The last occurrence of abundant *Perisseiasphaeridium pannosum* (68.97 m) is recorded near the top of the *A. eudoxus* Zone, above ammonite fauna horizon M22 at Milne Land (Piasecki 1996).

Assemblage: Dominated by *Perisseiasphaeridium pannosum* in association with *Circulodinium distinctum* and *Cribroperidinium* spp.

Age: Kimmeridgian, Late Jurassic.

A. autissiodorensis Zone (59.39–10.0 m): The first occurrence of abundant *Oligosphaeridium patulum* (59,39 m) is recorded at the basis of the *A. autissiodorensis* Zone between ammonite fauna horizon M22 and M23 at Milne Land (Piasecki 1996).

Assemblage: Dominated by *Oligosphaeridium patulum* and *Cribroperidinium* spp. in association with few e.g. *Circulodinium distinctum*, *Perisseiasphaeridium pannosum*, *Rhynchodiniopsis* spp. and *Senoniasphaera clavelli*.

Age: Latest Kimmeridgian, Late Jurassic.

***P. elegans* Zone** (10.0–2.96 m): Abundant *Oligosphaeridium patulum* occurs to the top of the Blokely core (0,0 m). The highest occurrence of *Oligosphaeridium patulum* is recorded below the *P. wheatleyensis* Zone (i.e. just above the *P. scitilus* Zone) below ammonite fauna horizon M25 at Milne Land (Piasecki 1996). The presence of *Rhynchodiniopsis* “*machaera*” (2.96 m) may mark the the top of the *P. elegans* Zone as recorded above the *P. elegans* Zone and ammonite fauna horizon M24 in Milne Land (Piasecki 1996).

Assemblage: Dominated by *Oligosphaeridium patulum* and *Cribroperidinium* spp. in association with *Circulodinium distinctum*, *Rhynchodiniopsis* spp. and *Senoniasphaera* spp.

Age: Earliest Volgian, Late Jurassic.

***P. scitilus* Zone** (2.96–0.0 m): The occurrence of *Rhynchodiniopsis* “*machaera*” (2.96 m) and the presence of abundant *Oligosphaeridium patulum* may indicate the *P. scitilus* Zone in the uppermost meters of the Blokely core. However, the actual zone has not been recorded in successions studied for ammonites in East Greenland (Birkelund *et al.* 1984) and is therefore indicated with hesitation.

Assemblage: Dominated by *Oligosphaeridium patulum* and *Cribroperidinium* spp. in association with *Circulodinium distinctum*, *Rhynchodiniopsis* spp. and *Sirmiodinium grossii*.

Age: Early Volgian, Late Jurassic.

The conclusive stratigraphy and dating of the drilled succession are illustrated in figure 3.2.29.

Analysis

Organic matter

The Oxfordian mudstones from 234.8–120.06 m of the core contain abundant coalified woody material (Figure 3.2.1F) as well as amorphous organic matter. The Kimmeridgian mudstones from 120.06–10.00 m are dominated by amorphous organic matter (Figure 3.2.1E) together with some structured, terrestrial material. The Volgian sandstones from 10.00–0.00 m is dominated by woody terrestrial material.

Dinoflagellate cysts

Due to unsuccessful break down and removal of amorphous organic matter in samples throughout the core the record of dinoflagellate cyst is sporadic and random. Furthermore,

the identification of species is limited due to paste of organic matter (Figure 3.2.1A-D). The dinoflagellates are also badly preserved and thin-walled specimens may have degraded due to heavy oxidation during preparation in the laboratory. However, important stratigraphic events are recognised, especially when based on robust and abundant species. The dinoflagellate records and events are illustrated in a stratigraphic range-chart (Figure 3.2.2).

Foraminifers and coccoliths

Three shale samples were analysed for microfossils and nannofossils at 190, 198 and 206 meters.

No foraminifers and no *in situ* coccoliths were recovered from these samples. The apparent absence of calcareous microscopic fossils in the Blokely core is probably due to the high content of pyrite and the consequent acidic conditions in the sediment which probably have dissolved calcareous microfossils.

3.2.2 Ammonite stratigraphy

The outcrops of the Hareelv Formation around the drill site at Blokelyv are characterized by a marked lack of ammonites. Various field work participants unsuccessfully attempted to collect and sample ammonites in the surroundings of the drill site in order to obtain a stratigraphical constraint on the top of the core. Not a single ammonite specimen was found. During drilling a few ammonites were recorded in the core. In the laboratory the core was systematically searched for ammonites and showed to contain a large number of ammonite bearing intervals. The uppermost ammonite occurrence is at depth well below the stratigraphic levels exposed in the area surrounding the drill site and may explain the unsuccessful search for ammonites at the surface. The mudstones in the uppermost part of the core are less consolidated than the lower core and therefore the ammonite preservation potential is markedly low. The lack of ammonites in the upper part of the core thus does not necessarily reflect an ammonite barren interval.

In addition to ammonites a number of various other macrofossil groups were recorded: belemnites - represented by both rostra and *Onychites* (hooks from belemnites; Fig. 3.2.3), bivalves (Fig. 3.2.4) and a few remains of vertebrates (bone fragments and teeth). Here focus is on the ammonites, which are a fossil group well-known for its importance for biostratigraphic age assessment.

Material and methods

Ammonites in the Blokelyv core mudstone succession are flattened impressions with the shell material dissolved. Ammonite impressions are generally well-preserved, sometimes excellently preserved. Fragments of ammonites are common. Most ammonites are cut by the drill and therefore only partly visible in the core. However a relatively large number of complete (small) ammonites are present.

In mudstone intervals the core split naturally along bedding-planes. It split particularly well at bedding planes where the presence of ammonite impressions weakens the bedding. Mudstone core pieces were systematically observed for macrofossils at bedding planes at the end of each piece. Ammonites are sometimes visible in section, when the relief of the ribbing forms a characteristic crenulated pattern (Figure 3.2.5). A few specimens were mechanically cleaned.

A total of 42 levels have been sampled for ammonites between depths 81.93 m – 213.84 m, i.e. exclusively in the Hareelv Formation/Katedralen Member. In addition a number of

levels with ammonite fragments were recorded, but estimated not to be of biostratigraphic importance due to bad preservation and accordingly not sampled.

Ammonites are identified mainly from comparison with key-literature with illustrations on Upper Jurassic ammonites from East Greenland (Spath 1935, 1936; Sykes & Surlyk 1976; Sykes & Callomon 1979; Callomon 1985). The ammonite zonation for the Oxfordian–Volgian interval was established by Surlyk *et al.* (1973), Surlyk (1978), Callomon & Birkelund (1980, 1982), Birkelund *et al.* (1984), Birkelund & Callomon (1985) and summarized in Surlyk (1991 fig. 6) (Figure 3.2.6). Callomon & Birkelund (1980, 1982), Birkelund & Callomon (1985) and Callomon (1993) established a succession of Middle–Upper Jurassic faunal horizons in Milne Land and Jameson Land. Faunal horizons are units of highest biostratigraphic resolution. The faunal horizons in Milne Land are labelled M1–M47 and the faunal horizons in Jameson Land are labelled J1–J41 (Figure 3.2.6). Note that at some intervals the resolution of faunal horizons in Greenland is lower than the standard Boreal zonation to which the horizons are referred. Successful identifications of ammonite specimens from the Blokely-1 core are referred to the succession of faunal horizons and their indications of ammonite chronostratigraphic ages.

Ammonite stratigraphy

From top-down:

***A. eudoxus* Zone, Faunal horizon M20**

The uppermost ammonite bearing level in the Blokely core at 81.93 m contains an ammonite referred to as *Amoeboceras* (*Euprionodoceras*) cf. *kochi* Spath, indicating the presence of the basal faunal horizon M20 of the *A. eudoxus* Zone.

***A. mutabilis* Zone, Faunal horizon M19**

The presence of this faunal horizon is indicated by ammonites between depths 85.58 m and 87.63 m mainly from specimens that are referred to the index species of this biostratigraphic unit.

***R. cymodoce* Zone**

This zone is indicated by the presence of *Pachypictonia?* at depth 91.87 m which is known to occur in faunal horizon M16. The ammonites occurring above are not sufficiently preserved to allow recognition of the faunal horizons M17 and 18. Ammonites of faunal horizon M15, the basal horizon of the *R. cymodoce* Zone, are also not recognized.

***P. baylei* Zone**

In Greenland, this zone is represented by one faunal horizon, M 14. The presence of this horizon in the Blokely core is indicated by the presence of *A. cf. ernsti* at depths 109.25 m and 119.85 m, the index species of the faunal horizon *Pictonia* cf. sp. A Callomon & Birkelund 1985 at depth 110.05 m, and *Amoeboceras* specimens that differs slightly from *A. ernsti* at depths 119.89 m and 120.29 m.

***A. rosenkrantzi* Zone – *A. regulare* Zone**

These zones are represented in Greenland by the undifferentiated faunal horizons M12-13. These are indicated in the Blokely core by the ammonites *Amoeboceras* cf. *bauhini* (depth 122.08 m.), *A. cf. rosenkrantzi* (depth 123.53 m), *A. cf. regulare* (depth 125.43 m), *A. rosenkrantzi* (depths 145.65 m and 155.65 m), *A. freboldi* and *A. cf. freboldi* (depth 147.99 m and 154.34 m, respectively), *Ringsteadia* sp. (depths 157.81 and 157.83 m), *A. regulare* (depth 158.80 m) and *A. cf. marstonense* (depth 159.13 m). In England the ammonite *A. regulare* is known to range only to the top of the *A. regulare* Zone suggesting that the boundary between the *A. regulare* and the *A. rosenkrantzi* Zones may be at a depth between 123.5 and 125.4 m in the Blokely core.

***A. serratum* Zone – *A. glosense* Zone**

The *A. serratum* Zone and the uppermost part of the underlying *A. glosense* Zone are in Greenland represented by the faunal horizon M11, which in the Blokely-1 core is indicated by the presence of an ammonite that resembles either *A. serratum* or *A. koldeweyense* (depth 169.17 m), *Amoeboceras* aff. *glosense* (depth 201.01 m), *A. (Priondoceras) serratum* and *A. (P.) cf. serratum* (depths 208.08 and 206.08 m, respectively). An ammonite referred to as *A. cf. glosense* at depth 208.13 m indicates the faunal horizons M10 or M11, since the species is known to occur in both horizons.

***C. tenuiserratum* Zone**

Ammonites referred to as *Cardioceras* (*Cawtoniceras*) aff. *blakei* or *cawtonense* (depths 211.30 m and 213.84 m) indicate the presence of the faunal horizon M8, which refers to a level close to upper Middle Oxfordian *C. tenuiserratum*.

On basis of ammonite finds all ammonite zones between the Middle Oxfordian *Cardioceras tenuiserratum* Zone and the Middle Kimmeridgian *Aulacostephanus eudoxus* Zone thus appear to be represented in the Blokely-1 core. The core thus seems to represent an interval of unbroken deposition, although the presence of all known Greenland subzones and faunal horizons are not proven by ammonites.

The ammonite stratigraphy is summarized in Table 3.2.27 and Figs 3.2.28–29.

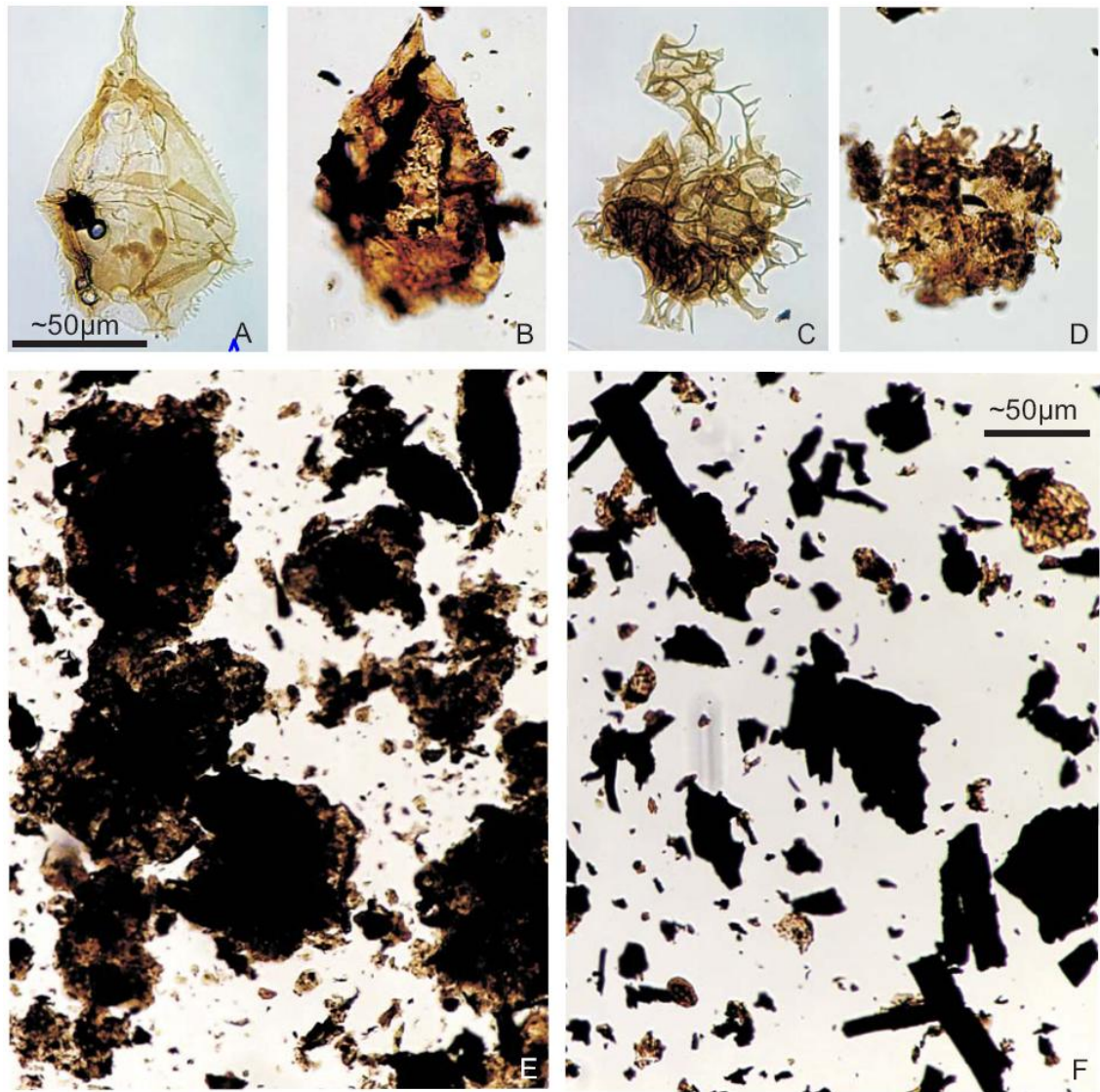


Figure 3.2.1: A-D illustrates the preservation of the fossil dinoflagellates in the Blokely core by comparing a species from the Blokely core (B & C) with a contemporaneous specimen of the same species from outcrop sample material from the near by Milne Land (A & B). A -B; *Gonyaulacysta jurassica* and C-D; *Adnathosphaeridium "hartzii"*. E: Amorphous organic material from the oil prone sediments in the Blokely core. F: Organic matter of black woody material from the Blokely core with no hydrocarbon potential.

Figure 3.2.2: Stratigraphic range-chart of dinoflagellates, acritarchs and algae in the Blokely core. Stratigraphic important dinoflagellate events and their correlation to ammonite zones are presented, together with the chronostratigraphic interpretation.

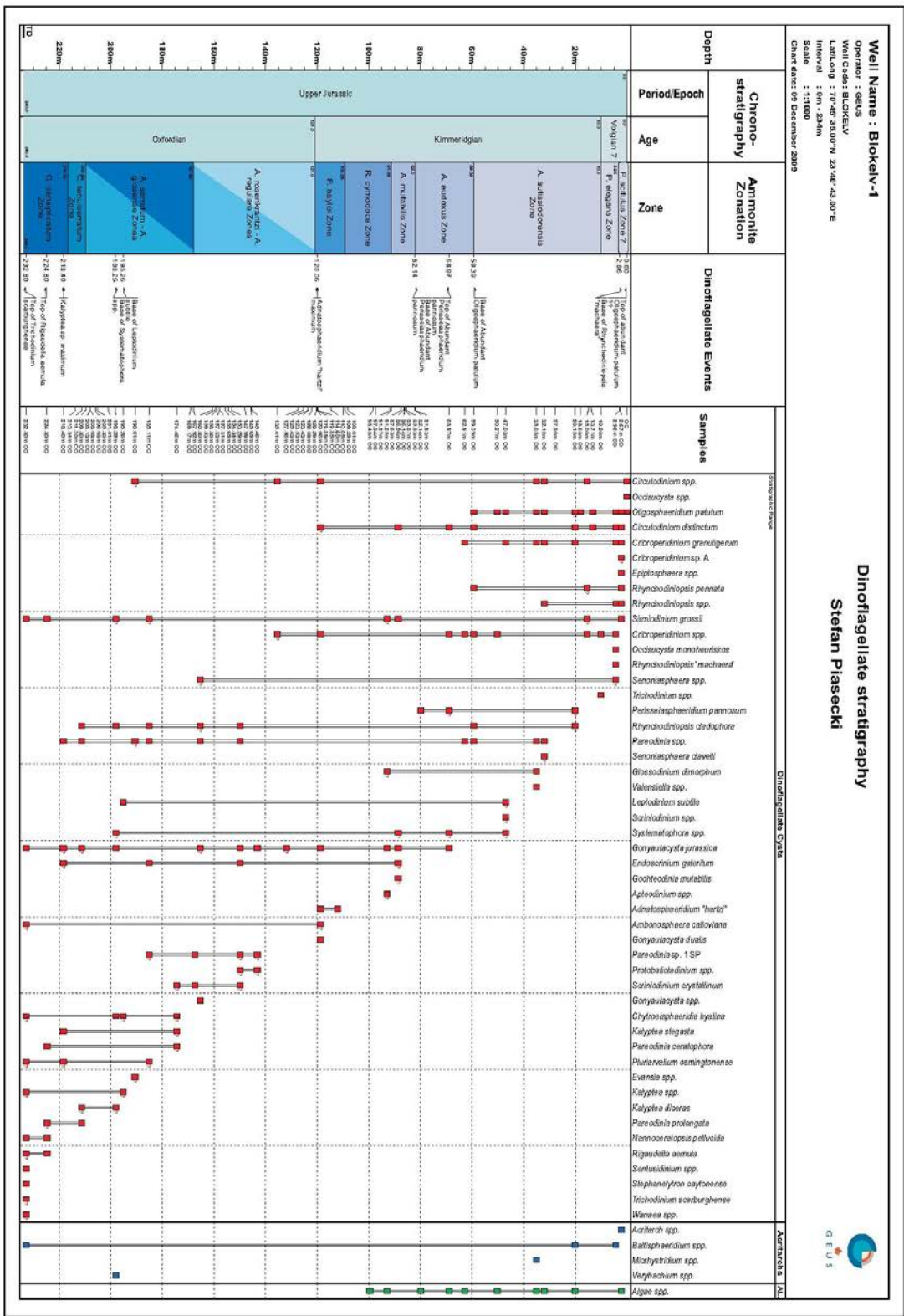




Figure 3.2.3: *Onychites*, hook from belemnite, from depth 34.01 m Diameter of core is 56 mm.

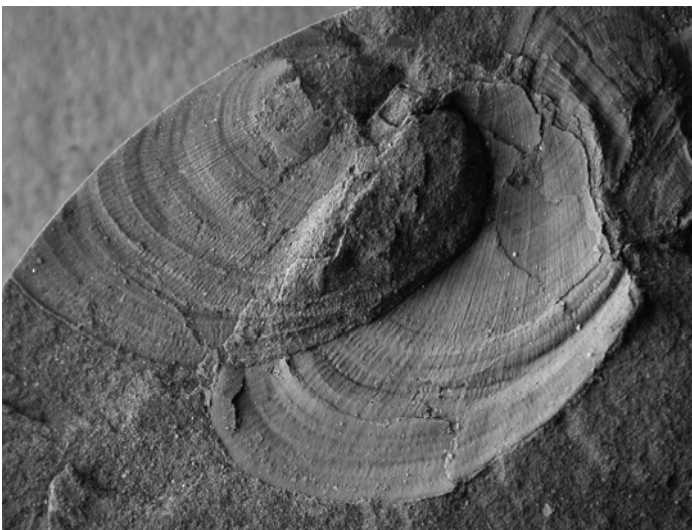


Figure 3.2.4: Bivalve with both valves lying in contact (from depth 87.32 m). The width of the photo is c. 3 cm.



Figure 3.2.5: Core piece viewed from side showing characteristic crenulations of bedding plane formed by ammonite ribbing. Diameter of core is 56 mm.

CHRONOSTRATIGRAPHY				AMMONITE STRATIGRAPHY			
System	Series	Stage	Substage	Zone/Subzone	Faunal horizons		
				Surlyk 1978a, 1991, Sykes & Callomon 1979, Callomon & Birkelund 1980, 1982, Birkelund et al. 1984, Birkelund & Callomon 1985	Index species in bold. Numbering from Jameson Land (J38-J41) after Callomon 1993, 2003; from Milne Land (M2-M47) after Callomon & Birkelund 1982, Birkelund et al. 1984, Birkelund & Callomon 1985		
Jurassic	Upper	Volgian	Upper	<i>Praechetaites tenuicostatus</i> Zone	M 47 <i>Laugeites groenlandicus</i> Spath, <i>Crenodontes</i> cf. aff. subgorei Spath <i>elegans</i> Spath <i>Crenodontes angustus</i> Spath, <i>Crenodontes egyptus</i> Spath, <i>Crenodontes leslei</i> Spath <i>Crenodontes subregularis</i> Spath, <i>Dorsoplanites</i> sp. M 46 <i>Pavlovia</i> aff. subgorei (Spath) M 45 <i>Dorsoplanites intermissus</i> Callomon & Birkelund M 44 <i>Pavlovia groenlandica</i> (Spath), <i>Pavlovia</i> sp., <i>Dorsoplanites</i> aff. <i>gracilis</i> Spath M 43 <i>Epipalasiceras pseudoapertum</i> Spath, <i>Epipalasiceras praecox</i> incl. <i>E. tumidum</i> Spath <i>Dorsoplanites maximus</i> Spath, <i>Dorsoplanites gracilis</i> Spath M 42 <i>Epipalasiceras acutifurcatum</i> Callomon & Birkelund M 41 <i>Epipalasiceras rotundiforme</i> Spath, <i>Dorsoplanites gracilis</i> Spath, <i>Dorsoplanites alderingi</i> Spath, <i>Dorsoplanites crassus</i> Spath, <i>Dorsoplanites triplex</i> var. <i>mutabilis</i> Spath, <i>Pavlovia</i> sp. M 40 <i>Dorsoplanites gracilis</i> & Spath, <i>Pavlovia</i> sp. M 39 <i>Dorsoplanites antiquus</i> Spath / <i>transitorius</i> Spath M 38 <i>Dorsoplanites iiostracus</i> Callomon & Birkelund, <i>Pavlovia corona</i> Callomon & Birkelund, <i>Dorsoplanites gracilis</i> y Spath, <i>Pavlovia</i> sp. M 37 <i>Dorsoplanites gracilis</i> & Spath M 36 <i>Pavlovia variocostata</i> Callomon & Birkelund M 35 <i>Pavlovia communis</i> Spath, <i>Pavlovia regularis</i> Spath, <i>Pavlovia subaperta</i> Spath, <i>Pavlovia perinflata</i> Spath, <i>Dorsoplanites gracilis</i> u Spath M 34 <i>Pavlovia rugosa</i> Spath, <i>Pavlovia alterniplicata</i> Spath / <i>kochi</i> Spath, <i>Pavlovia inflata</i> Spath, <i>Pavlovia alluvigatoides</i> Spath / <i>similis</i> Spath, <i>Pavlovia variabilis</i> Spath, <i>Dorsoplanites</i> sp. M 33 <i>Pavlovia latrensis</i> Ilovisky, <i>Dorsoplanites</i> cf. and aff. <i>dorsoplanis</i> (Vishniakov) M 32 <i>Dorsoplanites primus</i> Callomon & Birkelund, <i>Pavlovia</i> sp. M 31 <i>Paravirgatites</i> sp. B M 30		
			Middle	<i>Epipalasiceras pseudoapertum</i> Zone		M 29 <i>Paravirgatites</i> sp. A, P. aff. <i>devillei</i> Spath, P. cf. <i>boidini</i> Spath M 28 <i>Pectinatites eastlecoctensis</i> Salfeld, <i>Pectinatites</i> (<i>Pectinatites</i>) cf. <i>pectinatus</i> (Phillips), <i>Pectinatites</i> (<i>Pectinatites</i>) cf. <i>cornuifer</i> (Buckman) M 27 <i>Pectinatites groenlandicus</i> Spath, <i>Pectinatites</i> (<i>Pectinatites</i>) aff. <i>eastlecoctensis</i> Salfeld, <i>Pectinatites</i> (<i>Pectinatites</i>) cf. <i>cornuifer</i> (Buckman), <i>Pectinatites</i> (<i>Wheatleyites</i>) <i>rarescens</i> Buckman M 26 <i>Pectinatites</i> cf. <i>abbreviatus</i> Cope M 25 <i>Sphinctoceras</i> spp., <i>Pectinatites</i> (<i>Virgatospinctoides</i>) <i>smedmorensis</i> Cope, and <i>latiocostatus</i> Cope, <i>Sphinctoceras</i> (<i>Eosphinctoceras</i>) cf. or. aff. <i>magnus</i> Mesezhnikov, or <i>distant</i> Neaverson, M 24 <i>Pectinatites elegans</i> Cope, <i>Pectinatites</i> (<i>Virgatospinctoides</i>) major Cope, <i>Pectinatites</i> (<i>Virgatospinctoides</i>) spp.	
			Lower	<i>Pectinatites pectinatus</i> Zone		M 23 <i>Aulacostephanus</i> sp. cf. or aff. <i>Au. kirghisensis</i> (d'Orbigny) M 22 <i>Amoeboceras elegans</i> Spath M 21 <i>Amoeboceras</i> (<i>Hoplcardioceras</i>) <i>decipiens</i> Spath, <i>Aulacostephanus eudoux</i> (d'Orbigny) M 20 <i>Amoeboceras</i> (<i>Euprionodoceras</i>) <i>kochi</i> Spath M 19 <i>Rasenina borealis</i> Spath, <i>Aulacostephanus mutabilis</i> (Sowerby), <i>Aulacostephanus</i> (<i>Aulacostephanites</i>) cf. <i>Au. (A.) euclensis</i> Arkell, <i>Amoeboceras</i> (<i>Amoebites</i>) cf. <i>A. (A.) beaugrandi</i> (Sauvage), <i>Streblites?</i> cf. <i>S. fairmyensis</i> Mesezhnikov M 18 <i>Rasenina evoluta</i> Spath M 17 <i>Rasenina cymodoce</i> (d'Orbigny), <i>Amoeboceras</i> (<i>Amoebites</i>) aff. <i>A. (A.) subkitchini</i> Spath, <i>Amoeboceras</i> (<i>Amoebites</i>) aff. <i>A. (A.) rasense</i> Spath, M 16 <i>Rasenina inconstans</i> Spath, <i>Pachypictonia?</i> Sp. nov. C Birkelund & Callomon, <i>Amoeboceras</i> (<i>Amoebites</i>) aff. <i>A. (A.) subkitchini</i> Spath, <i>Amoeboceras</i> (<i>Amoebites</i>) aff. <i>A. rasense</i> Spath M 15 <i>Rasenina inconstans</i> Spath, <i>Amoeboceras</i> (<i>Amoebites</i>) <i>subkitchini</i> Spath, <i>Amoeboceras</i> (<i>Amoebites</i>) aff. <i>A. (A.) rasense</i> Spath M 14 <i>Pictonia</i> sp. nov. A Birkelund & Callomon, aff. <i>normandiana</i> Tornquist, <i>Amoeboceras</i> (<i>Amoebites</i>) <i>bayli</i> Birkelund & Callomon, A. (<i>Amoebites</i>) sp. aff. <i>A. (A.) schulginae</i> Mesezhnikov, A. (<i>Amoebites</i>) cf. <i>A. (A.) ernesti</i> (Fischer)	
				<i>P. paravirgatus</i> Subzone		M 12-13 <i>Amoeboceras regulare</i> Spath, <i>Amoeboceras rosenkrantzii</i> Spath, <i>Amoeboceras freboldi</i> Spath, <i>Amoeboceras marstonense</i> Spath, <i>Amoeboceras bauhini</i> (Oppel), <i>Ringsteadia</i> sp. cf. and aff. <i>pseudocordata</i> (Blake & Huddleston) M 11 <i>Amoeboceras</i> (<i>Prionodoceras</i>) <i>serratum</i> (Sowerby), <i>Amoeboceras</i> (<i>Prionodoceras</i>) <i>damoni</i> Spath, <i>Amoeboceras</i> (<i>Prionodoceras</i>) <i>glosense</i> (Bigot & Brasil), <i>Decipia</i> sp. M 10 <i>Amoeboceras</i> (<i>Prionodoceras</i>) cf. <i>glosense</i> (Bigot & Brasil) M 9 + J 41 <i>Amoeboceras</i> (<i>Prionodoceras</i>) <i>transitorius</i> Spath, <i>Amoeboceras</i> (<i>Prionodoceras</i>) <i>illoviskyi</i> (M. Sokolov), <i>Perisphinctes</i> spp., <i>Decipia</i> cf. <i>indensis</i> Arkell M 8 <i>Cardioceras</i> (<i>Cawtoniceras</i>) <i>cawtonense</i> (Blake and Huddleston), <i>Cardioceras</i> (<i>Maltoniceras</i>) cf. <i>maltonense</i> (Young and Bird), <i>Cardioceras</i> (<i>Maltoniceras</i>) <i>bodeni</i> Maire, <i>Cardioceras</i> (<i>Maltoniceras</i>) <i>tenuisserratum</i> (Oppel) M 7 <i>Perisphinctes</i> (<i>Krisphinctes</i>) cf. or aff. <i>maximum</i> (Young and Bird) M 6 + J 40 <i>Cardioceras</i> (<i>Vertebriceras</i>) <i>densiplicatum</i> Boden, <i>Cardioceras</i> ? <i>Cardioceras</i> cf. <i>bipplanum</i> Maire, <i>Cardioceras</i> <i>Plasmatoceas</i> cf. <i>popilaniense</i> Boden, <i>Cardioceras</i> <i>Scotcardioceras</i> <i>excavatum</i> (Sowerby) M 5 <i>Cardioceras</i> <i>Plasmatoceas</i> <i>tenuicostatum</i> (Nikitin), <i>Cardioceras</i> <i>Plasmatoceas</i> <i>popilaniense</i> Boden M 4 <i>Cardioceras</i> <i>Cardioceras</i> cf. <i>costicardia</i> Buckman, <i>Cardioceras</i> <i>Cardioceras</i> cf. <i>costicardia</i> var. <i>laqueus</i> Arkell, <i>Cardioceras</i> <i>Pachycardioceras</i> cf. <i>anacanthum</i> Buckman, <i>Cardioceras</i> <i>Pachycardioceras</i> cf. <i>magnicanthum</i> Arkell J 39 <i>Cardioceras</i> <i>alphanordatum</i> Spath M 3 + J 38 <i>Cardioceras</i> (<i>Scarburoceas</i>) cf. <i>scarburensse</i> (Young and Bird) trans. to Q woodhamense Arkell	
				<i>P. eastcottensis</i> Subzone			
				<i>Pectinatites huddlestoni</i> Zone			
				<i>Pectinatites wheateleyensis</i> Zone			
				<i>Pectinatites elegans</i> Zone			
			Kimmeridgian	Upper		<i>Aulacostephanus autissiodorensis</i> Zone	
				Middle		<i>Aulacostephanus eudoux</i> Zone	
						<i>Aulacostephanus mutabilis</i> Zone	
				Lower		<i>Rasenina cymodoce</i> Zone	
				<i>Pictonia baylei</i> Zone			
		Oxfordian		Upper	<i>A. rosenkrantzii</i> Zone	<i>A. (Amoebites)</i> <i>bauhini</i> Subzone <i>A. (Prionodoceras)</i> <i>marstonense</i> Subzone	
					<i>Amoeboceras regulare</i> Zone	<i>A. (Prionodoceras)</i> <i>serratum</i> Subzone <i>A. (Amoeboceras)</i> <i>koldewyense</i> Subzone	
					<i>Amoeboceras serratum</i> Zone		
				<i>Amoeboceras</i> (<i>Prionodoceras</i>) <i>glosense</i> Zone	<i>A. glosense</i> Subzone <i>A. (A.)</i> <i>illoviskii</i> Subzone		
			Middle	<i>Cardioceras tenuisserratum</i> Zone	<i>C. (Cawtonic)</i> <i>blakei</i> Subzone <i>C. (Mitcard)</i> <i>tenuisserratum</i> Subzone <i>C. (Maltoniceras)</i> <i>maltonense</i> Subzone		
				<i>Cardioceras densiplicatum</i> Zone			
			Lower	<i>Cardioceras cordatum</i> Zone	<i>C. (Vertebriceras)</i> <i>vertebrale</i> Subzone <i>Cardioceras cordatum</i> Subzone <i>Cardioceras costicardia</i> Subzone <i>Cardioceras bukowski</i> Subzone		
				<i>Quenstedtoceras mariae</i> Zone	<i>Cardioceras preacordatum</i> Subzone <i>Cardioceras scarburensse</i> Subzone		

Figure 3.2.6: Upper Jurassic chronostratigraphy with ammonite zonation and succession of faunal horizons recorded in East Greenland.



Figure 3.2.7: *Amoeboeceras (Prionodoceras) cf. kochi* Spath (GGU 511101-413) at level 81.93 m, indicates the faunal horizon M20 and the base of the *A. eudoxus* Zone. Diameter of core is 56 mm.



Figure 3.2.8: *Aulacostephanoides cf. mutabilis* (Sowerby) (GGU 511101-407) at level 85.58 m indicates the faunal horizon M19 and the *A. mutabilis* Zone. Diameter of core is 56mm.



Figure 3.2.9: *Aulacostephanoides cf. mutabilis* (Sowerby) (GGU 511101-402) at level 87.63 m indicates the faunal horizon M19 and the *A. mutabilis* Zone. Diameter of core is 56 mm.



Figure 3.2.10: *Pachypictonia*? (see Birkelund & Callomon 1985 pl. 15 fig. 1) (GGU 511101-420) from level 91.87 m indicates faunal horizon M16 and the *R. cymodoce* Zone. Diameter of core is 56 mm.



Figure 3.2.11: *Pictonia* cf. sp. A Birkelund & Callomon 1985 (GGU 511101-412) at level 110.05 m indicates faunal horizon 14 and the *P. baylei* Zone. Diameter of core is 56 mm.



Figure 3.2.12: *Amoeboceras* (*Amoebites*) cf. *ernsti* (Fischer) (GGU 511101-444) at level 119.85m indicates faunal horizon M14 and the *P. baylei* Zone. Diameter of core is 56 mm.



Figure 3.2.13: *Amoeboceras* (*Amoebites*) aff. *ernsti* (Fischer) (GGU 511101-445) at level 119.89m indicates faunal horizon M14 and the *P. baylei* Zone. Diameter of core is 56 mm.



Figure 3.2.14: *Amoeboceras* (*Amoebites*) aff. *ernsti* (Fischer) (GGU no. 511101-446) at level 120.29 m indicate faunal horizon M14 and the *P. baylei* Zone. Diameter of core is 56 mm.



Figure 3.2.15: *Amoeboceras* cf. *regulare* Spath (GGU 511101-451) at level 125.43 m indicates faunal horizon M12-13 and the *A. regolare* – *A. rosenkrantzi* Zones. Diameter of core is 56 mm.



Figure 3.2.16: *Amoeboceras rosenkrantzi* Spath (GGU 511101-454) at level 145.65 m indicates faunal horizon M12-13 and the *A. regulare* – *A. rosenkrantzi* Zones. Diameter of core is 56 mm.



Figure 3.2.17: *Amoeboceras freboldi* Spath (GGU 511101-434) at level 147.99 m indicates faunal horizon M12-13 and the *A. regulare* – *A. rosenkrantzi* Zones. Diameter of core is 56 mm.



Figure 3.2.18: *Amoeboceras rosenkrantzi* Spath (GGU 511101-435) at level 155.65 m indicates faunal horizon M12-13 and the *A. regulare* – *A. rosenkrantzi* Zones. Diameter of core is 56 mm.

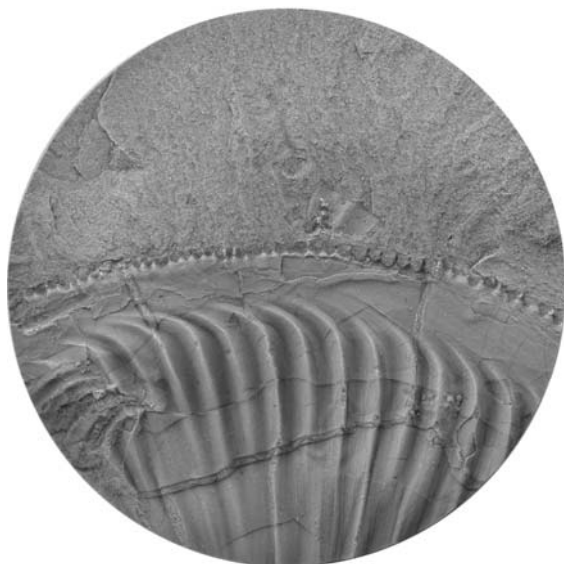


Figure 3.2.19: *Amoeboceras regulare* Spath (GGU 511101-457) at level 158.80m indicates faunal horizon M12-13 and the *A. regulare* – *A. rosenkrantzi* Zones. Diameter of core is 56 mm.



Figure 3.2.20: *Amoeboceras* cf. *marstonense* Spath (GGU 511101-439) at level 159.53 m indicates faunal horizon M12-13 and the *A. regulare* – *A. rosenkrantzi* Zones. Diameter of core is 56 mm.



Figure 3.2.21: *Amoeboceras* cf. *serratum* (Sowerby) or *koldeweyense* Sykes & Callomon (GGU 511101-424) at level 169.17m indicates faunal horizon M11 and the upper *A. glosense* – *A. serratum* Zones. Diameter of core is 56 mm.



Figure 3.2.22: *Amoeboceras* aff. *glosense* (Bigot & Brasil) (GGU 511101-431) at level 201.01m indicates faunal horizon M11 and the upper *A. glosense* – *A. serratum* Zones. Diameter of core is 56 mm.



Figure 3.2.23: *Amoeboceras* (*Prionodoceras*) *serratum* (Sowerby) (GGU 511101-425) at level 206.08 m indicates faunal horizon M11 and the upper *A. glosense* – *A. serratum* Zones. Diameter of core is 56 mm.



Figure 3.2.24: *Amoeboceras* (*Prionodoceras*) cf. *glosense* (Bigot & Brasil) (GGU 511101-426) at level 208.13m indicates faunal horizon M10-M11 and the upper *A. glosense* – *A. serratum* Zones. Diameter of core is 56 mm.



Figure 3.2.25: *Cardioceras* (*Cawtoniceras*) aff. *blakei* Spath or *cawtonense* (Blake & Huddleston) (GGU 511101-432) at level 211.30m indicates faunal horizon M8 and the *C. tenuiserratum* Zone. Diameter of core is 56 mm.

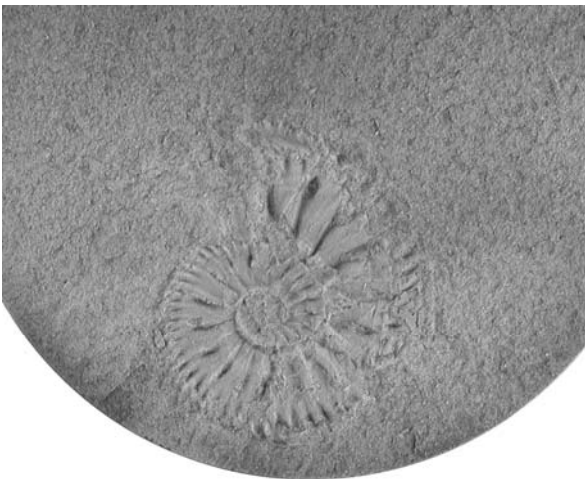


Figure 3.2.26: *Cardioceras* (*Cawtoniceras*) aff. *blakei* Spath or *cawtonense* (Blake & Huddleston) (GGU 511101-433) at level 213.84m indicates faunal horizon M8 and the *C. tenuiserratum* Zone. Diameter of core is 56 mm.

Depth	Ammonite taxon	Faunal horizon	Ammonite Zone
81.93 m	<i>Amoeboceras</i> (<i>Euprionodoceras</i>) cf. <i>kochi</i> Spath	M20	<i>A. eudoxus</i>
85.58 m	<i>Aulacostephanoides</i> cf. <i>mutabilis</i> (Sowerby)	M19	<i>A. mutabilis</i>
85.87 m	<i>Aulacostephanoides</i> cf. <i>mutabilis</i> (Sowerby)	M19	
86.14 m	<i>Aulacostephanoides</i> sp. indet.		
87.63 m	<i>Aulacostephanoides</i> cf. <i>mutabilis</i> (Sowerby)	M19	<i>A. mutabilis</i>
91.87 m	<i>Pachypictonia</i> ? sp	M16	<i>R. cymodoce</i>
97.34 m	<i>Amoeboceras</i> sp. indet.		
108.01 m	<i>Amoeboceras</i> sp. indet.		
108.93 m	<i>Amoeboceras</i> sp. indet.		
109.25 m	<i>Amoeboceras</i> (<i>Amoebites</i>) cf. <i>ernsti</i> (Fischer)	M14	<i>P. baylei</i>
110.05 m	<i>Pictonia</i> cf. sp. A Birkelund & Callomon 1985	M14	<i>P. baylei</i>
119.85 m	<i>Amoeboceras</i> (<i>Amoebites</i>) cf. <i>ernsti</i> (Fischer)	M14	<i>P. baylei</i>
119.89 m	<i>Amoeboceras</i> (<i>Amoebites</i>) aff. <i>ernsti</i> (Fischer)	M14	<i>P. baylei</i>
120.29 m	<i>Amoeboceras</i> (<i>Amoebites</i>) aff. <i>ernsti</i> (Fischer)	M14	<i>P. baylei</i>
122.08 m	<i>Amoeboceras</i> (<i>Amoebites</i>) cf. <i>bauhini</i> (Oppel)	M12-13	<i>A. regulare</i> - <i>A. rosenkrantzi</i>
123.53 m	<i>Amoeboceras</i> cf. <i>rosenkrantzi</i> Spath	M12-13	<i>A. regulare</i> - <i>A. rosenkrantzi</i>
125.43 m	<i>Amoeboceras</i> cf. <i>regulare</i> Spath	M12-13	<i>A. regulare</i> - <i>A. rosenkrantzi</i>
145.65 m	<i>Amoeboceras rosenkrantzi</i> Spath	M12-13	<i>A. regulare</i> - <i>A. rosenkrantzi</i>
147.99 m	<i>Amoeboceras freboldi</i> Spath	M12-13	<i>A. regulare</i> - <i>A. rosenkrantzi</i>
154.34 m	<i>Amoeboceras</i> cf. <i>freboldi</i> Spath	M12-13	<i>A. regulare</i> - <i>A. rosenkrantzi</i>
155.65 m	<i>Amoeboceras rosenkrantzi</i> Spath	M12-13	<i>A. regulare</i> - <i>A. rosenkrantzi</i>
157.81 m	<i>Ringsteadia</i> sp.	M12-13	<i>A. regulare</i> - <i>A. rosenkrantzi</i>
157.83 m	<i>Ringsteadia</i> sp.	M12-13	<i>A. regulare</i> - <i>A. rosenkrantzi</i>
158.80 m	<i>Amoeboceras regulare</i> Spath	M12-13	<i>A. regulare</i> - <i>A. rosenkrantzi</i>
159.53 m	<i>Amoeboceras</i> cf. <i>marstonense</i> Spath	M12-13	<i>A. regulare</i> - <i>A. rosenkrantzi</i>
169.17 m	<i>A.</i> cf. <i>serratum</i> (Sowerby) or <i>koldeweyense</i> Sykes & Callomon	M11	<i>A. glosense</i> - <i>A. serratum</i>
201.01 m	<i>Amoeboceras</i> aff. <i>glosense</i> (Bigot & Brasil)	M11	<i>A. glosense</i> - <i>A. serratum</i>
205.30 m	<i>Amoeboceras</i> sp. indet.		
206.08 m	<i>Amoeboceras</i> (<i>Prionodoceras</i>) cf. <i>serratum</i> (Sowerby)	M11	<i>A. glosense</i> - <i>A. serratum</i>
208.08 m	<i>Amoeboceras</i> (<i>Prionodoceras</i>) <i>serratum</i> (Sowerby)	M11	<i>A. glosense</i> - <i>A. serratum</i>
208.13 m	<i>Amoeboceras</i> (<i>Prionodoceras</i>) cf. <i>glosense</i> (Bigot & Brasil)	M10-M11	<i>A. glosense</i> - <i>A. serratum</i>
211.30 m	<i>Cardioceras</i> (<i>Cawtoniceras</i>) aff. <i>blakei</i> Spath or <i>cawtonense</i> (Blake & Huddleston)	M8	<i>C. tenuiserratum</i>
213.84 m	<i>Cardioceras</i> (<i>Cawtoniceras</i>) aff. <i>blakei</i> Spath or <i>cawtonense</i> (Blake & Huddleston)	M8	<i>C. tenuiserratum</i>

Table 3.2.27: Summary of ammonite samples used for biostratigraphic age assessment of the Blokely-1 core.

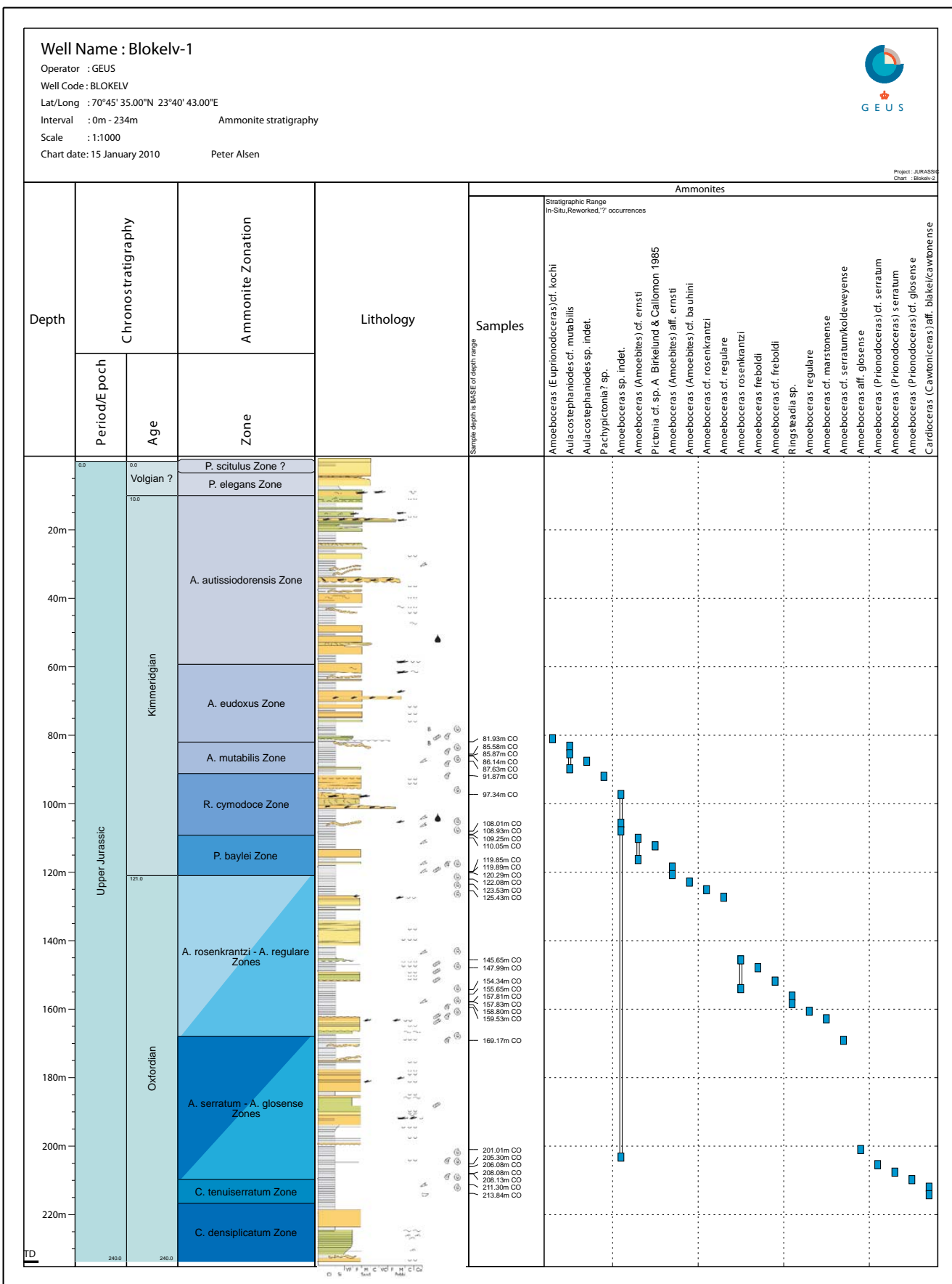


Figure 3.2.28 Chart summarising ammonite taxa recorded in the Blokely core, the ammonite ranges and the biostratigraphic subdivision of the core. Note that the subdivision into ammonite zones is also based on palynostratigraphic analysis (described elsewhere in this report, Section 3.2.1).

3.3 Chemostratigraphy

Chemostratigraphic analyses are applied to the Blokely core to reveal the characteristics of the lithologies, including their potential changes up through the succession. The advantages of whole rock geochemistry are that a large amount of samples can be measured both fast and cheap to give a general description of the mineralogy and thereby making comparisons to adjacent wells possible. The geochemistry further forms a good foundation for deciding where more sophisticated analyses should be carried out, as it gives an overview of representative and extraordinary intervals of the core. The bulk geochemical analyses include identification of major elements along with a large amount of trace elements. Some minerals can be deduced directly from the geochemistry, but SEM, XRD and thin section studies are necessary for precise determination of mineralogy.

Bulk geochemical analyses of 42 samples from the Blokely core were carried out. The selected intervals of the core included 29 sandstones, 4 heteroliths and 9 mudstones. The depths were chosen to give an overview of the various lithologies and facies (see also chapter 4). In addition, in some of the sampled levels other analyses have been carried out (Fig. 3.3.11). A combination of these methods is expected to give a better understanding of the Jurassic depositional environment.

3.3.1 Methods

The bulk geochemistry was measured by ICP-ES (Inductively Coupled Plasma Emission Spectroscopy) and ICP-MS (Inductively Coupled Plasma Mass Spectroscopy) by Acme-Labs, Canada. Two standard samples were made to ensure the quality of the measurements which proved very fine. Major oxides and several minor elements were found by ICP-ES, whereas trace elements were identified by ICP-MS. The REE (Rare Earth Elements), excluding Pm, were included in the measurements. The REE comprise the Light REE (LREE, La-Sm) and the Heavy REE (HREE, Eu-Lu). TOT/C (total carbon) and TOT/S (total sulphur) were measured by Leco analysers. LOI (Loss On Ignition) was measured after heating to 1000°C. The content of oxides is addressed as elements in the text. About 1–2 cm of a half core was used for each measurement, of which the surface of the core

was removed to avoid contamination from the drill mud. The samples were then crushed and 5 gram of each sample was used for the analyses.

3.3.2 Chemical trends

All measured elements of the bulk geochemistry in the 42 samples are listed in Appendix 11.4. Selected elements of the bulk geochemistry are included in Fig. 3.3.1 to give an overview of the chemostratigraphy. The variations in sandstone geochemistry up through the cored succession are shown in Fig. 3.3.2 by excluding the heterolith and mudstone samples. The sandstone samples have larger Si content (average: 77.4 wt%) than the heterolith samples (average: 61.9 wt%) and especially the mudstone samples (average: 51.2 wt%). This is associated with generally smaller contents of most other elements, e.g. Al averaging 7.3 wt% in the sandstones, 14.4 wt% in the heteroliths and 18.6 wt% in the mudstones (App. 11.4). The spread of Si in the sandstones is large (48.4–90.0 wt%), whereas it is more restricted in the heteroliths (57.6–67.4 wt%) and mudstones (44.9–56.6 wt%).

Six sandstone samples (at 37.72, 51.02, 56.43, 151.71, 166.95 and 193.66 m depth) have low Si contents that overlap with the other lithologies, while the remaining 23 sandstone samples have higher contents of Si than all the heterolith and mudstone samples. The 6 low-Si sandstone levels are in proportion to the other sandstone levels characterised by high contents of both Fe (3.8–5.9 wt%), Mg (1.9–5.5 wt%), Ca (2.9–11.7 wt%), Mn (0.07–0.14 wt%), Sr (120.3–342.9 ppm), C (2.0–5.5 wt%) and LOI (8.4–18.3 wt%). The LOI express the amount of volatiles escaping from structural water plus the amount of both organic and inorganic C (Heiri *et al.* 2001) and amounts to 1.6–19.8 wt% when including all samples. LOI correlates well with the C content (Fig. 3.3.1), and is large when the contents of Ca and Mg are large. U, Th and K are found to correlate linearly with the gamma log (Fig. 3.3.11, App. 11.4), but the U log values are almost twice the measured U amount (0.9–17.8 ppm), whereas the K log values are only slightly larger than the measured K (1.1–2.7 wt%), converted from K₂O (1.3–3.3 wt%). The Th values of log and measured chemistry (2.8–22.6 ppm) fit very well.

3.3.3 Chemostratigraphical highlights

The geochemical analyses show that the sandstones are quartz arenites (Fig. 3.3.3), while the mudstones plot in the Fe-rich field, following the classification of Herron (1988). Si is therefore largely expected to express the quartz content (Fig. 3.3.4), while Al is proportional to the content of clay minerals and feldspars. The impact of feldspars on the Al content is especially notable in the sandstones. This is shown by the steeper inclination of the most Si-rich sandstones in the Si-Al plot (Fig. 3.3.4), showing a larger decrease in Al content with increasing Si content.

Some sandstone samples fall outside the Si-Al trend with lower Si content than expected, whereas the Al content is normal. These samples appear to correlate (Fig. 3.3.2) very well with high amounts of Ca, Mg, C and LOI suggesting that a carbonate mineral is present in these samples. This could be dolomite $\text{CaMg}(\text{CO}_3)_2$ if only Ca and Mg were involved, but as also Fe and Mn are found to have some correlation it is assumed to be ankerite $\text{Ca}(\text{Fe,Mg,Mn})(\text{CO}_3)_2$. The absence of a good correlation of Fe to ankerite is due to the presence of Fe in other minerals. Mn is only present in small amounts in ankerite. The correlation of Sr and Ca is caused by substitution of Sr for Ca in the ankerite lattice.

The mudstones contain more Al and Fe than normal mudstone compositions of various ages and areas (Gromet *et al.* 1984) and less Ca, Mg and Mn, when subtracting the LOI values from the results (Table 3.3.1). This shows that the ankerite cementation in the sandstones has depleted the mudstones in these constituents. The Ca-LOI correlation of the ankerite-rich samples (Fig. 3.3.5) is caused by the inorganic C content in the ankerite, whereas the high LOI of the mudstones and heteroliths (Fig. 3.3.1) is caused by a combination of organic matter and structural water of the clay minerals.

The ankerite-rich samples have similar Al contents as the other sandstone samples (Fig. 3.3.4) indicating that the ankerite precipitation did not influence the formation of clay minerals. A small decrease in Al content is found up through the core in the sandstones (Fig. 3.3.6). The mudstones and heteroliths do not show this trend, which must therefore be caused by sandstone diagenesis, where enhanced clay mineral precipitation and feldspar dissolution correlates with increasing depth. The increasing Na content towards the top of the core (Fig. 3.3.7A) demonstrates that less feldspar has been dissolved in the upper part of the core. The feldspar origin of Na in the sandstones is shown by the trend in a Na-Al plot (Fig. 3.3.7C). The trend of decreasing K content up through the core (Fig. 3.3.7B) reveals that K is more dependent on the amount of clay minerals than Na is, as also shown

by the mutual trend of all lithologies in a K-Al plot (Fig. 3.3.7D). This indicates the presence of K-rich clay minerals like illite. However, the trend is less pronounced than for Al because of the presence of K in K-feldspar.

Zr is almost exclusively incorporated into zircon (ZrSiO_4), and no preferred distribution is found between the different lithologies (Fig. 3.3.8A). This reveals that the zircon grains are uniformly distributed among the sandstones, heteroliths and mudstones, but in varying quantities. The high amount of other elements typically associated with heavy minerals, such as Ti (Fig. 3.3.8B), in the mudstone samples is therefore caused by the high content of clay minerals. However, within the sandstones the Ti content is controlled by the heavy mineral content, as can be seen from the correlation between Ti and Zr. The fine correlation of Fe and S (Fig. 3.3.9) indicates that most S is inorganic and present in pyrite (FeS_2). The two deepest of the heterolith samples correlate with the mudstone trend on the Fe-S plot, whereas the two upper heterolith samples correlate with the sandstone trend. The same can be found on the Zr-Ti plot, but far less pronounced.

The mudstone samples reveal the highest REE-concentrations (Fig. 3.3.10) followed by the heterolith and sandstone samples. All samples are LREE-enriched and have a flat HREE chondrite-normalised pattern. This is a typical crustal composition along with the negative Eu-anomaly. Other trace elements than the REE also correlates to the lithology as exemplified in Fig. 3.3.1 where La and U follows each other closely. The trace elements being present in largest amounts in the mudstones are thus related to the content of clay minerals and organic matter. The ratios between the REE are very similar for almost all samples (Fig. 3.3.10). The only one that differs markedly is the topmost sample at 3.60 m depth being the most HREE-depleted, whereas its LREE content falls intermediary among the sandstone samples. This indicates that the REE have been mobilised and fractionation has favoured some of the HREE which have been removed by weathering near the land surface, whereas the second uppermost sample at 7.41 m depth show no deviation in the REE content.

3.3.4 Conclusions

The Jurassic sandstones of the Blokely core are quartz arenites and the mudstones are Fe-rich. High amounts of Ca and Mg identify the levels with large content of ankerite, which is found scattered in sandstones up through the core. LOI correlates to ankerite in the sand-

stones and to both organic matter and structural water in the mudstones. Precipitation of clay minerals and dissolution of feldspars have been enhanced with increasing depth, as shown by trends with depth in the content of Al, Na and K in the sandstones. The longer stay at slightly higher pressure and temperature for the lower part of the core has caused the mineral reactions to run faster, and the sealing nature of the sills has possibly also increased the diagenesis in the deepest part of the core. The VR results show that the maximum paleotemperature increases from 86 to 121°C down through the core, but the intrusions partly controls this trend (see chapters 7.1 and 10). Zr is largely proportional to the amounts of heavy minerals, which show no preferred distribution within the various lithologies and no correlation to burial depth. The REE displays a typical crustal composition, but some HREE has been mobilised in the uppermost sample due to weathering.

	SiO ₂	Al ₂ O ₃	Fe ₂ O ₃	MgO	CaO	Na ₂ O	K ₂ O	TiO ₂	P ₂ O ₅	MnO	Cr ₂ O ₃
27.38 m	63.95	20.32	8.77	1.43	0.58	0.71	3.11	0.84	0.26	0.02	0.02
60.54 m	63.22	22.80	7.33	1.29	0.42	0.69	3.18	0.90	0.12	0.02	0.02
74.99 m	60.40	22.93	10.15	1.25	0.50	0.63	2.98	0.89	0.23	0.03	0.02
120.20 m	62.19	21.77	7.36	1.49	1.64	0.96	3.36	0.96	0.22	0.04	0.02
142.83 m	63.27	22.61	6.77	1.19	0.31	0.84	3.75	1.05	0.15	0.03	0.03
178.32 m	55.95	27.50	8.84	1.11	0.21	0.73	4.10	1.38	0.11	0.04	0.03
185.23 m	64.77	21.54	6.85	1.19	0.29	0.58	3.46	1.08	0.17	0.04	0.02
209.88 m	62.88	21.12	7.53	1.31	1.65	0.83	3.33	0.95	0.36	0.04	0.02
218.50 m	62.19	22.60	7.31	1.16	0.88	0.60	3.71	1.13	0.38	0.02	0.02

Table 3.3.1. Major element compositions of the mudstone levels shown in wt%. The LOI (Loss On Ignition) wt% has been subtracted from the results.

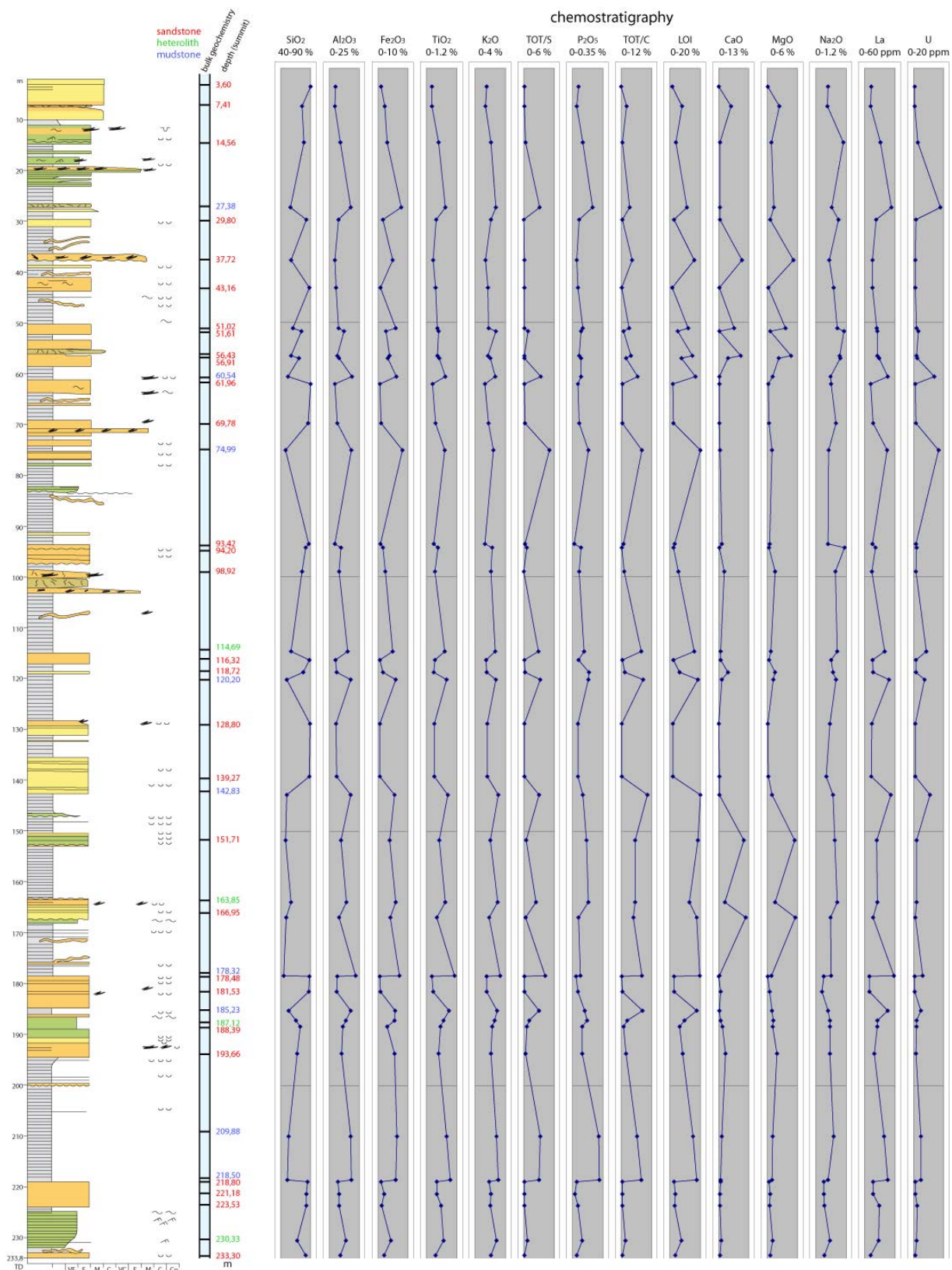


Fig. 3.3.1. Chemostratigraphy of 29 sandstone samples, 4 heteroloth samples and 9 mudstone samples from the Blokely core. The amounts are given in wt% and ppm. The legend of the log refers to Fig. 3.1.2.

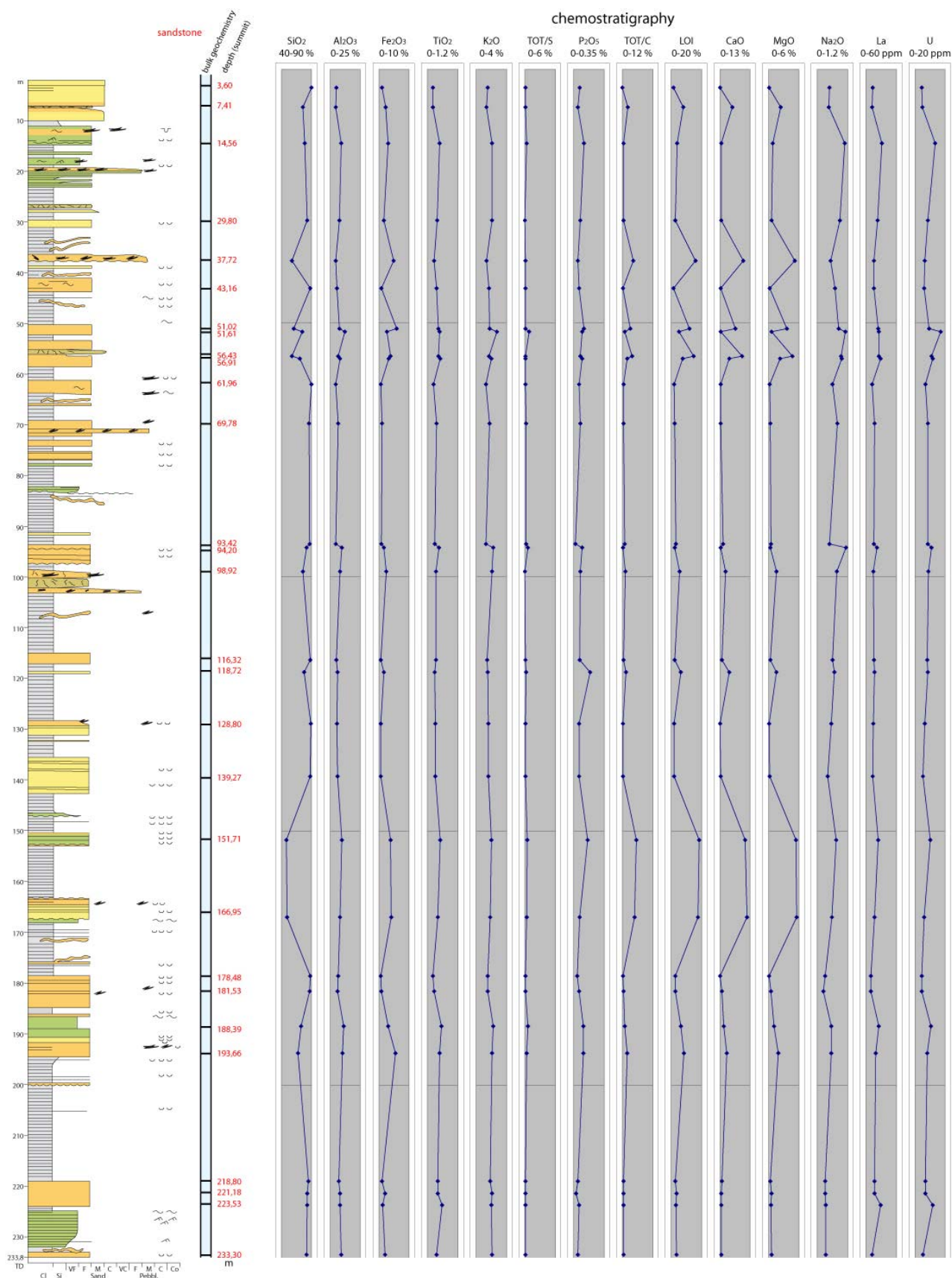


Fig. 3.3.2. Chemostratigraphy only including the 29 sandstone samples from the Blokely core. The amounts are given in wt% and ppm. The legend of the log refers to Fig. 3.1.2.

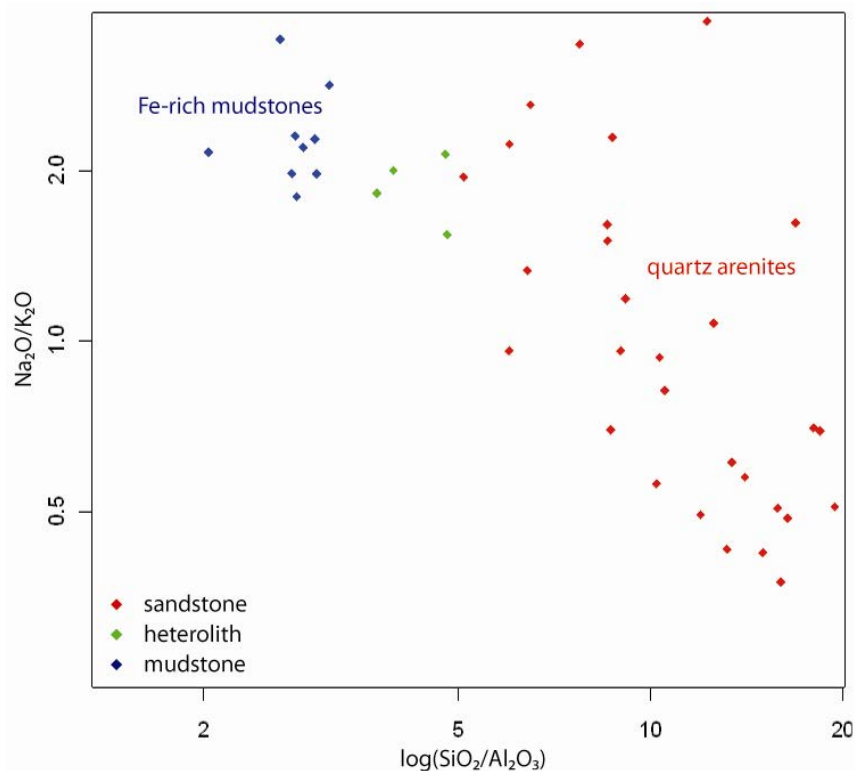


Fig. 3.3.3. Classification of the sandstones as quartz arenites after Herron (1988). The mudstones fall in the Fe-rich category.

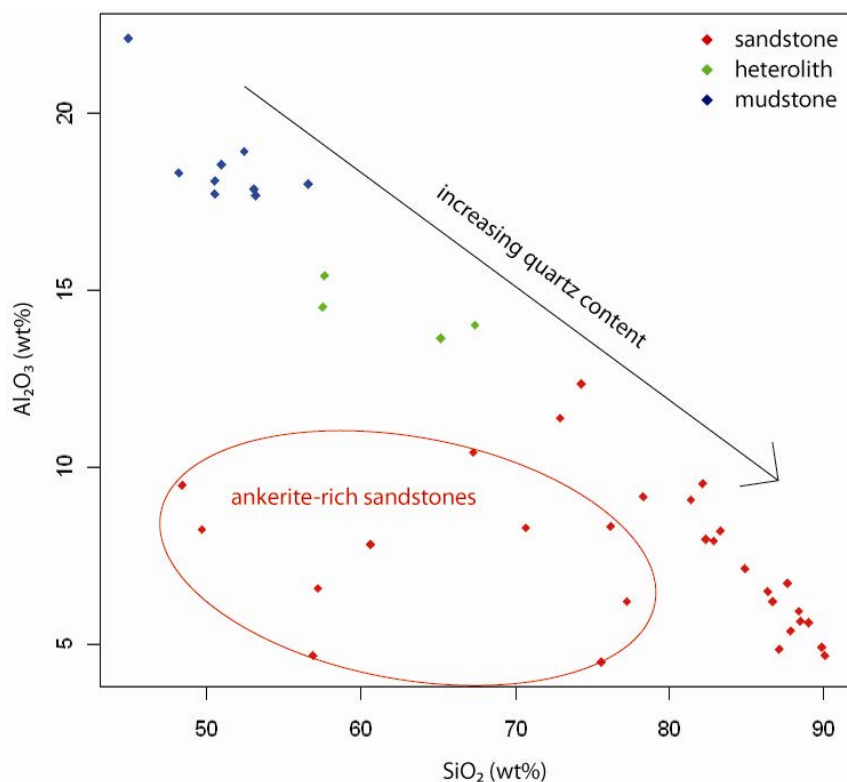


Fig. 3.3.4. The Si-Al ratio is partly proportional to quartz versus clay minerals. The low content of Si in some sandstone samples are caused by high content of ankerite.

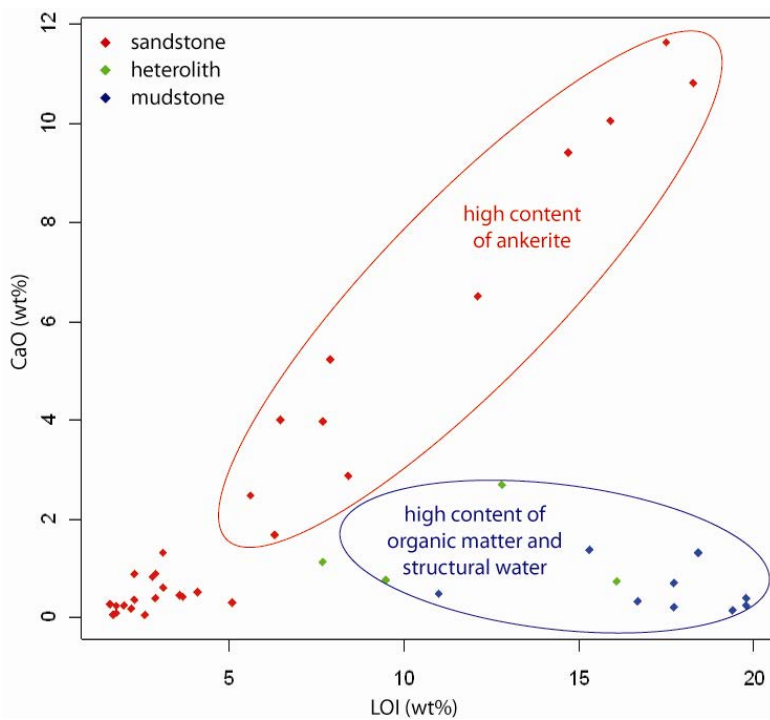


Fig. 3.3.5. The Ca-content expresses the dependency of LOI on the content of ankerite, whereas high LOI-content with no correlation to the Ca-content is caused by organic matter and structural water, which is primarily found in the heteroliths and mudstones.

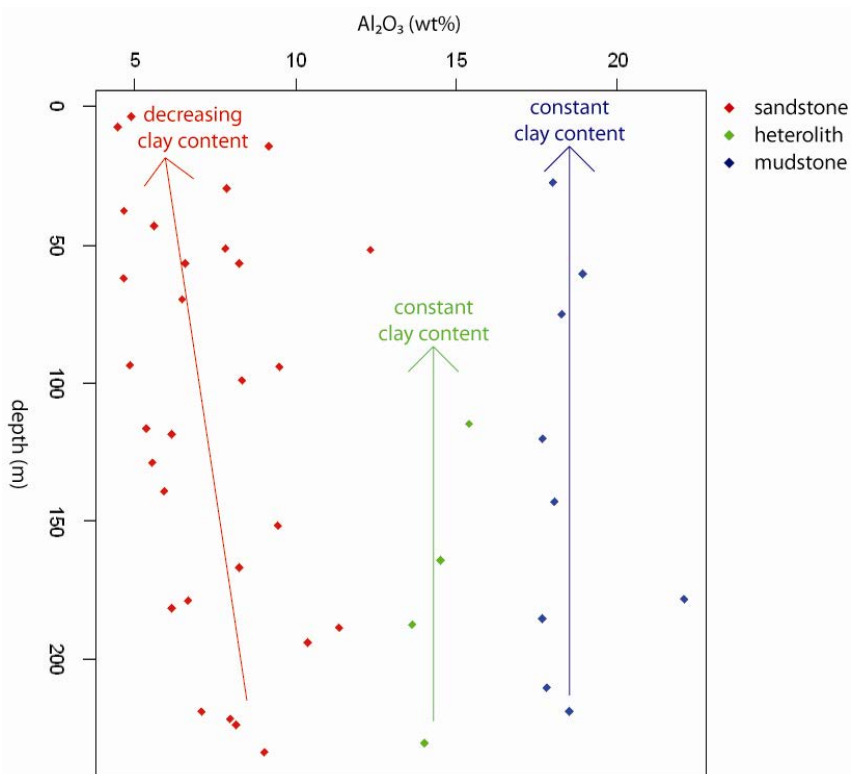


Fig. 3.3.6. The Al-content is largely proportional to the clay mineral content and it is decreasing up though the core for the sandstone samples.

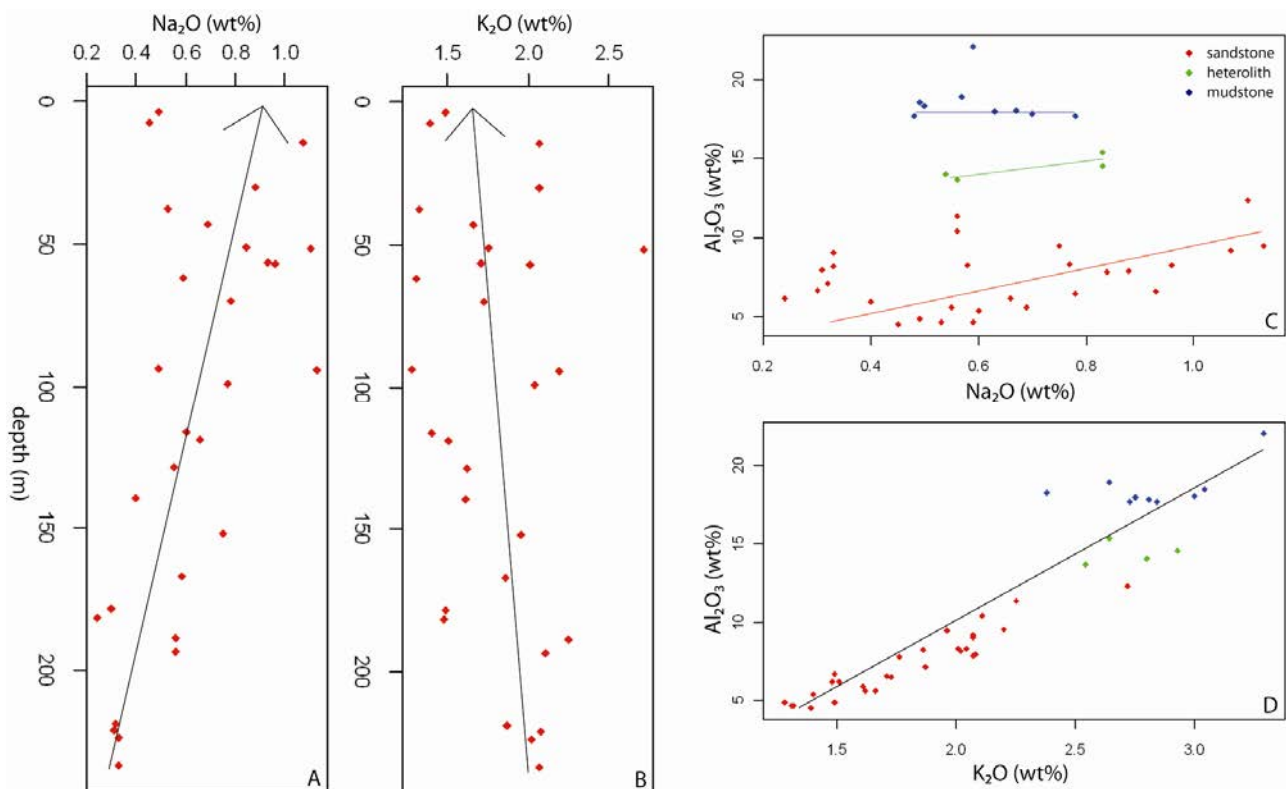


Fig. 3.3.7. A: Increasing Na-content in the sandstone levels up through the core. B: Slightly decreasing K-content. C: Na-Al correlation in the sandstones showing the dependency of Na on feldspar. D: K-Al correlation showing the dependency of K on both feldspar and clay minerals.

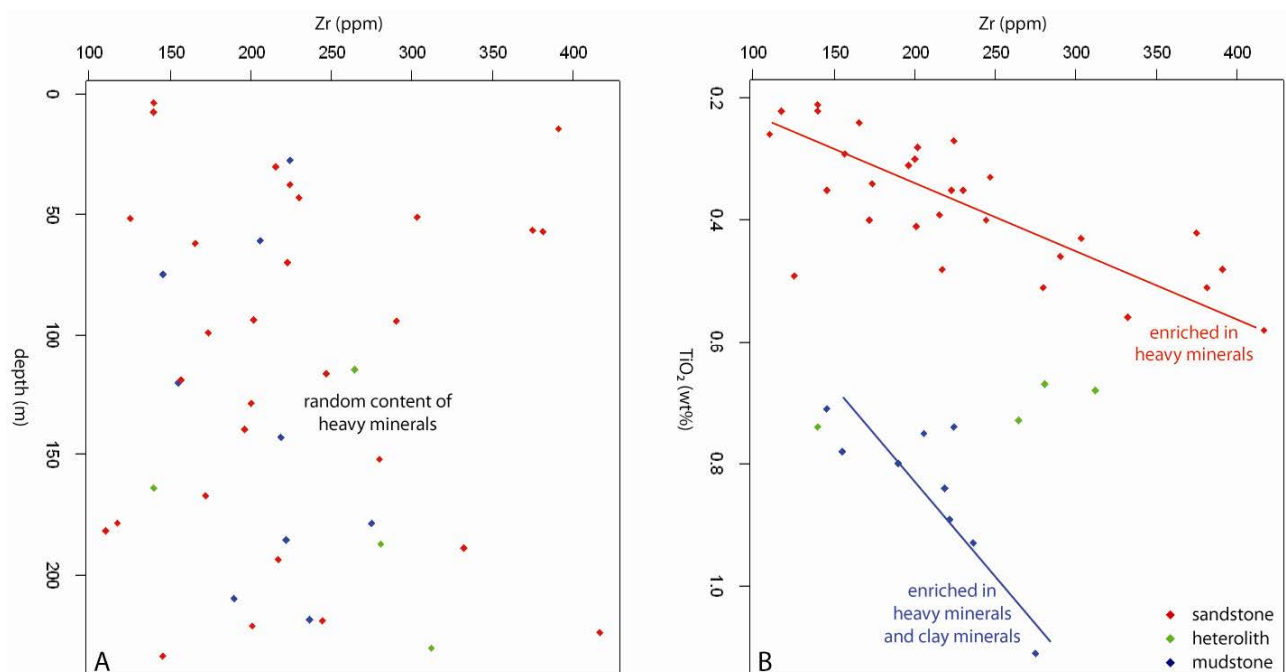


Fig. 3.3.8. A: Random distribution of Zr in the samples signifying random amounts of zircon. B: Zircon correlates with many other heavy minerals including the Ti-oxides. The high Ti-content of the mudstones shows that clay minerals also have an impact on the Ti-content.

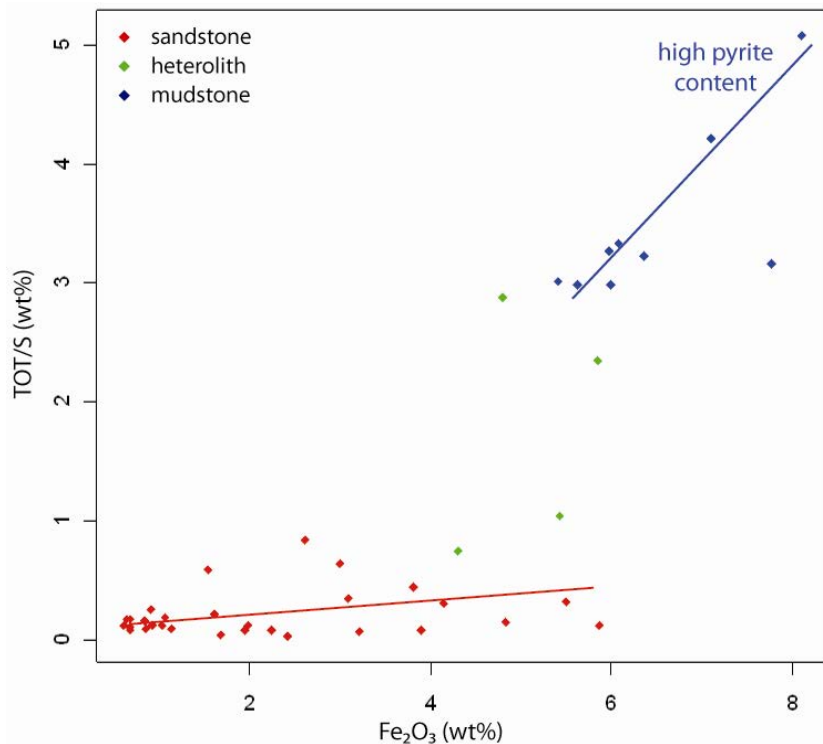


Fig. 3.3.9. The correlating increases in Fe and S shows that a large amount of pyrite is present in the mudstones, whereas only a low content is found in the sandstones.

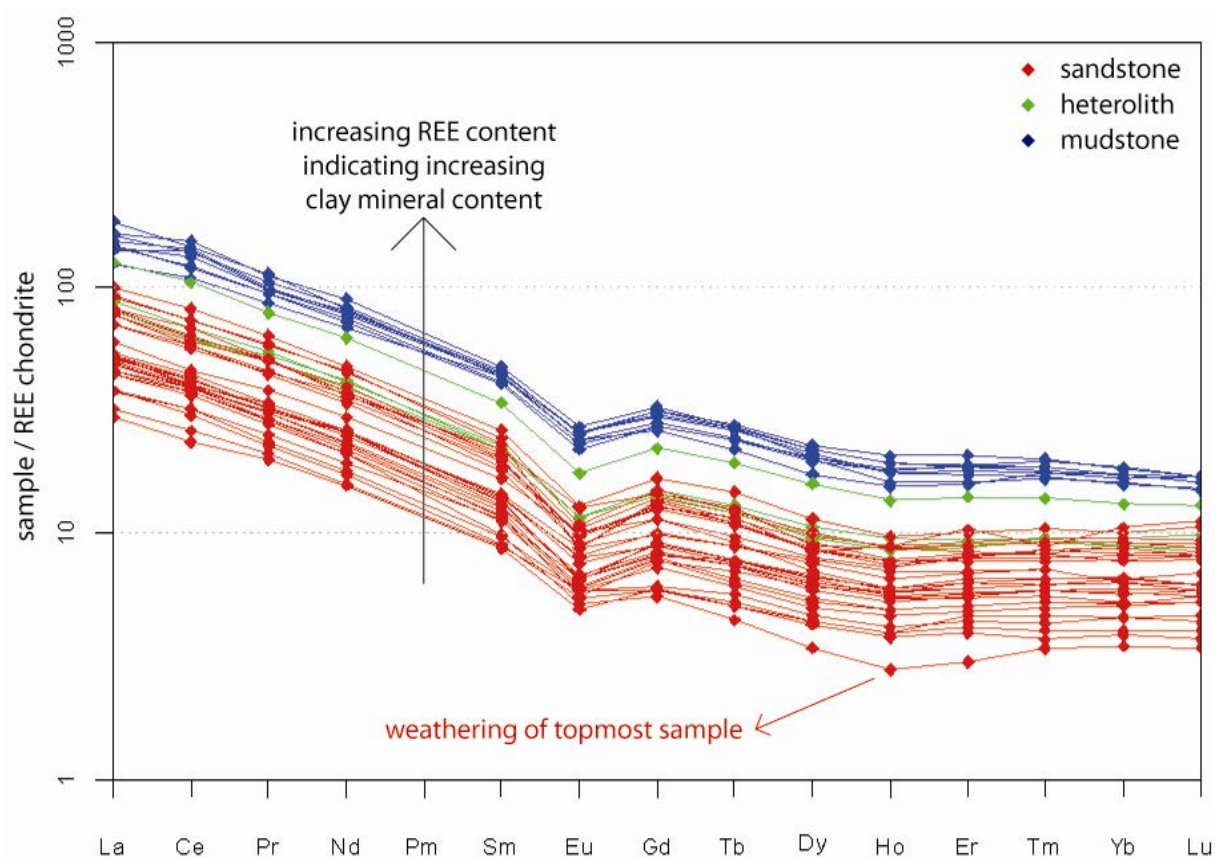


Fig. 3.3.10. The REE abundances are normalised to the chondrite composition of Boynton (1984). The HREE have been mobilised in the topmost sample due to weathering.

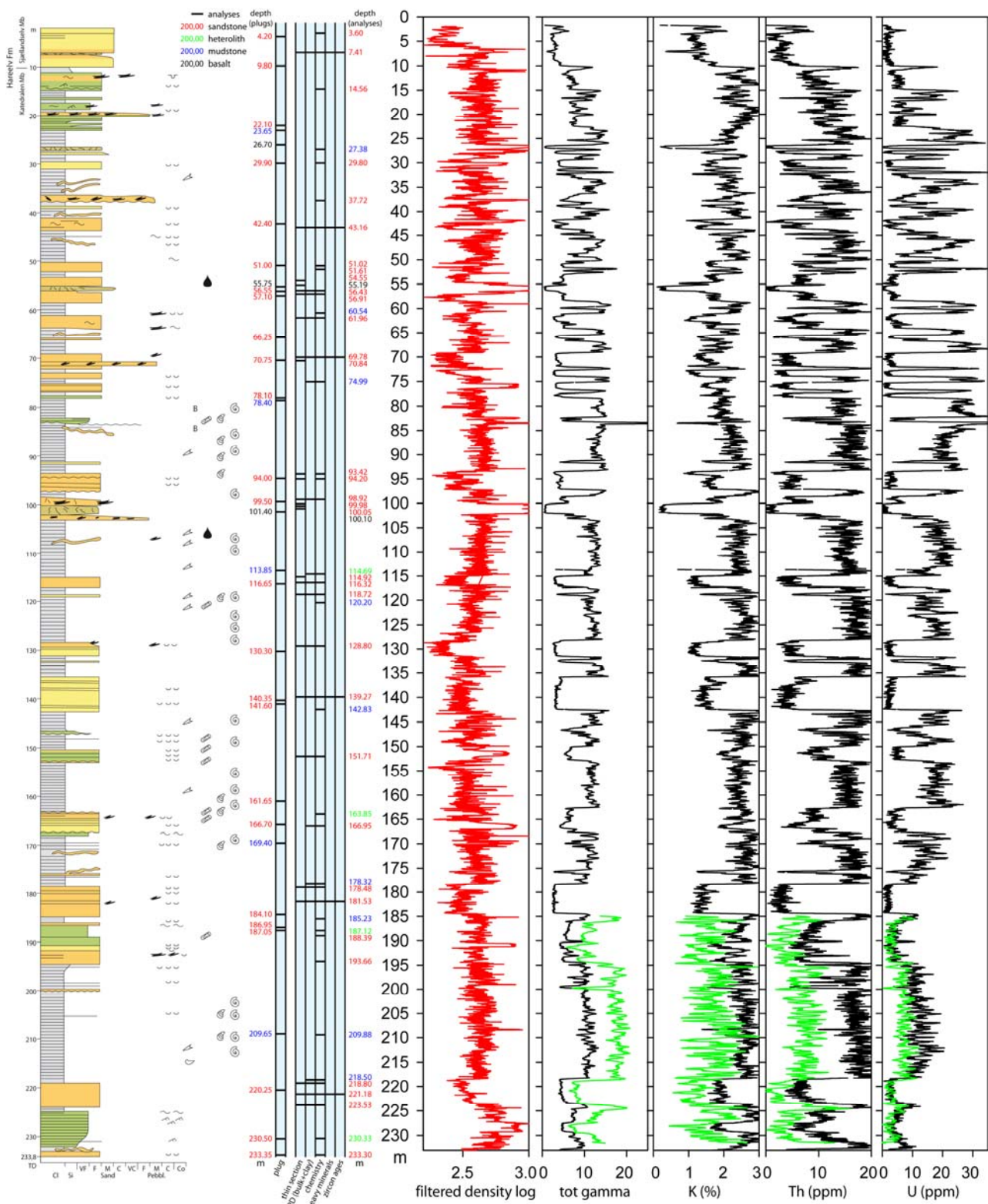


Fig. 3.3.11. Lithological log, filtered density log and spectral gamma log recorded on the core (the green spectral gamma log was recorded in the well). Sampling depths indicated. The legend of the sedimentological log refers to Fig. 3.1.2.

3.4 Petrophysical core log stratigraphy

Petrophysical logs recorded in the Blokely core well include a conductivity log and a spectral gamma log from 232–185 m (Fig. 3.4.1). In GEUS Core Laboratory a complete gamma spectral log and density log were recorded on the entire core and presented in a separate report (Fig. 3.4.2, Appendix 11.8). The petrophysical log stratigraphy combined with the sedimentological log is valuable for characterising the physical properties of lithological units e.g. variation of density in clean sandstone intervals. The spectral gamma log is useful for recording depositional trends in the mudstone dominated intervals.

3.4.1 Methods

A total of 232 meters of core were scanned. The cores were in good condition, with recovery close to 100%. A large majority of the core length presented a full diameter, cylindrical core to the scanner. The fundamental requirement of the scanning procedure, that the scanned material is cylindrical, was therefore fulfilled for a large majority of the cores. Disintegrated sections were very rare. The bulk density log trace gives a good indication of the quality of the core: core sections where significant parts of the core are missing have bulk density traces with large amplitude variations and minimum bulk density readings below 2.2 g/cc.

The core sections were scanned with the spectral gamma and bulk density scanner of GEUS Core Laboratory. The core sections were scanned sequentially with the core sections being fitted together to present the scanner to a continuous core slowly passing the detectors of the scanner. The core sections were scanned without removing the alumina foil because the alumina foil prevented the cores from falling apart. It is estimated that the thin foil had a negligible effect on both the gamma activity and the measured bulk densities, except at the ends of the core sections. At the ends of every core section several layers of alumina foil were present that caused a gap of 0.5 to 1.0 cm between the termination of one core section and the beginning of the next. This created a small attenuation of the spectral gamma activity, and also caused a biased bulk density signal at the core section ends.

Scanning was performed with a speed of 1 cm/min with read-out of the collected gamma and density data every 60 seconds. The spectral gamma data have intrinsically a low signal-to-noise ratio. To improve the readability of the gamma log the spectral gamma data were smoothed with a boxcar filter with a bandwidth of 10 cm. This procedure removes little spatial information from the data as the gamma scanner has a depth resolution of approximately 17 cm. The bulk density data were not smoothed, because these data intrinsically have a high signal-to-noise ratio and a depth resolution of approximately 1 cm. Therefore, smoothing is not necessary.

Filtering of the density data was done in order to remove the large amplitude variations caused by missing core, crushed core or from gaps between the termination of one core section and the beginning of the next. The filtering was performed in a way that the original high signal-to-noise ratio and depth resolution of approximately 1 cm is preserved.

The calculation of the K, U and Th concentrations assumes a bulk density of 2.4 g/cc. This value is determined as the mean value for the upper envelope of the bulk density log trace. More details of the analytical methods are presented in Appendix 11.8.

The Blokely core was partially water saturated during the spectral gamma and bulk density scanning. A total of 7 core pieces were weighed before scanning, after scanning, and finally after drying in an oven at 60 °C for at least 70 hours. The oven drying reduced the bulk density of the core pieces with 0.00–0.20 g/ml. Assuming a grain density of 2.65 g/ml for 3 core pieces of clean sandstone further indicated that these core pieces were nearly 100% saturated with water when they were scanned. These findings indicate that the spectral gamma and bulk density results of the present report pertain to a water saturated core.

The scanning was conducted in two runs, identified as Run A and Run B, each beginning with a calibration of the scanner. The cores of box numbers 1 to 31 were scanned in Run A and the cores of box number 31 to 63 were scanned in Run B. The cores of Box 31 were scanned in both Run A and Run B, and therefore, constitute a repeated section with information about reproducibility. Information about the repeated section and accuracy and reproducibility is presented in Appendix 11.8.

The spectral gamma log and the bulk density log are presented as follows in Appendix 11.8:

- 1) on a single A4 sheet at scale 1:1000 in Enclosure 1
- 2) on a single A3 sheet at scale 1:700 in Enclosure 2
- 3) on a single A4 sheet at scale 1:50 in Enclosure 3

3.4.2 Results

The conductivity log was measured in saline waters to avoid freezing of formation water in the well Fig 3.4.1. The log shows a prominent positive peak at the base of the casing at 21 m. The igneous intrusion at about 27 m is marked by a positive peak, whereas the igneous intrusions at about 55 m and 100 m are marked by combined positive and negative peaks. Positive excursions are recorded at 83 m, 110–118 m, 173 m, and from 195–218 m in predominantly mudstone dominated intervals.

Signatures of the density log and spectral gamma logs (Fig. 3.4.2.)

Sandstones are characterised by alternating units of low, medium and high densities. Total Gamma records in general low values in sandstones (2–5 cps). Massive homogenous sandstone units commonly record a box-shape log trace. Sandstones with abundant mudstone intraclasts show slightly higher gamma values. The potassium and thorium readings occasionally show an increasing upward trend in sandstone units, whereas the uranium readings are rather constant.

Mudstones are characterised by high Total Gamma values (9–8 cps). The Total Gamma in mudstones as reflected by the uranium signal show an overall upward increase stratigraphically, which can be subdivided into three main successions with several minor increasing and decreasing trends in the mudstone intervals of the Katedralen Member. The lower succession from 233–185 m is characterised by relatively low uranium values and shows an increasing trend followed by a decreasing trend. The middle succession from 185–103 m is characterised by medium uranium values, and shows an increasing upward trend in the lower part (178–168 m) and two decreasing upward trends from 128–119 m and 110–103 m. The upper succession from 103–10 m is characterised by relatively high uranium values in the mudstone units, and shows a prominent upward increasing trend from 91–83.5 m. Both potassium and thorium show no overall trends stratigraphically.

Heterolithic sandstone-mudstone intervals is characterised by intermediate Total Gamma values, and the variations reflects the overall sandstone to mudstone ratios. The main heterolithic intervals are recorded roughly from 231–225 m, 191–186 m and 23–12 m.

Igneous intrusions are characterised by very high density readings (around 3 g/cc). The Total Gamma values (<2 cps) are very low as represented by the potassium values.

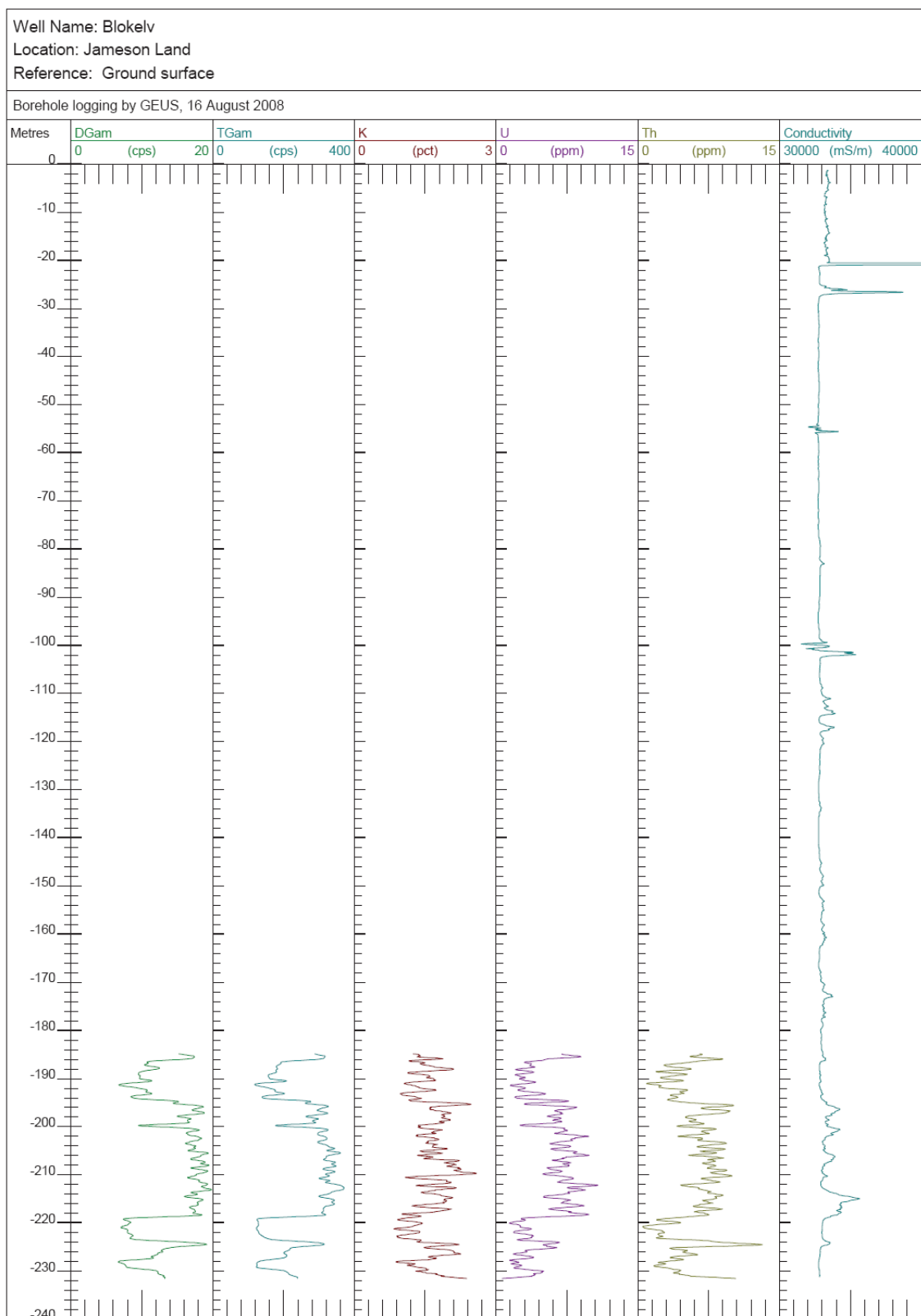


Fig. 3.4.1 Conductivity log and Spectral Gamma log recorded in the well.

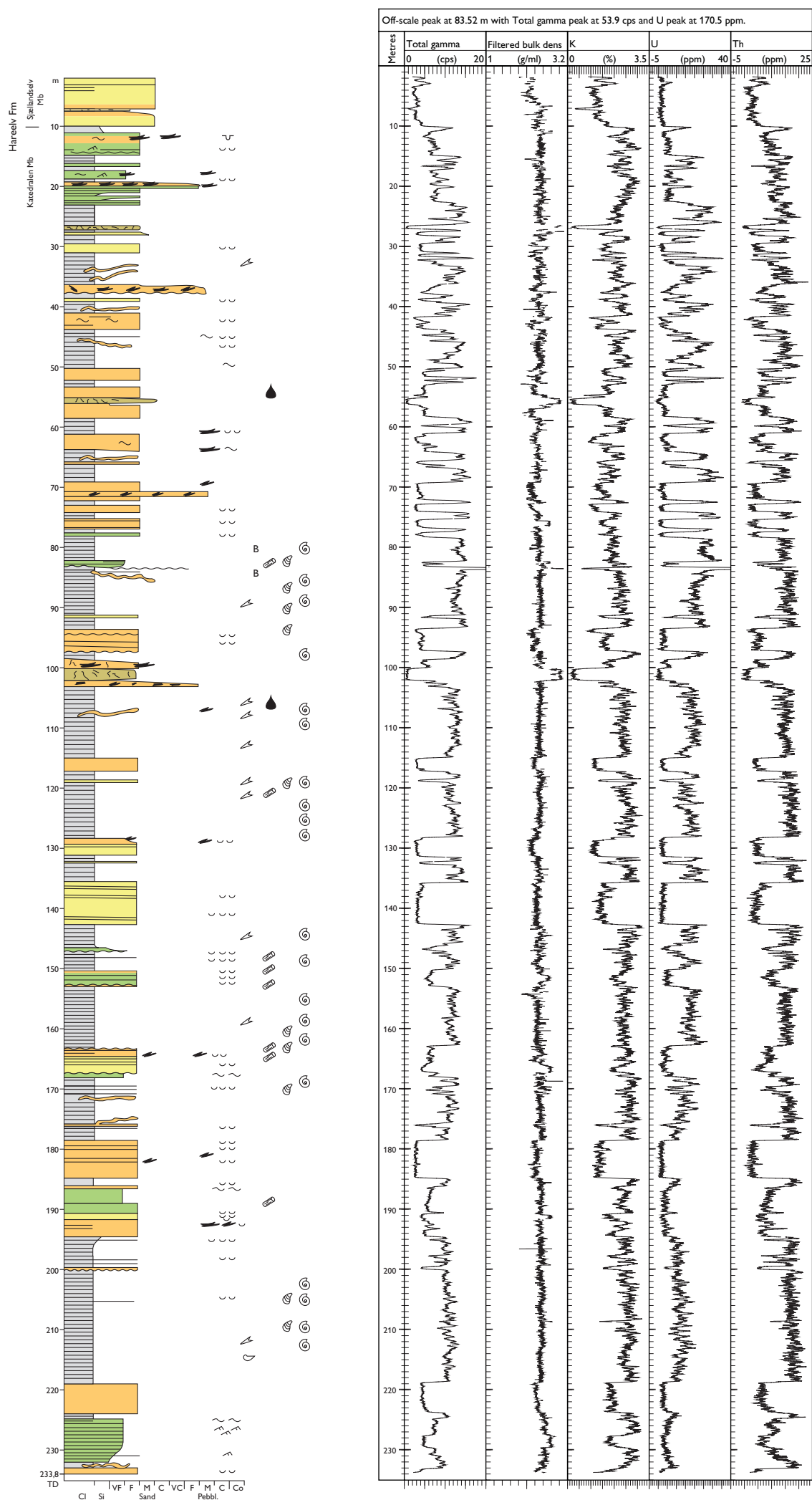


Fig. 3.4.2. Lithological log and Spectral Gamma Log measured on the core; for legend see Fig. 3.1.2.

3.5 Stratigraphic conclusions

The Blokely core represents the Sjøellandselv Member in the top 10 m and the Katedralen Member from 10 to 233.8 m TD, both of the Hareelv Formation. The basis of the Katedralen Member was not reached by the core-well suggesting a thickness in excess of 225 m of the Katedralen Member in the area, which is more than expected.

The cored succession is biostratigraphically dated by integrated dinoflagellate and ammonite zonations. The Sjøellandselv Member belongs to the lower Volgian as indicated by dinoflagellates and the Katedralen Member belongs to the Middle Oxfordian – Kimmeridgian dated by ammonites and dinoflagellates. The cored part of the Katedralen Member probably spans about 9 my, and the high resolution biostratigraphic data indicate a presumably continuous deposition from Middle Oxfordian to Early Volgian suggesting that hiatus if present are below biostratigraphic resolution.

The detailed ammonite and dinoflagellate biostratigraphy of the cored succession allows precise correlation to Upper Jurassic exposures in East and Northeast Greenland as well as other Boreal and Arctic Realms e.g. Svalbard, Siberia and northern Canada and to Upper Jurassic successions drilled in the North Sea Basin.

Composition of the organic material correlated to the spectral gamma log values in the mudstone intervals suggests a three fold subdivision of the cored part of the Katedralen Member. Overall the core shows an upward increasing marine signature in the organic content as reflected by increasing Uranium gamma values. This is interpreted as an overall rise in relative sea-level during the Oxfordian culminating in the Kimmeridgian (Figs. 2.3, 3.1.1). Increasing and decreasing upwards trends in the Uranium gamma signal within mudstone units is interpreted as respectively rising and falling relative sea-level.

The lower part of the succession from 233 m to about 185 m is represented by mainly the Middle Oxfordian and the organic material consist of marine algae with abundant terrestrial input (Fig 3.2.2, see also chapters 7.1 and 7.2) and relatively low Uranium gamma values in mudstone units. The middle succession from 185–103 m is represented by the Upper Oxfordian and lowermost Kimmeridgian. The organic material consist of marine algae with a terrestrial component and medium Uranium gamma values in mudstone intervals reflecting a rise in relative sea level. The upper succession is represented by mainly Kimmeridgian and the mudstones are characterised by the highest gamma values as reflected

by the Uranium gamma signals (Fig. 3.4.2). The organic matter mainly consists of marine algae, and limited terrestrial input reflecting a high relative sea level (Fig. 2.3). A marked transgression surface is defined at 83.5 m by a muddy shell bed (see also chapter 4), within an overall increasing Uranium gamma interval that reflects a period of sea level rise.

All sediments of the Katedralen Member in the Blokølv core have been deposited in dominantly anoxic bottom conditions which preserved the organic algal material and provided a high quality source rock of the Kimmeridgian mudstones and a medium quality source rock of the Oxfordian mudstones.

3.6 References

- Birkelund, T., Callomon, J.H. & Fürsich, F.T. 1984: The stratigraphy of the Upper Jurassic and Lower Cretaceous sediments on Milne Land, central East Greenland. *Bulletin Grønlands Geologiske Undersøgelse* **147**, 1–56.
- Birkelund, T. & Callomon, J.H. 1985: The Kimmeridgian ammonite faunas of Milne Land, central East Greenland. *Bulletin Grønlands Geologiske Undersøgelse* **153**, 1–56.
- Bojesen-Koefoed, J. Bjerager, M. & Piasecki, S. 2009: Shallow core drilling and petroleum geology related fieldwork in East and Northeast Greenland 2008. Geological Survey of Denmark and Greenland Bulletin **17**, 53–56.
- Callomon, J.H. 1985: The evolution of the Jurassic ammonite family *Cardioceratidae*. *Special papers in palaeontology* **33**, p. 49–90.
- Callomon, J.H. 1993: The ammonite succession in the Middle Jurassic of East Greenland. *Bulletin of the Geological Society of Denmark* **40**, 83–113.
- Callomon, J.H. & Birkelund, T. 1980: The Jurassic transgression and the mid-late Jurassic succession in Milne Land, central East Greenland. *Geological Magazine* **117**, 211–310.
- Callomon, J.H. & Birkelund, T. 1982: The ammonite zones of the Boreal Volgian (Upper Jurassic) in East Greenland. In: Embry, A.F.B. & Balkwill, H. R. (eds): *Arctic geology and Geophysics*, Canadian Society of Petroleum Geologists Memoir **8**, 349–369.
- Gromet, L.P., Dymek, R.F., Haskin, L.A. & Korotev, R.L. 1984: The "North American shale composite": Its compilation, major and trace element characteristics. *Geo. Cos. Acta* **48**, 2469–2482.
- Heiri, O., Lotter, A.F. & Lemcke, G. 2001: Loss on ignition as a method for estimating organic and carbonate content in sediments: reproducibility and comparability of results. *Journal of Paleolimnology* **25**, 101–110.
- Herron, M.M. 1988: Geochemical classification of terrigenous sands and shales from core or lag data. *Journal of Sedimentary Petrology* **58**, 820–829.

- Larsen, M., Piasecki, S. & Surlyk, F. 2003: Stratigraphy and sedimentology of a basement-onlapping shallow marine sandstone succession, the Charcot Bugt Formation, Middle-Upper Jurassic, East Greenland. In: Surlyk, F. & Ineson, J.R. (eds): The Jurassic of Denmark and Greenland. *Geology of Denmark Survey Bulletin* **1**, 893–930.
- Milner, P.S. & Piasecki, S. 1996: Boreal Middle Jurassic dinoflagellate cyst stratigraphy of Jameson Land, East Greenland. In: Piasecki, S. *et al.* (eds): Formation of source and reservoir rocks in a sequence stratigraphic framework, Jameson Land, East Greenland. Energy Research Programme EFP-93, Projects 1313/93 & 00171996/30, Vol. I & II. Danmarks og Grønlands Geologiske Undersøgelse Rapport, 46 pp.
- Piasecki, S. 1981: Middle to Late Jurassic dinoflagellate cyst stratigraphy from Milne Land and Jameson Land (East Greenland) correlated with ammonite stratigraphy, 167 pp. Unpublished Licentiat (Ph.D.) thesis, University of Copenhagen.
- Piasecki, S. 1996: Boreal dinoflagellate cyst stratigraphy of Middle to Upper Jurassic sediments of Milne Land, East Greenland. In: Piasecki, S. *et al.* (eds): Formation of source and reservoir rocks in a sequence stratigraphic framework, Jameson Land, East Greenland. Energy Research Programme EFP-93, Projects 1313/93 & 00171996/30, Vol. I & II. Danmarks og Grønlands Geologiske Undersøgelse Rapport, 100 pp.
- Riding, J.B. & Thomas, J.E. 1992: Dinoflagellate cysts of the Jurassic System. In: Powell, A.J. (ed.) A stratigraphic index of dinoflagellate cysts Chapman and Hall, 7–97.
- Smelror, M. 1988: Late Bathonian to Early Oxfordian dinoflagellate cyst stratigraphy of Jameson Land and Milne Land, East Greenland. Rapport Grønlands Geologiske Undersøgelse **137**, 135–159.
- Spath, L.F. 1935: The Upper Jurassic invertebrate faunas of Cape Leslie, Milne Land. I. Oxfordian and Lower Kimmeridgian. *Meddelelser om Grønland* **99**(2), 82 pp.
- Spath, L.F. 1936: The Upper Jurassic invertebrate faunas of Cape Leslie, Milne Land. II. Upper Kimmeridgian and Portlandian. *Meddelelser om Grønland* **99**(3), 180 pp.
- Sykes, R.M. & Callomon, J.H. 1979: The *Amoeboceras* fauna of the Boreal Upper Oxfordian. *Palaeontology* **22**, 839–903.
- Sykes, R.M. & Surlyk, F. 1976: A revised ammonite zonation of the Boreal Oxfordian and its application in northeast Greenland. *Lethaia* **9**, 421–436.
- Surlyk, F. 1978: Submarine fan sedimentation along fault scarps on tilted fault blocks (Jurassic–Cretaceous boundary, East Greenland). *Grønlands Geologiske Undersøgelse* **128**, 108 pp.
- Surlyk, F. 1991: Sequence stratigraphy of the Jurassic – lowermost Cretaceous of East Greenland. *The American Association of Petroleum Geologists Bulletin* **75**, 1468–1488.
- Surlyk, F., Callomon, J.H., Bromley, R.G. & Birkelund, T. 1973: Stratigraphy of the Jurassic – Lower Cretaceous sediments of Jameson Land and Scoresby Land, East Greenland. *Grønlands Geologiske Undersøgelse Bulletin* **105**, 76 pp.
- Woollam, R. & Riding, J.B. 1983: Dinoflagellate cyst stratigraphy of the English Jurassic. Institute of Geological Sciences, Report **83/2**, 41 pp.

Ziegler, P.A. 1982: Geological Atlas Western and Central Europe. Amsterdam: Elsevier.
130 pp.

4. Sedimentology

The Blokelv core was sedimentologically logged in 1:20 scale, and records the boundary between the sandstone dominated Sjøellandselv Member and the combined mudstone and sandstone dominated Katedralen Member of the Upper Jurassic Hareelv Formation. The lower boundary of the Katedralen Member was not reached in borehole. The sedimentological log sheets are presented in Appendix 11.1.

The Katedralen Member of the Hareelv Formation is characterised by remobilised sandstone units injected into black basinal mudstones. In fact, the formation is famously described as “...A Giant Sedimentary Injection Complex” in Surlyk & Noe-Nygaard, 2003; Surlyk *et al.* 2007. Based on these extensive outcrop studies all sandstone units in the Katedralen Member were considered to be post-depositionally remobilised, which obliterated all primary sedimentological structures (Surlyk *et al.* 2007). An obvious consequence of the remobilised sandstone units is that they make the interpretation of the original depositional processes of the Hareelv Formation challenging. In addition the three dimensional geometry of the potential reservoir sandstone bodies are difficult to predict.

The Blokelv core is of very high quality and has therefore enabled the recognition of a wide spectrum of facies where depositional processes can be accessed and interpreted, and it sheds new light to the depositional evolution of the Jameson Land Basin during the late Jurassic in terms of relative sea level changes and basin evolution. Special emphasis has focussed on the recognition of a wide range of post-depositional processes including water escape, slumping, fluidisation, liquefaction, injection and brecciation. Some of these processes acted almost syndepositionally, while others occurred after significant burial and compaction.

The overall deposition of the Upper Jurassic Hareelv Formation in the Blokelv core occurred in relatively deep water in the central part of the Jameson Land Basin. Interpretation of the depositional evolution of the cored succession show transitions from basinal setting to slope environments. Background sedimentation in the basinal setting was dominated by deposition of organic rich mud in oxygen depleted conditions. Episodic gravity flow sandstones were introduced into the basin and later remobilised (Surlyk *et al.* 2007).

4.1 Sedimentary facies.

Basinal mudstone (Fig. 4.2A).

The organic rich, very dark grey – black mudstones are laminated, and have a relatively high content of pyrite. Lamination is commonly shown by varying abundance of thin siltstone and very fine-grained sandstone pinstripe laminae. The fauna comprises commonly pyritised ammonites, and occasionally bivalves (see chapter 3.2.2). Trace fossils are virtually absent, only rare *Chondrites* have been found. Fragments, 0.3–0.5 cm thick, of extraformational coalified wood and plant remains are present in certain intervals.

The mudstones were deposited in a basinal setting in an oxygen depleted environment as basinal and/or distalmost turbidite deposits. Siltstone and fine sandstone laminae were deposited as distal low density turbidites.

Basinal mudstone with thin sandstone laminae (Fig. 4.2B)

The facies consists of organic and pyrite rich, dark grey – very dark grey laminated mudstone. In contrast to the previous facies, lamination is shown by abundant silt and very fine-grained sand laminae and lenses, up to a few mm thick. Faunal content comprises commonly pyritised ammonites, and occasionally bivalves. Clasts and branches, 0.3–0.5 cm thick, of coalified wood and plant remains are present in certain intervals.

The mudstones were deposited in a basinal to outer slope setting in an oxygen depleted environment. Siltstone and fine sandstone laminae were deposited as distal low density turbidites.

Muddy sandstone debrite

This facies consists of dark grey muddy sandstone with abundant mudstone intraclasts. The units are up to about 0.5 m thick and may show a fining upward trend. They are rather uncommon in the cored interval.

They are interpreted as gravity flow deposits, where the mudstone was eroded during flow.

Low density turbidites, heterolithic sandstone mudstone (Figs 4.2 C–D)

These facies consist of alternating beds and laminae of grey fine grained sandstone and dark grey to black mudstone, which commonly form up to ~1 m thick upward fining units. In certain intervals the laminae consist of mud intraclasts at the base that grade upwards into medium grained sandstone. Coalified wood fragments and plant remains are commonly associated with these deposits. These sedimentary units probably resemble the informally termed “tiger striped” beds in the literature (e.g. Guy 1992).

Sedimentological structures include planar lamination, wavy lamination, ripple lamination, and occasionally climbing ripple lamination. Convolute bedding and slump structures as well as fluidisation structures are common. Individual beds and laminae have sharp commonly erosional bases; the tops can be sharp, erosional or gradational. Individual laminae show uniform grain size, are normal graded or occasional inversely graded. Diminutive flute casts may occur.

Similar “tiger striped” heterolithic sandstone – mudstone intervals are interpreted as low density turbidites of Bouma subdivision types Tb-e in the literature (e.g. Lowe 1982; Guy 1992; Surlyk & Noe-Nygaard 2001); and this interpretation is also preferred here. The common occurrences of associated plant remains and coalified wood fragment suggest a fluvial sediment source for these turbidites. Alternative interpretations include deposition in turbidite channel leveed complexes (e.g. Posamentier & Walker 2006) or deposition as hyperpycnites in prodelta settings (e.g. Soyinka & Slatt 2008; Bhattacharya and MacEachern 2009).

High density turbidite massive sandstone (Figs 4.3A–B)

This facies consists of grey, fine to medium-grained and moderately to well-sorted sandstones. The sandstone units are 0.1-7 m thick and have sharp lower and upper boundaries. The bases are commonly erosional. The texture is general homogeneous, but occasionally planar and wavy bedding surfaces occur. Water escape structures are common in certain intervals. Grains are angular to subrounded and dominantly consist of quartz. Mica is also common and occasionally dominant at top of sandstone units. Small intraformational mudclasts, <0.5 cm or <0.2 cm in size, and evenly distributed within beds are common to abundant in certain intervals.

These in general massive sandstones are interpreted as high density turbidites, which were probably triggered by episodic collapse of the shelf marginal delta front (cf. Surlyk *et al.*

2007). Amalgamated sets of this facies characterise especially the Sjøllandselv Member. These gravity flows were initiated as sand debris flows and may have evolved into classical high density turbidite currents (cf. Larsen & Surlyk 2003; Bruhn & Surlyk 2004). Interpretations based on outcrop geometries suggested that these sandstones were deposited in pre-existing gullies or had a laterally sheet-like extension (Surlyk 1987; Surlyk & Noe-Nygaard 2003; Surlyk *et al.* 2007). The majority of these high density turbidites were prone to post depositional remobilisation (see next section).

Remobilised massive sandstone (Figs 4.3C–D)

This facies consists of grey, fine- to medium-grained and moderately to well-sorted sandstone units. The vertical thicknesses of the units recorded in the core are from a few cm to about 7 m. Measurements from the field record vertical thicknesses up to 50 m (Surlyk & Noe-Nygaard 2001). Both upper and lower boundaries commonly truncate the adjacent mudstones. The truncations may show a highly irregular surface or appear as planar. Truncation dip angles are up to 60°. Ptygmatically folded subvertical cm-scale dikes commonly protrude upwards from massive or bedded sandstone units. Grains are angular to sub-rounded and dominated by quartz. In addition, mica is also common and occasionally dominant at top of sandstone units. Certain intervals show common to abundant small intraformational mudstone clasts, <0.5 cm or <0.2 cm in size, with a relatively unimodal size frequency and evenly distributed in the sandy matrix. Consolidation surfaces are common in some units that have relatively high content of mudstone intraclasts. Large irregular and angular mudstone intraclasts are in general few and randomly distributed, but occasionally common to abundant in certain units (see next section).

The small ptygmatic folded sub-vertical dikes were injected during the early burial as they were folded during further burial and compaction of the mudstone. Water escape structures in dish shapes and vertical pipes are also associated with early remobilisation. Later remobilisation includes large scale liquefaction of the sand, and during flow the adjacent compacted mudstones were brecciated and ripped apart forming large angular clasts that were incorporated randomly in the massive sandstone injections (cf. Surlyk & Noe-Nygaard 2001; Hurst *et al.* 2003; Jonk *et al.* 2005; Surlyk *et al.* 2007). Remobilisation of the sands occurred at many levels. Locally, an entire unit can be completely liquefied and homogenised. In other cases the liquefied parts were confined to only parts of a unit, while other parts still show the primary depositional structures.

Mudstone conglomerate (Fig 4.4A–B)

This facies type consists of mm to dm scale angular mudstone clasts in a fine – medium grade sandstone matrix. Some intervals are clasts supported while others are matrix supported. Structures include apparent layering but also highly irregular distributions.

The facies is interpreted to result from sand remobilisation and injection at a relatively late burial stage. Consolidated mudstone clasts were ripped out during protrusion and injection of remobilised sand and incorporated into the sandy matrix.

Muddy shell bed (Fig. 4.4C)

This facies occurs as a distinct 3 cm thick bed at 83.5 m depth. It consists of abundant shell fragments of bivalves and minor sand grade quartz grains in a muddy matrix. It has a very high gamma ray reading caused by a high content of Uranium. Two thin <1 cm layers with wood fragments are present below the bed.

The bed was deposited as a bioclastic debris flow and it is considered a prominent marker bed probably reflecting a surface of transgression.

Bentonite-rich mudstone (Fig. 4.4D)

The grey bentonite-rich mudstone laminae or beds, 0.3–8 cm thick, occur at four levels (25.75 m, 78.95 m, 82.6 m and 83.15 m). They have a characteristic greasy nature and shows prominent swelling after the surface was cleaned with water.

The bentonite beds are interpreted as diagenetically altered volcanic ash layers associated with the initial break up of the northern Atlantic.

4.2 Discussion and conclusions

Deposition of the Katedralen Member occurred in an anoxic environment with dark grey to black laminated mudstones in central part of the Jameson Land Basin. The organic content of the mudstones is predominantly marine, however with an increasing terrestrial proportion

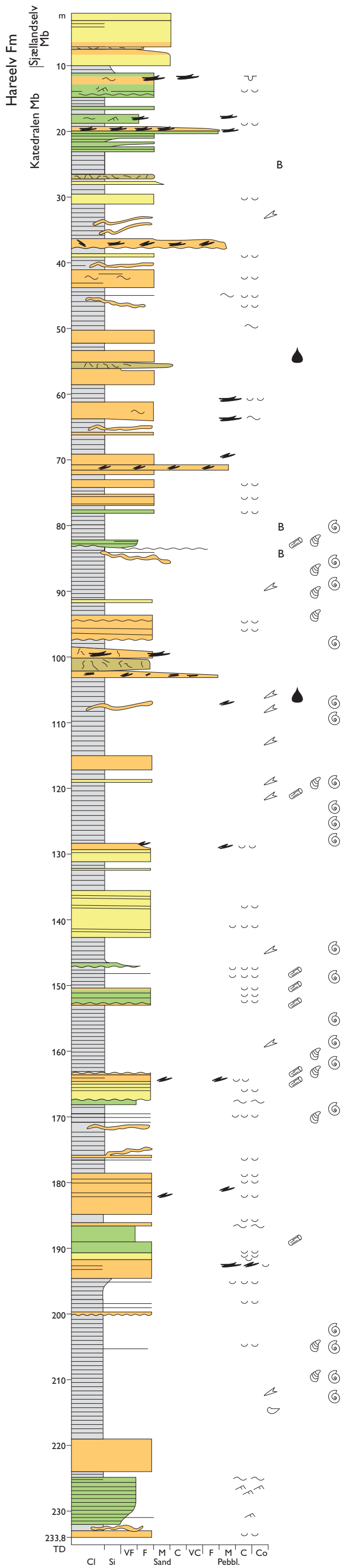
in the deeper part of the core, i.e. the interval 100–233.8 m. Massive fine to medium grained sand beds were deposited by gravity flows in the deeper part of the basin possibly as a result of episodic collapse of the sandy shelf margin. Some evolved into high density turbidite sandstones that after deposition were later fluidised and remobilised to form complex geometrical bodies in the mudstone dominated succession. Some sandstone injectites where formed during early burial and where later folded during continuous compaction and burial. Remobilisation of sandstones occurred locally and shows transitions from sandstones with local water escape structures to completely remobilised massive sandstones. Sandstone injectites commonly carry irregular mudstone clasts that were ripped from the hostrock during injection, occasionally forming mudstone conglomerates with sand matrix. Heterolithic intervals are present in the lower, middle and upper part of the cored Katredalen Member and they are interpreted as deposited from mainly low density turbidite currents that may have been associated with relative sea-level falls.

The medium to coarse grained sandstones of the Sjøellandselv Member represents mass-flows sandstones deposited from collapse of the prograding shelf-margin sandstones during relative lowering of sea-level.

4.3 References

- Bhattacharya, J.P. & Mac Eachern, J.A. 2009: Hyperpycnal rivers and prodeltaic shelves in the Cretaceous Seaway of North America. *Journal of Sedimentary Research* **79**, 184–209.
- Bruhn, R., & Surlyk, F. 2004: Sand-grade density flow evolution on a shelf-edge–slope–basin floor complex in the Upper Jurassic Olympe Formation, East Greenland: *Petroleum Geoscience* **10**, 81–92.
- Guy, M. 1992, Facies analysis of the Kopervik sand interval, Kilda Field, Block16/26, UK North Sea, in R.F.P. Hardman (ed.) *Geological Society Special Publication* **67**, 187–220.
- Hurst, A., & B. T. Cronin 2001: The origin of consolidation laminae and dish structures in some deepwater sandstones: *Journal of Sedimentary Research* **71**, 136–143.
- Hurst, A., Cartwright, J., Duranti, D. 2003: Fluidization structures produced by upward injection of sand through a sealing lithology. In Van Rensbergen, P., Hillis, R.R., Maltman, A.J., Morley, C.K. (eds): *Subsurface Sediment Mobilization*. *Geological Society Special Publication* **216**, 123–137.

- Jonk, R., Hurst, A., Duranti, D., Parnell, J., Mazzini, A. & Fallick, A.E. 2005: Origin and timing of sand injection, petroleum migration, and diagenesis in Tertiary reservoirs, south Viking Graben, North Sea: AAPG Bulletin **89**, 329–357.
- Larsen, M., & F. Surlyk 2003: A shelf-edge delta and slope system of the upper Callovian–middle Oxfordian Olympen Formation, East Greenland. In Ineson, J.R. & Surlyk, F. (eds): The Jurassic of Denmark and Greenland: Geological Survey of Denmark and Greenland Bulletin **1**, 893–930.
- Lowe, D.R. 1982: Sediment Gravity flows: II Depositional models with specific reference to the deposits of high-density turbidity currents. Journal of Sedimentary Petrology **52**, 279–297.
- Posamentier, H.W. & Walker, R.G. 2006: Deep-water turbidites and submarine fans. In Posamentier, H.W. & Walker, R.G. (eds): Facies models revisited. SEPM Special Publication **84**, 397–520.
- Soyinka, O.A. & Slatt, R.M. 2008: Identification and micro-stratigraphy of hyperpynites and turbidites in Cretaceous Lewis Shale, Wyoming. Sedimentology **55**, 1117–1133.
- Surlyk, F. 1987: Slope and deep shelf gully sandstones, Upper Jurassic, East Greenland: AAPG Bulletin **71**, 464–475.
- Surlyk, F. 2003: The Jurassic of East Greenland: A sedimentary record of thermal subsidence, onset and culmination of rifting. In Ineson, J. R. & Surlyk, F. (eds): The Jurassic of Denmark and Greenland: Geological Survey of Denmark and Greenland Bulletin **1**, 659–722.
- Surlyk, F. & Noe-Nygaard, N. 2001: Sand remobilisation and intrusion in the Upper Jurassic Hareelv Formation of East Greenland: Bulletin of the Geological Society of Denmark **48**, 169–188.
- Surlyk, F., & N. Noe-Nygaard 2003: A giant sand injection complex: The Upper Jurassic Hareelv Formation of East Greenland: Geologia Croatica **56**, 69–81.
- Surlyk, F. Noe-Nygaard, N., Gjelberg, J. 2007: The Upper Jurassic Hareelv Formation of East Greenland: A Giant Sedimentary Injection Complex. In Hurst, A. & Cartwright, J. (eds): Sandinjectites: Implications for Hydrocarbon exploration and production. American Association of Petroleum Geologists (AAPG) Memoir **87**, 141–149.



Legend

- Sandstone, intrusive
- Sandstone, low density turbidite
- Sandstone, high density turbidite
- Mudstone
- Igneous intrusion
- Planar lamination/bedding
- Cross-lamination
- Wavy bedding
- Slump
- Sandstone intrusion
- Burrow
- Mudstone intra clast
- Large mudstone clast
- B Bentonite
- Coal
- Belemnite
- Bitumen
- Ammonite
- Bivalve
- Brachiopod

Figure 4.1 Lithological log of the Blokely core.

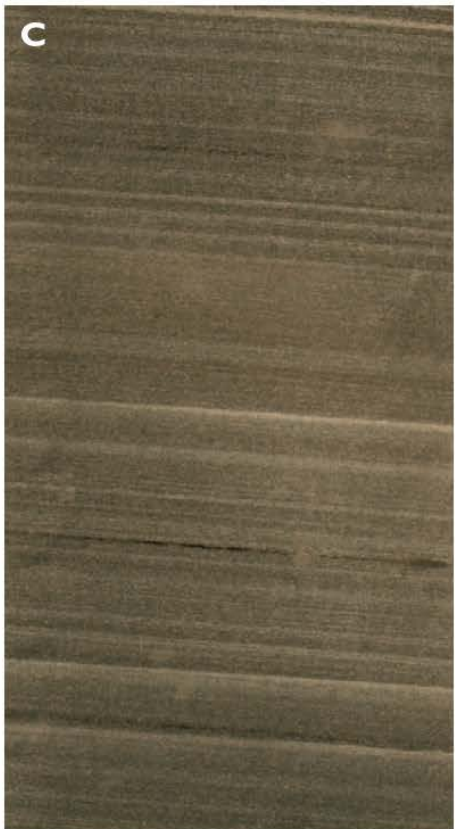


Fig 4.2. Core photographs of the Upper Jurassic Katedralen Member (Hareelv Formation); core section height: 10 cm. A) Black laminated organic rich mudstone, 68.4 m. B) Dark grey organic rich mudstone with abundant low density siltstone and fine grained sandstone laminae, 109.5 m. C) Planar laminated heterolithic sandstone mudstone, 146.5 m. D) Heterolithic sandstone mudstone showing ripple lamination, convoluted bedding and fluidisation structures, 224.8 m.



Fig. 4.3. Core photographs of the Upper Jurassic Katedralen Member (Hareelv Formation); core section height: 10 cm. A) Massive homogenous sandstone, 223.5 m. B) Sandstone; bedded in the upper part and remobilised and injected in the lower part, 96.8 m. C) Remobilised sandstone with mudstone intraclasts, 152.8 m. D) Sandstone dike, 232.7 m.



Fig 4.4. Core photographs of the Upper Jurassic Katedralen Member (Hareelv Formation); core section height: 10 cm. A–B) Mudstone conglomerates 71.2–71.4 m. C) Muddy shell bed overlying a coalified wood fragment, 83.5 m. D) Bentonite bed, 82.6 m.

5. Mineralogy and Diagenesis

Mineralogical and diagenetic investigations of the Blokely core were done to evaluate to which degree the sedimentary rocks have been subjected to diagenetic transformations. This knowledge is valuable as these alteration processes affect the chemistry, porosity and permeability of the rocks. A combination of methods was used to assess both the general and the detailed mineralogical and diagenetic effects by determining bulk mineralogy and clay mineralogy in different degrees of detail. The results allow the establishment of a diagenetic sequence including events of burial, basalt intrusion and exhumation.

5.1 Data

XRD (X-Ray Diffraction) analyses of 22 samples were carried out for both bulk and clay mineralogy, where the selected levels included 18 sandstones, 1 heterolith and 3 mudstones (Fig. 3.3.11). The sandstone intervals were chosen to reflect the various facies (see chapter 4), and some samples were taken close to the mudstones contact to unravel if the proximity had an effect on the diagenesis. Thin sections of 25 sandstone samples were made, covering levels of diagenetic relevance including both representative and diverging lithologies. Point counts were made in thin sections of 8 sandstone samples, which overlap with the XRD analyses in order to make the mineralogy determination as quantitative as possible. SEM (Scanning Electron Microscopy) analyses were carried out on 12 sandstone samples, which were chosen as to give an overview of the morphology of the various mineral precipitations and of the relative timing of diagenetic processes.

5.2 Methods

5.2.1 X-Ray Diffraction

The bulk mineralogy was measured by XRD (X-Ray Diffraction) at the University of Copenhagen. About 3-4 cm of a half-core was used for each measurement and the surface of the

core was removed to avoid contamination. Crushing to $<63\ \mu\text{m}$ preceded the analyses. The Bragg-Bretano method was used with powder diffraction run as reflection in a Bruker Advance D8 diffractometer with a Lynx-Eye detector. The quantity of minerals was decided by the Rietveld method.

The clay mineralogy was measured by XRD at GEUS, where the amount of clay minerals was found qualitatively. About 5-6 cm of a half-core was used for each measurement where sand dominated and about 1-2 cm where clay dominated. The samples were gently hand ground to pass a $250\ \mu\text{m}$ sieve. XRD was carried out on randomly oriented specimens using a Philips 1050 goniometer with fixed divergence, anti-scatter slits and $\text{Co-K}\alpha$ radiation (pulse-high selection and Fe-filter). Organic matter was removed in the chemical pretreatment using NaOCl of pH 9.0. The samples were dispersed ultrasonically in distilled water in order to obtain the clay fraction $<2\ \mu\text{m}$ for analysis. The fraction $>30\ \mu\text{m}$ was removed by sedimentation and the $2\text{-}30\ \mu\text{m}$ by centrifugation in a centrifugal particle size analyser (Slater & Cohen 1962). The suspensions were flocculated in 1 M NaCl . Excess salt was removed by centrifugation and washing with water and ethanol. The fraction was then air-dried. Three oriented specimens were prepared for each sample by the pipette method as follows: Mg-saturated air-dry, Mg-saturated with glycerol added to the suspension and K-saturated air-dry heated for 1 hour at 300°C . The clay fractions were investigated by XRD producing a diffractogram for each of the three saturated specimens for each sample. The discrete minerals were identified from peak positions on the XRD diffractograms.

5.2.2 Thin sections and point counts

Thin sections were produced by Basel University, Schweiz, and by GeoTech Labs, Canada. Polished thin sections were prepared from $3.6 \times 2.4 \times 0.5\ \text{cm}$ sandstone samples using blue epoxy for the impregnation to help the identification of free pore space (Appendix 11.3). Half of each thin section was etched and stained with sodium cobaltinitrite for K-feldspar identification. Quantitative point count of 8 thin sections was done by identification of 300 mineral grains in each by the use of a microscope with a crossed nicols function. The free pore spaces were counted additionally.

5.2.3 Scanning Electron Microscopy

SEM (Scanning Electron Microscopy) analyses were made by GEUS, Copenhagen, on a Philips XL40SEM equipped with a ThermoNoran EDX (Energy Dispersive X-ray spectrometry) detector. EDX was used for making elemental analyses of the grains to give a qualitative identification of the minerals. The SEM analyses were performed on carbon-coated thin sections of sandstone and gold-coated sandstone samples placed on carbon tape. The carbon coating was produced in Ar vacuum of 0.02 mbar after cleaning the thin sections with 2-propanol. At first they were exposed to 3 V in 1 min. and then they were coated at 8 V in 5 sec. The gold coating was made in Ar vacuum of 0.3 mbar by exposing the samples to 25 kV in 15 min. The long exposure time was necessary due to the relatively high porosity.

5.3 Results

5.3.1 Mineralogy

The results of the XRD analyses for bulk mineralogy are shown in Table 5.1 and for clay mineralogy in Table 5.2. An overview of both is given in Fig. 5.1, whereas Fig. 5.2 presents the same results solely for the sandstone samples. This is done in order to better visualise the mineralogical trends of the sandstone levels up through the core. Examples of the XRD interpretations are shown in Fig. 5.3 of the bulk mineralogy and in Fig. 5.4 of the clay mineralogy. The point counts of thin sections are given in Table 5.3. Photos of thin sections are numbered Figs 5.5–5.8 and SEM images are shown in Figs 5.9–5.14. The different kinds of quartz are abbreviated as DQ (detrital quartz), MQ (microquartz) and QO (quartz overgrowth, also called macroquartz) where differentiation between them has been possible.

The mineralogy estimated through XRD should only be regarded as an approximate indication, whereas the low number of point counts limits the possibility for making quantitative averages. The quartz content is lower in the point counts (Table 5.3) than in the XRD analyses (Table 5.1), as more categories are possible to identify in the point counts including rock fragments, heavy minerals and organic matter. The average quartz content of the

sandstone intervals is 66 wt% according to the results of the Rietveld XRD analyses (Table 5.1, Fig. 5.1), whereas it is 17 wt% for the mudstones. Only one heterolith sample has been analysed by XRD and falls in-between the sandstone and mudstone values, but resembles the latter the most. The quartz grains are chiefly monocrystalline (Table 5.3) and the amount of authigenic quartz overgrowths (Fig. 5.6C & D) is about constant down through the core.

The content of mica plus clay minerals amounts to 14 wt% on average for the sandstones and 69 wt% for the mudstones. The amount of clay minerals usually exceeds the amount of mica markedly (Table 5.3). Muscovite is by far the most common mica mineral (Table 5.3, Fig. 5.5), but some biotite and chlorite is also present. The mica is usually oriented parallel to the layering along with the organic bioclasts (Fig. 5.6A).

Albite and K-feldspar are the feldspars present in largest amounts (Fig. 5.5B), but a small part of the feldspars identified as albite in fact consists of low-Ca plagioclase, which has been recognised through SEM. The low plagioclase content is apart from the Rietveld results also seen by the fairly good correlation of albite (Fig. 5.1) with Na (Fig. 3.3.1), whereas no correlation of albite and Ca is recognisable because of the presence of Ca in other phases. Albite is on average found in slightly higher amounts than K-feldspar, and both are widespread in the sandstones and mudstones, where the average contents of albite and K-feldspar are 5 and 3 wt% (Table 5.1), respectively. However, intergrowth of albite and K-feldspar is commonly observed, wherefore these categories should be regarded as overlapping in the point counts (Table 5.3). Moreover, albite and plagioclase are difficult to separate during the replacement process.

Pyrite is by far more abundant in the mudstone intervals than in the sandstones, amounting on average to 6 wt% and 1 wt% (Table 5.1), respectively. The S content is only large (Fig. 3.3.1) in samples with large amounts of pyrite (Fig. 5.1), while Fe also is widespread in other phases. The proportionality of the S-concentration with the pyrite content is useful in the levels where the mineralogy is not measured. Framboidal pyrite is reported in a number of levels (Table 5.3) and is predominantly found in organic bioclasts (Fig. 5.7). Pyrite is also commonly associated with ammonites in the mudstones (chapter 4). The heavy mineral category (Table 5.3) is most likely dominated by pyrite, which cannot be distinguished from certain other heavy minerals when it is not precipitated in framboidal shape.

Ankerite is present with 10 wt% in the sandstones on average and 1 wt% in the mudstones (Table 5.1). However, large fluctuations in the content are found (Fig. 5.5). Hence, 7 samples of the sandstones analysed by XRD show ankerite contents >9 wt%, whereas the 11

remaining samples all show ankerite contents <5 wt%. Dolomite $\text{CaMg}(\text{CO}_3)_2$ and ankerite $\text{Ca}(\text{Fe}^{2+}, \text{Mg}, \text{Mn})(\text{CO}_3)_2$ are difficult to distinguish in transmitted light microscope and by XRD because of their quite similar crystal structure, so the XRD results can only reveal that one of them is present in the rocks. It is only possible to distinguish them by the use of SEM. The chemostratigraphy show a very strict correlation of Ca and Mg all the way through the stratigraphy (Fig. 3.3.1), whereas the relationship to the Fe content is less distinct and the Mn content is low. However, the EDX measurements have shown that Fe is always present in the carbonate minerals, but often in varying amounts from rim to core. Therefore it can be concluded that low-Mn ankerite is the carbonate-phase present (Table 8.4), being proportional with the relatively high contents of Ca and Mg in the intervals where only geochemistry has been measured.

The individual clay minerals are identified from XRD diffractograms, as shown by the example in Fig. 5.4. Here the Mg^{2+} air-dry analysis show that illite and kaolinite are present, as they are identified by the peaks at 10 and 7 Å, respectively. Kaolinite must be present in the largest amount as shown by the high peak. The presence of a peak at 14 Å indicates that smectite, vermiculite or chlorite must be present. Quartz is found to be present in the mudstone as well. Second and third orders of the clay minerals and quartz can also be seen, but are of minor importance. Reduction of the 14 Å peak and creation of an 18 Å peak when treated with Mg^{2+} glycerol indicates that smectite is present. The complete disappearance of the 14 Å peak when treated with K^+ heating shows that no chlorite is present in its clay mineral form. The Mg^{2+} glycerol 14 Å peak must therefore have been caused by vermiculite.

5.3.2 Burial induced diagenesis

The diagenesis has begun with dissolution of albite and plagioclase during the eogenesis (Fig. 5.15). Plagioclase is only found in small amounts suggesting that it has been dissolved or replaced by ankerite as the Ca content in plagioclase is important as source to the ankerite formation. The early dissolution is documented by microquartz surrounding the albite fragments (Fig. 5.9C) and by the gradual ankerite replacement of parts of the albite grains (Fig. 5.10). The growth of microquartz on grain surfaces (Fig. 5.12C) has also begun relatively early (Fig. 5.15) when the pore fluids were Si-rich. The early nature of microquartz is revealed by its restricting influence on the growth of other mineral phases like ankerite (Fig. 5.10D) where the microquartz has precipitated. Nucleations on undisturbed surfaces

have promoted free growth of some of the crystals, resulting in larger crystals with regular intervals (Fig. 5.9B).

Ankerite began to precipitate when albite was still undergoing dissolution (Fig. 5.10A) and the growth continued for some time after the precipitation of microquartz had ceased (Fig. 5.15). The typical layered growth of ankerite is shown in Fig. 5.10B, and the perfect crystal shapes formed in free pore space is shown in Fig. 5.10C. The varying content of Si and Al in the EDX measurements of ankerite has a constant Si/Al ratio of about 3:1 revealing that the Si and Al are associated with the partly replaced feldspars. Pure pore-filling ankerite without any association to feldspars is also found (Figs 5.5C, D), where it for instance forms between flakes of mica (Fig. 5.14A). The Ca-ions of the feldspars liberated by the plagioclase alteration have eased the ankerite nucleation along with those Ca-ions released from the transition from smectite to illite and from dissolution of shell fragments.

It can be seen in the bulk mineralogy that smectite is largely missing in the intervals where ankerite has formed (Fig. 5.1). However, the content of illite does not vary much, so some of the smectite might have dissolved completely thereby also releasing Fe and Mg used for the ankerite formation. This is supposed to have happened primarily in the mudstone levels (Kantorowicz 1985), where some smectite is still present. The mudstone clasts within some sandstone units must have contributed to the ankerite precipitation, whereas dissolution of heavy minerals with Fe and Mg not seem to have had any influence (Table 8.3). The C has presumably been supplied from thermal decarboxylation of organic matter and principally from partly degradation of bioclasts (Hendry 2003), which are found in many sandstone levels of the core. The remaining part of organic matter (Table 5.3) is still fairly large in those samples where the accessible part of the organic matter has been used in the ankerite formation.

The early start of microquartz precipitation has depleted the pore fluids from much of the Si gained from the dissolved feldspars, so formation of a non-siliceous mineral like ankerite was favoured. In addition, the early growth of ankerite was favoured by the flow of cation-rich pore fluids between the unconsolidated mudstones and the still high-porous sandstones during the early compaction. The ankerite contains slightly more Fe than Mg, which confirms its diagenetic origin (Hendry 2003). Furthermore, burial-formed ankerite is typically zoned, which is seen as an increase in Fe and decrease in Ca and especially Mg from rim to core of the grains. This is also seen as an increasing total Fe content of ankerite down through the core (Table 8.4), where the higher degree of diagenesis in the lower part of the core is evident from the longer growth period of ankerite. The Fe-rich nature of the mud-

stones (Fig. 3.3.3) explains why the pore fluids gradually have been depleted in other metals.

The sedimentary rocks have not experienced a high degree of diagenesis as no chlorite has been formed (Fig. 5.4), but it has not been low either as smectite largely has been transformed into illite and mixed-layer clay minerals in the sandstone intervals (Fig. 5.10A). Other sources for illite and mixed-layer clays include feldspars and presumably also some muscovite, which have been partly replaced in some places. The class of mixed-layer clays constitutes various combinations of clay minerals, which are usually interlayered with illite and therefore hard to recognise on the SEM images. However, illite-smectite is a common precursor to pure illite, and small contents of Mg, Fe, Ca and Na often found in the illite show the presence of the mixed-layer clays. The decreasing Al content up through the core (Fig. 3.3.6) indicates that more extensive clay mineral precipitation has happened in the lower part of the core due to the higher temperatures the rocks have been exposed to. Illite has precipitated later than microquartz (Figs 5.9C & 5.11D) and both simultaneously and later than ankerite (Figs 5.10B & 5.12A).

The macroquartz was formed from continued growth of some of the microquartz crystals during the mesogenesis (Fig. 5.15) when the pore fluids were less Si-saturated resulting in fewer nucleations on free grain surfaces. The quartz overgrowths have formed perfect euhedral crystal shapes where they have grown undisturbed into free pore space (Fig. 5.9A), whereas they in many places have been both interrupted and overgrown by illite (Fig. 5.11). Ankerite was still forming when the growth of macroquartz began (Fig. 5.11A).

Authigenic apatite is occasionally found (Fig. 5.9C), where it has precipitated after microquartz and simultaneously with illite. The rare precipitation of apatite is probably caused by the Ca-depletion of the pore fluids due to the ankerite cementation.

The pyrite formation of single crystals happened later than ankerite (Fig. 5.11A) and thus did not deplete the Fe content of the pore fluid thereby making precipitation of ankerite possible. However, the framboidal pyrite must have formed early as it has precipitated between muscovite grains before the mica compaction. It has most commonly formed within bioclasts, as observed in thin sections (Fig. 5.7). The amount of pyrite (Fig. 5.1) correlates well with the C content (Fig. 3.3.1) confirming the affiliation to organic matter. Pyrite is together with e.g. garnet and Fe-oxides responsible for those variations in Fe that does not correlate with ankerite. Ti-oxides have formed simultaneously with illite (Fig. 5.12D), which commonly show intergrowth of the small heavy mineral crystals. The precipitation of Ti-

oxides like rutile and anatase occurred contemporary with pyrite, but continued for some time after the pyrite formation ended (Fig. 5.11A).

5.3.3 Basalt sill induced diagenesis

The basalt sills that have intruded three places in the cored succession and all have affected the diagenesis of the surrounding sandstones (Fig. 5.15). However, the changes caused by the enhanced heat flow are only evident very close to the sills. These changes involved a second episode of microquartz precipitation (Fig. 5.9D), where the microquartz has formed on macroquartz surfaces simultaneously with continued illite precipitation. This is quite unusual as it requires a significant Si-enrichment of the pore fluids, which has probably been injected via releasing of dissolved constituents of the basalt sills, e.g. volcanic glass and plagioclase phenocrysts. Furthermore, this fresh supply of cations has promoted precipitation of clay minerals with a diverse cation composition and thereby prevented subsequent formation of kaolinite close to the sills (Fig. 5.1). The presence of the sills has restricted the flow of meteoric water, so the kaolinite replacement of feldspars has also been prevented near the sills because volcanic glass is easier dissolved by meteoric water than feldspars.

The mudstone at 27.38 m depth has a higher Si content and lower C content than the other mudstone samples (Fig. 3.3.1), as it has been sampled close to the sill that occurs at 26.4-27.1 m depth. The sandstone at 56.47 m depth is the only XRD tested sample that lacks kaolinite (Fig. 5.1), as it has been sampled close to the sill that occurs at 55.2-56.4 m depth. Moreover, it has a high content of ankerite signifying that a second episode of ankerite precipitation might have happened due to the fresh supply of Ca from the dissolved plagioclase phenocrysts. The sandstone at 56.91 m is sampled further from the contact to the sill and has normal kaolinite content (Table 5.2). The sandstone at 100.10 m depth contains a lot of second phase microquartz (Fig. 5.9D) and no kaolinite, as it has been sampled close to the lowermost sill (about 100.1-102.0 m depth). This trend is also visible in the sandstone at 100.05 m depth (Figs 5.9C & 5.11D), but it is not as pronounced because of the additional distance to the sill. Baryte is found to have precipitated locally around the lower sill in large amounts.

5.3.4 Exhumation induced diagenesis

Dissolution of K-feldspar has primarily happened during the telogenesis (Fig. 5.15). This is indicated by the free pore spaces in the dissolved parts of the grains (Fig. 5.11D), which have neither been reduced through compaction nor filled with authigenic phases. The higher stability of K-feldspar compared to albite explains why the albite break-down occurred early during the burial, whereas K-feldspar dissolution did not take place to any significant degree until exhumation. There is an inverse proportional relationship between illite and K-feldspar (Fig. 5.1), showing that illite was still being formed when K-feldspar began to dissolve. This is also seen by illite being the only mineral occasionally precipitated within the secondary porosity of K-feldspar (Fig. 5.9C).

Initial dissolution of the surfaces of K-feldspar grains is commonly associated with surrounding illite precipitation (Fig. 5.12A). Kaolinite is here found to have formed around the partly dissolved grains, but not within the K-feldspar pore-space because the concentration of K-ions was too large. Kaolinite is the last authigenic phase, as can be seen from its overgrowing nature (Fig. 5.10C). This agrees well with the usual behaviour of kaolinite showing precipitation at shallow depths due to the interaction with circulating meteoric water. Kaolinite precipitation occurred after the illite formation had ceased (Fig. 5.12D) and often took place as replacement of albite grains, which is evident by the filling of large pore spaces (Fig. 5.12B). The mineral is often found as perfect platy growths close to feldspar grains (Fig. 5.12C), and the near-constant ratio of kaolinite to feldspar in both sandstones and mudstones (Fig. 5.1) confirms the feldspar-origin of the precipitates. The growth of kaolinite fans is occasionally found to force open the cleavage planes of mica (Fig. 5.14B).

5.3.5 Diagenetic causes and effects

The three lowest XRD analyses from 218.80 to 221.18 m depth were carried out of samples from the top, middle and bottom of the same sandstone layer. The very similar results of these samples (Tables 5.1 & 5.2) thereby prove the XRD mineral identifications to be quite accurate. The analyses further indicate that the diagenesis has taken place independently of the proximity to the mudstone intervals. The concordant results of XRD analyses and point counts (Figs 5.1 & 5.3) also demonstrate the former method to be rather precise.

The formation of ankerite cement in the sandstone levels of the Blokely core is found to be dependent on the presence of sufficient feldspar grains and especially organic bioclasts, and on high flux of pore fluids from the mudstone intervals induced by compaction. However, other conditions also act to favour the formation of ankerite cement, as shown by the very extensive precipitation of ankerite in certain levels only. These levels are also characterised by a mature Ti-distribution, i.e. the Ti-carrying mineral phases are depleted in Fe and enriched in Ti (Fig. 8.5). However, this relationship is somewhat tentative since only 6 heavy mineral analyses have been made. Immature Ti-mineral content is correlating with low ankerite content e.g. in 221.18 m depth with 0.3 wt% ankerite of the heavy minerals, whereas the mature Ti-mineral distribution in 139.27 m depth corresponds to an ankerite content of 13.5 wt%. This may indicate that the ankerite precipitation primarily was controlled by the depositional rate, or by the number of temporary alluvial and shallow marine depositions along the transport pathway. Low depositional rate or several redepositional phases probably resulted in subsequent widespread formation of ankerite cement. Ca, Fe and Mg are present in slightly lower amounts in the sandstone levels closest to the mudstone levels, confirming that slow deposition, allowing a high degree of weathering, favoured ankerite precipitation. The intrusive nature of some of the sandstone bodies does not seem to have influenced the weathering and diagenetic processes.

The deformation induced by burial has not been pronounced in the sandstones as the grains are generally not fractured (Fig. 5.5). Thus, the veins found in some grains can be attributed to dissolution processes initiating in weak zones of unstable grains, rather than to deformation during burial. In addition, no pressure dissolution of quartz grains parallel to the layering has been observed. However, the horizontal orientation of the mica minerals, which often folds around other detrital grains (Fig. 5.5), reveals that some degree of compaction has occurred. The organic bioclasts are also orientated parallel to the layering (Fig. 5.6A), but the compaction has not been strong enough to destroy the fine structure of the cellular tissue found in many bioclasts (Fig. 5.8). The content of organic matter show a strong correlation with the content of ankerite (Table 5.3) indicating that this is very important in facilitating ankerite precipitation. Large cellular bioclasts dominate the organic matter in the samples with much ankerite cementation.

Ankerite cementation is commonly reported in Jurassic sandstones from the North Sea Basin (e.g. Kantorowicz 1985; Morad *et al.* 1996; Hendry *et al.* 2000; Burns *et al.* 2005), where ankerite concretions and precipitation of dolomite and siderite often are found along with the ankerite cement. This is likely caused by the differences in detrital mineralogy, however small, and the commonly deeper and longer burial histories of the North Sea rocks than the Blokely rocks. Hendry *et al.* (2000) found ankerite to be a fairly early cement asso-

ciated with bioclast dissolution, as in the present study. Kantorowicz (1985) supposed the smectite-illite transition to release all necessary cations for the ankerite formation. It was further proposed that the precipitation overlapped with hydrocarbon generation as a downwards decrease in CaCO_3 was observed, as in the present study. The accumulating hydrocarbons displaced the saturated pore waters downwards causing ankerite precipitation both below the oil-water contact and within the oil. The supply of Fe, Mg and bicarbonate from the hydrocarbon source rocks was thus sufficient to ensure extensive ankerite cementation.

Free pore space has in places been preserved between quartz overgrowths (Figs 5.9A & 5.12D), and smaller pore spaces are found within the open structure of the precipitated fibrous illite (Fig. 5.11A). Less pore space has been preserved in places where kaolinite has replaced albite grains (Fig. 5.12B), while the ankerite replacements effectively have used all the available space (Fig. 5.10A). The average quartz content of the sandstone intervals is increased from 66 to 73 wt% when the authigenic minerals ankerite and pyrite are subtracted from the Rietveld results (Table 5.1), so the effects of the authigenesis are not major in this respect. However, the precipitation of ankerite cement and clay minerals has a major influence on the porosity when looking at specific levels (Table 5.3). Secondary porosity has been formed by dissolution of primarily K-feldspar (Figs 5.9C & 5.11D), whereas more extensive mineral dissolution must have happened locally in the levels of very high porosity (Table 5.3). Stylolites of mica and organic matter are found in some of the porous sandstone levels (Fig. 5.6B) where the high porosity is caused by either dissolution of early cement after the deformation or by poor thin section production. Stylolites have previously been reported in Jurassic rocks of East Greenland (Baron & Parnell 2007), where they were interpreted as indicating burial depths of several kilometers. Euhedral quartz overgrowths are both found in depths of low and high porosity (Figs 5.6C & D). The basalt sills also have had an impact on the porosity, which is much reduced in the sandstones close to the sills (Fig. 5.13B) due to the enhanced heat flux, whereas the influence is minimal in sandstones less than a meter away from the sills (Fig. 5.13A). The mesoge-netic mineral precipitations like e.g. macroquartz correlates with the AFTA and VR results (See chapter 10) as the estimated overburden of at least 2 km is necessary for the degree of diagenesis. The burial cannot have been much deeper either, as this would have lead to authigenesis of chlorite and albite.

5.4 Conclusions

The reservoir quality of the Blokely sandstones is mainly influenced by porosity reduction caused by local ankerite cementation and deformation of ductile grains through mechanical compaction. Much porosity has been preserved by precipitation of microquartz and macroquartz, whereas secondary porosity has been formed where K-feldspar has dissolved during exhumation. The sill-affected sandstone levels have experienced a second episode of mineral precipitations, mainly due to the new injection of cations to the pore fluids, which have prevented the subsequent formation of kaolinite in these levels.

Ankerite cement, amounting to up to 41 wt%, is the only carbonate mineral found in the Blokely core. The growth has occurred both as replacement of feldspars and as a filling of primary pore spaces. The formation has been controlled by the presence of sufficient plant bioclasts, and has been possible through the supply of metal ions from the mudstone. The precipitation has been favoured in rocks that have been exposed to a large amount of weathering.

5.5 References

- Baron, M. & Parnell, J. 2007: Relationships between stylolites and cementation in sandstone reservoirs: Examples from the North Sea, U.K. and East Greenland. *Sedimentary Geology* **194**, 17-35.
- Burns, F.E., Burley, S.D., Gawthorpe, R.L. and Pollard, J.E. 2005: Diagenetic signatures of stratal surfaces in the Upper Jurassic Fulmar Formation, Central North Sea, UKCS. *Sedimentology* **52**, 1155-1185.
- Hendry, J.P., Wilkinson, M., Fallick, A.E. and Haszeldine, R.S. 2000: Ankerite cementation in deeply buried Jurassic sandstone reservoirs of the Central North Sea. *Journal of Sedimentary Research* **70**, 227-239.
- Hendry, J.P. 2003: Ankerite (in sediments). In: Middleton, G.V. (ed.), *Encyclopedia of Sediments and Sedimentary Rocks*. Kluwer Academic Publishers, pp. 19-21.
- Kantorowicz, J.D. 1985: The origin of authigenic ankerite from the Ninian Field, UK North Sea. *Nature* **315**, 214-216.
- Morad, S., De Ros, L.F., Al-Aasm, I.S. 1996: Origin of low $\delta^{18}\text{O}$, pre-compactional ferroan carbonates in the marine Stø Formation (Middle Jurassic), offshore NW Norway. *Marine Petroleum Geology* **13**, 263-276.
- Slater, C. & Cohen, L. 1962: A centrifugal particle size analyser. *Journal of Scientific Instruments* **39**, 614-617.

m	lithology	quartz	clay+mica	albite	K-feldspar	pyrite	ankerite
7.41	sandstone	60	10	4	3	0	24
43.16	sandstone	77	13	5	3	1	1
56.43	sandstone	42	13	13	3	0	29
56.91	sandstone	50	22	13	4	0	11
61.96	sandstone	79	11	5	3	1	1
69.78	sandstone	74	15	7	4	1	0
74.99	mudstone	19	68	2	3	8	1
98.92	sandstone	68	13	5	4	0	11
114.69	heterolith	33	55	6	2	4	0
116.32	sandstone	69	16	8	3	2	2
118.72	sandstone	63	15	8	3	2	9
128.80	sandstone	79	13	4	3	1	0
139.27	sandstone	79	14	3	2	1	1
151.71	sandstone	35	21	8	5	1	30
166.95	sandstone	34	16	3	5	1	41
178.32	mudstone	11	76	5	2	5	1
178.48	sandstone	80	15	2	2	1	0
181.53	sandstone	80	10	1	4	1	4
218.50	mudstone	22	61	8	4	4	1
218.80	sandstone	75	14	3	3	1	4
221.18	sandstone	77	15	2	3	1	2
223.53	sandstone	76	16	1	3	1	3

Table 5.1. Bulk mineralogy determined by XRD of 18 sandstone samples, 1 heterolith sample and 3 mudstone samples from the Blokely core. The amounts are given in wt% determined by the Rietveld method.

m	lithology	kaolinite	illite	vermiculite	smectite	mixed-layer
7.41	sandstone	62	23	0	0	15
43.16	sandstone	44	19	19	6	13
56.43	sandstone	0	50	0	0	50
56.91	sandstone	62	23	0	0	15
61.96	sandstone	58	17	0	0	25
69.78	sandstone	54	23	0	0	23
74.99	mudstone	41	18	18	18	6
98.92	sandstone	47	27	0	0	27
114.69	heterolith	41	18	12	12	18
116.32	sandstone	57	21	0	0	21
118.72	sandstone	54	23	0	0	23
128.80	sandstone	60	30	0	0	10
139.27	sandstone	67	25	0	0	8
151.71	sandstone	64	27	0	0	9
166.95	sandstone	43	21	21	7	7
178.32	mudstone	44	19	13	6	19
178.48	sandstone	67	25	0	0	8
181.53	sandstone	67	17	0	0	17
218.50	mudstone	44	19	19	6	13
218.80	sandstone	54	23	0	0	23
221.18	sandstone	54	23	0	0	23
223.53	sandstone	54	23	0	0	23

Table 5.2. Clay mineralogy determined by XRD of 18 sandstone samples, 1 heterolith sample and 3 mudstone samples from the Blokely core. The amounts are given in qualitative wt%.

depth (m)		7.41	61.96	98.92	118.72	128.80	151.71	178.48	181.53	223.53
quartz	monocrystalline	45.7	50.3	46.0	45.0	65.3	21.3	60.7	61.0	53.0
	polycrystalline	2.0	10.7	4.7	2.3	0.7	1.3	1.0	1.0	3.0
	authigenic	6.0	5.0	3.7	6.3	4.0	3.7	5.0	4.7	5.3
feldspar	albite/plagioclase	5.7	5.3	4.7	10.3	5.7	7.0	4.0	3.3	1.3
	K-feldspar	4.7	7.3	5.3	2.3	4.3	8.0	4.7	7.7	6.3
mica	muscovite	4.0	4.0	6.7	5.0	6.0	7.0	4.7	4.3	6.3
	biotite	0.3	0.0	1.0	0.7	1.0	0.7	0.3	0.0	0.3
	chlorite	0.0	0.3	0.0	0.0	0.0	0.0	0.3	0.0	0.0
	rock fragments	4.0	1.0	0.0	0.0	0.0	0.0	0.0	0.0	0.3
	heavy minerals	0.0	1.0	0.3	0.7	1.0	0.0	0.7	0.0	1.0
	framboidal pyrite	0.7	0.3	0.0	1.0	0.0	0.0	0.7	0.0	0.3
	clay minerals	7.0	10.3	4.0	12.0	10.3	10.0	17.0	13.7	19.3
	ankerite	17.7	1.0	13.0	10.3	0.0	32.3	0.0	3.0	2.0
	organic matter	2.3	3.3	10.7	4.0	1.7	8.7	1.0	1.3	1.3
	porosity	2.0	4.7	0.0	0.0	19.0	0.0	16.3	18.7	1.3

Table 5.3. Quantitative bulk mineralogy of 8 sandstone samples from the Blokely core determined by point count in thin sections. The porosity wt% is separate from the wt% of the minerals.

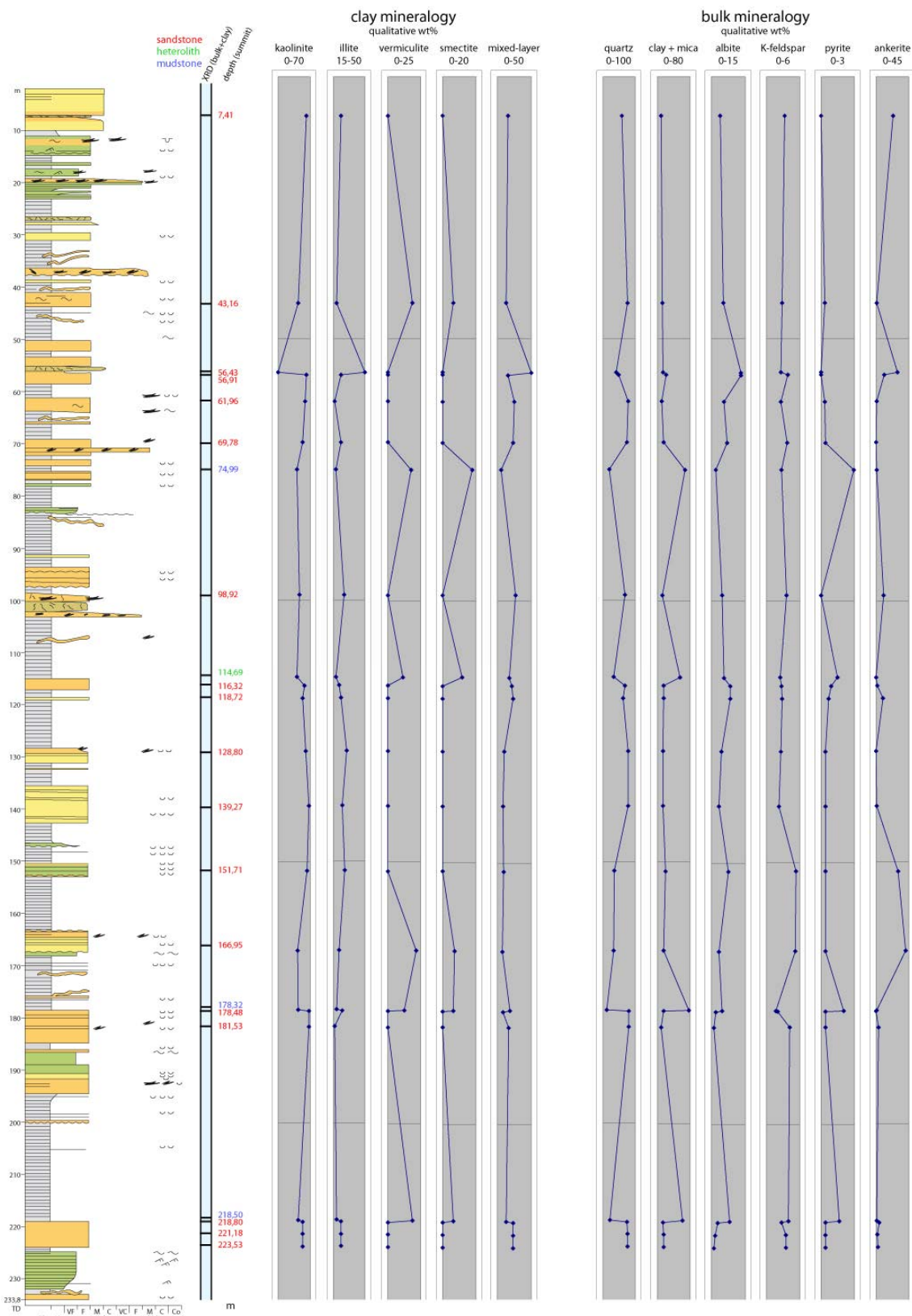


Fig. 5.1. Mineralogy overview of 18 sandstone samples, 1 heterolith sample and 3 mudstone samples from the Blokely core. The bulk mineralogy is determined by the Rietveld method, whereas the clay mineralogy is determined more qualitatively. The log legend refers to Fig. 3.1.2.

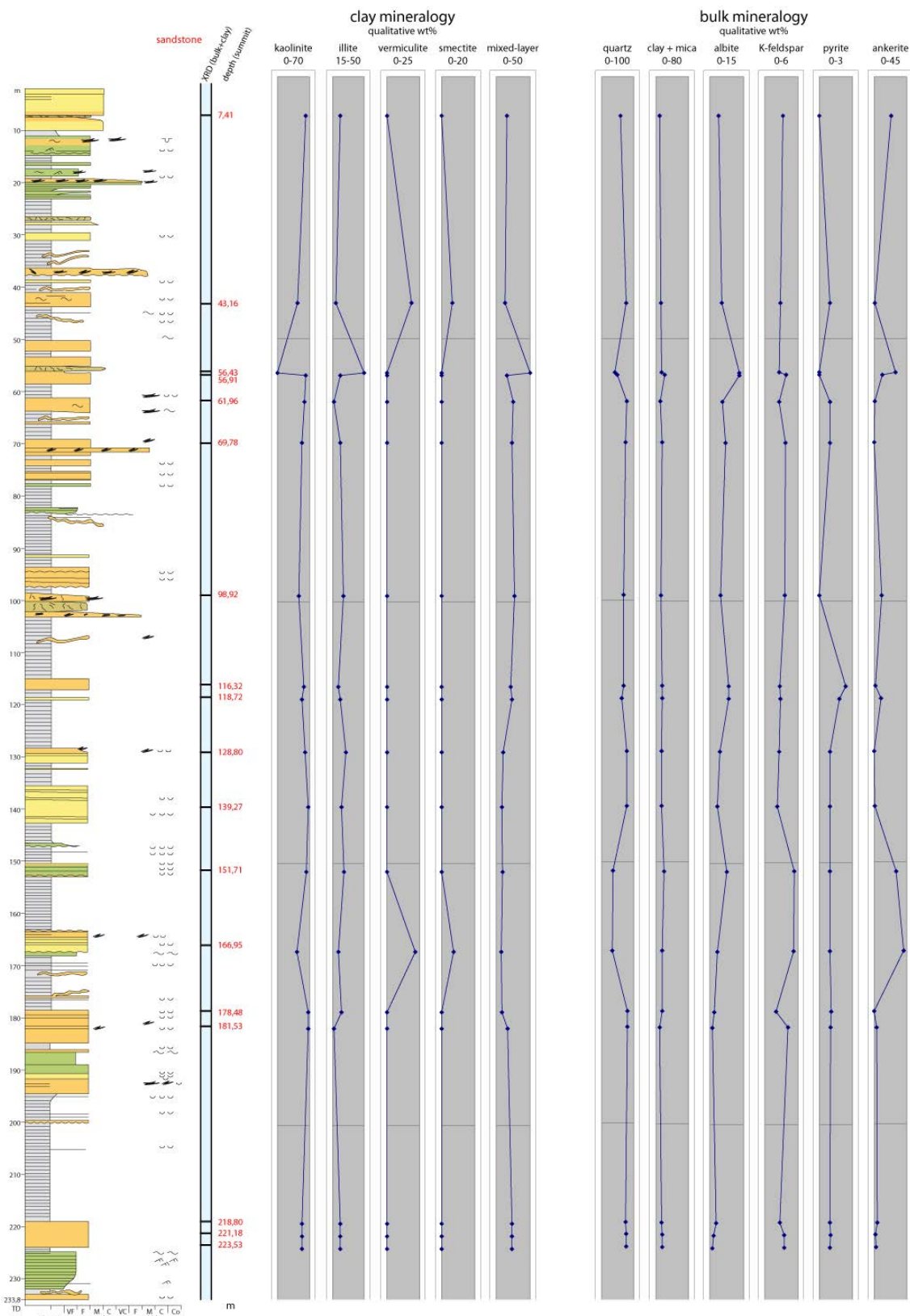


Fig. 5.2. Mineralogy only including the 18 sandstone samples from the Blokely core. The log legend refers to Fig. 3.1.2.

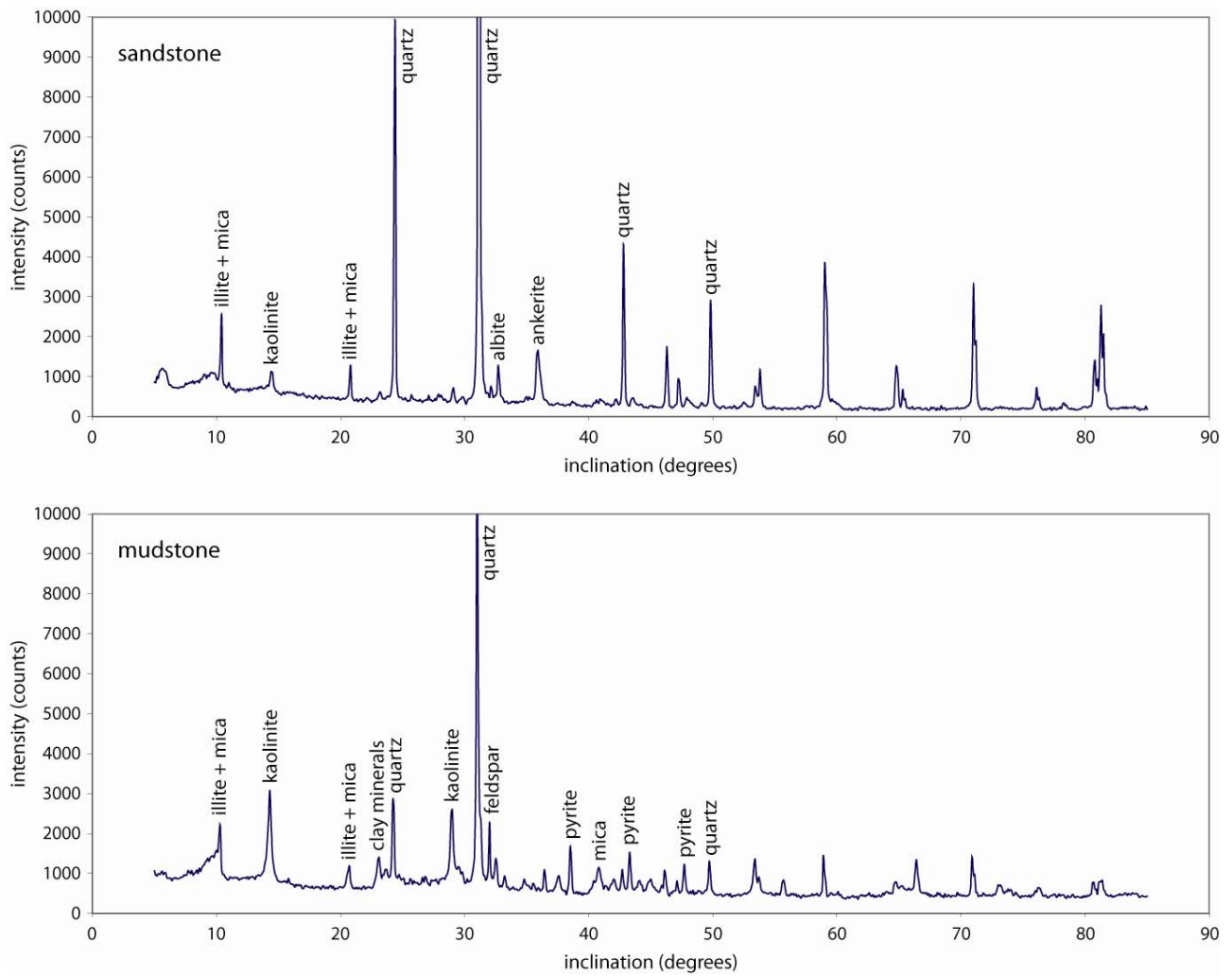


Fig. 5.3. XRD diffractograms with indication of the minerals present in largest amounts identified by their crystal lattice constants. The sandstone in 118.72 m depth and mudstone in 178.32 m depth are used as examples.

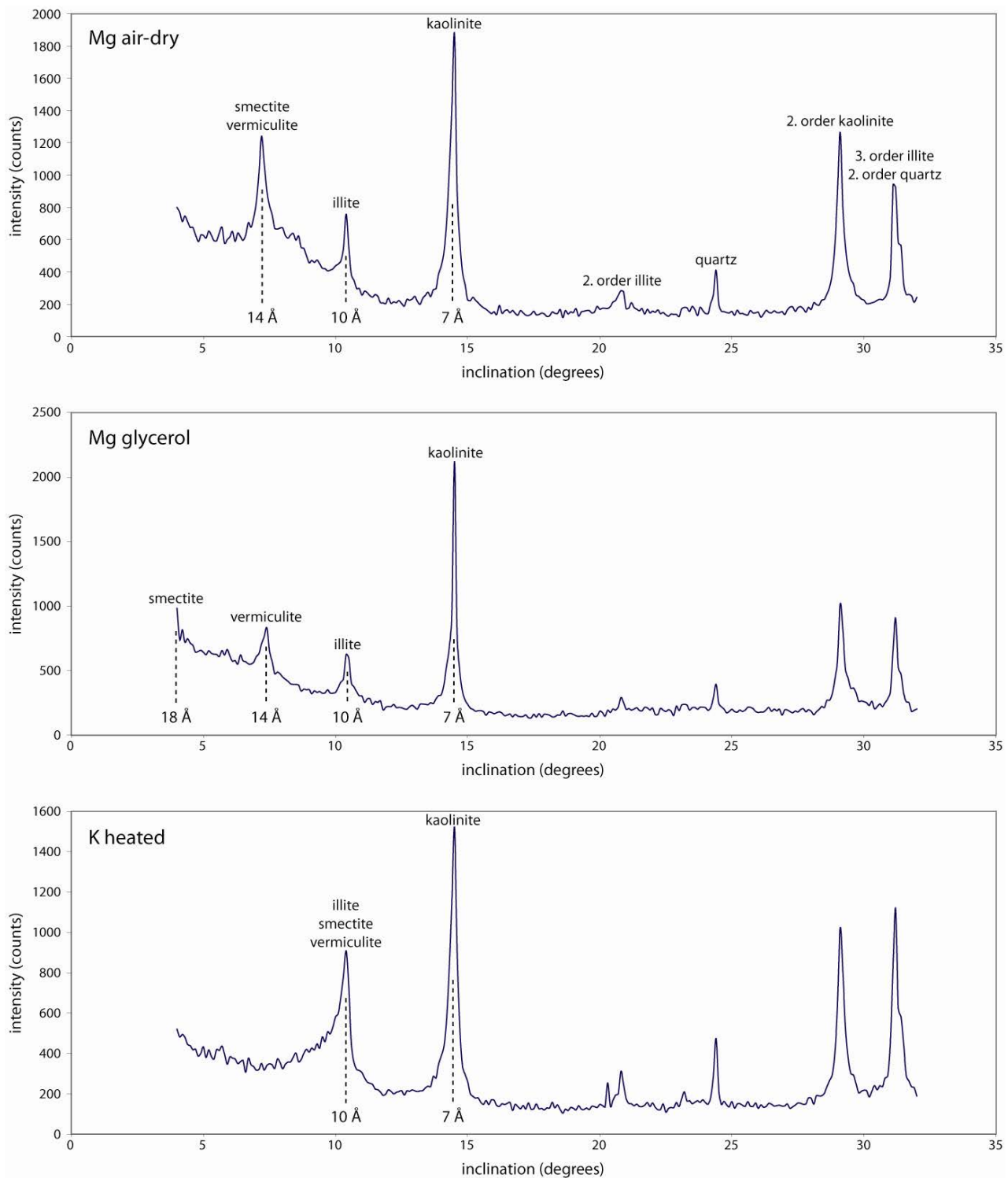


Fig. 5.4. XRD diffractograms of clay that has been saturated with Mg^{2+} air-dry, Mg^{2+} glycerol and K^+ heated. The changes in crystal lattice parameters when exposed to the different conditions reveal the nature of the clay minerals. The clay fraction of the mudstone in 74.99 m depth is used as an example.

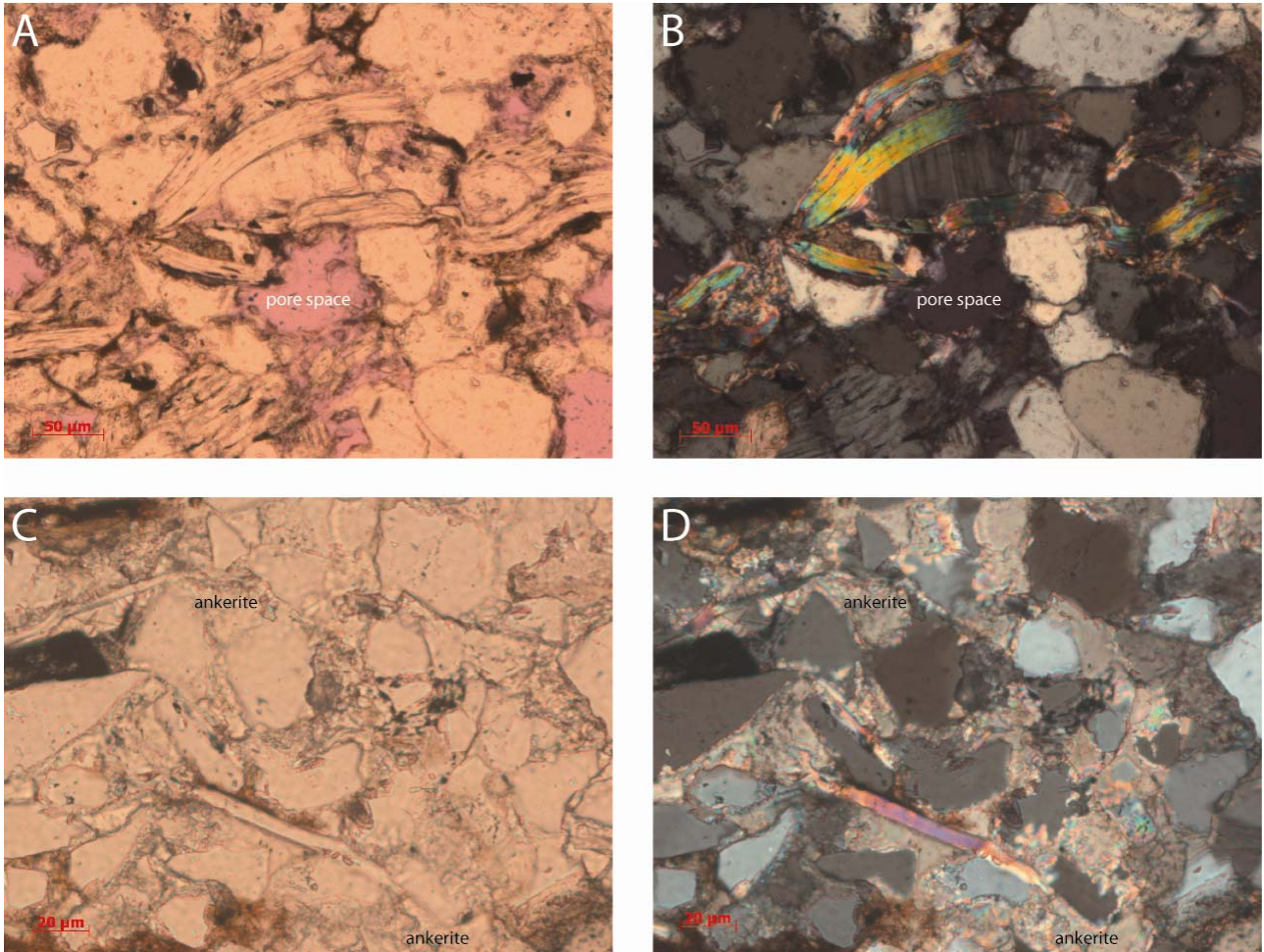


Fig. 5.5. Paired thin section photos with crossed nicols on B and D. Porous sandstone is shown in A and B in 181.53 m depth, where the pink colour in A indicates the free pore space. Ankerite cemented sandstone is shown in C and D in 151.71 m depth, where the pastel colours in D indicates the ankerite.

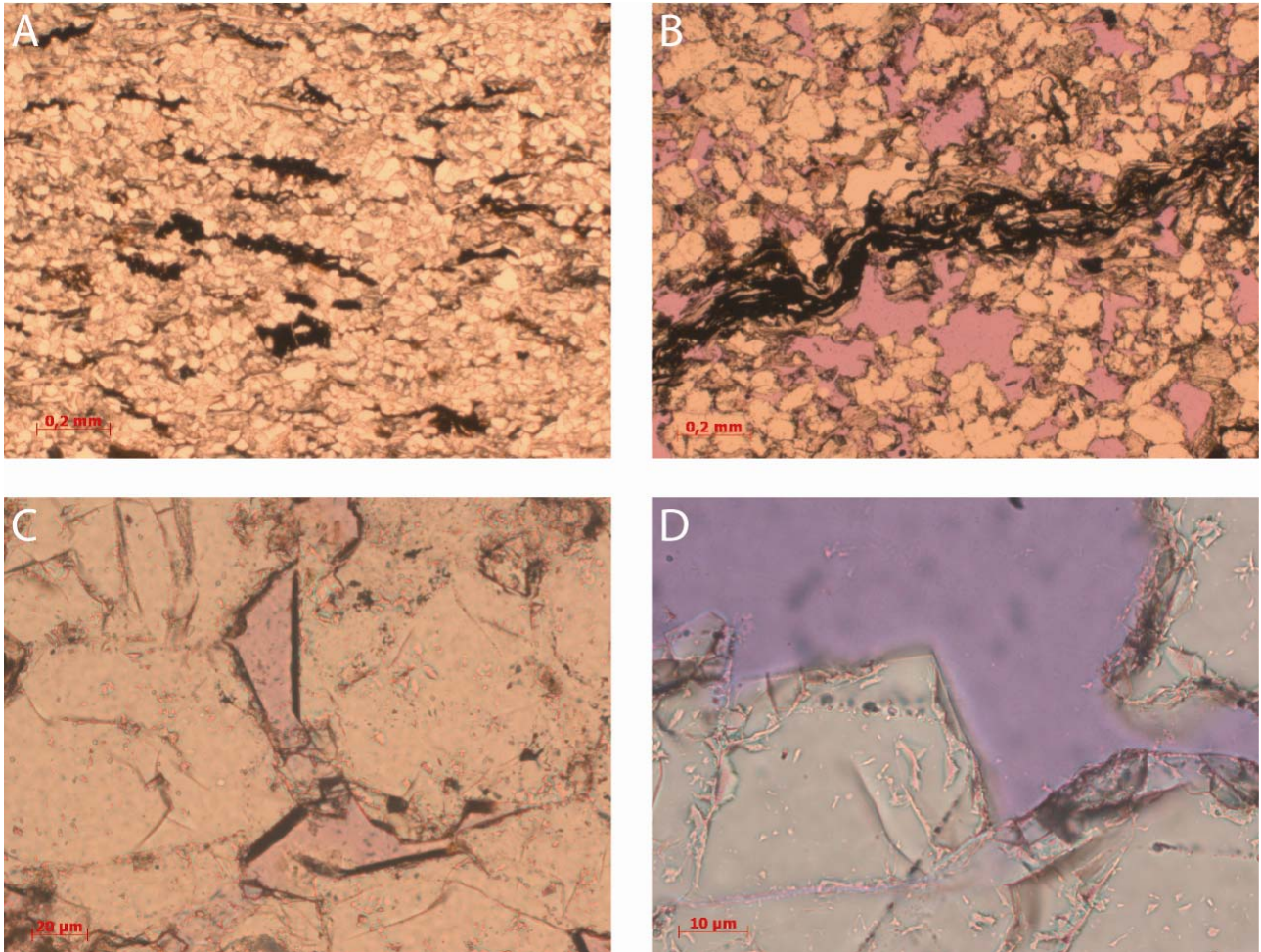


Fig. 5.6. Thin section photos with pink indication of free pore space. A: Ankerite cemented sandstone in 151.71 m depth with horizontal orientation of mica and bioclasts. B: Porous sandstone in 178.48 m depth with stylolites. C: Quartz overgrowths in sandstone in 61.96 m depth. D: Quartz overgrowths in porous sandstone in 181.53 m depth.

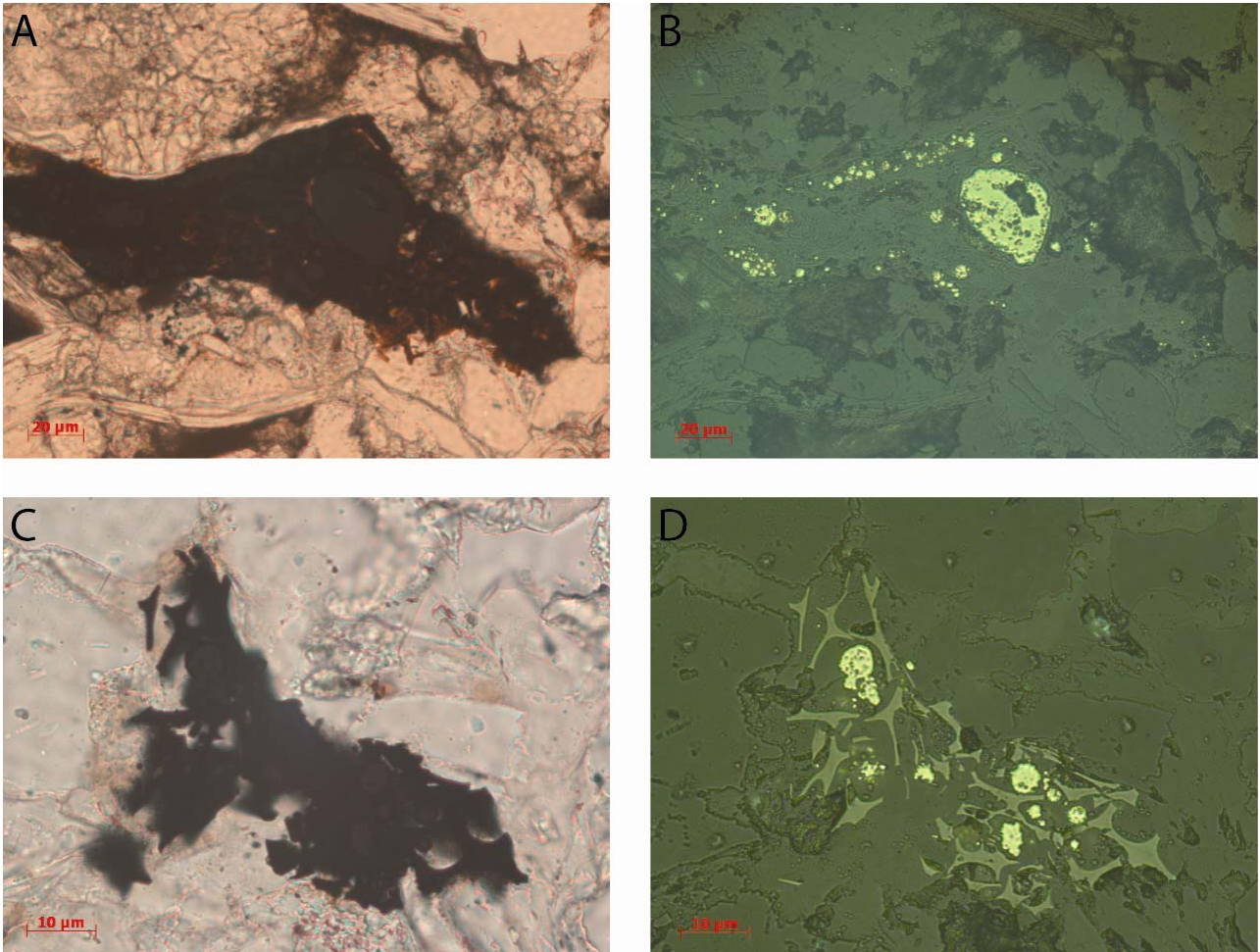


Fig. 5.7. Paired thin section photos of bioclasts of plant material. Reflected light in B and D enables recognition of the yellow pyrite. Framboidal pyrite has precipitated within some of the bioclasts. All photos are from 151.71 m depth.

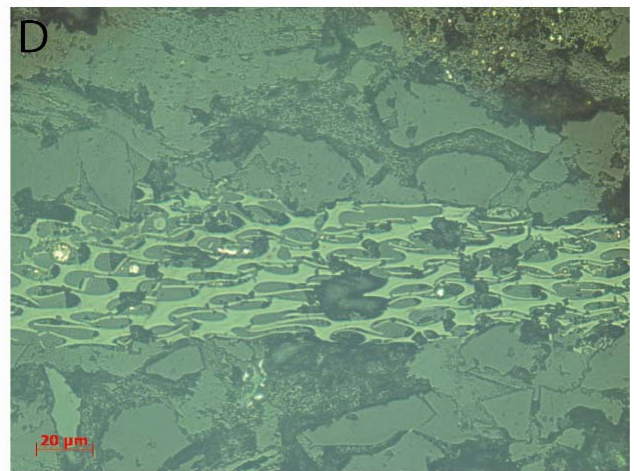
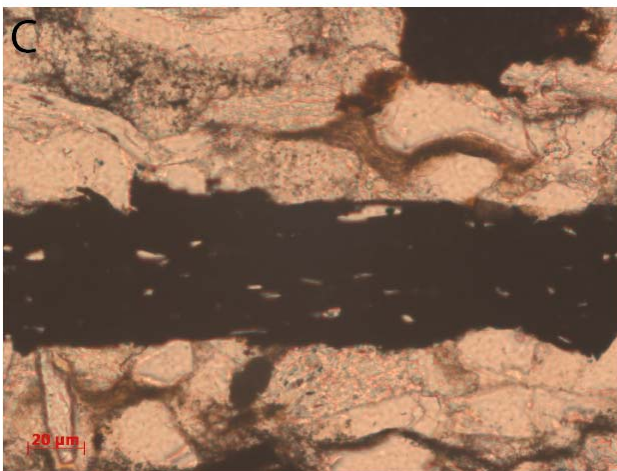
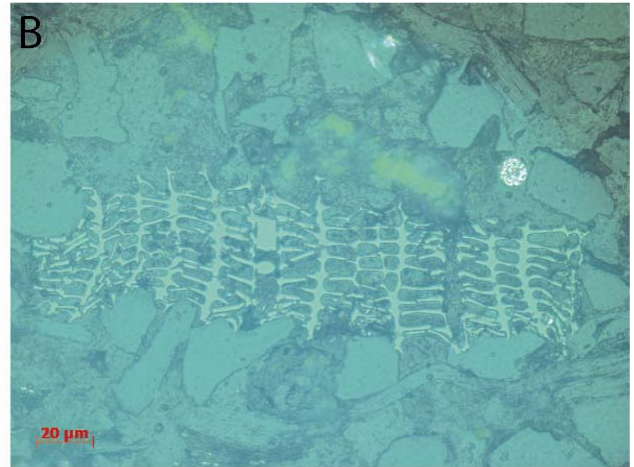
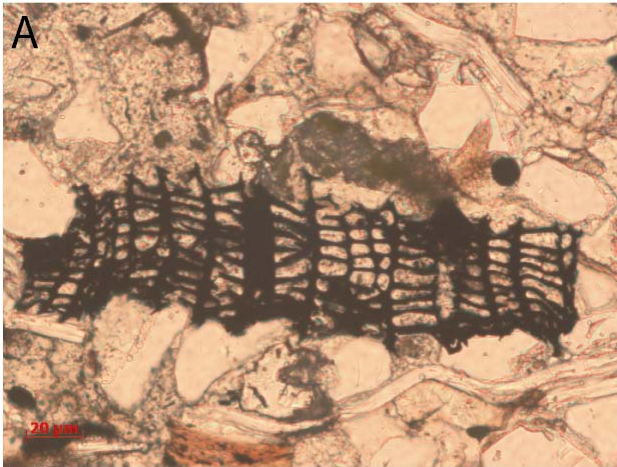


Fig. 5.8. Paired thin section photos of bioclasts of plant material. Reflected light in B and D makes the cellular tissue easily recognisable. The yellow colour above the bioclast on B is caused by the staining for K-feldspar. All photos are from 151.71 m depth.

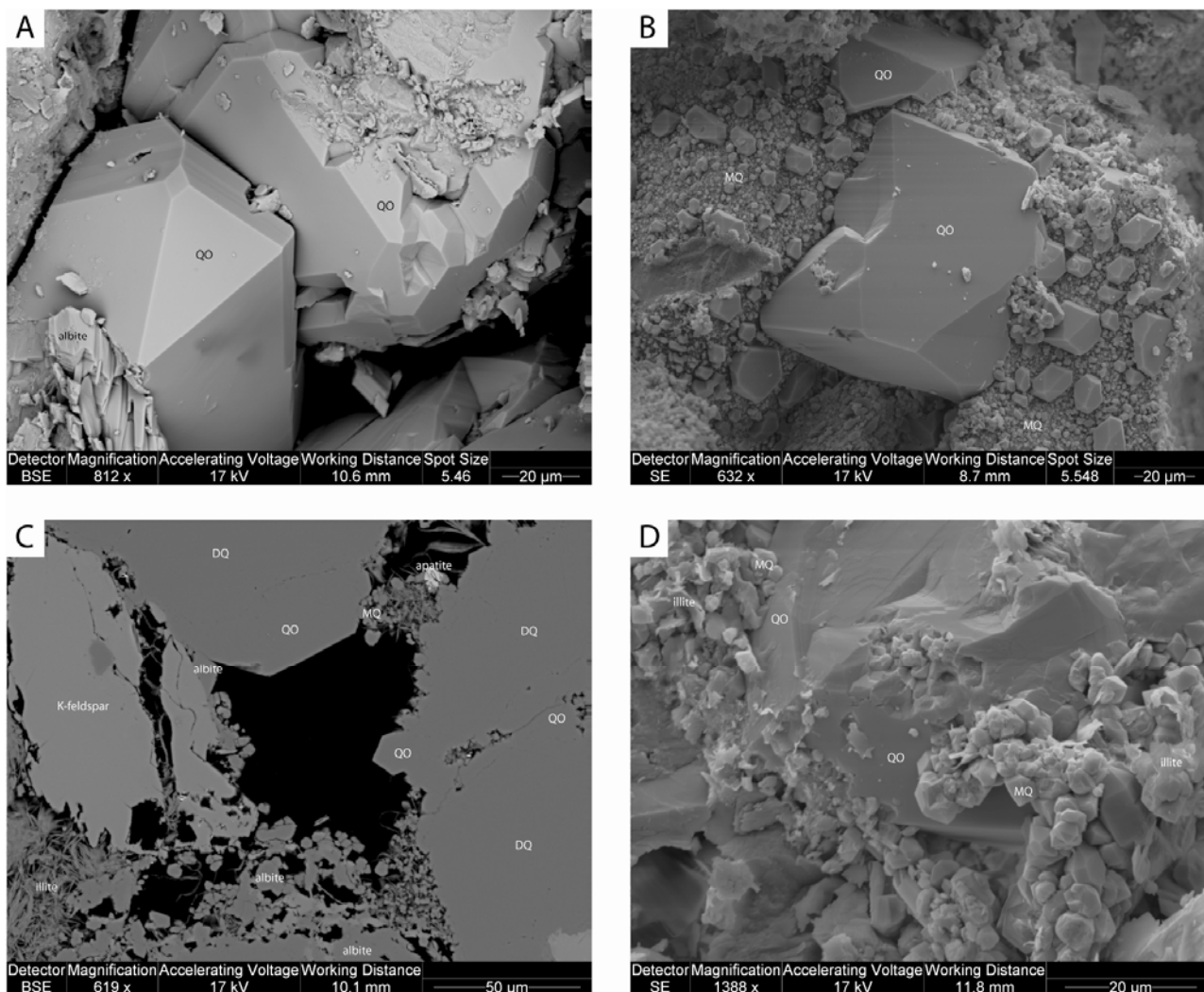


Fig. 5.9. SEM images of quartz precipitation. A: Sandstone with extensive quartz overgrowth in 7.41 m depth. B: Sandstone with quartz overgrowth (QO) on the grain in the middle surrounded by microquartz (MQ) nucleations in various dimensions in 43.16 m depth. C: Thin section of sandstone with feldspar dissolution and growth of microquartz, macroquartz (QO), illite and apatite in 100.05 m depth (DQ=detrital quartz). D: Sandstone showing a second episode of microquartz precipitation which has restricted the growth of macroquartz in 100.10 m depth.

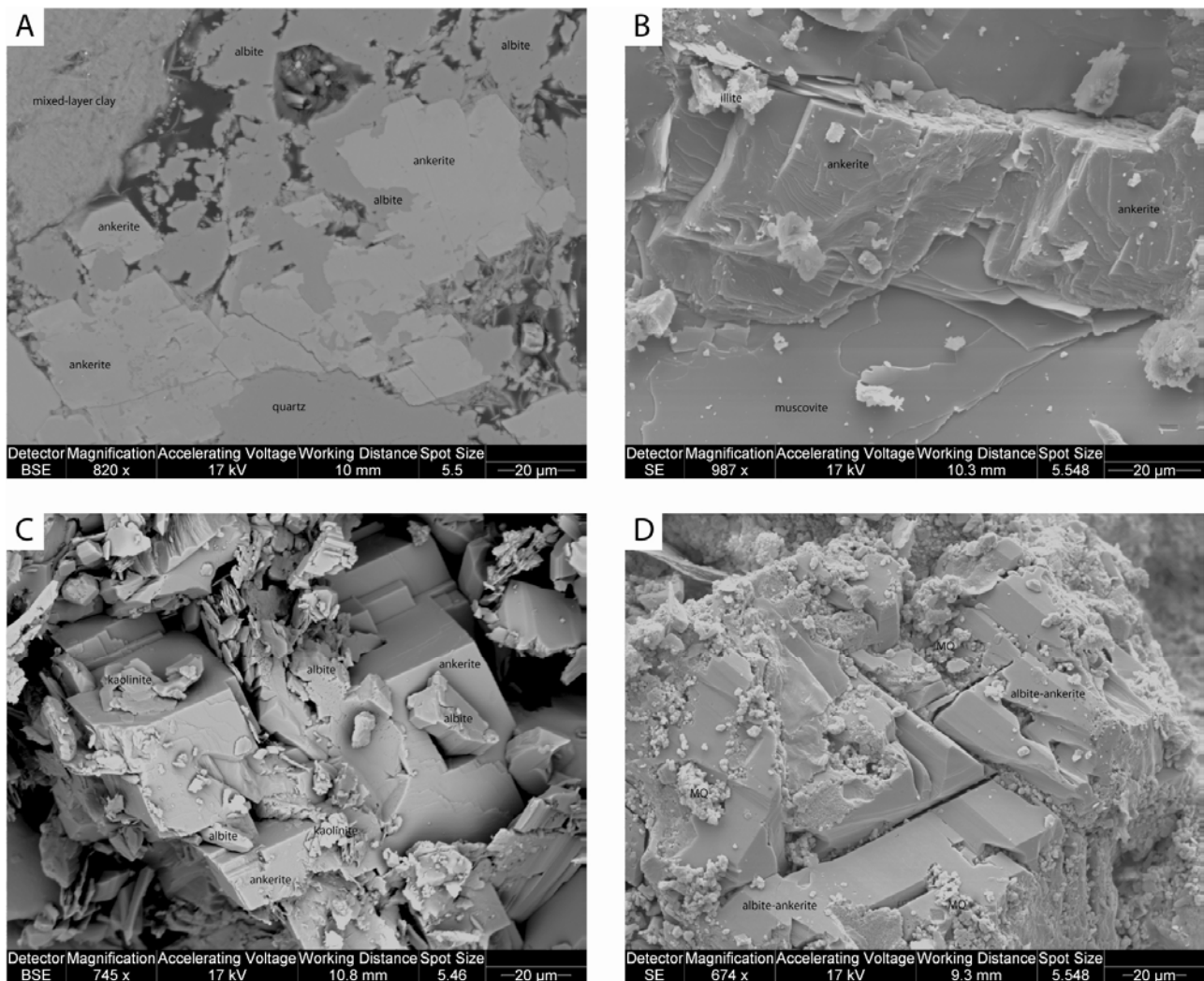


Fig. 5.10. SEM images of ankerite precipitation. A: Thin section of sandstone showing partly replacement of albite with ankerite in 100.05 m depth. Growth of quartz and mixed-layer clay minerals. B: Sandstone with growth of ankerite followed by illite in 56.43 m depth. C: Sandstone showing replacement of albite with ankerite followed by kaolinite precipitation in 7.41 m depth. D: Sandstone with beginning ankerite replacement of albite and intergrowth of microquartz in 69.78 m depth.

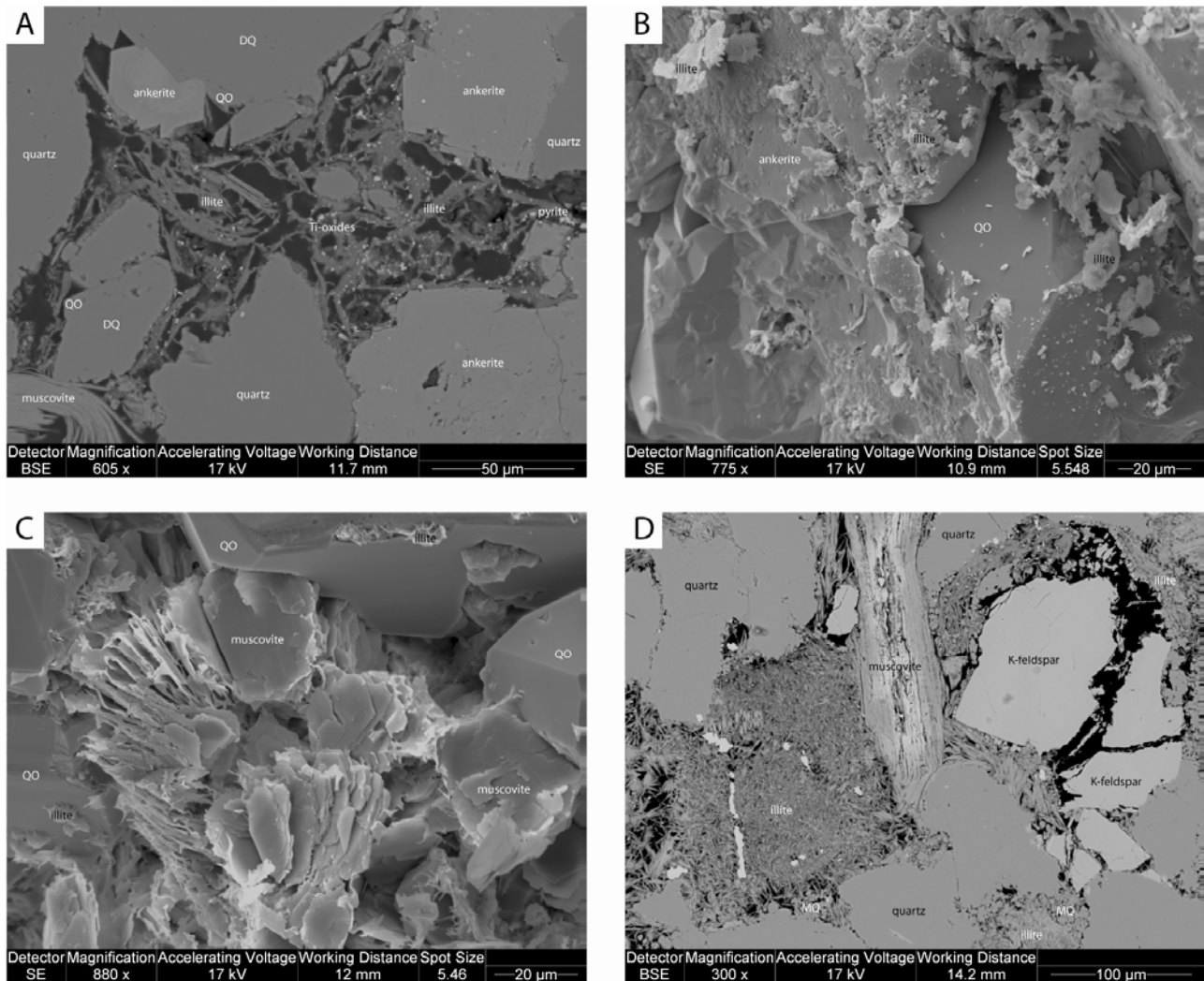


Fig. 5.11. SEM images of illite precipitation. A: Thin section of sandstone with growth of ankerite, macroquartz (QO), illite, pyrite and lastly Ti-oxides in 7.41 m depth (DQ=detriral quartz). B: Sandstone with intergrowth of macroquartz and illite in 139.27 m depth. C: Sandstone with intergrowth of macroquartz and illite in 221.18 m depth. D: Thin section of sandstone with growth of microquartz (MQ) and illite and lastly K-feldspar dissolution as shown by the free pore space in 100.05 m depth.

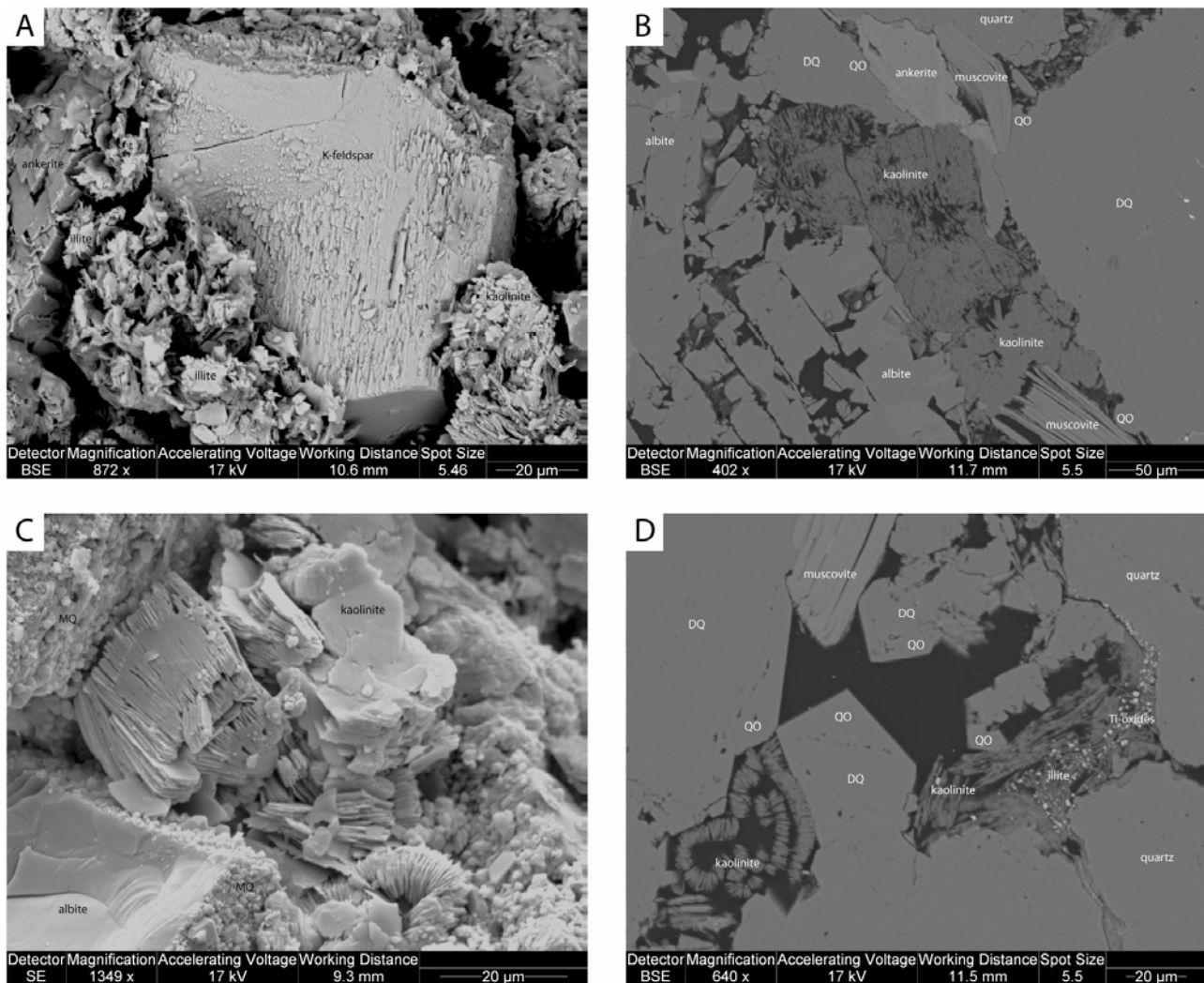


Fig. 5.12. SEM images of kaolinite precipitation. A: Sandstone with growth of ankerite, illite and kaolinite in 7.41 m depth. Slight K-feldspar dissolution is associated with the kaolinite precipitation. B: Thin section of sandstone with albite dissolution and growth of ankerite, macroquartz (QO) and kaolinite in 7.41 m depth (DQ=detriral quartz). The kaolinite has formed as a replacement of albite. C: Sandstone with microquartz (MQ) growth on the albite grains and kaolinite growth in free pore space in 69.78 m depth. D: Thin section of sandstone with growth of macroquartz, illite, Ti-oxides and lastly kaolinite in 7.41 m depth.

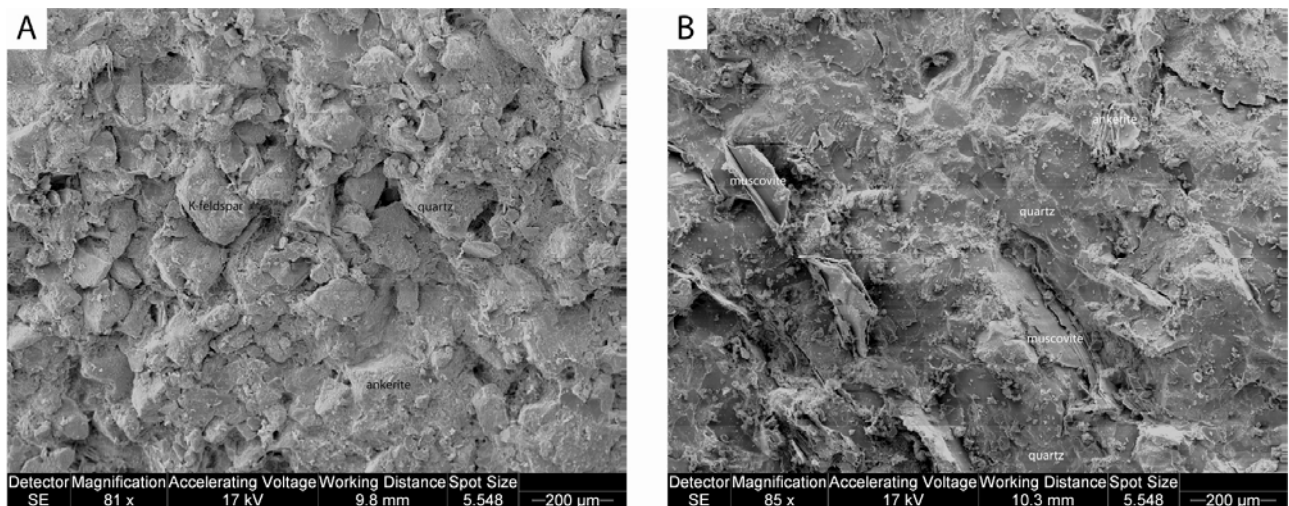


Fig. 5.13. SEM images illustrating the texture of the sandstones. A: Lithology overview in 56.91 m depth about 0.53 m from a basalt sill showing that the outlines of most grains are preserved. B: Lithology overview in 56.43 m depth about 0.05 m from a basalt sill showing smooth quartz surfaces and protruding muscovite.

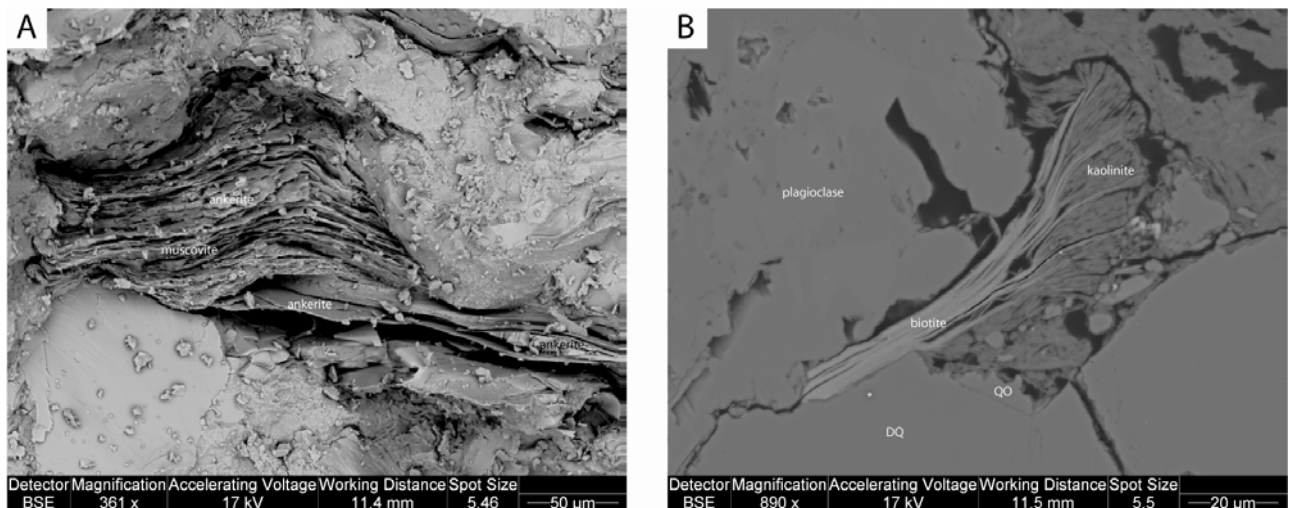


Fig. 5.14. SEM images of micas with intergrowing minerals. A: Sandstone with intergrowth of ankerite in flakes of muscovite in 166.95 m depth. B: Thin section of sandstone with growth of kaolinite fans between flakes of biotite in 7.41 m depth (DQ=detrital quartz, QO=quartz overgrowth).

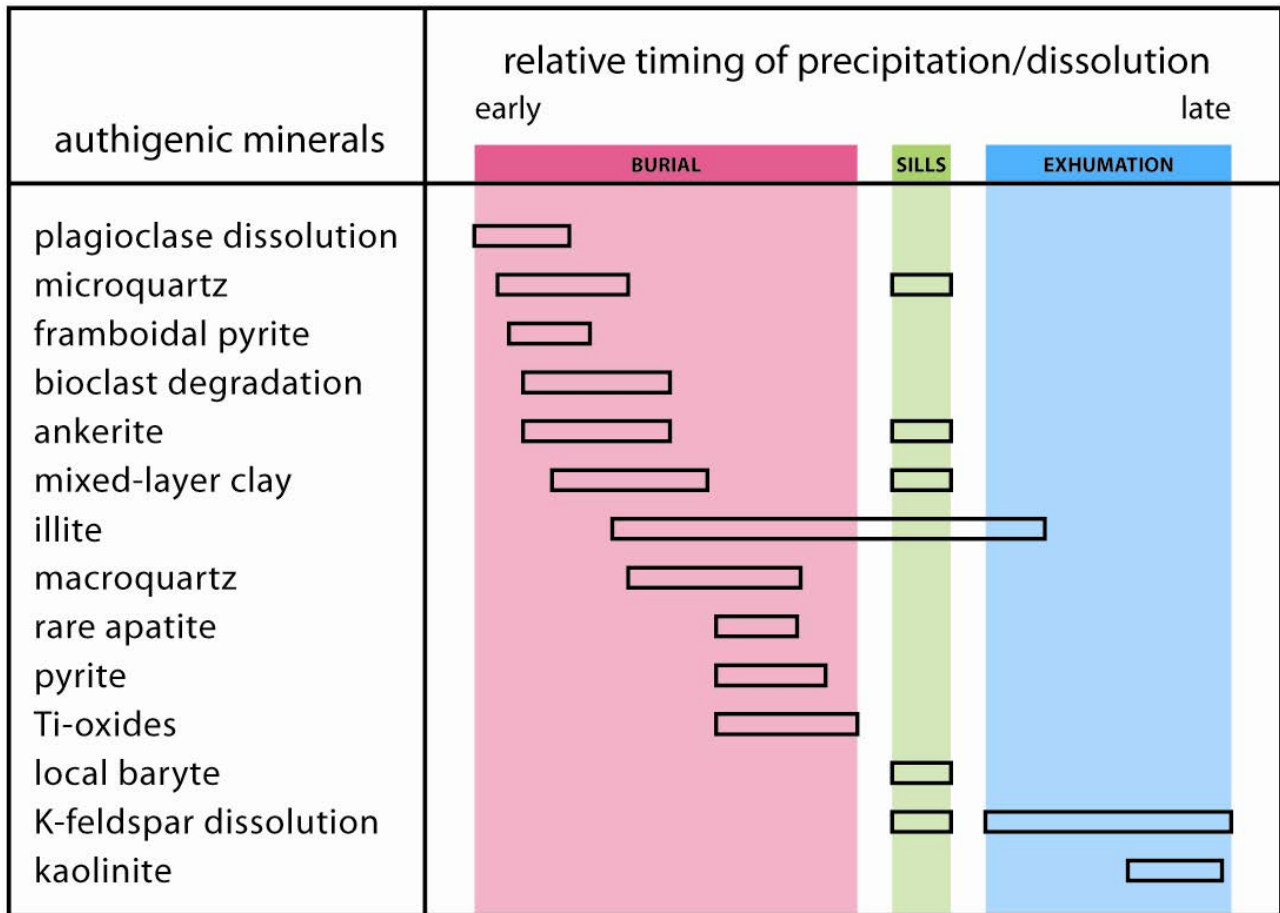


Fig. 5.15. Diagenetic sequence of the Blokely core showing the events of burial, basalt intrusion and exhumation. The local heat-flow around the basalt sills has caused a second episode of precipitation of mainly microquartz, whereas the dissolution of K-feldspar was initiated.

6. Porosity, Permeability and Grain Density

Conventional core analysis was conducted on 35 plugs of sandstone (25 horizontal plugs and two vertical plugs), mudstone (5 vertical plugs) and igneous intrusions (3 horizontal plugs).

6.1 Methods

The conventional core analysis (CCAL) of the Blokely core was carried out at GEUS Core Laboratory. For a more detailed description of methods, instrumentation and principles of calculation, the reader is referred to American Petroleum Institute (API) recommended practice for core-analysis procedure (API 1998).

The present description only encounters CCAL of plugs taken from the well core. A description of the logging of the core is provided in a separate report (Appendix 11.8).

Plugging

Plugging of the core was carried out from selected sandstone, mudstone and igneous intrusions (basalt) at irregular intervals. Plugs were taken as 1.5" plugs using tap water as coolant and both horizontal and vertical plugs were retrieved. Location and orientation of plugs are presented in Table 6.2. Plugs oriented horizontal (parallel to bedding) are indicated with H and vertical oriented plugs (normal to bedding) are indicated with V.

Cleaning and drying

Following plugging, the samples were placed in a Soxhlet extractor, which continuously soaks and washes the samples with methanol. This process removes water and dissolves salt precipitated in the pore space of the rock. Extraction was terminated when no chloride ions were present in the methanol. No further cleaning was carried out since the samples did not contain hydrocarbons.

Following cleaning, the samples were left to evaporate the major part of the methanol at laboratory room temperature ($20 \pm 2^\circ\text{C}$) for 24 h and subsequently dried at 40°C for 24 h.

Gas permeability, uncorrected (GEUS steady state instrument)

Each cleaned and dried plug was mounted in a Hassler core holder, and a confining pressure of 400 psi (27.6 bar) was applied to the sleeve. The uncorrected permeability to gas was measured by flowing nitrogen gas through a plug of known dimensions at differential pressures between 0 and 14.5 psi (0 and 1 bar). No back pressure was applied. The readings of the digital gas permeameter are checked regularly by routine measurement of permeable steel reference plugs (Core Laboratories™ gas permeability reference plug set). Using the digital flowmeter-reading, the lower limit for permeability measurements is 0.05 mD (Tables 6.1, 6.2).

He-porosity and grain density

The porosity of each cleaned and dried plug was determined by subtraction of the measured grain volume from the measured bulk volume. The Helium technique, employing Boyle's Law, was used for grain volume determination, applying a double chambered Helium porosimeter with digital readout. The sample bulk volume was measured by submersion of the plug in a mercury bath using Archimedes principle. Grain density was calculated from the grain volume measurement and the weight of the cleaned and dried sample.

Before measurements, the Helium porosimeter was calibrated using a set of steel plugs (Core Laboratories™ volume reference plug set). The bulk volume apparatus is checked frequently as a laboratory routine using a steel plug with known volume.

Precision of analytical data

Table 6.1 shows the precision (= reproducibility) at the 68% level of confidence (+/- 1 standard deviation) for routine core analysis measurements performed at the GEUS Core Laboratory.

6.2 Results

Results of the conventional core analyses are presented in Table 6.2 and Figures 6.1–6.5.

Sandstone porosity varies between 1–26% with an average of 15.0%. The permeability of the sandstones ranges from <0.05–412 mD. A cross plot of porosity and permeability in sandstones shows good correlation (Fig. 6.1).

Sandstones with high porosities >15% are recorded in the entire cored succession. Sandstones with porosities >20% are present in the upper 0–130 m of the core. Sandstones with low to medium porosities (<15%) are recorded in the entire cored interval (Fig. 6.3). Sandstones with high porosity (>15%) record permeabilities of 20–400mD (Fig 6.1), except for the sample at 220.25 m which record a porosity of 16.1% and a permeability of 5 mD (Table 6.2).

The grain density of sandstones ranges from 2.43–2.75 g/cc, with an average of 2.68 g/cc. High porosity (>15%) sandstones show densities of 2.62–2.70 g/cc, whereas medium to low porosity (<15%) sandstones in general records densities of 2.65–2.76 g/cc. Sandstones with high densities ~2.75 g/cc are in general associated with low porosity and low permeability (Fig. 6.2).

The mudstones have porosities below 6% and permeability <0.05 mD. Both grain density and porosity of the mudstone samples show general upward increasing trends, although only based on five measurements (Figs. 6.3, 6.5).

Igneous intrusions (basalt) have very low porosity (<2%) and very low permeability (<0.05 mD). The grain density is very high, 3.0–3.05 g/cc (Fig 6.5), which is also shown in the bulk density log (Fig. 3.4.2, Appendix 11.8).

6.3 Discussion and conclusions

High porosities (>15%) were measured on half of the sandstones plugs and are generally recorded in the massive sandstone units (see chapter 4). Low porosity and low permeability sandstone plugs in general have a high degree of cementation commonly of ankerite (see chapter 5). Sandstones with high densities (~2.68–2.76 g/cc) are recorded e.g. at 151.65 m and 166.70 m and are in general attributed to diagenetic precipitated ankerite, which has a grain density of 3.0–3.11 g/cc. Calculation of grain density in sandstones with 30% ankerite and 70% quartz results in a grain density of 2.75 g/cc. A high ankerite content of up to about 41 wt% is recorded in the sandstones, and resulted in a markedly reduction of the porosity and permeability (see chapter 5). The sandstones in vicinity of the igneous intrusions (e.g. at 56.55 m), also show low porosity and permeability and a high grain density, which is also attributed to ankerite precipitation in the pore spaces.

The low porosity sandstones at depths of 186.95 m and 187.05 m, respectively, have low densities, which are associated with laminated fine-grained sandstone with thin mudstone laminae and mudstone intraclasts (Table 6.2, Appendix 11.1).

The massive sandstones with high porosity are potential good reservoir beds depending on thickness and lateral extent. These massive sandstone beds were deposited as elongated mass flow – high density turbidites with limited lateral extent and highly variable thicknesses or as laterally extensive sheets; and they are commonly post depositionally remobilised (chapter 4, Surlyk & Noe-Nygaard 2001; Surlyk *et al.* 2007). The reservoir extent and quality may thus be difficult to access due the geometrical complexity of the remobilised sandstones.

All sandstone units in the drilled succession are potential excellent carrier beds for hydrocarbon migration laterally into the shelf margin sandstones of the Raukelv Formation (see chapters 3 and 4). All analysed mudstones are considered as potential seals.

6.4 References

- American Petroleum Institute (API) 1998: Recommended Practices For Core Analysis. Exploration and Production Department, American Petroleum Institute, Second edition.
- Surlyk, F. & Noe-Nygaard, N. 2001: Sand remobilisation and intrusion in the Upper Jurassic Hareelv Formation of East Greenland: Bulletin of the Geological Society of Denmark, **48**, 169–188.
- Surlyk, F. Noe-Nygaard, N. & Gjelberg, J. 2007: The Upper Jurassic Hareelv Formation of East Greenland: A Giant Sedimentary Injection Complex. In Hurst, A. & Cartwright, J. (eds): Sandinjectites: Implications for Hydrocarbon exploration and production. American Association of Petroleum Geologists (AAPG) Memoir, **87**, 141-149.

Measurement	Range	Precision
Grain density		0.003 g/cc
Porosity		0.1 porosity-%
Permeability:	0.05-0.1 mD	15%
(Conventional)	> 0.1 mD	4%

Table 6.1 Precision of analytical data.

Plug	Depth [m]	Plug H/V	Lithology	Porosity _(He) [%]	Gas permeability [mD]	Grain density [g/cc]
601	4,20	H	SAND	21,96	411,86	2,643
602	9,80	H	SAND	14,38	4,54	2,65
603	22,10	H	SAND	8,50	0,14	2,753
604V	22,10	V	SAND	11,41	0,10	2,708
605**	23,65	H	MUDSTONE	5,64	#I/T	2,522
606B	26,70	H	BASALT	1,71	#I/T	3,035
607	29,90	H	SAND	20,55	21,42	2,678
608	42,40	H	SAND	21,30	37,90	2,664
609	51,00	H	SAND	9,63	0,21	2,754
610B	55,75	H	BASALT	0,37	#I/T	3,008
611	56,55	H	SAND	6,37	0,05	2,748
612	57,10	H	SAND	23,81	56,10	2,687
613	66,25	H	SAND	14,61	2,57	2,652
614	70,75	H	SAND	19,74	20,44	2,624
615	78,10	H	SAND	13,40	0,63	2,686
616V	78,40	V	MUDSTONE	2,23	#I/T	2,469
617	94,00	H	SAND	24,99	32,91	2,651
618	99,50	H	SAND	14,28	0,31	2,671
619B	101,40	H	BASALT	0,39	#I/T	3,048
620V	113,85	V	MUDSTONE	1,85	#I/T	2,429
621	116,65	H	SAND	21,51	53,76	2,657
622	130,30	H	SAND	25,69	179,72	2,651
623	140,35	H	SAND	18,13	45,76	2,657
624	141,60	H	SAND	17,85	43,27	2,658
625	151,65	H	SAND, muddy	1,63	#I/T	2,719
626	166,70	H	SAND, cem	1,11	#I/T	2,752
627V	169,40	V	MUDSTONE	0,82	#I/T	2,374
628	184,10	H	SAND	17,55	30,79	2,651
629V	186,95	V	SAND	7,40	#I/T	2,651
630	187,05	H	SAND	7,92	0,29	2,656
631V	209,65	V	MUDSTONE	1,58	#I/T	2,576
632	220,25	H	SAND	16,11	5,00	2,675
633	230,50	H	Heterolith	4,08	0,13	2,658
634	233,35	H	SAND	14,88	0,45	2,681

**** Broken plug - permeability not measured #I/T = Permeability below 0.05 mD**

Table 6.2 Porosity, permeability and grain density of plugs.

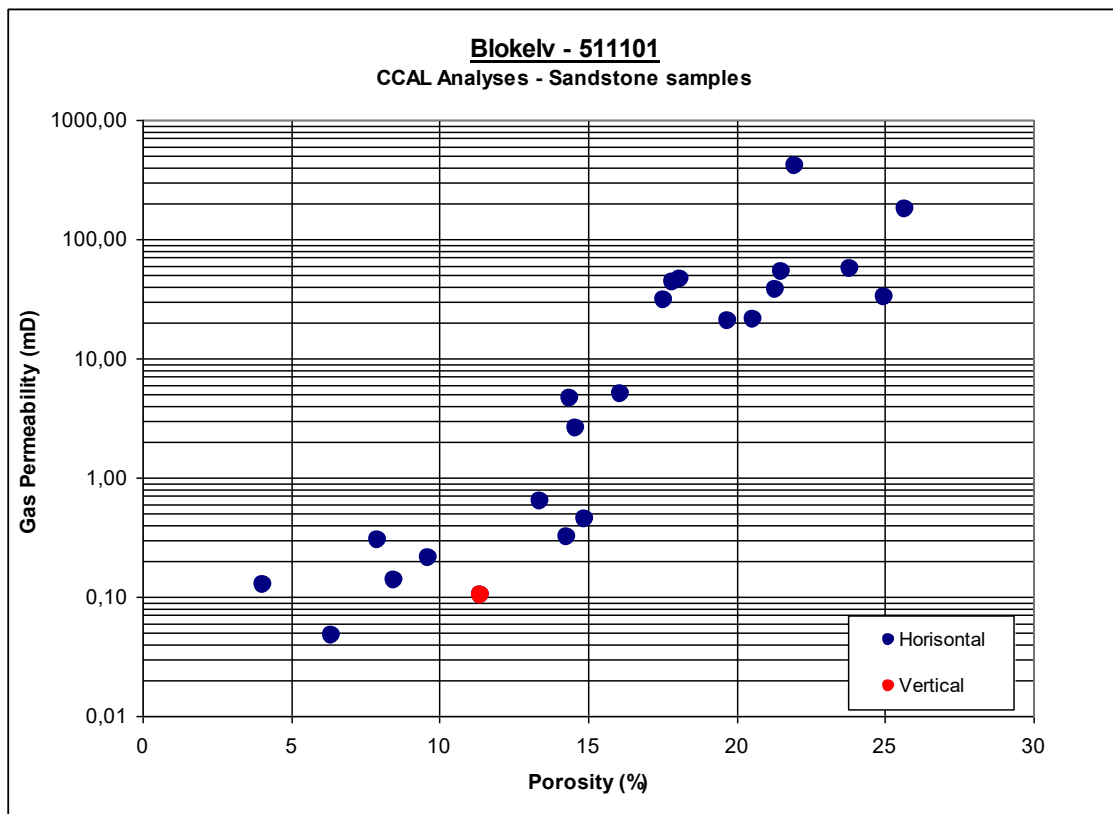


Fig. 6.1 Porosity and Permeability cross plot of sandstone samples.

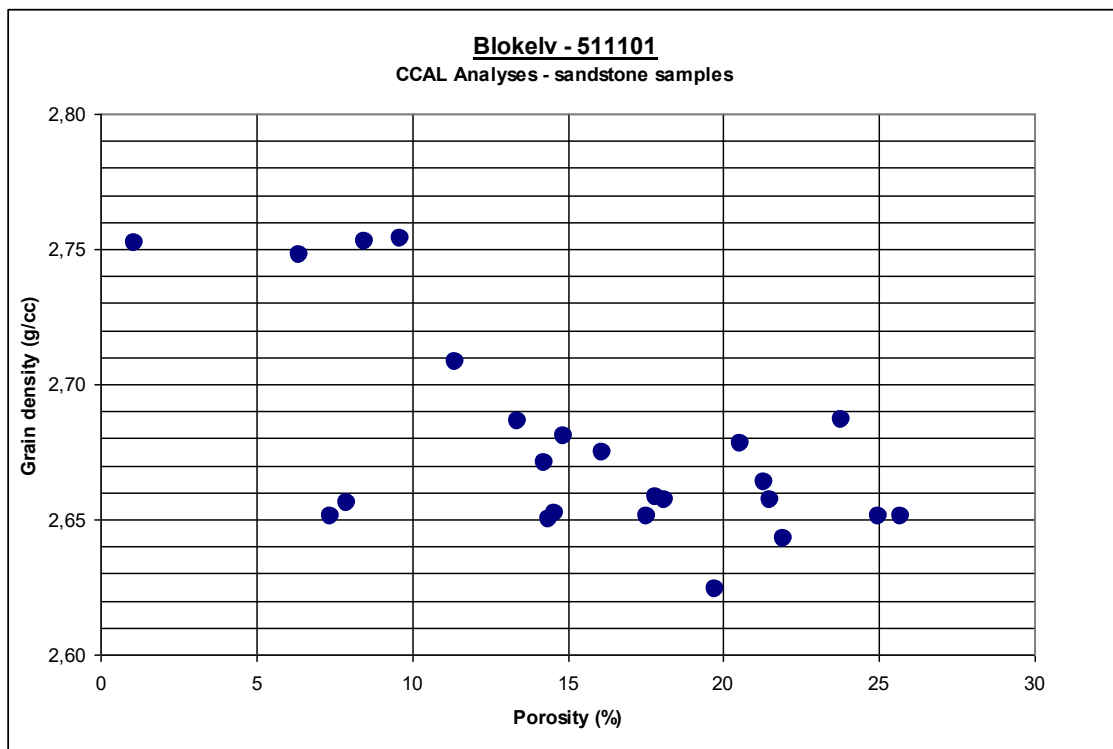


Fig. 6.2 Porosity and Grain density cross plot of sandstone samples.

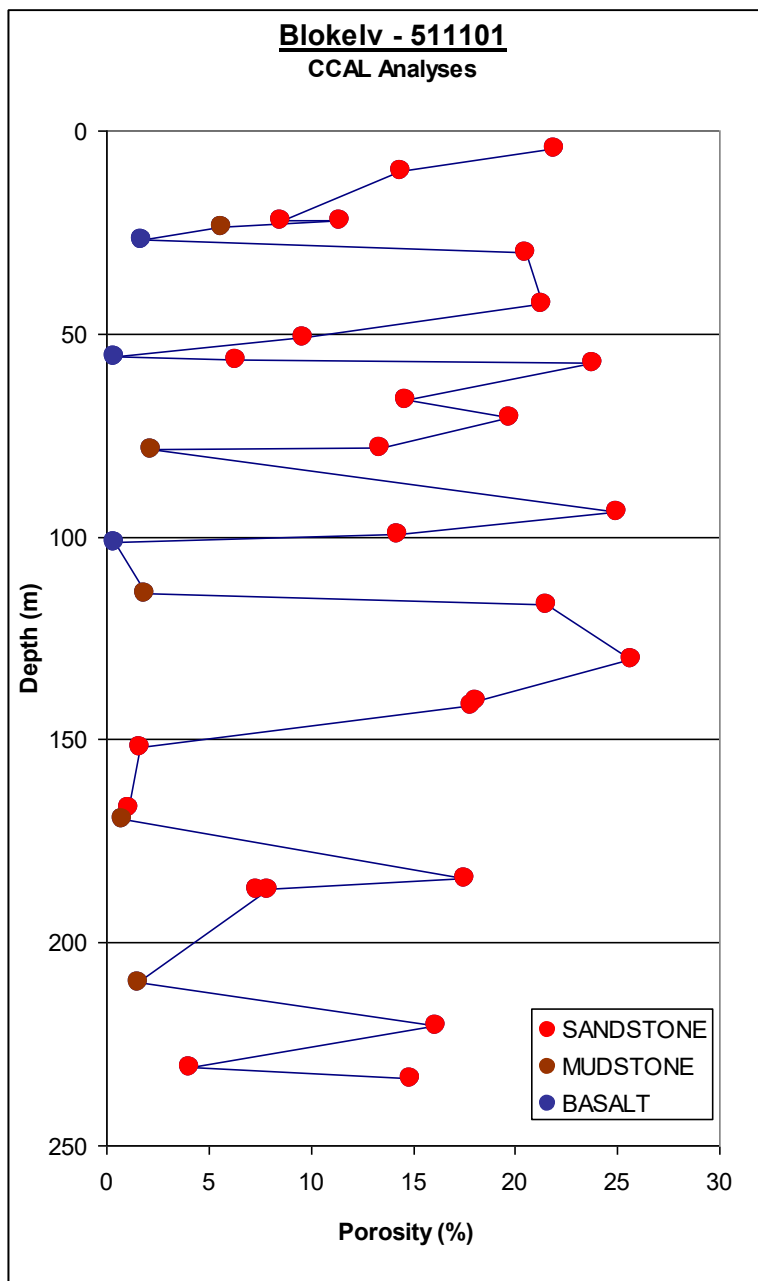


Fig. 6.3 Porosity with depth.

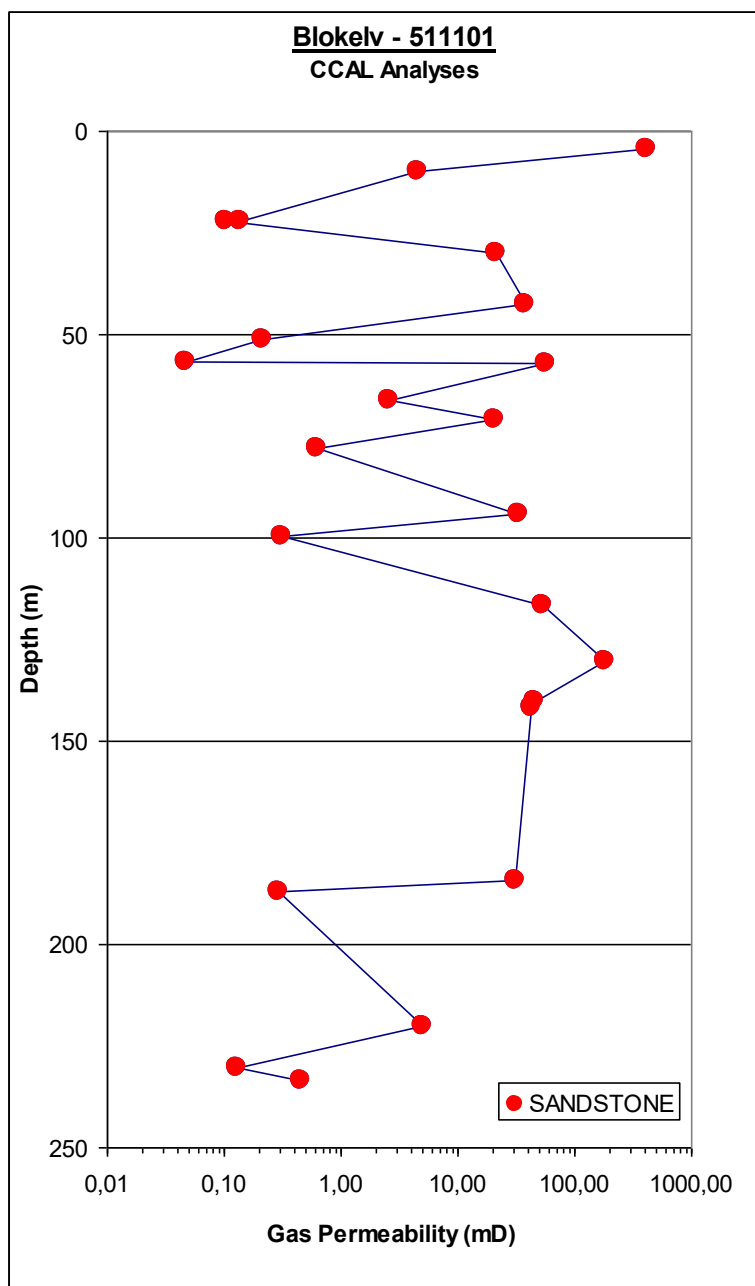


Fig. 6.4 Gas permeability in sandstones with depth.

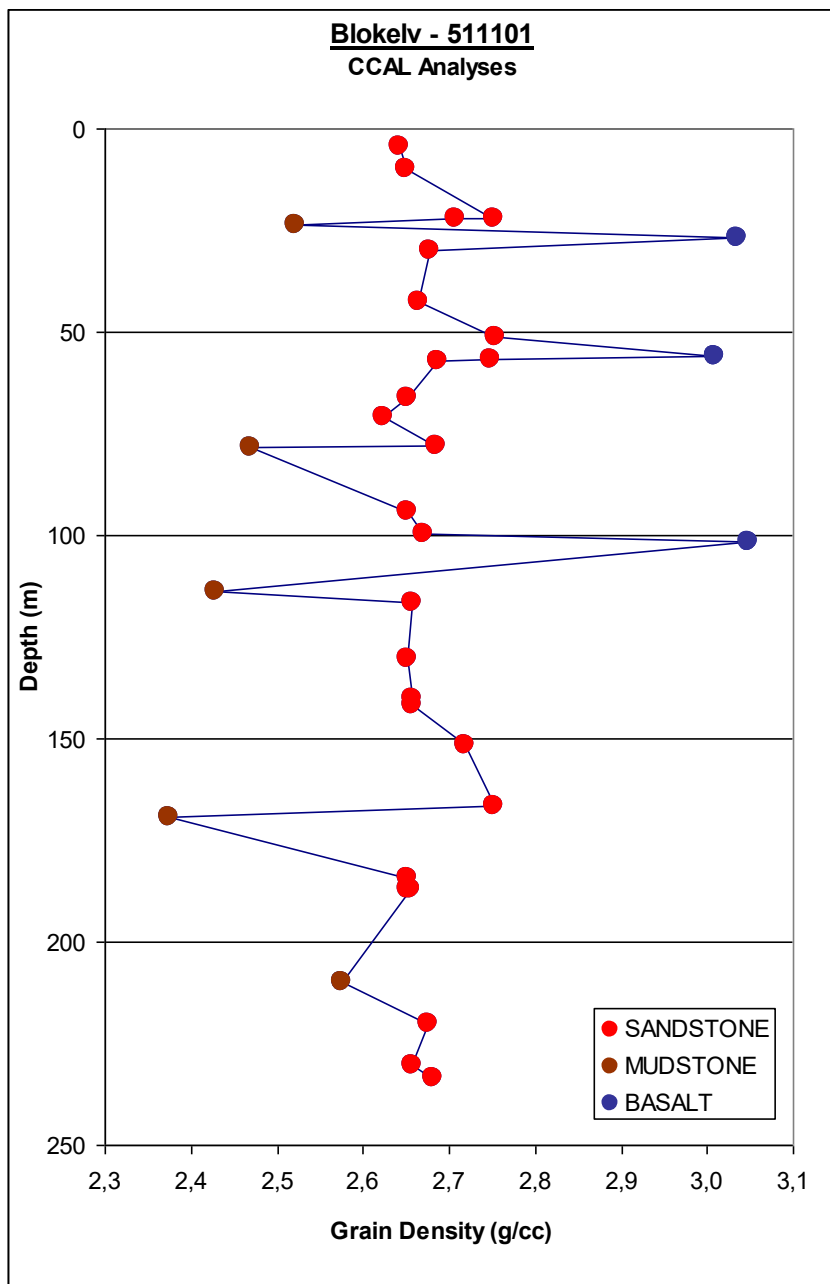


Fig. 6.5 Grain density with depth.

7. Petroleum Geology

7.1 Screening data and vitrinite reflectance - Source rock quality and thermal maturity

The Blokely core-well drilled c. 230 m of marine black mudstones (Fig. 7.1.1), sandstones and three basalt sills of the Upper Jurassic Hareelv Formation (principally the Katedralen Member) on the southern tip of Jameson Land. A total of 139 samples were collected from the cores and subjected to organic geochemical and petrographic analyses in order to establish (i) the source rock quality of the marine black mudstones and (ii) the organic maturity of the mudstones. A bitumen sample and an oil sample were also collected, the latter from a belemnite (Fig. 7.1.2). These samples are described in Section 7.2.

7.1.1 Methods

All 139 samples were analysed for the content of total organic carbon (TOC, wt%) and total sulphur (TS, wt%) by combustion in a LECO CS-200 induction furnace (Table 7.1.1). Before TOC determination, carbonate-bonded carbon was removed by HCl treatment. The samples were further pyrolysed on a Humble Instruments and Services source rock analyzer (SRA), which yields similar data as the Rock-Eval instrument (Table 7.1.1).

Particulate blocks suited for reflected light microscopy were prepared of 14 samples according to international standards (Taylor *et al.* 1998). Vitrinite reflectance (VR) measurements (random) were performed by means of a Leitz MPV-SP system in monochromatic light (546 nm) and after calibration with standards of 0.515% R_o and 0.92% R_o . The average VR for each depth was calculated from a population of VR readings selected from the measured VR histogram (Table 7.1.2). A number of samples were also qualitatively inspected in reflected white light and fluorescing-inducing blue light using a Zeiss microscope.

7.1.2 Kerogen composition

The organic matter in the black mudstones consists of algal-derived sapropelic kerogen. The kerogen is mainly composed of fluorescing amorphous organic matter (AOM), which is intimately associated with the mineral matrix (Fig. 7.1.3A, B). Structured alginite is present as discrete bodies with morphologies similar to the marine algae *Leiosphaerida* and *Tasmanites* or as laminated alginite (Fig. 7.1.3A, B). The organic matter in the mudstones corresponds to marine Type II kerogen according to the S_2/TOC kerogen classification plot (Fig. 7.1.4). Some terrestrial organic matter is present in the form of huminite or inertinite (Fig. 7.1.3C). Framboidal pyrite is abundant in the samples in agreement with marine, oxygen-deficient depositional conditions. This suggests that a considerable part of the relative high TS contents in the mudstones (Table 7.1.2; average $TS_{mudstone} = 3.47 \text{ wt\%}$) are derived from inorganic sulphur bound in pyrite, which agrees with the chemostratigraphic results (see section 3.3).

7.1.3 Source rock quality

The mudstones show a wide range of TOC, ranging from 1.98 wt% to 18.97 wt%, but most values vary between ~5 wt% and ~10 wt% (Table 7.1.1). An average TOC content of 7 wt% indicates that the mudstones are extraordinary rich in organic matter (Table 7.1.2). The TOC content shows a gradual increase with depth, reaching high values between approximately 125 m and 170 m followed by a minor decrease (Fig. 7.1.5).

The mudstones display a wide range in the Hydrogen Index (HI), ranging from 30–363 mg HC/g TOC (Table 7.1.1). The generation capacity of the predominantly Type II kerogen dominated mudstones is considered to be gas for $HI < 200 \text{ mg HC/g TOC}$, mixed gas and oil for $HI = 200\text{--}300 \text{ mg HC/g TOC}$, and oil for $HI > 300 \text{ mg HC/g TOC}$ (thresholds from Peters & Cassa 1994). The majority of the mudstones have HI values from 200–300 mg HC/g TOC indicating a potential for gas- and oil-generation, but parts of the mudstones have HI values $> 300 \text{ mg HC/g TOC}$ and are thus oil-prone (Fig. 7.1.6). The levels in the well with these high HI values occur in the upper half, whereas HI shows a weak decreasing trend below about 120 m (Fig. 7.1.7). This slight decreasing trend in HI may be a combination of initial generation in the early part of the oil window and a more terrestrial-influenced kerogen (see below and the Section 7.2 on biomarkers and section 3.2.1 on dinoflagellates).

The combination of organic richness and Type II kerogen results overall in good to excellent source rock quality of the mudstones (Fig. 7.1.8). The average HI of the mudstones is 265 mg HC/g TOC (Table 7.1.2), which is a measure of the current bulk petroleum generation potential of the kerogen present in the mudstones. The kerogen is, as mentioned above, a mixture of a dominant proportion of oil-prone (sapropelic) kerogen and more gas-prone (huminite) and inert organic material (Fig. 7.1.3). The source rock quality is the average of this mixture of organic matter. It is, however, possible to estimate the HI for the generative (or „live“) kerogen (HI_{live}). The intercept TOC value of the gradient in a S_2 versus TOC cross-plot may be absorptive capacity of the mineral matrix (Langford & Blanc-Valleron 1990), or dead organic carbon, i.e. non-generative kerogen (Cornford *et al.* 1998). Dahl *et al.* (2004) used the equation $HI_{live} = 100 \times S_2 / (TOC_{measured} - TOC_{dead\ carbon})$ to estimate the average HI for the generative kerogen. This method has been used to calculate the HI_{live} for the immature to early mature mudstones (Fig. 7.1.9). The intersect of the regression line on the TOC axis shows that on average the mudstones contain 0.84 wt% dead carbon (non-reactive). Elimination of this $TOC_{dead\ carbon}$ yields an average HI_{live} of 303 mg HC/g TOC for the generative kerogen. This indicates oil-prone kerogen.

The drilled succession contains three basalt sills and below and above the sills the source rock quality of the mudstones is significantly altered due to local elevated heat flow (Figs 7.1.10 and 7.1.11). The effect of the elevated heat flow can be observed up to about a few meters below and above the ~0.6 m thick sill at 26.4 m, whereas the mudstones on both sides of the ~2 m thick sill at about 100 m are affected up to 4 m or more. The HI declines drastically towards the sills due to local maturation of the mudstones (see below).

7.1.4 Thermal maturity and the oil window

The VR histograms permit the selection of several populations for the calculation of average VR's (Figs 7.1.12 and 7.1.13; Table 7.1.3). However, coupled with T_{max} and Production Index (PI) gradients VR trend 2 is considered to represent the correct maturity gradient. On a semi-log plot trend 2 defines a well-constrained straight line with a correlation coefficient of 0.84. If the top of the oil window is set at a maturity level corresponding to c. 0.6% R_o , the mudstones are thermally immature down to a depth of approximately 130 m and early mature below this depth (Figs 7.1.12 and 7.1.13). The VR gradient intersects the surface at a VR of ~0.45% R_o , which is too high a value for peaty organic matter (e.g. Cohen *et al.* 1987). This shows that the succession at the well-site has been exhumed and parts of the strata have been removed by erosion.

T_{\max} values of the mudstones show a gradual increase with depth (Fig. 7.1.14). The oil window can for Type II kerogen be defined between T_{\max} of 435–460°C (Bordenave *et al.* 1993; Peters & Cassa 1994). Below approximately 100 m, T_{\max} ranges from 435–445°C indicating early maturity. Around the basalt sills significantly increased T_{\max} values correspond to the mudstones being mature to overmature with regard to oil generation (Fig. 7.1.14).

Generally PI increases from approximately 0.1–0.4 from the onset of oil generation and through the oil window (Espitalié *et al.* 1985, 1986). PI is generally below 0.1 in the Blokely well, but it ranges from 0.03–0.12, averaging 0.08, in the mudstones and in the lower part of the borehole PI is close to 0.1 or above (Fig. 7.1.15; Table 7.1.2). In the sill-affected parts of the mudstones PI ranges from 0.07–0.70, averaging 0.35, showing that these mudstones due to the local increase in heat flow have passed through the oil window and generated oil (Fig. 7.1.15; Table 7.1.2).

In summary three independent data sets indicate that the mudstones somewhere below 100 m in the Blokely borehole are within the early part of the oil window:

- (i) VR values show a gradual increase with depth and exceed 0.6% R_o below ~130 m
- (ii) T_{\max} values show a gradual increase with depth and exceed 435°C below ~100 m
- (iii) PI values are close to or exceed 0.1 below ~160 m

7.1.5 Conclusions

The marine black mudstones of the Hareelv Formation are rich source rocks composed of sapropelic Type II kerogen. The average TOC amounts to 7 wt% and HI reaches 363 mg HC/g TOC, averaging 265 mg HC/g TOC. Overall the mudstones are gas-/oil-prone to oil-prone and the source rock quality can be classified as good to excellent. However, calculation of the generation potential of the reactive part of the kerogen yields an HI_{live} of 303 mg HC/g TOC, indicating an oil-generative potential. Basalt sills have locally deteriorated the remaining source rock potential due to local maturation of the mudstones. VR, T_{\max} and PI increase with depth through the well and it appears that the mudstones in the lower part of the drilled section have entered the earliest part of the oil window. Around the sills the mudstones are well within or beyond the oil window and oil has been generated.

7.1.6 References

- Bordenave, M. L., Espitalié, J., Leplat, P., Oudin, J. L. & Vandenbrouke, M. 1993: Chapter II-2: Screening techniques for source rock evaluation. In: Bordenave, M.L. (ed.), *Applied petroleum geochemistry*. Paris, Éditions Technip, 219–278.
- Cohen, A. D., Raymond, R. Jr., Archuleta, L. M. & Mann, D. A. 1987: Preliminary study of the reflectance of huminite macerals in recent surface peat. *Organic Geochemistry*, **11**, 429–430.
- Cornford, C., Gardner, P. & Burgess, C. 1998: Geochemical truths in large data sets. I: Geochemical screening data. *Organic Geochemistry*, **29**, 519–530.
- Dahl, B., Bojesen-Koefoed, J. A., Holm, A., Justwan, H., Rasmussen, E. & Thomsen, E. 2004: A new approach to interpreting Rock-Eval S₂ and TOC data for kerogen quality assessment. *Organic Geochemistry*, **35**, 1461–1477.
- Espitalié, J., Deroo, G. & Marquis, F. 1985: La pyrolyse Rock-Eval et ses applications. Part II. *Revue de l'Institut Français du Pétrole*, **40**, 755–784.
- Espitalié, J., Deroo, G. & Marquis, F. 1986: La pyrolyse Rock-Eval et ses applications. Part III. *Revue de l'Institut Français du Pétrole*, **41**, 73–89.
- Langford, F. F. & Blanc-Valleron, M.-M. 1990: Interpreting Rock-Eval pyrolysis data using graphs of pyrolyzable hydrocarbons vs. total organic carbon. *American Association of Petroleum Geologists Bulletin*, **74**, 799–804.
- Peters, K. E. & Cassa, M. R. 1994: Applied source rock geochemistry. In: Magoon, L. B. & Dow, W. G. (eds): *The petroleum system – from source to trap*. American Association of Petroleum Geologists Memoir, **60**, 93–120.
- Taylor, G. H., Teichmüller, M., Davis, A., Diessel, C. F. K., Littke, R. & Robert, P. 1998: *Organic Petrology*. Berlin, Stuttgart, Gebrüder Borntraeger, 704 pp.

Lab. no.	Sample no.	Depth, base (m)	TOC	TC	TS	T _{max} °C	S ₁	S ₂	HI mg HC/g TOC	PI	PC
			wt. %				mg HC/g rock				
16813	511101-204	0	10.15	10.45	2.04	441	2.17	26.19	258	0.08	2.35
16701	511101-101	2.67	2.97	2.97	1.38	434	0.07	0.90	30	0.07	0.08
16702	511101-102	2.96	1.98	2.09	0.75	431	0.05	0.60	30	0.08	0.05
16820	511101-1	3.51	0.06	0.08	0.14	431	-	-	-	-	-
16703	511101-103	6.44	0.08	1.85	0.09	376	-	-	-	-	-
16704	511101-104	9.17	0.13	0.38	0.31	438	-	-	-	-	-
16705	511101-105	10.21	4.59	4.78	1.90	423	0.62	11.56	252	0.05	1.01
16706	511101-106	10.61	1.81	1.78	1.65	427	0.15	2.19	121	0.06	0.19
16821	511101-4	11.73	0.32	0.89	0.46	438	0.01	0.08	25	0.11	0.01
16707	511101-107	12.62	5.15	5.26	3.17	431	0.43	16.37	318	0.03	1.39
16708	511101-108	13.04	18.97	18.98	6.51	434	1.37	42.91	226	0.03	3.68
16709	511101-109	13.71	3.08	3.34	2.09	433	0.30	7.50	244	0.04	0.65
16710	511101-110	16.42	5.56	5.60	3.11	431	1.18	20.20	363	0.06	1.77
16711	511101-111	17.00	6.05	6.05	4.44	426	0.79	19.01	314	0.04	1.64
16712	511101-112	18.77	5.29	5.34	3.38	427	0.85	16.15	305	0.05	1.41
16713	511101-113	20.15	4.94	5.00	3.36	428	0.69	15.72	318	0.04	1.36
16714	511101-114	20.67	1.53	1.88	1.46	436	0.19	2.18	143	0.08	0.20
16715	511101-115	22.55	3.91	3.98	4.90	433	0.63	11.56	295	0.05	1.01
16716	511101-116	23.35	5.48	5.69	4.13	435	1.07	16.83	307	0.06	1.49
16822	511101-8	23.59	5.21	5.28	3.87	436	1.45	16.95	326	0.08	1.53
16717	511101-117	24.26	5.17	5.27	4.92	438	1.01	14.38	278	0.07	1.28
16738	511101-139	24.68	3.94	4.11	3.71	437	0.47	5.89	149	0.07	0.53
16737	511101-138	24.92	4.08	4.30	3.31	437	0.64	5.40	132	0.11	0.50
16718	511101-118	25.15	3.94	4.01	3.68	442	0.89	5.55	141	0.14	0.53
16736	511101-137	25.24	4.03	4.17	2.91	437	0.88	3.67	91	0.19	0.38
16735	511101-136	25.59	3.49	3.71	3.60	328	1.02	0.96	27	0.52	0.16
16719	511101-119	25.76	3.16	3.45	3.22	324	0.41	0.38	12	0.52	0.07
16734	511101-135	25.88	3.91	4.11	4.67	329	0.51	0.22	6	0.70	0.06
16733	511101-134	26.00	4.45	4.77	3.23	328	0.60	0.44	10	0.58	0.09
16720	511101-120	26.15	4.16	4.49	5.66	357	1.05	1.58	38	0.40	0.22
16721	511101-121	26.23	4.50	4.70	2.51	421	0.52	1.82	40	0.22	0.19
16722	511101-122	27.11	2.65	3.03	3.41	305	0.12	0.25	9	0.32	0.03
16739	511101-140	27.31	3.85	4.04	3.23	462	0.23	0.10	3	0.70	0.03
16740	511101-141	27.46	4.05	4.31	3.03	397	0.56	1.13	28	0.33	0.14
16741	511101-142	28.30	4.04	4.23	3.68	318	0.88	0.50	12	0.64	0.11
16723	511101-123	28.33	4.02	4.30	3.87	346	1.55	1.71	42	0.48	0.27
16742	511101-143	28.49	4.40	4.60	3.62	435	1.98	3.08	70	0.39	0.42
16743	511101-144	28.69	2.76	2.93	3.17	447	0.83	1.92	70	0.30	0.23
16724	511101-124	29.24	4.80	4.89	3.79	439	0.71	7.74	161	0.08	0.70
16725	511101-125	32.10	4.74	4.73	3.79	437	0.78	12.54	264	0.06	1.11
16823	511101-12	32.78	4.14	4.16	2.37	439	1.06	12.73	307	0.08	1.14
16726	511101-126	34.33	6.68	6.76	4.05	434	1.55	18.41	275	0.08	1.66
16727	511101-127	35.05	5.06	5.17	4.08	431	1.01	12.14	240	0.08	1.09
16728	511101-128	35.87	4.68	4.78	3.84	431	0.96	10.76	230	0.08	0.97
16729	511101-129	39.43	6.53	6.66	5.43	426	1.18	16.98	260	0.06	1.51
16730	511101-130	41.53	6.76	6.90	4.51	429	1.16	17.81	263	0.06	1.57
16824	511101-16	44.80	0.29	0.55	0.41	437	0.11	0.18	63	0.38	0.02
16731	511101-132	45.87	6.77	6.88	3.82	430	1.22	18.95	280	0.06	1.67

16732	511101-133	46.53	5.66	5.86	3.38	432	0.89	13.64	241	0.06	1.21
16744	511101-145	47.08	5.66	5.77	3.07	432	0.85	15.36	272	0.05	1.35
16745	511101-146	50.27	6.54	6.63	4.12	433	1.03	18.61	285	0.05	1.63
16746	511101-147	51.99	6.92	7.06	5.72	438	1.02	14.24	206	0.07	1.27
16825	511101-20	56.66	0.10	3.79	0.04	433	-	-	-	-	-
16747	511101-148	59.39	7.00	7.15	3.59	433	1.47	20.28	290	0.07	1.81
16748	511101-149	60.64	6.39	6.49	3.26	431	1.18	17.91	280	0.06	1.58
16749	511101-150	64.91	7.14	7.24	5.08	432	1.54	20.95	294	0.07	1.87
16750	511101-151	67.17	7.13	7.21	4.39	432	1.93	19.39	272	0.09	1.77
16751	511101-152	68.02	7.30	7.50	5.23	432	2.00	19.69	270	0.09	1.80
16752	511101-153	68.73	7.64	7.79	4.72	432	2.12	20.56	269	0.09	1.88
16826	511101-24	68.77	8.22	8.47	6.12	432	2.83	27.00	328	0.09	2.48
16763	511101-154	68.97	8.43	8.45	7.56	430	2.19	23.49	279	0.09	2.13
16765	511101-162	74.61	9.99	10.29	5.65	433	2.99	31.01	310	0.09	2.82
16766	511101-163	79.96	5.48	5.86	3.46	435	1.82	17.97	328	0.09	1.64
16827	511101-28	80.77	5.34	5.54	4.10	433	1.78	15.70	294	0.10	1.45
16767	511101-164	82.14	5.97	6.14	4.36	434	1.99	20.41	342	0.09	1.86
16768	511101-165	84.03	6.45	6.75	6.01	433	1.53	20.16	312	0.07	1.80
16769	511101-166	85.41	6.71	7.13	4.51	433	1.59	20.25	302	0.07	1.81
16770	511101-167	86.56	5.72	6.17	3.27	434	1.32	16.73	292	0.07	1.50
16771	511101-168	87.28	6.52	6.69	4.13	433	1.39	18.78	288	0.07	1.67
16772	511101-169	88.19	6.46	6.59	3.27	434	1.24	18.46	286	0.06	1.64
16773	511101-170	89.22	6.29	6.71	3.77	434	1.50	19.25	306	0.07	1.72
16774	511101-171	90.12	6.75	6.99	4.07	433	1.51	19.07	283	0.07	1.71
16775	511101-172	91.25	6.16	6.48	4.32	433	1.56	17.83	290	0.08	1.61
16776	511101-173	92.21	6.69	6.92	3.39	432	1.64	19.75	295	0.08	1.78
16828	511101-32	92.74	6.48	6.53	4.62	432	1.79	17.51	270	0.09	1.60
16777	511101-174	93.02	6.92	7.14	3.65	433	1.94	20.42	295	0.09	1.86
16778	511101-175	97.42	6.81	7.07	4.47	447	3.43	7.84	115	0.30	0.94
16779	511101-176	98.48	4.70	5.21	5.01	473	0.73	0.54	12	0.57	0.11
16780	511101-177	103.98	5.20	5.51	3.93	331	1.04	1.05	20	0.50	0.17
16829	511101-36	104.79	6.04	6.39	3.35	451	2.52	7.64	127	0.25	0.84
16781	511101-178	105.72	6.25	6.64	3.40	444	1.82	14.65	234	0.11	1.37
16782	511101-179	106.59	7.46	7.76	3.53	437	2.15	19.74	264	0.10	1.82
16783	511101-180	108.47	7.35	7.50	3.26	434	1.63	19.11	260	0.08	1.72
16784	511101-181	110.86	8.22	8.60	3.45	433	1.94	22.87	278	0.08	2.06
16785	511101-182	112.79	7.18	7.55	4.12	435	1.75	20.59	287	0.08	1.85
16786	511101-183	114.60	7.39	7.73	4.94	434	1.96	22.50	304	0.08	2.03
16830	511101-40	116.82	5.28	5.21	2.73	438	1.22	14.92	282	0.08	1.34
16795	511101-186	117.73	5.20	5.39	2.58	433	1.19	15.90	306	0.07	1.42
16796	511101-187	120.06	8.04	8.26	3.08	436	1.47	21.39	266	0.06	1.90
16797	511101-188	121.62	8.73	8.84	3.54	437	1.73	24.02	275	0.07	2.14
16798	511101-189	123.71	6.22	6.74	2.28	438	0.97	12.71	204	0.07	1.14
16799	511101-190	125.32	7.02	7.65	2.53	436	1.43	18.28	260	0.07	1.64
16800	511101-191	127.56	10.41	10.75	2.62	435	2.16	27.52	264	0.07	2.46
16831	511101-44	128.77	0.23	0.18	0.13	443	0.01	-	-	-	0
16801	511101-192	131.65	9.01	9.30	4.88	434	1.93	23.30	259	0.08	2.09
16802	511101-193	133.36	7.75	7.87	2.80	435	1.51	19.87	256	0.07	1.77
16803	511101-194	135.41	10.37	10.44	3.75	435	2.03	27.40	264	0.07	2.44
16832	511101-48	140.75	0.09	0.21	0.09	447	-	-	-	-	-
16804	511101-195	142.84	10.63	10.65	2.62	436	2.36	29.59	278	0.07	2.65
16805	511101-196	145.46	11.07	11.27	3.29	437	2.26	29.71	268	0.07	2.65
16806	511101-197	147.27	9.14	9.21	2.33	437	1.46	23.37	256	0.06	2.06

16807	511101-198	149.48	9.36	9.62	2.58	437	1.80	24.48	262	0.07	2.18
16833	511101-52	152.75	1.06	2.01	0.61	448	0.12	0.72	68	0.14	0.07
16808	511101-199	153.29	8.78	9.01	3.79	438	1.79	22.39	255	0.07	2.01
16809	511101-200	155.20	8.41	8.73	3.36	441	1.35	18.19	216	0.07	1.62
16810	511101-201	156.89	8.95	9.20	2.72	440	2.08	24.28	271	0.08	2.19
16811	511101-202	158.83	10.03	10.27	1.99	441	2.66	28.54	285	0.09	2.59
16812	511101-203	160.80	9.47	9.58	1.93	440	2.53	27.27	288	0.08	2.47
16834	511101-56	164.82	12.50	12.48	4.02	435	2.12	26.48	212	0.07	2.37
16814	511101-205	167.92	10.42	10.71	2.22	439	1.87	28.83	277	0.06	2.55
16815	511101-206	170.67	11.20	11.38	2.46	440	2.39	27.39	245	0.08	2.47
16816	511101-207	172.62	6.73	6.90	3.63	443	1.59	16.33	243	0.09	1.49
16817	511101-208	174.46	6.95	6.98	2.73	442	1.78	19.24	277	0.08	1.74
16818	511101-209	176.44	8.65	8.96	3.00	441	2.16	23.41	271	0.08	2.12
16835	511101-60	176.77	5.97	6.17	3.14	440	1.51	16.59	278	0.08	1.50
16819	511101-210	178.36	7.03	7.35	3.16	443	1.59	16.35	232	0.09	1.49
16841	511101-211	185.11	7.77	8.22	3.24	443	1.78	19.23	247	0.08	1.74
16842	511101-212	186.36	4.91	5.20	2.41	443	0.79	9.59	195	0.08	0.86
16836	511101-64	188.77	3.03	3.65	1.76	445	0.34	3.43	113	0.09	0.31
16843	511101-213	190.61	7.03	7.20	2.83	442	1.07	15.83	225	0.06	1.40
16844	511101-214	195.26	7.02	7.28	3.00	441	1.53	19.26	275	0.07	1.73
16845	511101-215	196.42	7.09	7.50	2.75	444	1.52	15.96	225	0.09	1.45
16846	511101-216	198.25	3.35	3.52	2.52	443	0.57	5.58	166	0.09	0.51
16847	511101-217	200.22	6.29	6.74	3.33	443	1.51	16.76	266	0.08	1.52
16837	511101-68	200.76	8.22	8.46	2.83	440	1.74	19.65	239	0.08	1.78
16848	511101-218	202.05	6.15	6.29	2.42	443	1.16	14.39	234	0.07	1.29
16849	511101-219	203.91	7.28	7.60	3.06	444	1.82	17.44	240	0.09	1.60
16850	511101-220	205.84	7.18	7.83	3.01	444	2.01	20.53	286	0.09	1.87
16851	511101-221	207.77	4.37	4.65	2.71	447	1.04	8.55	195	0.11	0.80
16852	511101-222	209.82	4.60	4.93	2.56	447	1.33	10.39	226	0.11	0.97
16853	511101-223	211.79	4.26	4.70	2.88	448	1.19	8.76	205	0.12	0.83
16838	511101-72	212.77	4.48	4.78	2.53	447	1.32	9.52	212	0.12	0.90
16854	511101-224	213.81	8.44	8.74	2.80	445	2.5	22.76	270	0.10	2.10
16855	511101-225	215.83	8.66	8.99	3.41	446	2.18	19.00	219	0.10	1.76
16856	511101-226	218.5	6.39	6.74	3.17	446	1.54	15.74	246	0.09	1.43
16857	511101-227	224.00	6.16	6.39	4.46	445	0.97	13.49	219	0.07	1.20
16839	511101-76	224.74	3.25	3.43	1.26	445	0.29	4.14	128	0.07	0.37
16858	511101-228	232.05	7.18	7.53	3.77	446	0.84	13.74	191	0.06	1.21
16840	511101-79	233.71	0.20	1.37	0.15	453	0	0.04	19	-	0

Table 7.1.1. Source rock data, Blokely core

Type	TOC			HI			PI		
	Min	Max	Average	Min	Max	Average	Min	Max	Average
Mudstone	1.98	18.97	7.00	30	363	265	0.03	0.12	0.08
Sandstone	1.06	12.50	4.50	68	282	173	0.04	0.14	0.08
Sill-aff. mudst.	2.65	6.92	4.37	6	206	69	0.07	0.70	0.35

Table 7.1.2. Minimum, maximum and average values, Blokely core.

Lab. no.	Sample no.	Depth base m	Total			Trend 1			Trend 2 ^a			Trend 3			Trend 4		
			%R _o	Std	n	%R _o	Std	n	%R _o	Std	n	%R _o	Std	n	%R _o	Std	n
16822	511101-8	23.59	0.63	0.127	89	0.52	0.056	43	0.52	0.056	43	0.69	0.065	45	0.69	0.065	45
16823	511101-12	32.78	0.60	0.117	118	0.54	0.058	84	0.54	0.058	84	0.69	0.039	24	0.69	0.039	24
16826	511101-24	68.77	0.63	0.112	112	0.50	0.041	39	0.50	0.041	39	0.64	0.065	73	0.64	0.065	73
16827	511101-28	80.77	0.61	0.113	121	0.55	0.063	82	0.55	0.063	82	0.73	0.063	50	0.73	0.063	50
16828	511101-32	92.74	0.58	0.081	106	0.55	0.048	90	0.56	0.06	97	0.70	0.058	26	0.70	0.058	26
16829*	511101-36	104.79	1.31	0.123	125	1.28	0.097	107	-	-	-	-	-	-	-	-	-
16830	511101-40	116.82	0.61	0.123	118	0.55	0.048	95	0.56	0.059	101	0.72	0.072	23	0.72	0.072	23
16833	511101-52	152.75	0.63	0.079	50	0.60	0.053	44	0.61	0.063	47	0.75	0.056	10	0.75	0.056	10
16834	511101-56	164.82	0.68	0.045	150	0.68	0.045	150	0.68	0.045	150	-	-	-	-	-	-
16835	511101-60	176.77	0.67	0.126	106	0.62	0.056	86	0.62	0.056	86	0.84	0.06	21	0.84	0.06	21
16836	511101-64	188.77	0.74	0.175	102	0.65	0.041	77	0.65	0.041	77	0.79	0.048	9	0.79	0.048	9
16837	511101-68	200.76	0.72	0.133	132	0.63	0.05	79	0.66	0.075	107	0.78	0.071	60	0.85	0.047	26
16838	511101-72	212.77	0.79	0.080	101	0.78	0.062	98	0.78	0.062	98	-	-	-	-	-	-
16839	511101-76	224.74	0.80	0.121	67	0.74	0.06	48	0.74	0.06	48	0.91	0.051	19	0.92	0.056	20

^aTrend 2 is considered to represent the VR gradient in the well

^bSill-affected sample; value not included in VR trends

Std: standard deviation

n: number of samples included in calculation of the average vitrinite reflectance value

Table 7.1.3. Vitrinite reflectance values and calculated VR trends, Blokely core



Fig. 7.1.1. The cored black mudstones of the Hareelv Formation at Blokely, depth 206.80–210.62 m.



Fig. 7.1.2. Bitumen found in a fracture within an igneous intrusion at 55.4 m, and oil observed within a belemnite at 105.25 m. See Section 7.2.

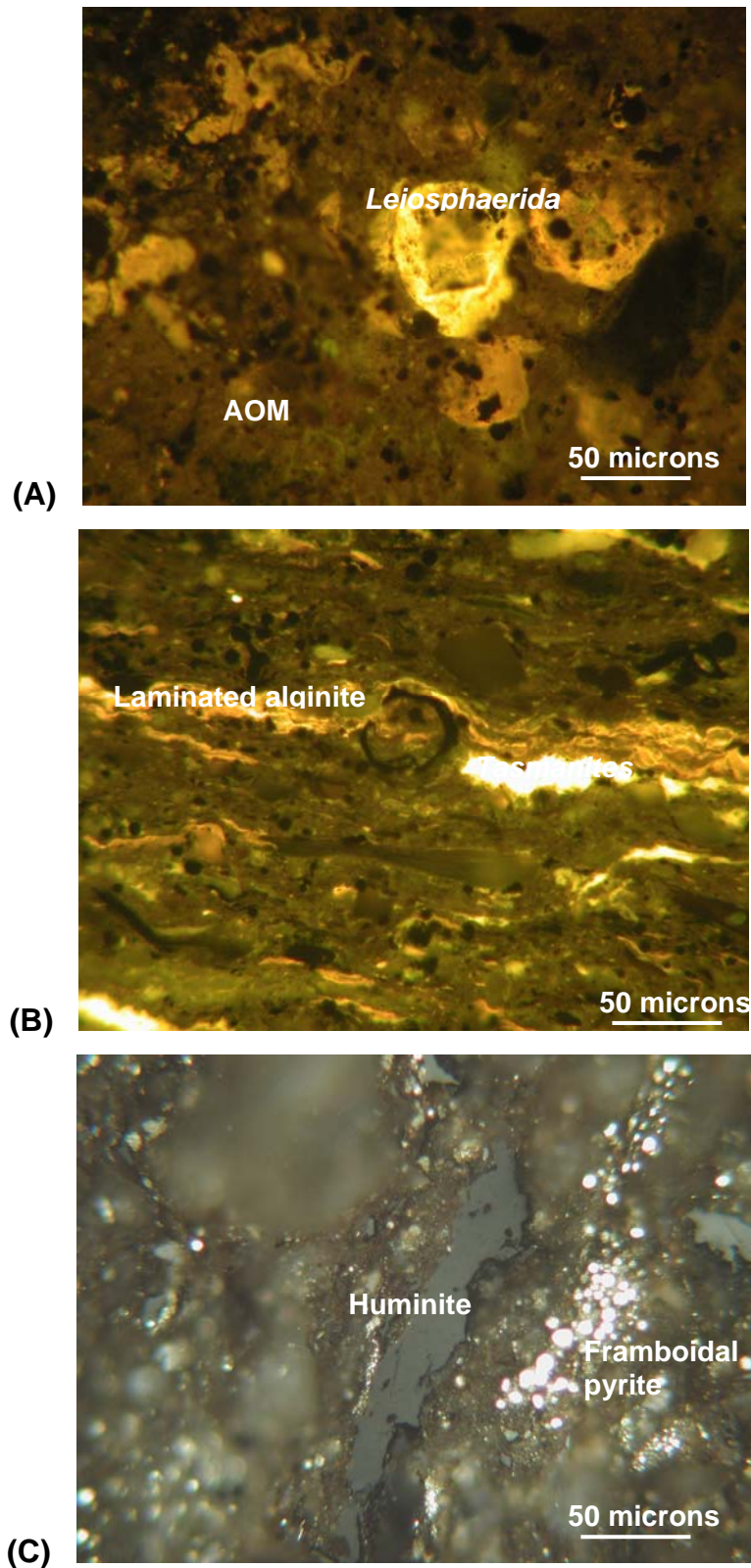


Fig. 7.1.3. Photomicrographs (incident light, oil immersion) of the kerogen in the mudstones. (A) and (B) in fluorescing-inducing blue light excitation, (C) in reflected white light. **(A)**: Sample 16710, 16.42 m. Fluorescing AOM and alginite with *Leiosphaerida* morphology. **(B)**: Sample 16767, 82.14 m. Fluorescing AOM and alginite with *Tasmanites* morphology. **(C)**: Sample 16822, 23.59 m. Huminite particle and abundant framboidal pyrite.

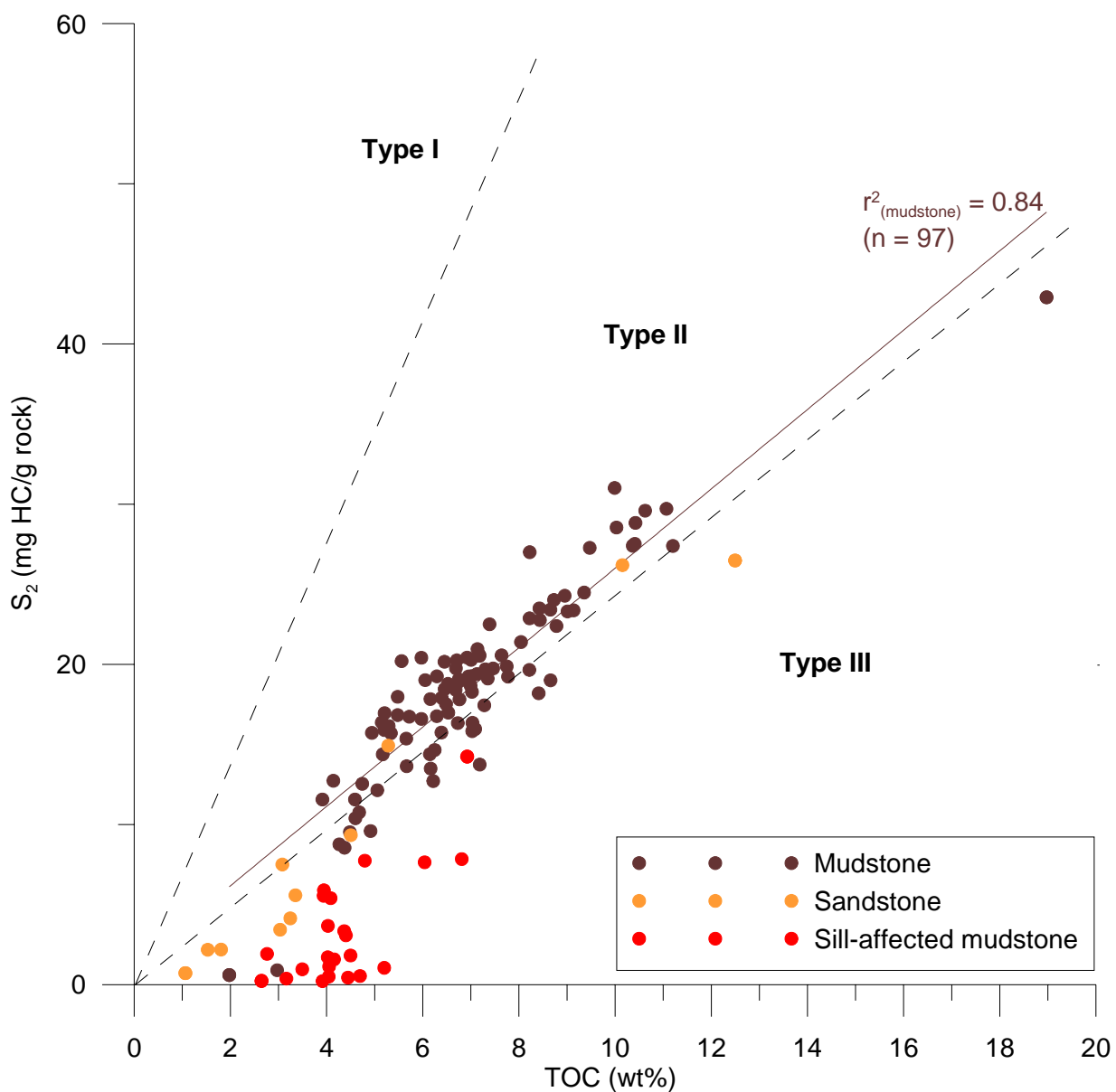


Fig. 7.1.4. Kerogen classification showing that the mudstones contain Type II kerogen. Samples with $S_2 < 0.2$ mg HC/g TOC and TOC < 0.5 wt% have been omitted from the plot to avoid unreliable data.

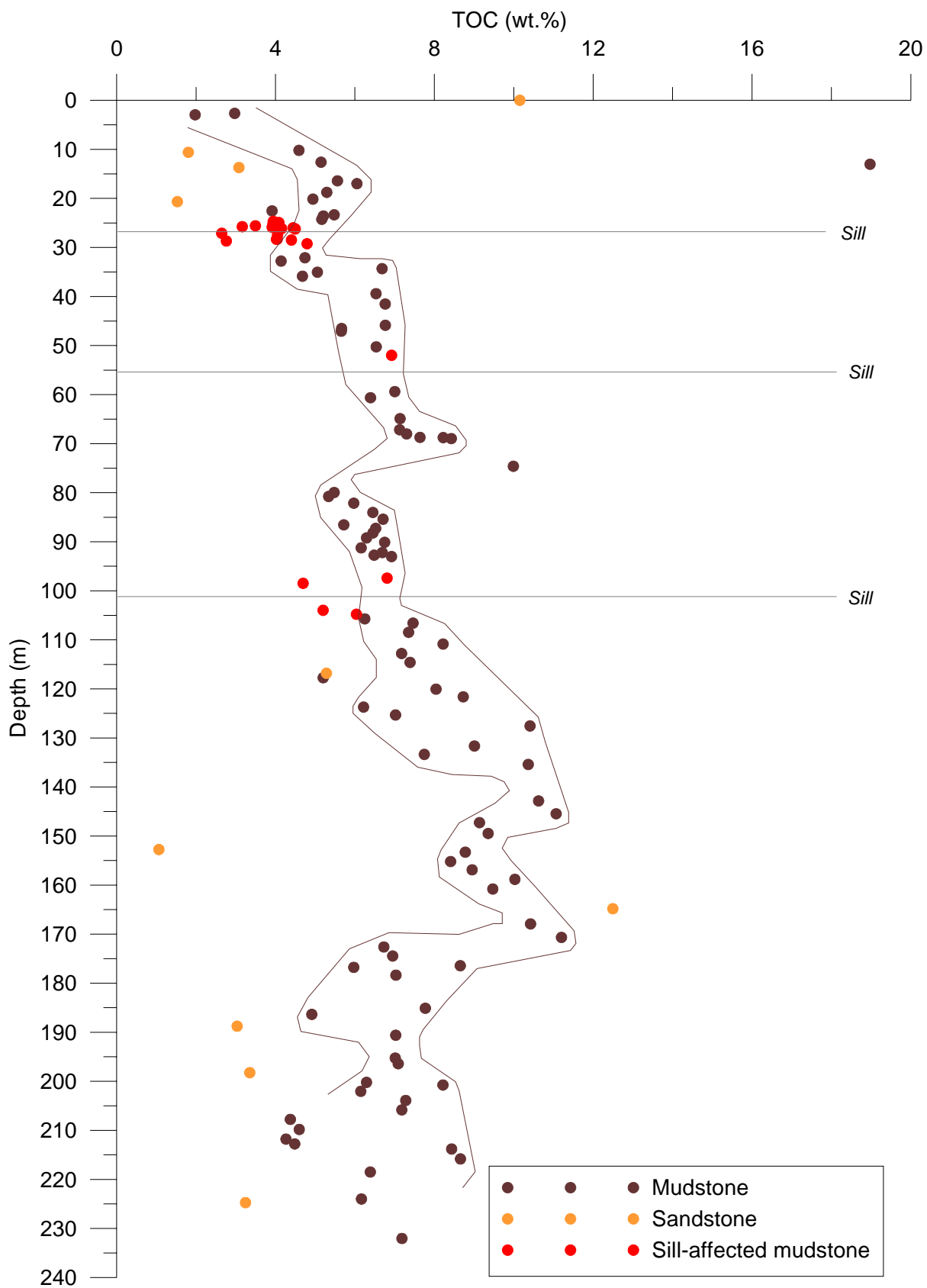


Fig. 7.1.5. Variation in TOC content through the Blokely borehole.

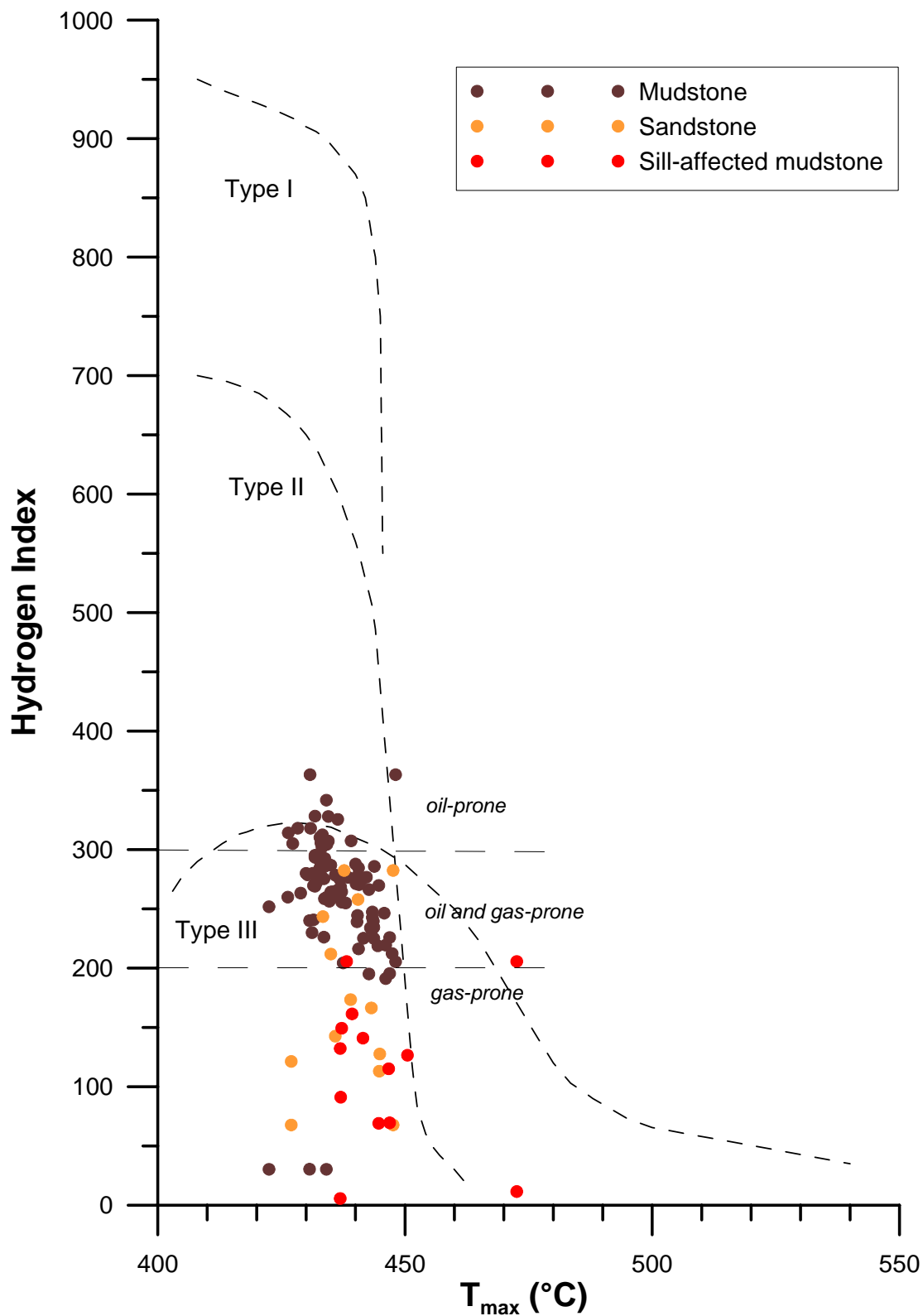


Fig. 7.1.6. HI- T_{max} plot showing that the mudstones are gas/oil-prone to oil-prone. Mudstones close to the sills are gas-prone to non-generative due to local increased maturity and HC generation (exhaustion of generation potential).

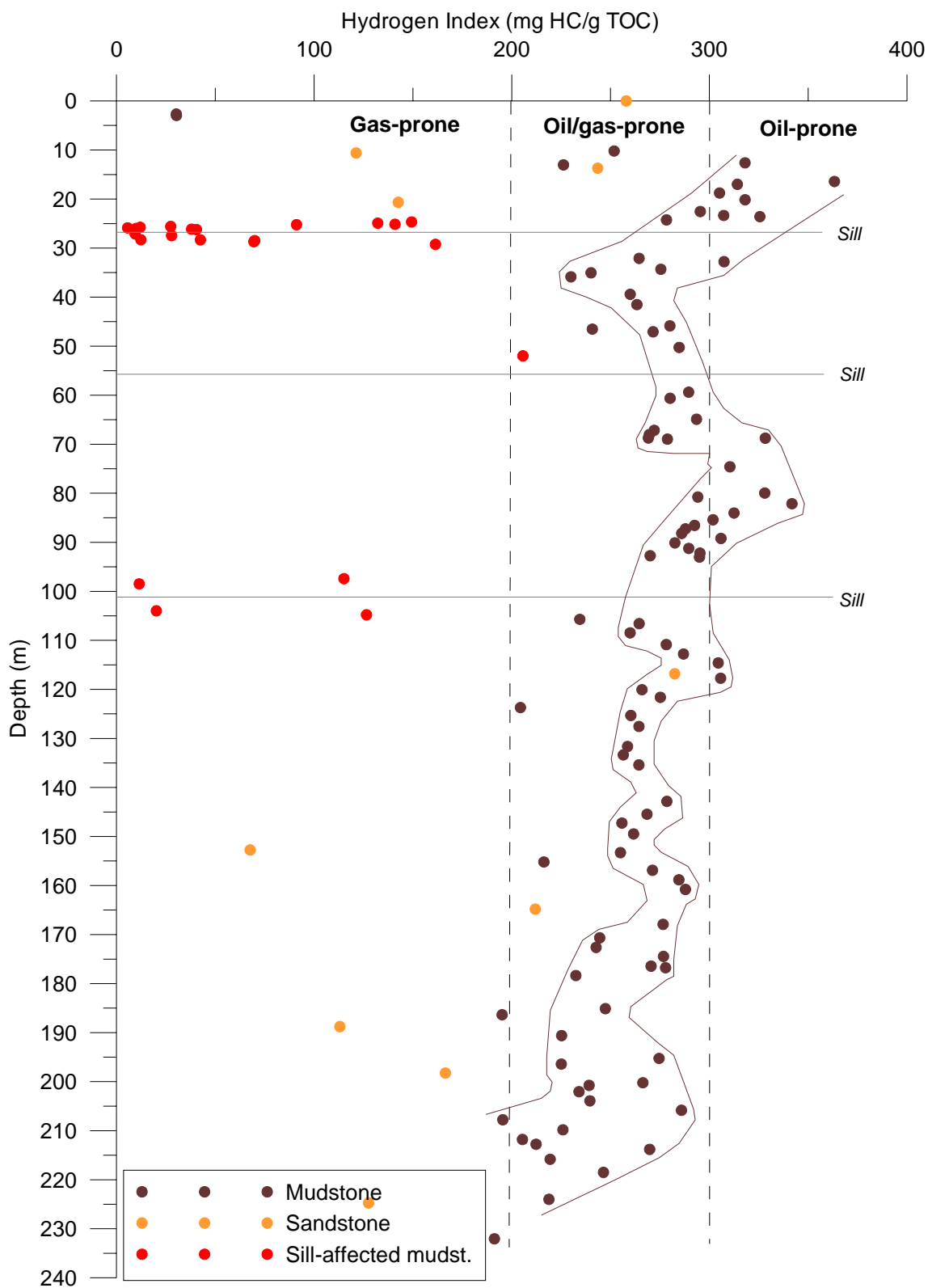


Fig. 7.1.7. Variation in HI through the Blokely borehole. Note low HI values associated with the basalt sills.

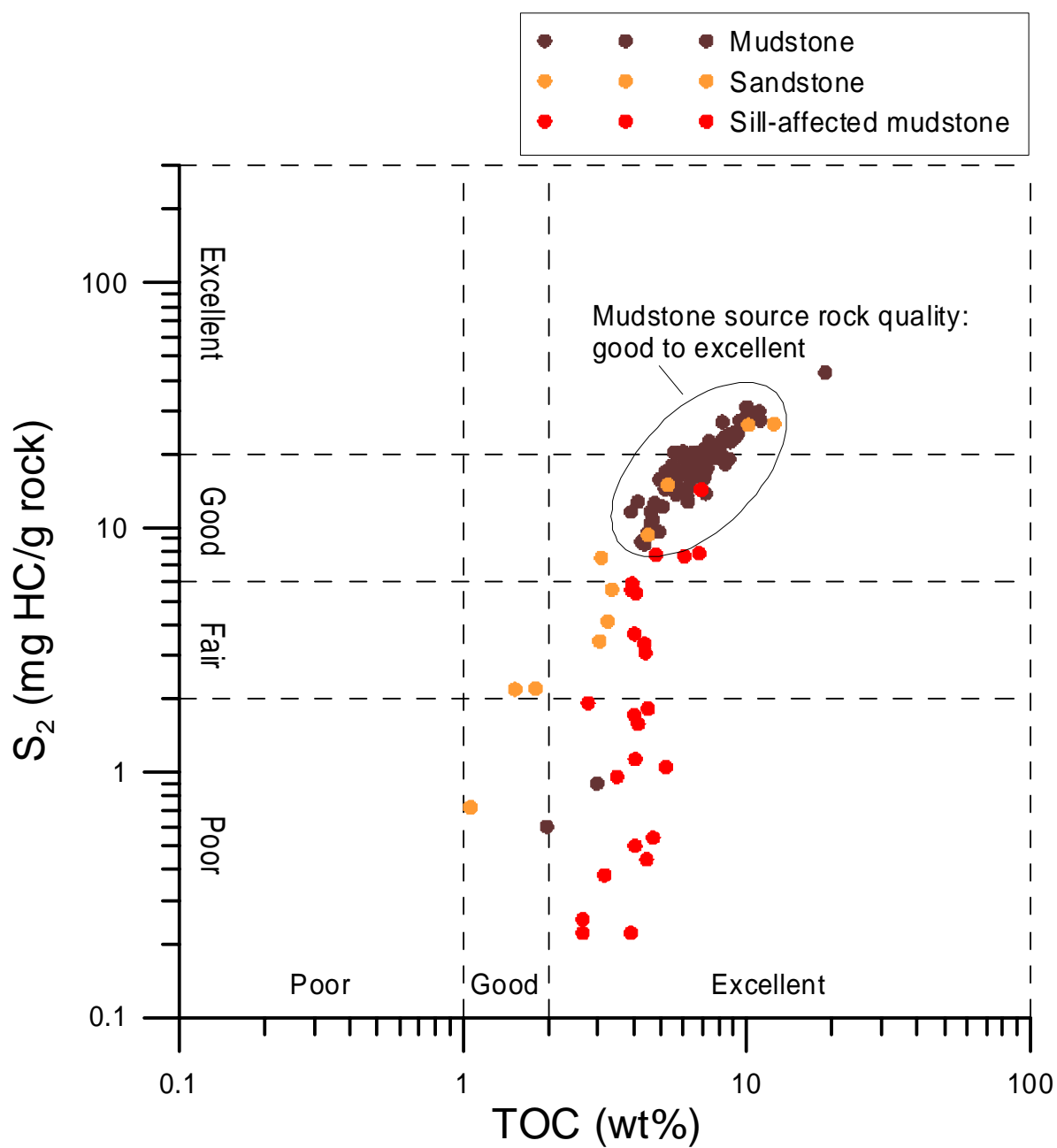


Fig. 7.1.8. S_2 -TOC plot showing that the source rock quality of the mudstones is good to excellent. Samples with $S_2 < 0.2$ mg HC/g TOC and TOC < 0.5 wt% have been omitted from the plot to avoid unreliable data.

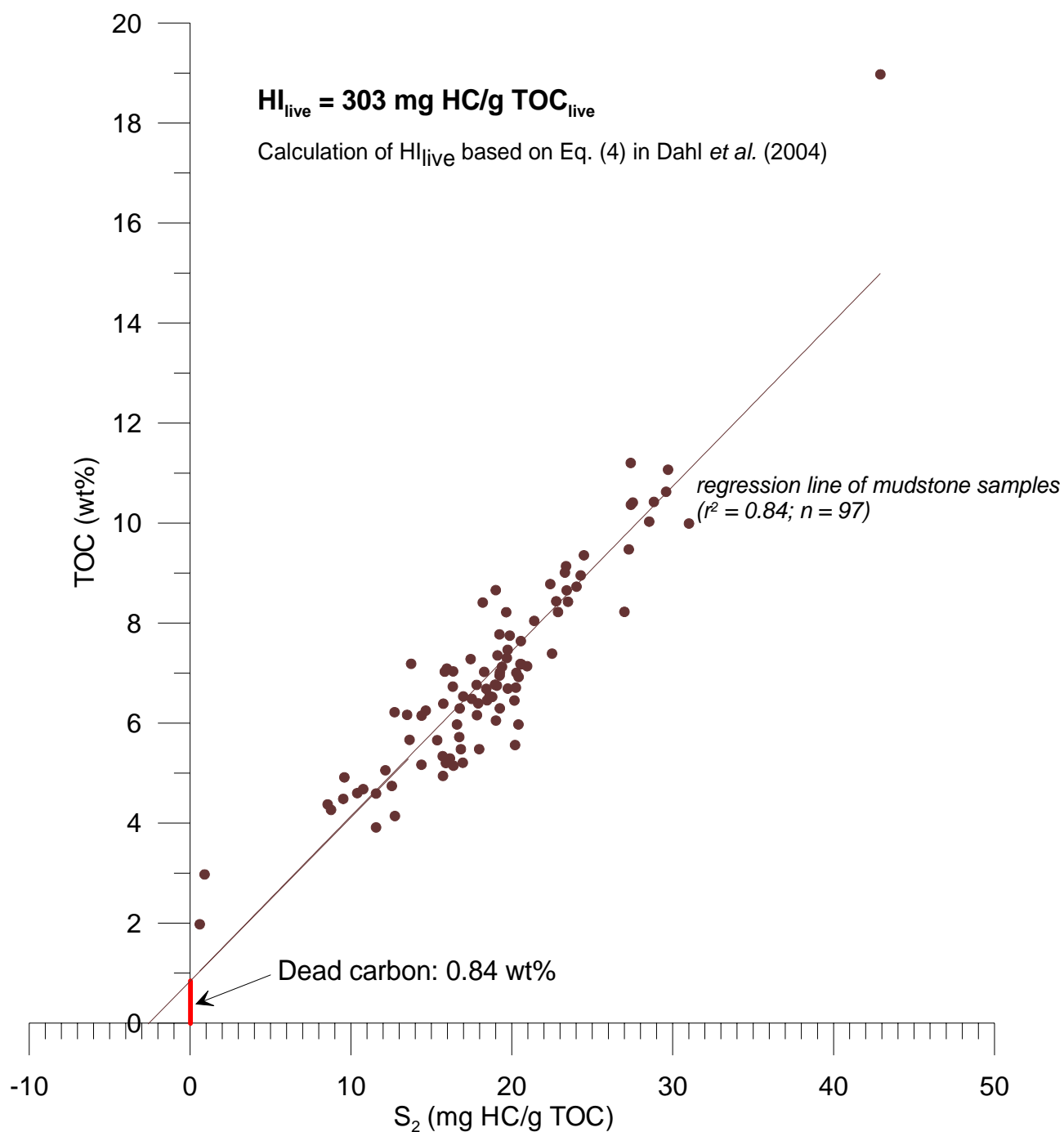


Fig. 7.1.9. Calculation of the generation potential (HI_{live}) of the reactive kerogen using the method of Dahl *et al.* (2004). The mudstones contain on average 0.84 wt% dead carbon and the HI_{live} is 303 mg HC/g TOC.

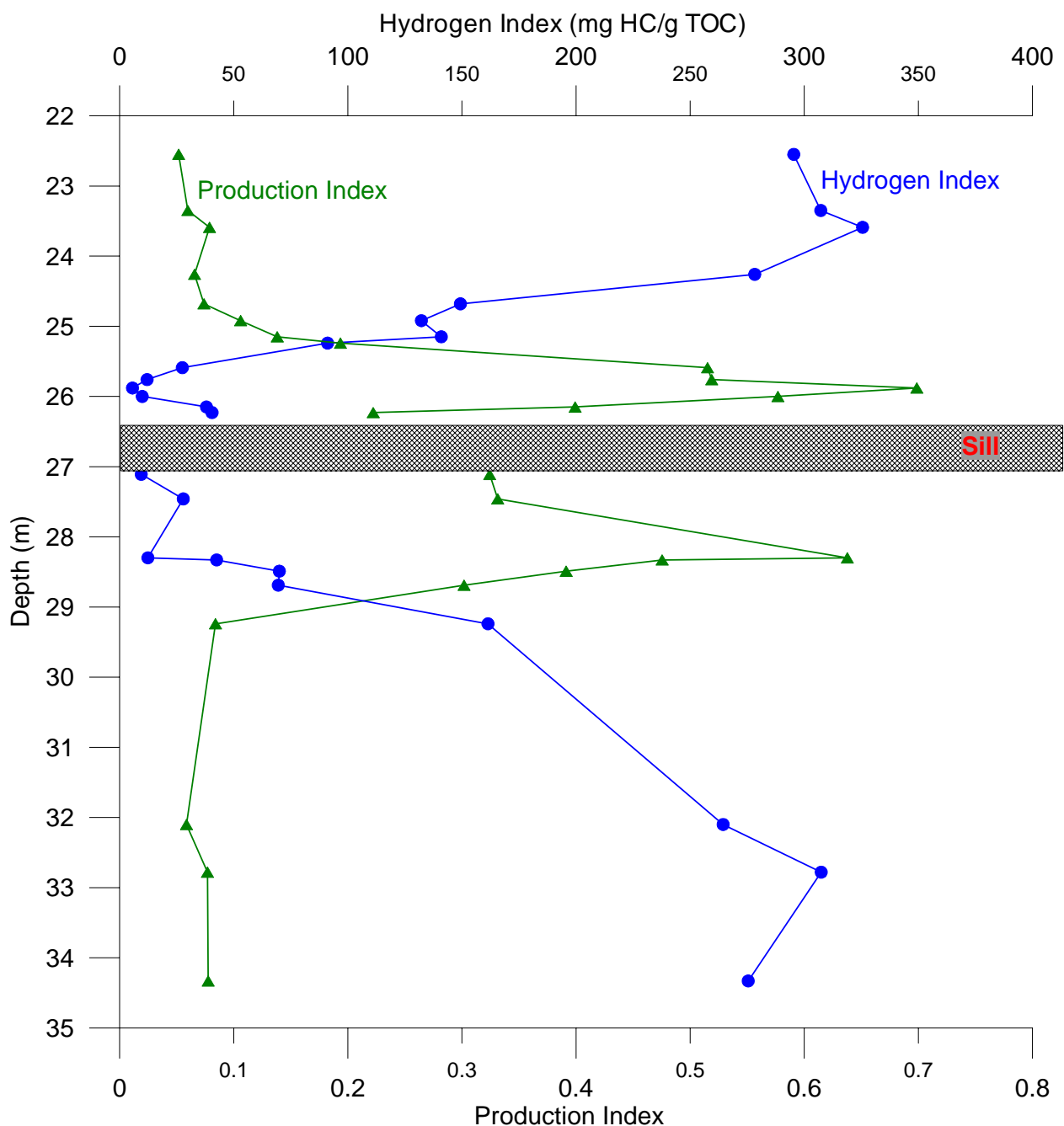
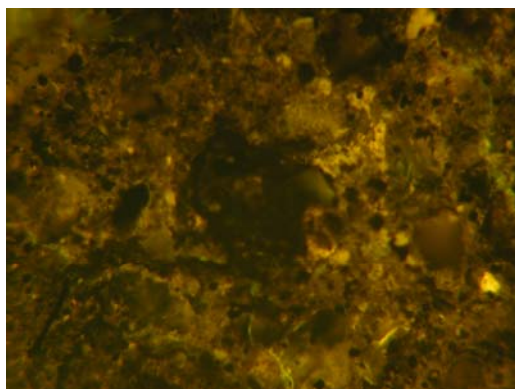
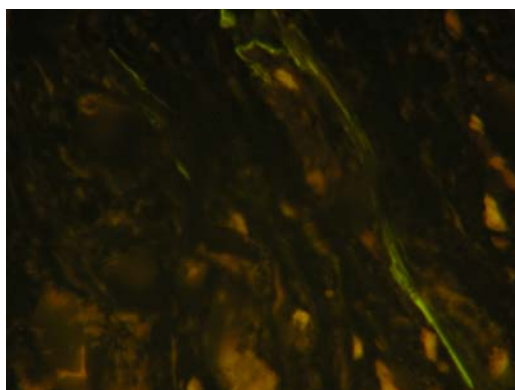


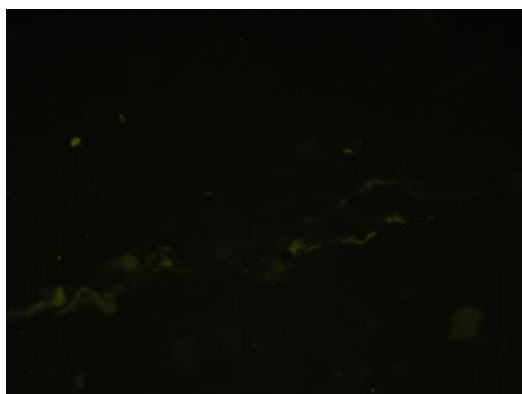
Fig. 7.1.10. **(A)** Close-up of the sill-affected mudstones at about 26.4 m in the well. Towards the sill the mudstones are increasingly matured due to the local elevated heat flow. HI decreases and PI increases due to HC generation. Closest to the sill PI declines, probably caused by extreme heat and volatilization of the liquid hydrocarbons. **(B, next page)** In agreement with increasing maturity of the mudstones towards the basalt sill and hydrocarbon generation the fluorescence intensity of the sapropelic kerogen diminishes and finally disappears. Closest to the sill only carbon-rich residues are present in the form of pyrobitumen, coke and natural chars.



25.15 m



25.76 m



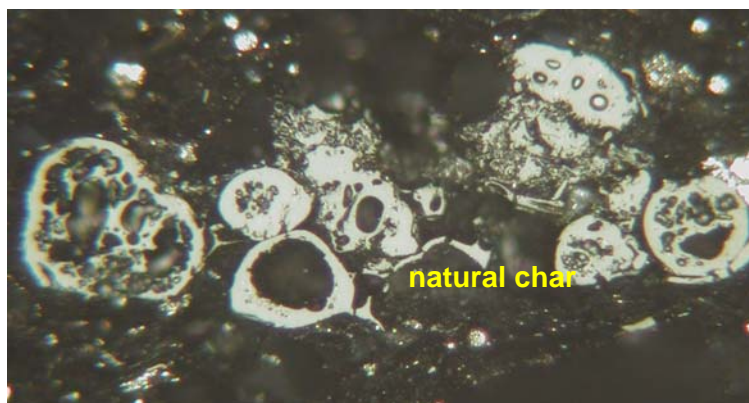
26.23 m

Decreasing fluorescence
towards sill due to
enhanced maturity



pyrobitumen

coke



natural char

26.23 m

(Fig. 7.1.10 B, see caption in previous page)

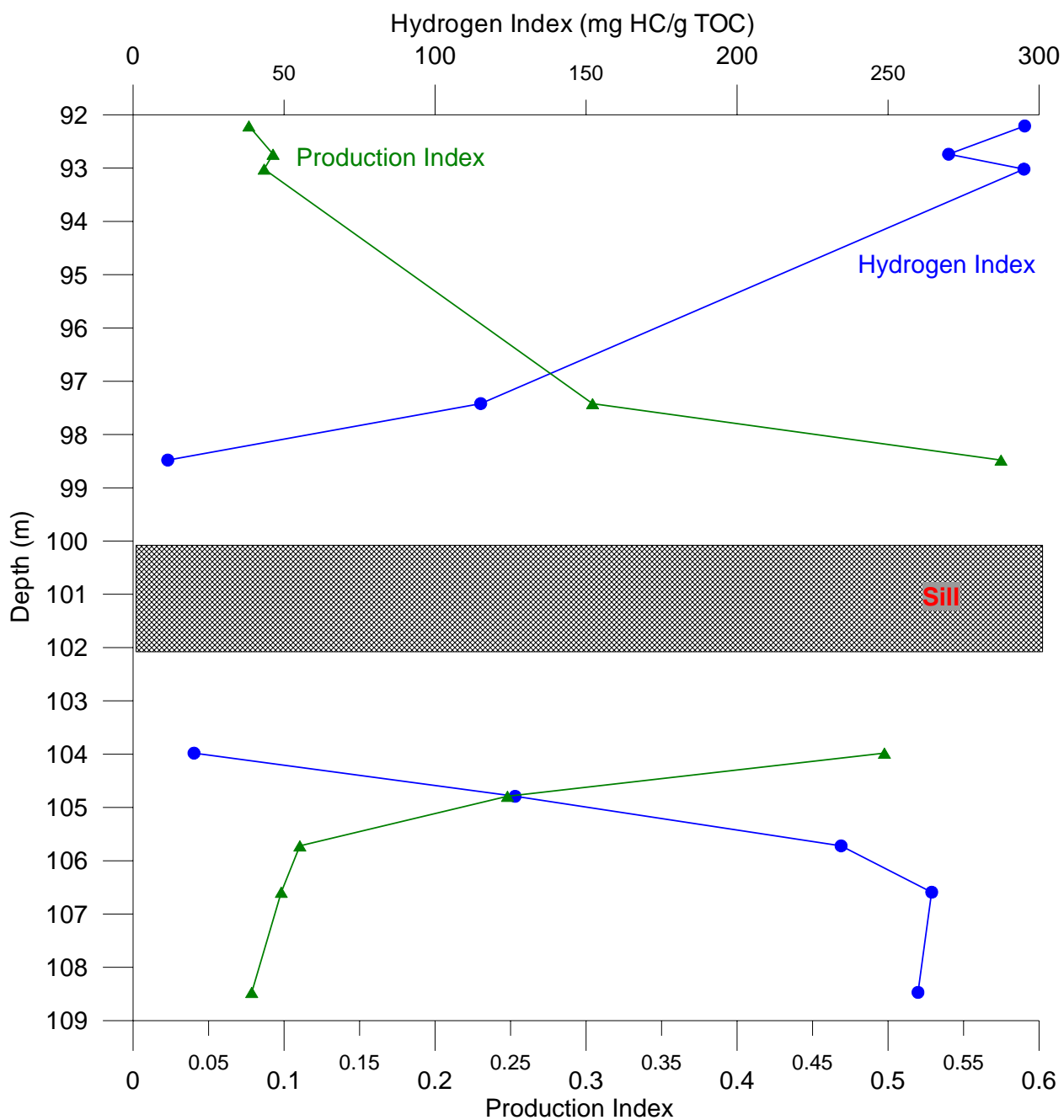


Fig. 7.1.11. Close-up of the sill-affected mudstones at about 100 m in the well. Towards the sill the mudstones are increasingly matured due to the local elevated heat flow, and accordingly HI decreases and PI increases due to HC generation. The mudstones are affected up to 4 m or more on both sides of the ~2 m thick sill.

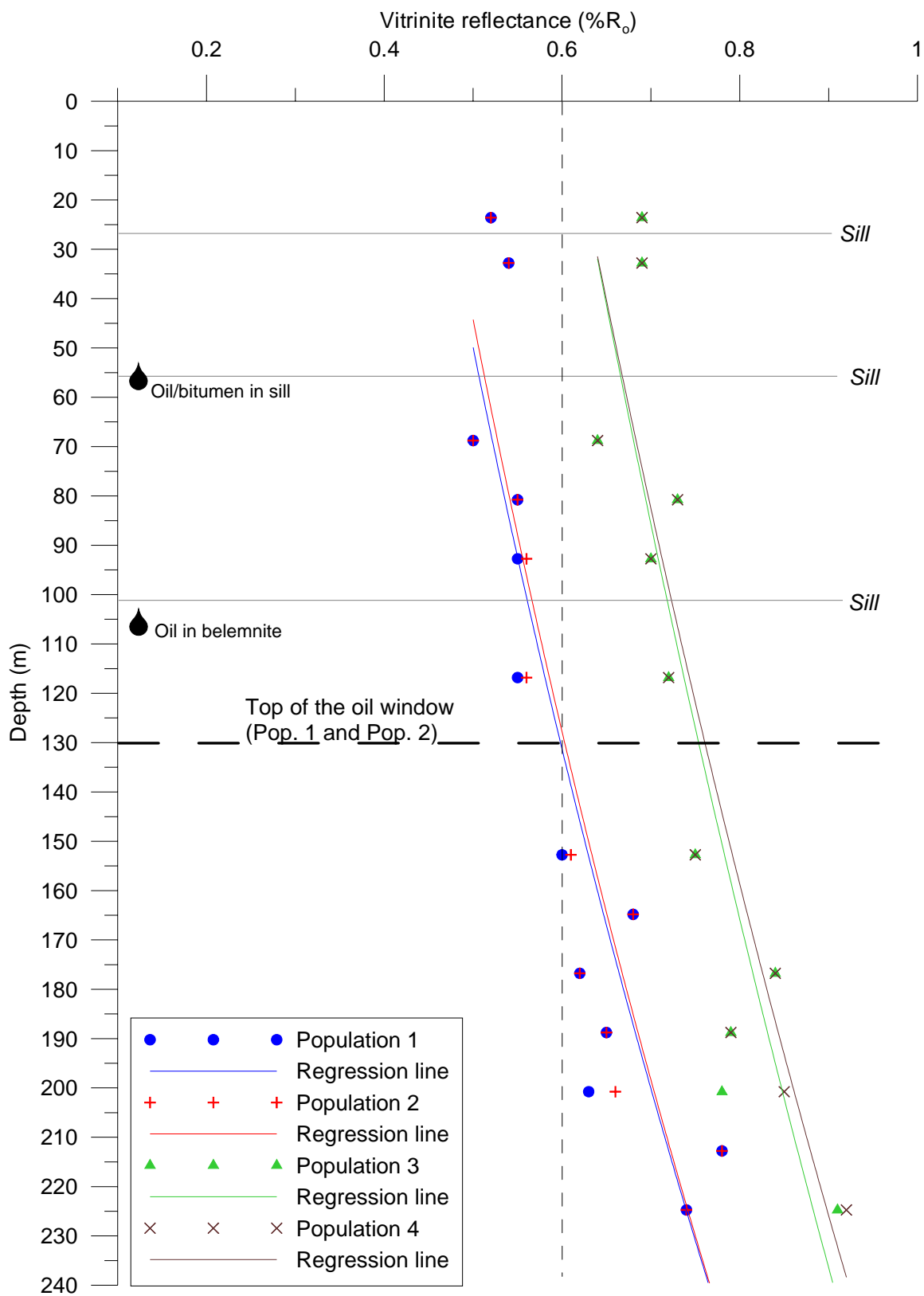


Fig. 7.1.12. Possible VR gradients based on selected populations in the VR histograms. Trend 2 (red) is considered to represent the correct maturity gradient.

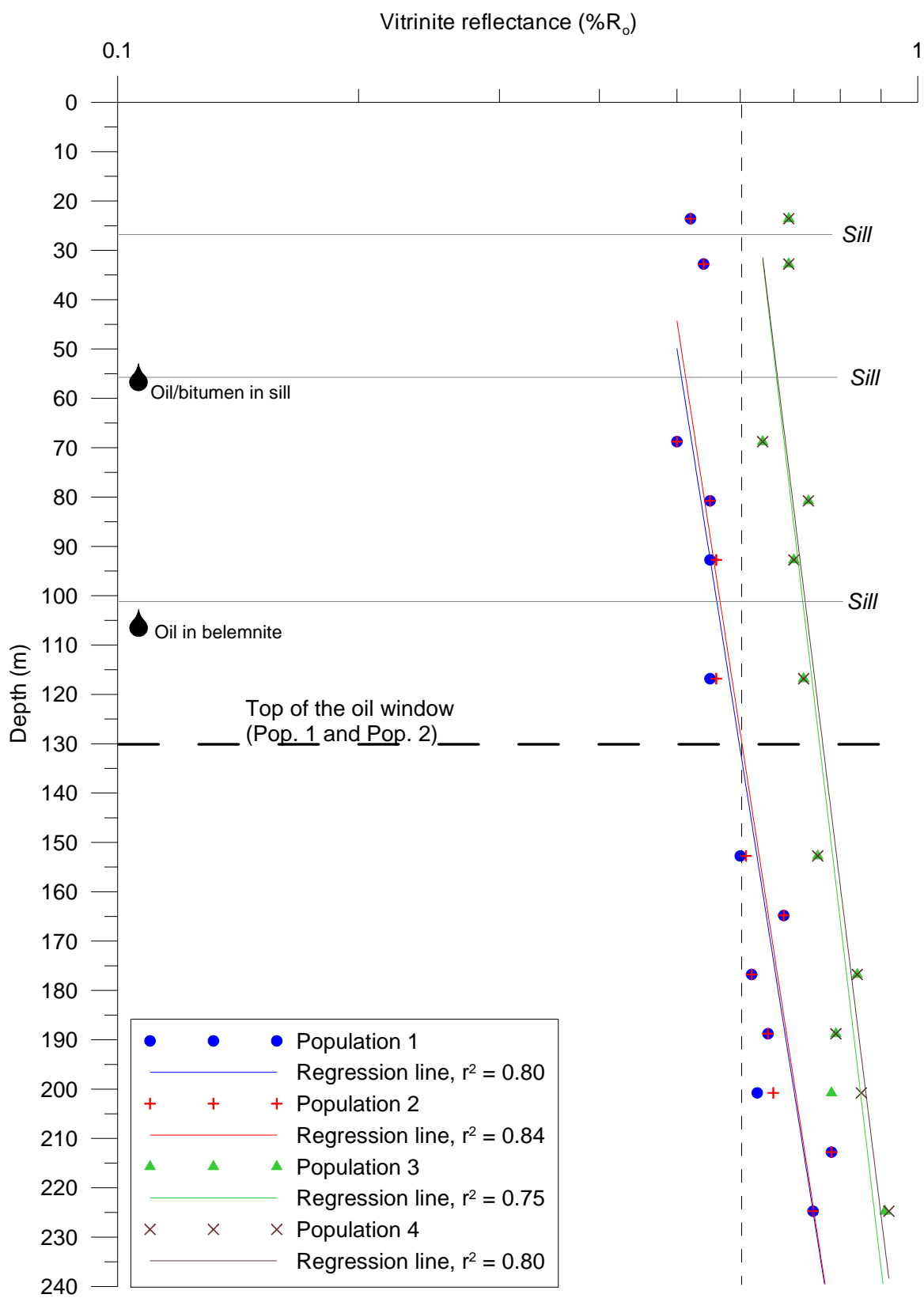


Fig. 7.1.13. Semi-log plots showing well-defined straight VR gradients.

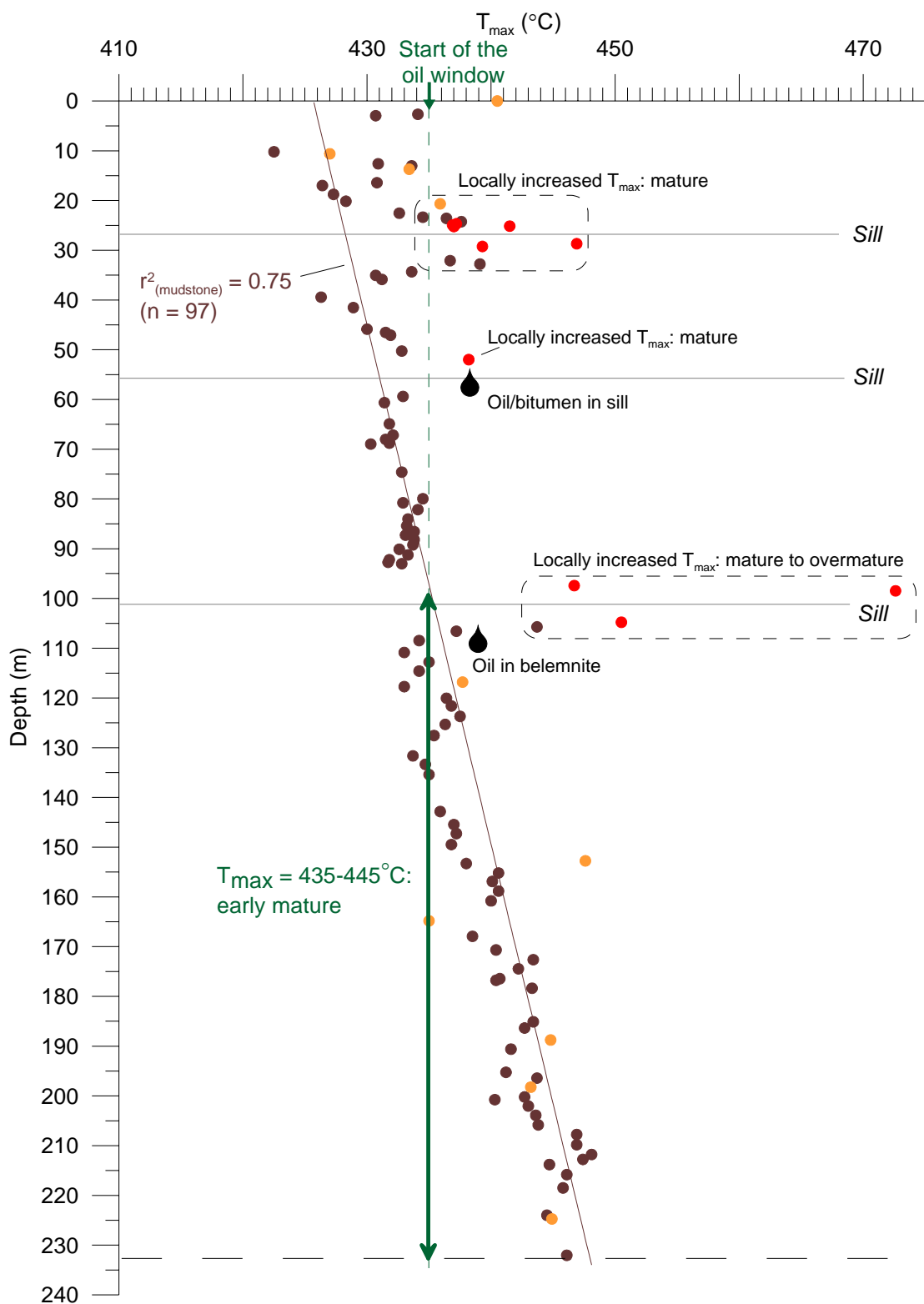


Fig. 7.1.14. T_{max} -depth plot showing a gradual increase in T_{max} interrupted by significantly increased T_{max} values close to the sills. T_{max} values from 435–445°C below about 100 m suggest that the mudstones below this depth are early mature.

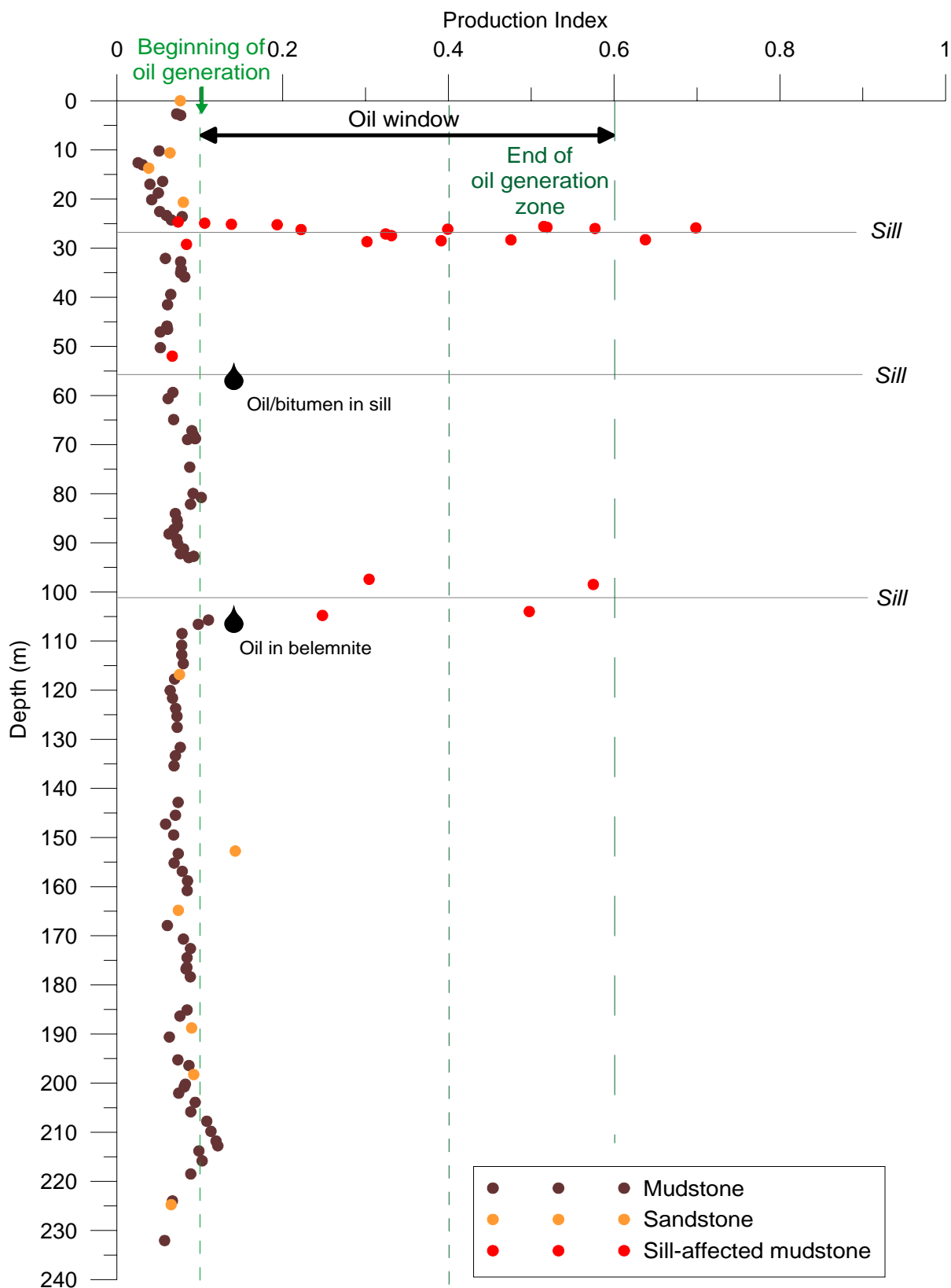


Fig. 7.1.15. PI-depth plot showing that PI is close to or exceeds 0.1 below approximately 160 m. High PI values associated with the sills indicate HC generation due to local elevated heat flow.

7.2 Biomarker analysis – Extraction, MPLC-separation, GC, GC-MS and GC-MS-MS

A total of 139 samples were collected from the cores of which 40 mudstone samples were selected for solvent extraction, MPLC-separation, gas chromatography (GC) and gas chromatography-mass spectrometry (GC-MS and GC-MS-MS) of the saturated fraction (Table 7.2.1). Two samples of bitumen and oil found near the basalt sills around 55 m and 104 m were also analysed.

7.2.1 Methods

Extraction and separation

Crushed mudstone samples were extracted with methanol/dichloromethane 7:93 vol/vol using a Soxtec equipment (extraction yield: Fig. 7.2.1). Traces of oil/bitumen on core samples were dissolved in dichloromethane (no crushing). The asphaltenes (Fig. 7.2.2) were removed from the extracts by precipitation in *n*-pentane. Subsequent medium pressure liquid chromatography (MPLC) fractionation of the maltenes yielded a saturated hydrocarbon, an aromatic hydrocarbon and a polar fraction (composition: Fig. 7.2.3). Only the saturated fraction was analysed by GC, GC-MS and GC-MS-MS.

Gas chromatography (GC)

Gas chromatography was performed using a Shimadzu GC-2010 instrument equipped with a splitless injector and a ZB-1 capillary column (25 m x 0.25 mm i.d., film thickness 0.10 µm). The temperature program was 5°C/min from 80 to 300°C, followed by 15 min at 300°C. Pristane/phytane ratios (Fig. 7.2.4) and relative concentrations of isoprenoids (Figs 7.2.5 and 7.2.6) were obtained from peak areas in the gas chromatograms.

Gas chromatography-mass spectrometry (GC-MS and GC-MS-MS)

Gas chromatography-mass spectrometry was carried out using an Agilent 6890N gas chromatograph connected to a Waters (Micromass) Quattro Micro GC tandem quadrupole mass spectrometer. A Phenomenex ZB-5 column (30 m x 0.25 mm i.d., film thickness 0.10 µm) was used. The injection temperature was 70°C (2 min hold). The temperature program was 30°C/min from 70 to 100°C and 4°C/min from 100 to 308°C followed by 8 min at 308°C. Argon was used as collision gas for MS-MS experiments. The saturated hydrocarbons were analysed by GC-MS in SIM-mode and by GC-MS-MS using relevant transitions for C₂₆-C₃₀ steranes and C₂₇-C₃₅ hopanes. Four separate GC-MS and GC-MS-MS methods were used. Samples were dissolved in isooctane. The concentration for GC and GC-MS analysis was 3 mg / ml isooctane. The same concentration was used for GC-MS-MS in most cases. However, the four lowermost samples and samples near the sills had a lower concentration of biomarkers (Fig. 7.2.7) and the concentration was increased to 5-20 mg / ml isooctane in order to obtain the same signal/noise ratio. Hopanes and steranes could not be quantified in extracts from three of the sill-affected mudstones (25.76, 28.33 and 103.98 m).

GC-MS, SIM

	71.1 <i>n</i> -alkanes
177.16	25-norhopanes
191.18	hopanes
205.20	methylhopanes
217.20	steranes
218.20	steranes
231.21	methylsteranes
253.20	monoaromatic steranes (should be absent in sat. fraction)
355.35	25- and 28-norhopanes
369.35	hopanes

GC-MS-MS Steranes:

358.36 → 217.20	C ₂₆ steranes
372.38 → 217.20	C ₂₇ steranes
386.39 → 217.20	C ₂₈ steranes
400.41 → 217.20	C ₂₉ steranes
414.42 → 217.20	C ₃₀ steranes

412.41 → 191.18	C ₃₀ hopanes
414.42 → 259.24	TPP

GC-MS-MS Hopanes:

370.36 → 191.18	C ₂₇ hopanes
384.38 → 191.18	C ₂₈ hopanes
398.39 → 191.18	C ₂₉ hopanes
412.41 → 191.18	C ₃₀ hopanes
412.41 → 369.35	C ₃₀ hopanes
426.42 → 191.18	C ₃₁ hopanes
440.44 → 191.18	C ₃₂ hopanes
454.45 → 191.18	C ₃₃ hopanes
468.47 → 191.18	C ₃₄ hopanes
482.49 → 191.18	C ₃₅ hopanes

GC-MS-MS: C₃₃ + C₃₄ hopanes and isohopanes (only two transitions for better signal/noise ratio).

454.45 → 191.18	C ₃₃ hopanes
468.47 → 191.18	C ₃₄ hopanes

Hopanes and steranes were quantified using peak areas from the relevant MS-MS transitions. GC-MS-MS allows quantification of C₂₇-C₃₀ steranes (Table 7.2.2, Figs 7.2.8–7.2.17) with little interference from co-eluting gas chromatographic peaks which is not possible using only GC-MS. Biomarker ratios obtained using GC-MS-MS will, in some cases, be slightly different to those obtained from the usual *m/z* 191,217 and 218 fragmentograms because of different response factors.

GC-MS and GC-MS-MS chromatograms showing the most important biomarkers have been included as pdf-files in Appendix 11.6.

Biomarker ratios and other data can be found on three tables.

Table 7.2.1: extraction, MPLC-separation and GC

Table 7.2.2: sterane data

Table 7.2.3: hopane data

7.2.2 Organic matter

The composition of biomarkers in extracts from the mudstones resembles that of typical marine source rocks. However, various biomarker ratios also show an increase in the proportion of terrestrial-influenced kerogen below ~ 120 m.

Pristane/phytane (Pr/Ph) is around 2 in samples above 120 m (Fig. 7.2.4) which is slightly higher than for most oils and source rocks from the Danish North Sea. A rapid increase in Pr/Ph can be seen below 120 m. Similarly, the relative abundances of C₂₇, C₂₈, and C₂₉ steranes are almost equal above 120 m (Fig. 7.2.8) whereas C₂₉ steranes dominate below 120 m. C₃₀ steranes (24-*n*-propylcholestanes) is the most powerful means in order to identify input of marine organic matter to the source rock (Peters *et al.* 2005). The relative proportion of C₃₀ steranes varies from around 8% (C₂₇+C₂₈+C₂₉+C₃₀ = 100 %) in the top (10-85 m) to 2.7 % in the bottom (232 m).

Extended hopanes (C₃₁-C₃₅) show little odd-over-even-predominance (HOEP, Bishop & Farrimond 1995, Table 7.2.3). More of the higher homohopanes are preserved under anoxic depositional conditions and the C₃₅ homohopane index (HHI, Table 7.2.3, Fig. 7.2.18) can thus be used as an indicator of redox potential in marine sediments during diagenesis (Peters *et al.* 2005). The C₃₅ homohopane index is around 0.08 above 120 m. Similar values are found for most oils from the Danish North Sea. Higher carbon number hopanes are less stable than the lower homologues and a decrease in the C₃₅ homohopane index can be seen near the sills.

Isohopanes can be used in a similar way. Isohopanes are novel extended hopanes having a side chain with an additional methyl branch (C₃₃ and higher). All C₃₃ and C₃₄ isohopanes have recently been identified by comparison with synthetic standards (Nytoft 2007, 2009). Details concerning the identification and use of isohopanes will be reported elsewhere. The relative abundance of isohopanes is low in oils sourced from marine organic matter deposited under anoxic conditions and very high in oils having a coaly source. Figure 7.2.19 shows the variation in the C₃₃-C₃₄ isohopane ratio (IHR) through the Blokelyv borehole.

High concentrations of 28,30-Bisnorhopane (BNH, C₂₈, Moldowan & Seifert 1984; Schoell *et al.* 1992; Seifert *et al.* 1978) are typical of petroleum source rocks deposited under anoxic conditions although the absence does not exclude sedimentation under anoxic conditions (Peters *et al.* 2005). The relative abundance of BNH is high but somewhat variable in the Blokelyv mudstones (Fig. 7.2.20). No higher carbon number 28-norhopanes were detected. Most North Sea crude oils and several oils and source rocks from West Greenland

contain both BNH and higher 28-norhopanes (C_{29} - C_{34} , Nytoft *et al.* 2000; Bojesen-Koefoed *et al.* 1999).

The $17\alpha,21\beta$ (H)-norhopane/ $17\alpha,21\beta$ (H)-hopane ratio (H29/H30) is close to 0.65 throughout the Blokelyv core (Fig. 7.2.21) which is typical of marine mudstones (Peters *et al.* 2005). $17\beta,21\alpha$ (H)-hopanes or moretanes decrease with depth (Fig. 7.2.22).

Gammacerane is almost absent in the Blokelyv mudstones. Gammacerane is highly specific for water-column stratification (commonly due to hypersalinity) during source rock deposition (Sinninghe Damsté *et al.* 1995).

The relative abundance of C_{27} and C_{29} neohopanes (Ts and 29Ts) is surprisingly low in the mudstones considering the maturity of the samples. Neohopane/hopane ratios are determined by both source and maturity. No clear trend can be seen from top to bottom of the core (Fig. 7.2.23). The two most abundant series of rearranged hopanes in the Blokelyv samples are 17α -diahopanes and the so-called “early eluting rearranged hopanes” (Moldovan *et al.* 1991; Farrimond *et al.* 1996). The relative abundance of the C_{30} members of the two series (30D and 30E) can be found in Table 7.2.3. 30E is more abundant than 30D in many samples. 30D is usually the major rearranged hopane in oils and source rocks from other locations.

Tricyclic terpanes can be seen in the m/z 191 fragmentograms. They are, however, minor compounds in all samples and they were not quantified.

The C_{26} 24/(24 + 27) nordiacholestane ratio (not tabulated) is close to 0.23 throughout the Blokelyv core in accordance with the Jurassic age of the mudstones.

Tetracyclic polyprenoids (TPP, Holba *et al.* 2000, 2003) are markers for lacustrine matter input. They were identified in the mudstones, but the TPP ratio (data not shown) was low in all samples.

Traces of oil/bitumen was found near the sills at 55.4 m and 105.18 m. The composition of the “oil” from 105.18 m was similar to that of extracts from the nearest mudstone samples (104.79 and 105.72 m). The oil at 55.4 was generally similar to the nearest mudstone extracts but it also showed some differences such as a higher relative abundance of C_{35} hopanes.

7.2.3 Maturity

The relative concentration of isoprenoids (Figs 7.2.5 and 7.2.6) and the various cyclic biomarkers (hopanes and steranes) decreases with maturity (depth) and near the basalt sills (Fig. 7.2.7) due to preferential generation of *n*-alkanes and cracking of the less stable hopanes and steranes. Three samples from sill-affected parts of the mudstones were almost devoid of hopanes and steranes. The “natural” maturation of biomarkers is affected near the sills. In general, high molecular compounds are more susceptible to cracking and a relative increase in low molecular-weight compounds such as short-chain steranes (C_{21} and C_{22} , m/z 217 and m/z 218, not quantified) can be seen near the sills.

The $22S/(22S + 22R)$ ratio for C_{31} hopanes and other extended hopanes is close to equilibrium (~ 0.60) in all samples (Table 7.2.3). The $20S/(20S + 20R)$ ratio of C_{29} steranes (ethylcholestanes) shows a gradual increase with depth (Table 7.2.2, Fig. 7.2.15) until ~ 100 m where the ratio is close to equilibrium ($0.52 - 0.55$) indicating that the mudstones are within the oil window. The $20S/(20S + 20R)$ ratio decreases in the order $C_{27} > C_{28} > C_{29} > C_{30}$ (Table 7.2.2). Isomerization at C-14 and C-17 in steranes causes an increase in the $\beta\beta/(\alpha\alpha + \beta\beta)$ ratio with maturity (depth) until approximately 170 m (Figs 7.2.11–7.2.14). The C_{27} steranes show a lower $\beta\beta/(\alpha\alpha + \beta\beta)$ ratio than the C_{28} - C_{30} steranes in all samples.

The diasteranes/(diasteranes + regular steranes) ratio increases with depth through the Blokelyv borehole (Figs 7.2.15–7.2.17). The relative proportion of C_{27} diasteranes is influenced by both thermal maturity and the depositional environment.

7.2.4 Conclusions

Extracts of the Blokelyv black mudstones show the typical characteristics of a marine source rock but with an increasing proportion of terrestrial-influenced kerogen below ~ 120 m. The deeper parts of the core are within the oil window.

7.2.5 References

Bishop, A.N. & Farrimond, P. 1995: A new method of comparing extended hopane distributions. *Organic Geochemistry* **23**, 987-990.

- Bojesen-Koefoed, J.A., Christiansen, F.G., Nytoft, H.P. & Pedersen, A.K. 1999: Oil seepage onshore West Greenland: evidence of multiple source rocks and oil mixing. In Fleet, A.S. & Boldy, S. (eds.): *Petroleum Geology of NW-Europe*, proceedings of the 5th Conference, 305-314.
- Farrimond, P. & Telnaes, N. 1996: Three series of rearranged hopanes in Toarcian sediments (northern Italy). *Organic Geochemistry* **25**, 165-177.
- Holba, A.G., Tegelaar, E., Ellis, L., Singletary, M.S. & Albrecht, P. 2000: Tetracyclic polyprenoids: indicators of freshwater (lacustrine) algal input. *Geology* **28**, 251-254.
- Holba, A.G., Dzou, L.I., Wood, G.D., Ellis, L., Adam, P., Schaeffer, P., Albrecht, P., Greene, T. & Hughes, W.B. 2003: Application of tetracyclic polyprenoids as indicators of input from fresh-brackish water environments. *Organic Geochemistry* **34**, 441-469.
- Moldowan, J.M. & Seifert, W.K. 1984: Structure proof and significance of stereoisomeric 28,30-bisnorhopanes in petroleum and petroleum source rocks. *Geochimica et Cosmochimica Acta* **48**, 1651-1661.
- Moldowan, J.M., Fago, F.J., Carlson, R.M.K., Young, D.V., Van Duyne, G., Clardy, J., Schoell, M., Pillinger, C.T. & Watt, D.S. 1991: Rearranged hopanes in sediments and petroleum. *Geochimica et Cosmochimica Acta* **55**, 3333-3353.
- Nytoft, H.P. 2009: Novel isohopanes II. The 24rd International Meeting on Organic Geochemistry. 6-11 September, 2009-12-03. Bremen, Germany. European Association of Organic Geochemists. Book of Abstracts, p-172.
- Nytoft, H.P. 2007: Novel "isohopanes" and their use as source markers. The 23rd International Meeting on Organic Geochemistry. 9-14 September, 2007. Torquay, England. European Association of Organic Geochemists. Book of Abstracts, 273-274.
- Nytoft, H.P., Bojesen-Koefoed, J.A. & Christiansen, F.G. 2000: C₂₆ and C₂₈-C₃₄ 28-norhopanes in sediments and petroleum. *Organic Geochemistry* **31**, 25-39.
- Peters, K.E., Walters, C.C. & Moldowan, J.M. 2005: *The Biomarker Guide Second Edition Volume 2: Biomarkers and Isotopes in Petroleum Exploration and Earth History*. Cambridge University Press.
- Schoell, M., McCaffrey, M.A., Fago, F.J. & Moldowan, J.M. 1992: Carbon isotopic compositions of 28,30-bisnorhopanes and other biological markers in a Monterey crude oil. *Geochimica et Cosmochimica Acta* **56**, 1391-1399.
- Seifert, W.K., Moldowan, J.M., Smith, G.W. & Whitehead, E.W. 1978. First proof of structure of a C₂₈-pentacyclic triterpane in petroleum. *Nature* **271**, 436-437.
- Sinninghe Damsté, J.S., Kenig, F., Koopmans, M.P., Köster, J., Schouten, S., Hayes, J.M. & de Leeuw, J.W. 1995: Evidence for gammacerane as an indicator of water column stratification. *Geochimica et Cosmochimica Acta*, **59**, 1895-1900.

Lab no.	Sample no.	Depth Bottom	Yield mg/g TOC	% Asph.	% Sat.	% Aro.	% Polars	Pristane/ phytane	Pristane/ nC17	Phytane nC18
2009003-16707	511101-107	12,62	38,63	35,18	11,95	13,55	74,50	2,55	1,75	0,87
2009003-16710	511101-110	16,42	54,21	32,70	11,11	12,22	76,67	2,36	1,98	1,05
2009003-16713	511101-113	20,15	47,11	43,68	12,45	11,67	75,88	2,25	2,62	1,47
2009003-16822	511101-8	23,59	67,03	23,74	13,40	12,89	73,71	2,01	1,66	1,06
2009003-16717	511101-117	24,26	70,61	34,91	11,33	11,33	77,34	1,95	1,34	0,87
2009003-16738	511101-139	24,68	60,65	34,73	10,50	10,50	79,01	1,88	0,98	0,65
2009003-16718	511101-118	25,15	90,85	34,21	11,59	9,87	78,54	1,91	0,91	0,59
2009003-16736	511101-137	25,24	103,04	33,23	12,87	10,40	76,73	1,92	1,07	0,69
2009003-16719	511101-119	25,76	37,14	13,91	11,81	16,46	71,73	1,77	0,08	0,05
2009003-16734	511101-135	25,88	26,51	12,69	8,37	21,18	70,44	1,93	0,84	0,57
2009003-16721	511101-121	26,23	48,11	13,63	17,12	13,96	68,92	1,84	0,82	0,49
2009003-16722	511101-122	27,11	42,45	16,30	19,90	12,24	67,86	1,86	0,91	0,50
2009003-16740	511101-141	27,46	60,55	13,73	17,75	18,18	64,07	1,77	0,67	0,41
2009003-16723	511101-123	28,33	84,14	15,27	24,87	14,29	60,85	1,62	0,32	0,23
2009003-16743	511101-144	28,69	83,95	19,80	15,93	11,54	72,53	2,64	0,67	0,28
2009003-16724	511101-124	29,24	73,14	38,61	7,43	9,41	83,17	1,84	0,91	0,60
2009003-16725	511101-125	32,10	68,38	31,94	8,40	13,87	77,73	1,92	1,02	0,66
2009003-16823	511101-12	32,78	57,47	28,29	9,83	12,39	77,78	1,96	1,55	1,03
2009003-16745	511101-146	50,27	56,37	42,31	7,14	12,05	80,80	2,06	1,10	0,60
2009003-16749	511101-150	64,91	50,65	35,02	11,17	14,89	73,94	2,10	1,62	0,96
2009003-16826	511101-24	68,77	70,14	25,43	10,00	13,91	76,09	1,97	1,19	0,71
2009003-16827	511101-28	80,77	65,88	27,65	13,86	12,05	74,10	2,14	1,97	1,20
2009003-16767	511101-164	82,14	68,82	28,95	15,05	12,90	72,04	1,89	1,91	1,30
2009003-16773	511101-170	89,22	53,13	41,38	13,48	13,48	73,03	2,42	2,20	1,19
2009003-16828	511101-32	92,74	48,67	34,58	10,87	15,22	73,91	2,36	2,43	1,25
2009003-16777	511101-174	93,02	53,86	38,07	10,61	13,88	75,51	2,16	2,20	1,21
2009003-16778	511101-175	97,42	107,57	19,55	16,06	12,39	71,56	1,99	1,11	0,62
2009003-16779	511101-176	98,48	18,68	12,03	3,77	23,27	72,96	2,67	0,60	0,24
2009003-16780	511101-177	103,98	28,04	7,76	14,87	33,85	51,28	2,74	0,10	0,04
2009003-16829	511101-36	104,79	80,40	14,12	26,55	26,18	47,27	2,43	1,19	0,56
2009003-16781	511101-178	105,72	66,15	21,32	21,79	26,92	51,28	2,50	1,98	0,94
2009003-16782	511101-179	106,59	48,68	22,32	21,49	30,17	48,35	2,71	2,66	1,18
2009003-16795	511101-186	117,73	48,63	33,85	18,54	30,73	50,73	2,60	2,36	0,95
2009003-16804	511101-195	142,84	38,52	39,63	14,85	36,14	49,01	3,08	2,06	0,80
2009003-16812	511101-203	160,80	48,12	30,57	20,70	37,89	41,41	3,52	2,30	0,73
2009003-16835	511101-60	176,77	47,51	26,75	23,56	34,62	41,83	3,83	1,84	0,54
2009003-16850	511101-220	205,84	47,76	29,48	23,39	34,86	41,74	3,66	1,97	0,60
2009003-16858	511101-228	232,05	19,59	39,58	27,37	25,26	47,37	5,77	2,32	0,41
2009003-16764	511101 oil	105,18	n.a.	18,58	41,50	10,46	48,04	2,31	2,97	1,34
2008007-16053	511206 oil	55,4	n.a.	n.a.	n.a.	n.a.	n.a.	2,05	0,90	0,58

Table 7.2.1 Extraction, MPLC-separation and GC

			Diasteranes/ (diasteranes + reg. steranes)				$\beta\beta$ steranes/ ($\beta\beta$ steranes + $\alpha\alpha$ steranes)				Steranes 20S/(20S + 20R)				% C27, 28 & 29 Sum = 100 % Regular steranes only			% C27, 28 & 29 Sum = 100 % Diasteranes only			% C27, 28 & 29 Sum = 100 % Diasteranes + reg. steranes			% C30
Lab no.	Sample no.	Depth Bottom	C27 D/(R+D)	C28 D/(R+D)	C29 D/(R+D)	C30 D/(R+D)	C27 B/(B+A)	C28 B/(B+A)	C29 B/(B+A)	C30 B/(B+A)	C27 S/(S+R)	C28 S/(S+R)	C29 S/(S+R)	C30 S/(S+R)	C27 R-st	C28 R-st	C29 R-st	C27 Dia	C28 Dia	C29 Dia	C27 D+R	C28 D+R	C29 D+R	C30 D+R
2009003-16707	511101-107	12,62	0,72	0,74	0,71	0,72	0,19	0,34	0,33	0,30	0,48	0,39	0,35	0,31	31,1	30,5	38,4	30,2	33,3	36,5	30,5	32,5	37,0	7,5
2009003-16710	511101-110	16,42	0,67	0,68	0,67	0,66	0,18	0,34	0,33	0,30	0,49	0,40	0,37	0,34	32,1	30,6	37,3	31,8	31,6	36,6	31,9	31,3	36,8	8,1
2009003-16713	511101-113	20,15	0,71	0,73	0,71	0,70	0,20	0,35	0,34	0,30	0,49	0,40	0,36	0,34	32,1	31,7	36,2	30,7	34,1	35,2	31,1	33,4	35,5	8,0
2009003-16822	511101-8	23,59	0,66	0,68	0,65	0,63	0,20	0,35	0,33	0,32	0,49	0,43	0,41	0,39	33,6	34,1	32,3	32,8	36,8	30,3	33,1	35,9	31,0	8,3
2009003-16717	511101-117	24,26	0,66	0,68	0,65	0,63	0,22	0,36	0,34	0,31	0,52	0,45	0,43	0,40	34,2	33,4	32,4	33,2	36,1	30,7	33,5	35,2	31,3	8,8
2009003-16738	511101-139	24,68	0,66	0,67	0,65	0,62	0,25	0,39	0,36	0,31	0,53	0,46	0,46	0,41	34,5	33,0	32,6	34,5	34,9	30,6	34,5	34,2	31,3	8,6
2009003-16718	511101-118	25,15	0,75	0,77	0,75	0,73	0,39	0,51	0,48	0,47	0,59	0,53	0,50	0,46	36,4	33,0	30,6	35,5	34,7	29,8	35,7	34,3	30,0	8,9
2009003-16736	511101-137	25,24	0,83	0,84	0,83	0,79	0,48	0,58	0,58	0,55	0,63	0,62	0,54	0,49	38,0	33,1	28,9	37,0	34,7	28,3	37,1	34,4	28,4	8,2
2009003-16719	511101-119	25,76	n.a.	n.a.	n.a.	n.a.	n.a.	n.a.	n.a.	n.a.	n.a.	n.a.	n.a.	n.a.	n.a.	n.a.	n.a.	n.a.	n.a.	n.a.	n.a.	n.a.	n.a.	n.a.
2009003-16734	511101-135	25,88	0,81	0,83	0,81	0,80	0,30	0,45	0,44	0,41	0,55	0,46	0,43	0,42	38,9	31,5	29,6	37,5	34,0	28,6	37,7	33,5	28,8	7,6
2009003-16721	511101-121	26,23	0,68	0,68	0,67	0,63	0,24	0,35	0,35	0,32	0,48	0,43	0,40	0,36	36,0	32,4	31,5	36,1	33,3	30,6	36,1	33,0	30,9	8,1
2009003-16722	511101-122	27,11	0,68	0,70	0,70	0,67	0,25	0,35	0,36	0,32	0,45	0,41	0,40	0,36	38,2	31,5	30,3	36,1	32,9	31,0	36,7	32,5	30,8	7,7
2009003-16740	511101-141	27,46	0,73	0,74	0,72	0,69	0,28	0,40	0,39	0,37	0,50	0,44	0,42	0,39	36,3	31,9	31,8	36,5	33,2	30,3	36,5	32,9	30,7	7,5
2009003-16723	511101-123	28,33	n.a.	n.a.	n.a.	n.a.	n.a.	n.a.	n.a.	n.a.	n.a.	n.a.	n.a.	n.a.	n.a.	n.a.	n.a.	n.a.	n.a.	n.a.	n.a.	n.a.	n.a.	n.a.
2009003-16743	511101-144	28,69	0,83	0,85	0,82	0,82	0,50	0,59	0,58	0,55	0,61	0,57	0,55	0,51	33,4	27,6	39,0	33,1	31,4	35,5	33,1	30,8	36,0	6,2
2009003-16724	511101-124	29,24	0,71	0,73	0,70	0,68	0,31	0,43	0,43	0,39	0,55	0,49	0,49	0,43	33,4	33,4	33,1	32,3	36,2	31,5	32,6	35,4	32,0	8,7
2009003-16725	511101-125	32,10	0,65	0,67	0,64	0,63	0,21	0,34	0,34	0,30	0,49	0,43	0,42	0,37	34,0	33,8	32,2	33,0	36,5	30,5	33,3	35,6	31,1	7,5
2009003-16823	511101-12	32,78	0,68	0,70	0,67	0,66	0,20	0,35	0,33	0,30	0,50	0,43	0,41	0,36	32,8	33,2	34,0	32,6	35,8	31,6	32,7	35,0	32,4	8,3
2009003-16745	511101-146	50,27	0,66	0,67	0,66	0,64	0,21	0,35	0,34	0,29	0,54	0,46	0,45	0,40	33,4	30,0	36,6	33,1	31,3	35,5	33,2	30,9	35,9	8,4
2009003-16749	511101-150	64,91	0,68	0,70	0,68	0,66	0,24	0,37	0,36	0,32	0,54	0,48	0,46	0,42	34,0	31,3	34,7	33,5	33,1	33,5	33,6	32,5	33,9	8,0
2009003-16826	511101-24	68,77	0,68	0,66	0,66	0,62	0,24	0,37	0,36	0,32	0,53	0,48	0,47	0,43	34,4	30,2	35,4	36,3	29,9	33,7	35,7	30,0	34,3	7,2
2009003-16827	511101-28	80,77	0,72	0,72	0,72	0,69	0,27	0,39	0,37	0,36	0,54	0,49	0,48	0,43	35,2	30,4	34,5	35,0	31,0	34,0	35,0	30,8	34,1	8,9
2009003-16767	511101-164	82,14	0,73	0,73	0,73	0,69	0,29	0,40	0,40	0,35	0,56	0,50	0,49	0,46	37,3	29,7	33,0	37,7	29,7	32,6	37,6	29,7	32,7	8,7
2009003-16773	511101-170	89,22	0,74	0,74	0,73	0,71	0,31	0,43	0,40	0,34	0,56	0,50	0,49	0,46	30,6	27,4	41,9	31,3	27,5	41,2	31,1	27,5	41,4	6,2
2009003-16828	511101-32	92,74	0,75	0,75	0,74	0,73	0,31	0,44	0,40	0,37	0,57	0,52	0,50	0,44	30,4	26,9	42,7	31,6	27,3	41,1	31,3	27,2	41,5	5,8
2009003-16777	511101-174	93,02	0,74	0,74	0,73	0,72	0,31	0,43	0,41	0,39	0,57	0,53	0,50	0,45	31,7	26,4	41,9	32,2	26,8	41,0	32,1	26,7	41,2	5,4
2009003-16778	511101-175	97,42	0,81	0,80	0,80	0,77	0,50	0,58	0,57	0,58	0,60	0,60	0,55	0,47	36,5	28,8	34,7	37,4	28,3	34,3	37,2	28,4	34,4	4,7
2009003-16779	511101-176	98,48	0,73	0,72	0,70	0,68	0,38	0,47	0,44	0,43	0,55	0,50	0,46	0,42	32,0	25,1	42,9	34,9	25,9	39,2	34,1	25,6	40,3	5,0
2009003-16780	511101-177	103,98	n.a.	n.a.	n.a.	n.a.	n.a.	n.a.	n.a.	n.a.	n.a.	n.a.	n.a.	n.a.	n.a.	n.a.	n.a.	n.a.	n.a.	n.a.	n.a.	n.a.	n.a.	n.a.
2009003-16829	511101-36	104,79	0,79	0,78	0,76	0,74	0,47	0,54	0,55	0,53	0,59	0,58	0,53	0,47	32,4	26,9	40,7	35,6	27,2	37,1	34,9	27,2	37,9	4,6
2009003-16781	511101-178	105,72	0,74	0,73	0,70	0,70	0,35	0,45	0,43	0,40	0,58	0,54	0,51	0,45	28,5	25,5	46,0	31,0	26,5	42,6	30,3	26,2	43,5	5,4
2009003-16782	511101-179	106,59	0,76	0,75	0,72	0,72	0,35	0,46	0,44	0,40	0,57	0,54	0,50	0,44	29,4	27,2	43,4	32,2	27,9	39,9	31,5	27,7	40,8	5,8
2009003-16795	511101-186	117,73	0,77	0,76	0,74	0,76	0,33	0,45	0,42	0,41	0,58	0,54	0,50	0,43	38,1	25,6	36,4	41,4	25,7	32,9	40,6	25,7	33,7	7,1
2009003-16804	511101-195	142,84	0,77	0,76	0,74	0,73	0,39	0,48	0,48	0,45	0,60	0,54	0,52	0,46	28,1	22,7	49,2	30,7	23,4	45,8	30,1	23,3	46,7	6,5
2009003-16812	511101-203	160,80	0,79	0,74	0,73	0,74	0,44	0,51	0,52	0,50	0,58	0,56	0,50	0,42	33,5	19,5	47,0	40,4	18,3	41,3	38,7	18,6	42,7	4,3
2009003-16835	511101-60	176,77	0,84	0,83	0,81	0,82	0,45	0,54	0,53	0,50	0,58	0,56	0,49	0,48	28,2	21,4	50,5	31,9	21,9	46,2	31,2	21,8	47,0	5,2
2009003-16850	511101-220	205,84	0,80	0,78	0,78	0,75	0,48	0,56	0,54	0,51	0,58	0,54	0,53	0,49	20,4	19,8	59,8	22,1	19,7	58,2	21,7	19,7	58,6	4,1
2009003-16858	511101-228	232,05	0,83	0,83	0,85	0,80	0,44	0,53	0,55	0,51	0,59	0,57	0,50	0,52	19,5	21,3	59,3	18,5	19,6	61,9	18,7	19,8	61,5	2,7
2009003-16764	511101 oil	105,18	0,78	0,77	0,73	0,70	0,41	0,48	0,47	0,42	0,56	0,53	0,53	0,48	30,0	25,7	44,3	33,6	27,2	39,2	32,7	26,8	40,4	5,2
2008007-16053	511206 oil	55,4	0,72	0,72	0,73	0,69	0,24	0,37	0,37	0,32	0,53	0,50	0,47	0,40	33,0	28,1	38,9	33,2	27,2	39,7	33,1	27,4	39,5	5,9

Table 7.2.2 Sterane data

			Hopanes, relative abundance, 17 α ,21 β (H)-HOPANE = 1																		Hopane ratios							
Lab no.	Sample no.	Depth	C27	C27	C28	C29	C29	C30	C30	C30	C30	C30	C31	C31	C32	C32	C33	C33	C34	C34	C35	C35	Ts/	29Ts/	C31	C31-35	C35	C34,35
		Bottom	27Ts	27Tm	BNH	29 α β	29Ts	30E	30D	30 α β	30Ts	30 β α	22S	22R	22S	22R	22S	22R	22S	22R	22S	22R	(Ts + Tm)	29Ts/ (H29 + 29Ts)	S/(S+R)	HOEP	HHI	IHR
2009003-16707	511101-107	12,62	0,075	0,295	0,170	0,560	0,138	0,111	0,078	1,000	0,055	0,132	0,375	0,271	0,164	0,127	0,105	0,080	0,084	0,065	0,073	0,056	0,20	0,20	0,58	1,07	0,092	0,061
2009003-16710	511101-110	16,42	0,083	0,348	0,923	0,632	0,131	0,135	0,091	1,000	0,055	0,134	0,372	0,267	0,168	0,131	0,122	0,099	0,093	0,076	0,101	0,080	0,19	0,17	0,58	1,15	0,120	0,059
2009003-16713	511101-113	20,15	0,083	0,332	0,111	0,596	0,136	0,133	0,080	1,000	0,052	0,126	0,347	0,245	0,146	0,106	0,094	0,071	0,071	0,056	0,058	0,048	0,20	0,19	0,59	1,11	0,085	0,066
2009003-16822	511101-8	23,59	0,063	0,289	0,318	0,634	0,092	0,049	0,051	1,000	0,029	0,124	0,285	0,216	0,106	0,084	0,074	0,055	0,047	0,035	0,041	0,031	0,18	0,13	0,57	1,24	0,074	0,065
2009003-16717	511101-117	24,26	0,060	0,289	0,244	0,620	0,087	0,051	0,052	1,000	0,030	0,125	0,278	0,204	0,109	0,082	0,074	0,055	0,047	0,033	0,041	0,029	0,17	0,12	0,58	1,22	0,074	0,066
2009003-16738	511101-139	24,68	0,054	0,269	0,109	0,552	0,081	0,042	0,049	1,000	0,025	0,126	0,265	0,191	0,114	0,081	0,068	0,051	0,039	0,029	0,033	0,023	0,17	0,13	0,58	1,16	0,063	0,066
2009003-16718	511101-118	25,15	0,061	0,295	0,080	0,550	0,063	0,061	0,060	1,000	0,022	0,127	0,288	0,208	0,149	0,109	0,086	0,061	0,050	0,036	0,040	0,029	0,17	0,10	0,58	1,06	0,065	0,071
2009003-16736	511101-137	25,24	0,077	0,305	0,013	0,578	0,071	0,071	0,061	1,000	0,022	0,121	0,309	0,223	0,181	0,124	0,100	0,072	0,060	0,042	0,042	0,032	0,20	0,11	0,58	1,01	0,062	0,068
2009003-16719	511101-119	25,76	n.a.	n.a.	n.a.	n.a.	n.a.	n.a.	n.a.	n.a.	n.a.	n.a.	n.a.	n.a.	n.a.	n.a.	n.a.	n.a.	n.a.	n.a.	n.a.	n.a.	n.a.	n.a.	n.a.	n.a.	n.a.	n.a.
2009003-16734	511101-135	25,88	0,063	0,269	0,237	0,658	0,102	0,143	0,079	1,000	0,033	0,113	0,302	0,245	0,151	0,119	0,098	0,077	0,057	0,042	0,049	0,034	0,19	0,13	0,55	1,14	0,071	0,092
2009003-16721	511101-121	26,23	0,062	0,299	0,405	0,664	0,079	0,078	0,083	1,000	0,035	0,134	0,377	0,294	0,174	0,142	0,120	0,100	0,072	0,060	0,069	0,059	0,17	0,11	0,56	1,18	0,087	0,068
2009003-16722	511101-122	27,11	0,086	0,285	0,027	0,677	0,106	0,122	0,109	1,000	0,042	0,120	0,398	0,298	0,188	0,150	0,124	0,108	0,083	0,068	0,084	0,070	0,23	0,13	0,57	1,15	0,098	0,056
2009003-16740	511101-141	27,46	0,076	0,296	0,404	0,680	0,086	0,089	0,087	1,000	0,033	0,128	0,324	0,260	0,154	0,133	0,102	0,094	0,061	0,049	0,061	0,047	0,20	0,11	0,55	1,17	0,085	0,069
2009003-16723	511101-123	28,33	n.a.	n.a.	n.a.	n.a.	n.a.	n.a.	n.a.	n.a.	n.a.	n.a.	n.a.	n.a.	n.a.	n.a.	n.a.	n.a.	n.a.	n.a.	n.a.	n.a.	n.a.	n.a.	n.a.	n.a.	n.a.	n.a.
2009003-16743	511101-144	28,69	0,068	0,340	0,031	0,735	0,061	0,052	0,049	1,000	0,017	0,135	0,354	0,255	0,196	0,143	0,091	0,070	0,055	0,040	0,030	0,021	0,17	0,08	0,58	0,94	0,041	0,093
2009003-16724	511101-124	29,24	0,053	0,276	0,196	0,542	0,068	0,058	0,052	1,000	0,025	0,119	0,269	0,195	0,140	0,102	0,086	0,061	0,051	0,034	0,049	0,034	0,16	0,11	0,58	1,09	0,081	0,067
2009003-16725	511101-125	32,10	0,070	0,366	0,491	0,660	0,099	0,060	0,060	1,000	0,035	0,129	0,303	0,232	0,137	0,105	0,087	0,066	0,055	0,040	0,055	0,040	0,16	0,13	0,57	1,15	0,085	0,060
2009003-16823	511101-12	32,78	0,062	0,311	0,496	0,656	0,081	0,065	0,053	1,000	0,032	0,121	0,297	0,216	0,123	0,095	0,087	0,067	0,055	0,040	0,061	0,046	0,17	0,11	0,58	1,24	0,098	0,062
2009003-16745	511101-146	50,27	0,072	0,377	0,438	0,675	0,108	0,097	0,079	1,000	0,056	0,139	0,443	0,314	0,218	0,160	0,122	0,090	0,083	0,057	0,081	0,058	0,16	0,14	0,58	1,05	0,086	0,075
2009003-16749	511101-150	64,91	0,081	0,297	0,663	0,628	0,107	0,084	0,070	1,000	0,039	0,111	0,324	0,234	0,139	0,100	0,107	0,074	0,061	0,043	0,066	0,044	0,21	0,15	0,58	1,28	0,092	0,062
2009003-16826	511101-24	68,77	0,075	0,296	0,378	0,612	0,099	0,073	0,072	1,000	0,040	0,108	0,331	0,242	0,150	0,104	0,099	0,070	0,060	0,044	0,062	0,043	0,20	0,14	0,58	1,19	0,087	0,070
2009003-16827	511101-28	80,77	0,082	0,256	0,558	0,653	0,102	0,080	0,066	1,000	0,035	0,111	0,343	0,241	0,149	0,107	0,109	0,078	0,076	0,049	0,069	0,046	0,24	0,13	0,59	1,20	0,091	0,066
2009003-16767	511101-164	82,14	0,074	0,216	0,177	0,570	0,110	0,075	0,074	1,000	0,041	0,101	0,324	0,235	0,151	0,108	0,106	0,074	0,071	0,048	0,074	0,045	0,25	0,16	0,58	1,17	0,096	0,069
2009003-16773	511101-170	89,22	0,068	0,302	0,104	0,654	0,084	0,053	0,064	1,000	0,037	0,114	0,353	0,245	0,154	0,111	0,103	0,074	0,067	0,044	0,059	0,037	0,18	0,11	0,59	1,17	0,077	0,073
2009003-16828	511101-32	92,74	0,062	0,344	0,114	0,660	0,090	0,064	0,067	1,000	0,040	0,128	0,376	0,266	0,167	0,115	0,109	0,077	0,073	0,051	0,062	0,044	0,15	0,12	0,59	1,15	0,079	0,081
2009003-16777	511101-174	93,02	0,071	0,354	0,274	0,686	0,087	0,067	0,068	1,000	0,038	0,121	0,379	0,264	0,165	0,115	0,106	0,076	0,072	0,047	0,062	0,042	0,17	0,11	0,59	1,15	0,078	0,075
2009003-16778	511101-175	97,42	0,081	0,405	0,074	0,758	0,040	0,050	0,051	1,000	0,015	0,113	0,339	0,244	0,186	0,129	0,098	0,071	0,055	0,034	0,039	0,026	0,17	0,05	0,58	1,03	0,053	0,081
2009003-16779	511101-176	98,48	0,099	0,449	0,403	0,727	0,065	0,042	0,046	1,000	0,024	0,130	0,416	0,307	0,221	0,167	0,096	0,074	0,059	0,043	0,045	0,030	0,18	0,08	0,58	0,93	0,052	0,095
2009003-16780	511101-177	103,98	n.a.	n.a.	n.a.	n.a.	n.a.	n.a.	n.a.	n.a.	n.a.	n.a.	n.a.	n.a.	n.a.	n.a.	n.a.	n.a.	n.a.	n.a.	n.a.	n.a.	n.a.	n.a.	n.a.	n.a.	n.a.	n.a.
2009003-16829	511101-36	104,79	0,057	0,328	0,085	0,704	0,033	0,028	0,035	1,000	0,013	0,128	0,329	0,231	0,168	0,115	0,082	0,063	0,050	0,033	0,031	0,021	0,15	0,05	0,59	1,01	0,046	0,089
2009003-16781	511101-178	105,72	0,054	0,316	0,211	0,655	0,064	0,029	0,035	1,000	0,023	0,110	0,302	0,220	0,131	0,093	0,076	0,053	0,053	0,037	0,043	0,029	0,15	0,09	0,58	1,09	0,069	0,079
2009003-16782	511101-179	106,59	0,066	0,353	0,378	0,694	0,075	0,041	0,053	1,000	0,032	0,107	0,335	0,233	0,144	0,101	0,092	0,062	0,062	0,041	0,049	0,035	0,16	0,10	0,59	1,13	0,072	0,088
2009003-16795	511101-186	117,73	0,075	0,385	0,770	0,685	0,100	0,068	0,070	1,000	0,039	0,113	0,363	0,258	0,179	0,116	0,111	0,083	0,076	0,053	0,071	0,048	0,16	0,13	0,58	1,12	0,088	0,073
2009003-16804	511101-195	142,84	0,053	0,468	0,400	0,721	0,070	0,064	0,085	1,000	0,040	0,118	0,470	0,327	0,208	0,146	0,112	0,079	0,085	0,057	0,056	0,039	0,10	0,09	0,59	1,03	0,060	0,086
2009003-16812	511101-203	160,80	0,049	0,348	0,952	0,633	0,058	0,032	0,063	1,000	0,032	0,087	0,412	0,285	0,182	0,127	0,091	0,067	0,065	0,043	0,040	0,026	0,12	0,08	0,59	1,03	0,049	0,087
2009003-16835	511101-60	176,77	0,065	0,298	0,432	0,608	0,094	0,047	0,080	1,000	0,046	0,090	0,393	0,277	0,192	0,130	0,099	0,067	0,065	0,044	0,038	0,027	0,18	0,13	0,59	1,00	0,049	0,083
2009003-16850	511101-220	205,84	0,064	0,253	0,095	0,548	0,069	0,040	0,073	1,000	0,032	0,082	0,366	0,263	0,177	0,128	0,084	0,063	0,059	0,040	0,030	0,022	0,20	0,11	0,58	0,97	0,042	0,107
2009003-16858	511101-228	232,05	0,059	0,356	0,013	0,674	0,064	0,046	0,099	1,000	0,033	0,101	0,440	0,333	0,193	0,140	0,076	0,057	0,046	0,031	0,020	0,012	0,14	0,09	0,57	0,98	0,024	0,121
2009003-16764	511101 oil	105,18	0,044	0,267	0,124	0,634	0,023	0,024	0,028	1,000	0,011	0,125	0,324	0,240	0,169	0,120	0,093	0,070	0,063	0,046	0,056	0,037	0,14	0,04	0,57	1,03	0,076	0,077
2008																												

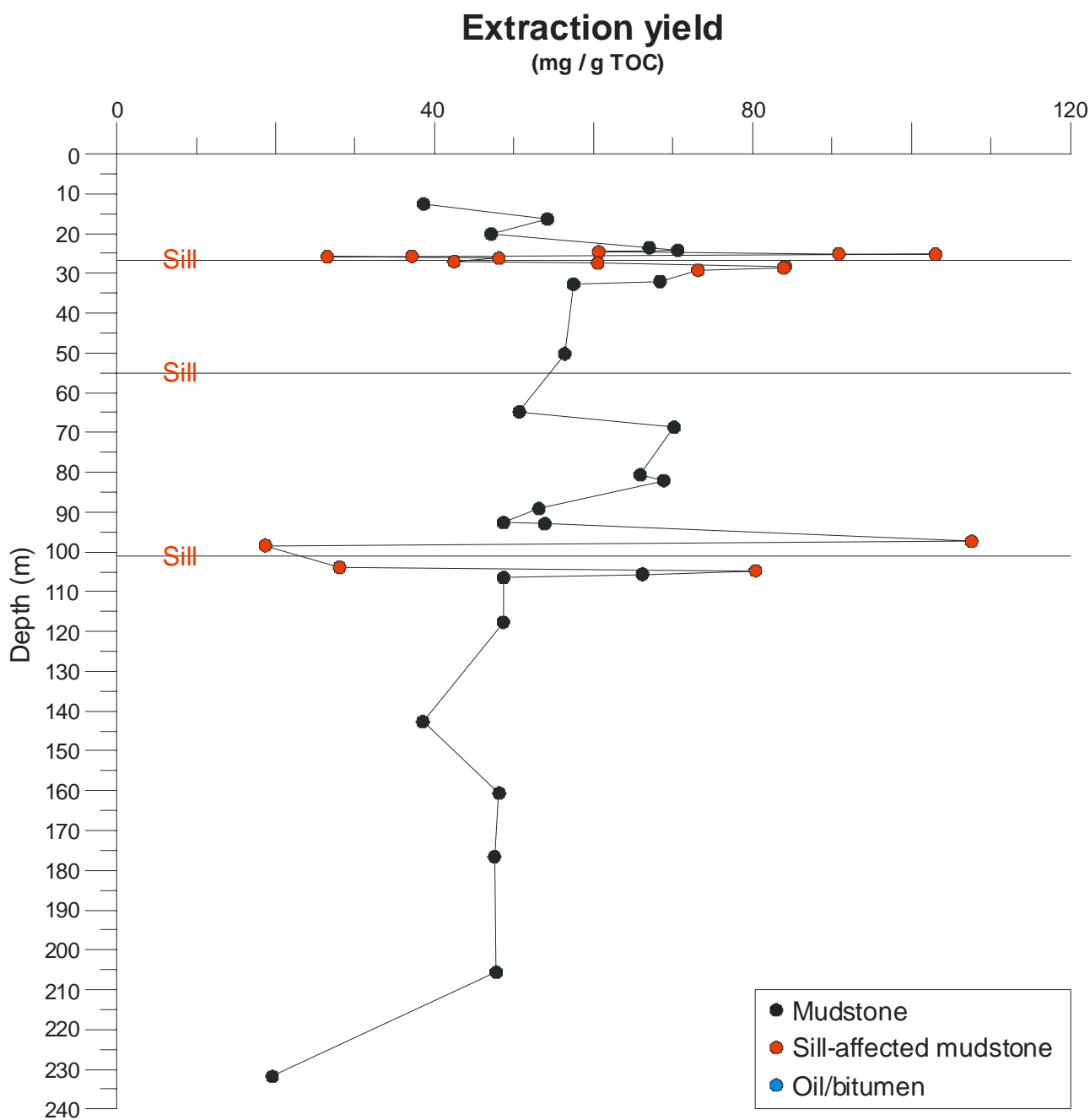


Fig. 7.2.1. Variation in extract yield through the Blokely-1 well. Towards the sills the mudstones are increasingly matured and like PI, the extract yield increases due to HC generation. Closest to the sills the extract yield declines, probably caused by cracking of high molecular compounds and volatilization of the liquid hydrocarbons.

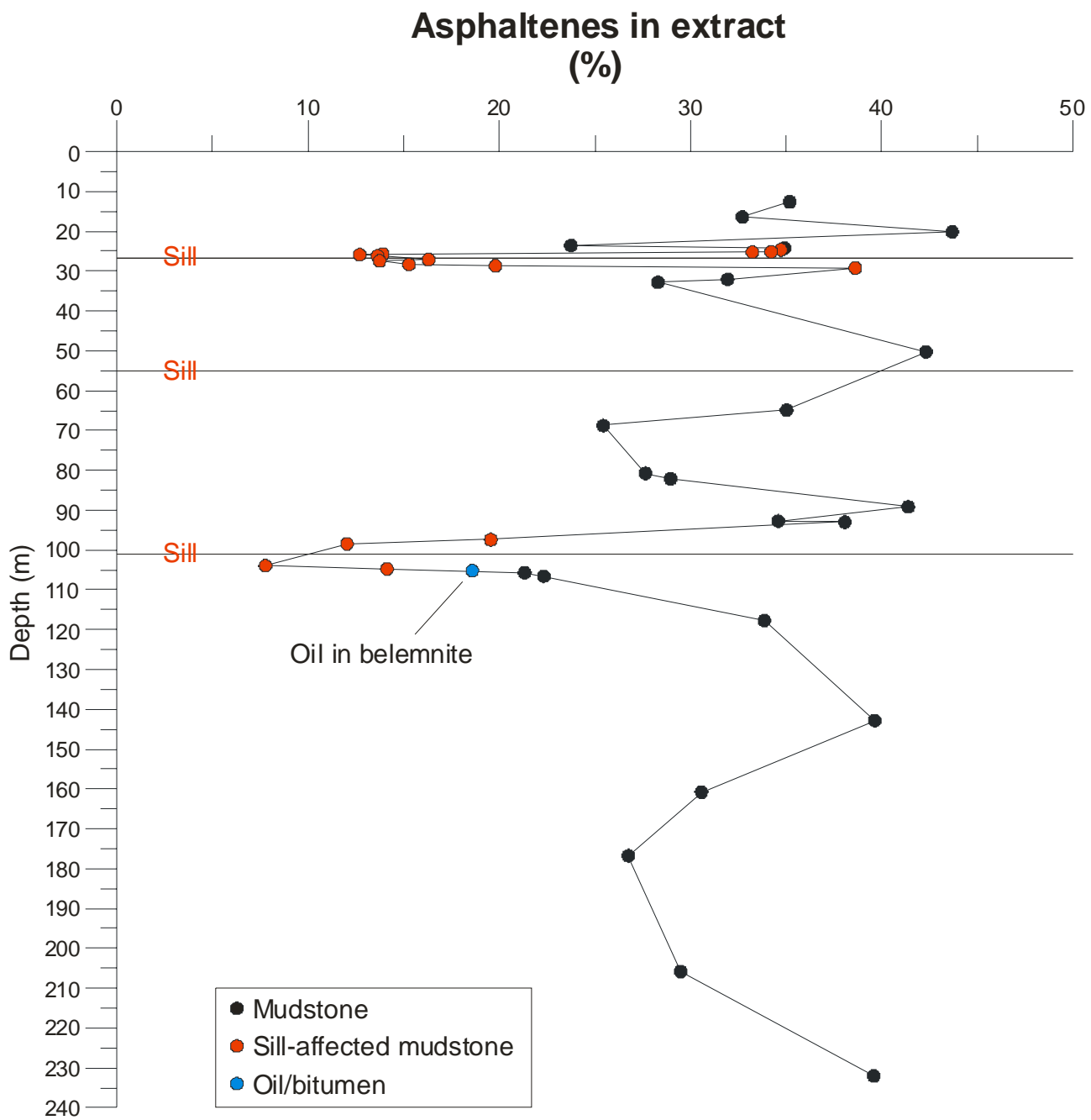


Fig. 7.2.2. Asphaltene-content in extracts through the Blokely-1 well.

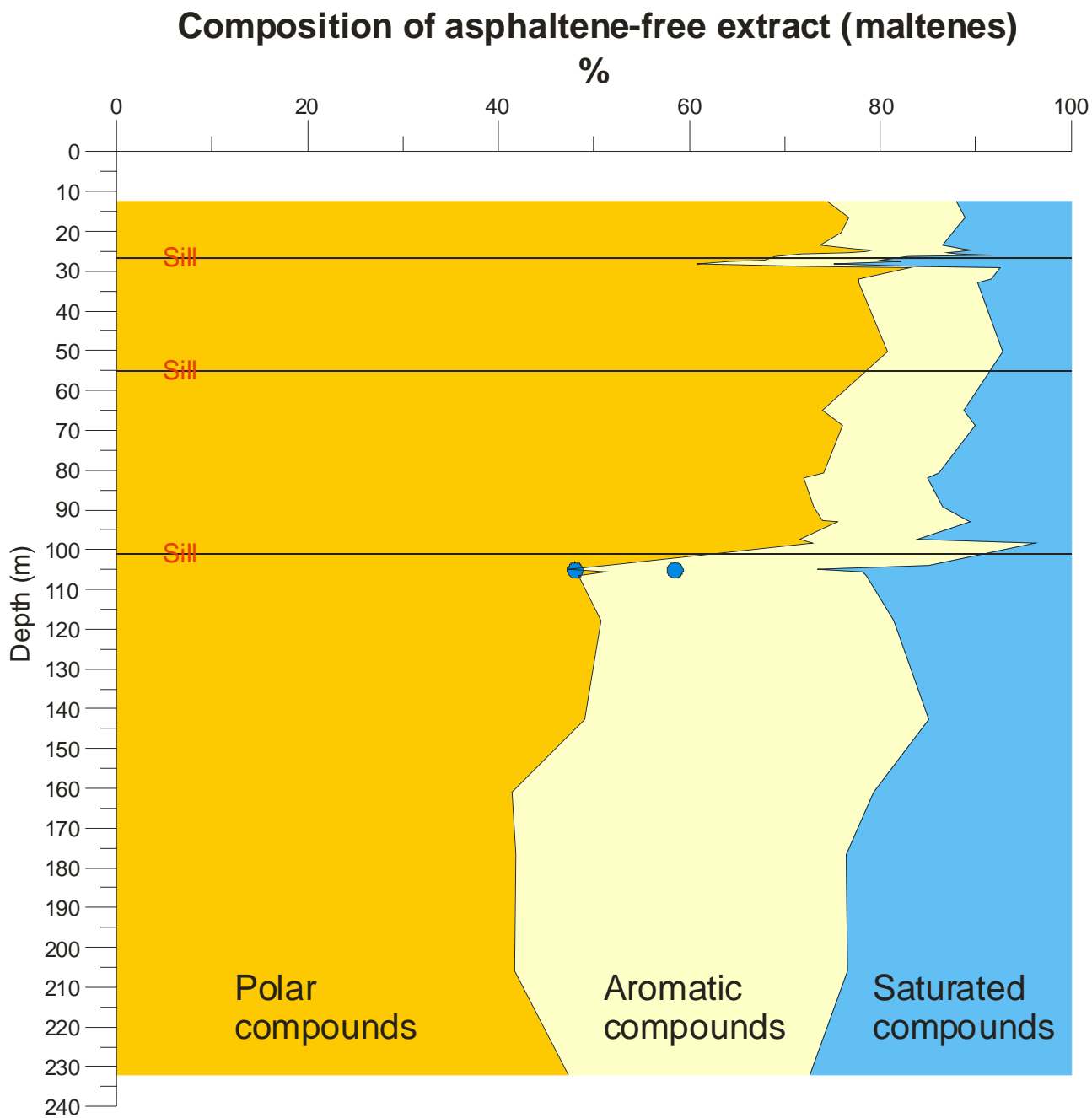


Fig. 7.2.3. Composition of asphaltene-free extract (maltenes) in extracts through the Blokely-1 well. The relative content of saturated- and aromatic hydrocarbons increases with maturity (depth) and near the sills.

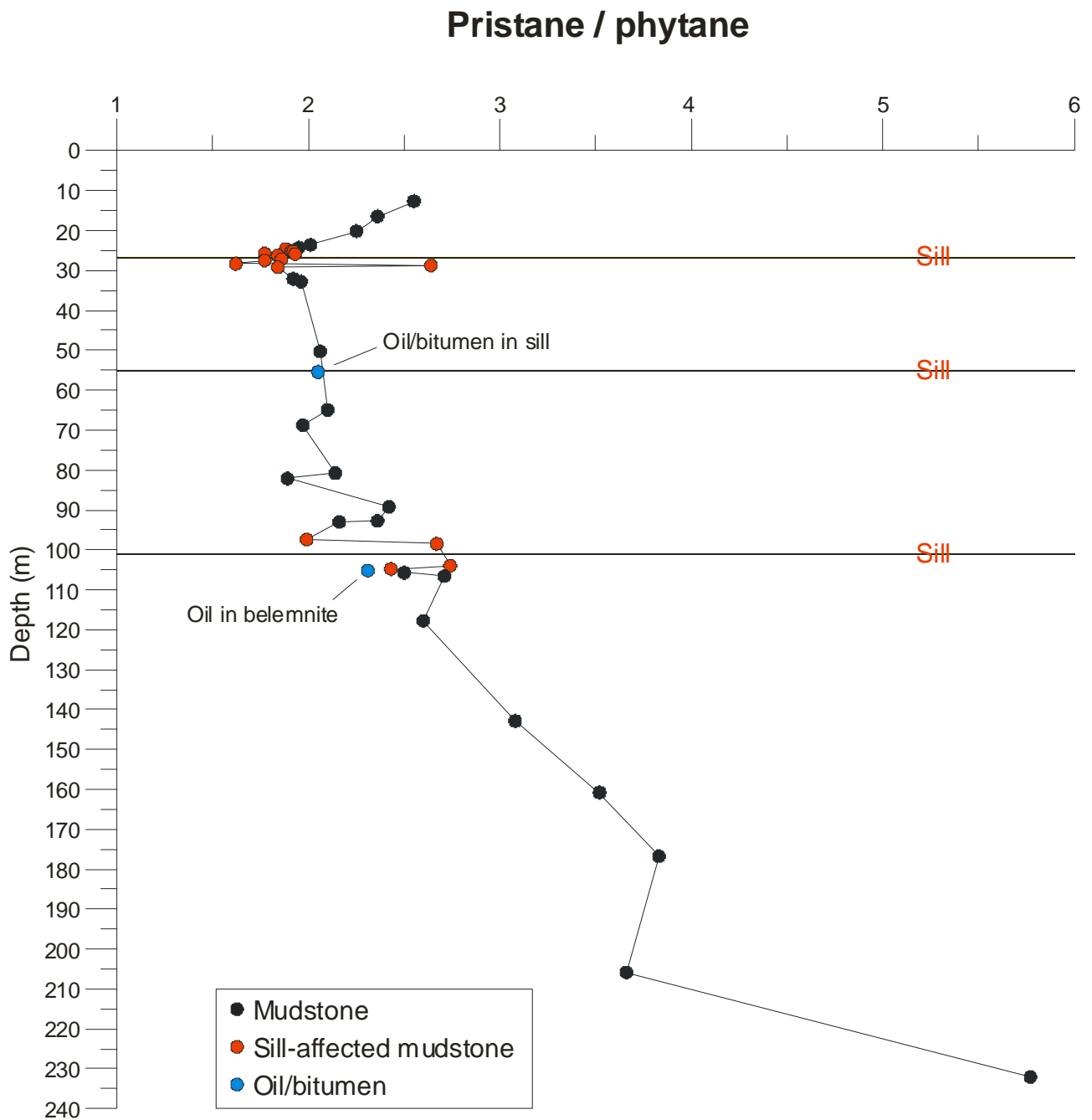


Fig. 7.2.4. Pristane/phytane ratios (Pr/Ph) measured using gas chromatography. Below 120 m the increasing Pr/Ph indicates a more terrigenous organic matter input under oxic conditions.

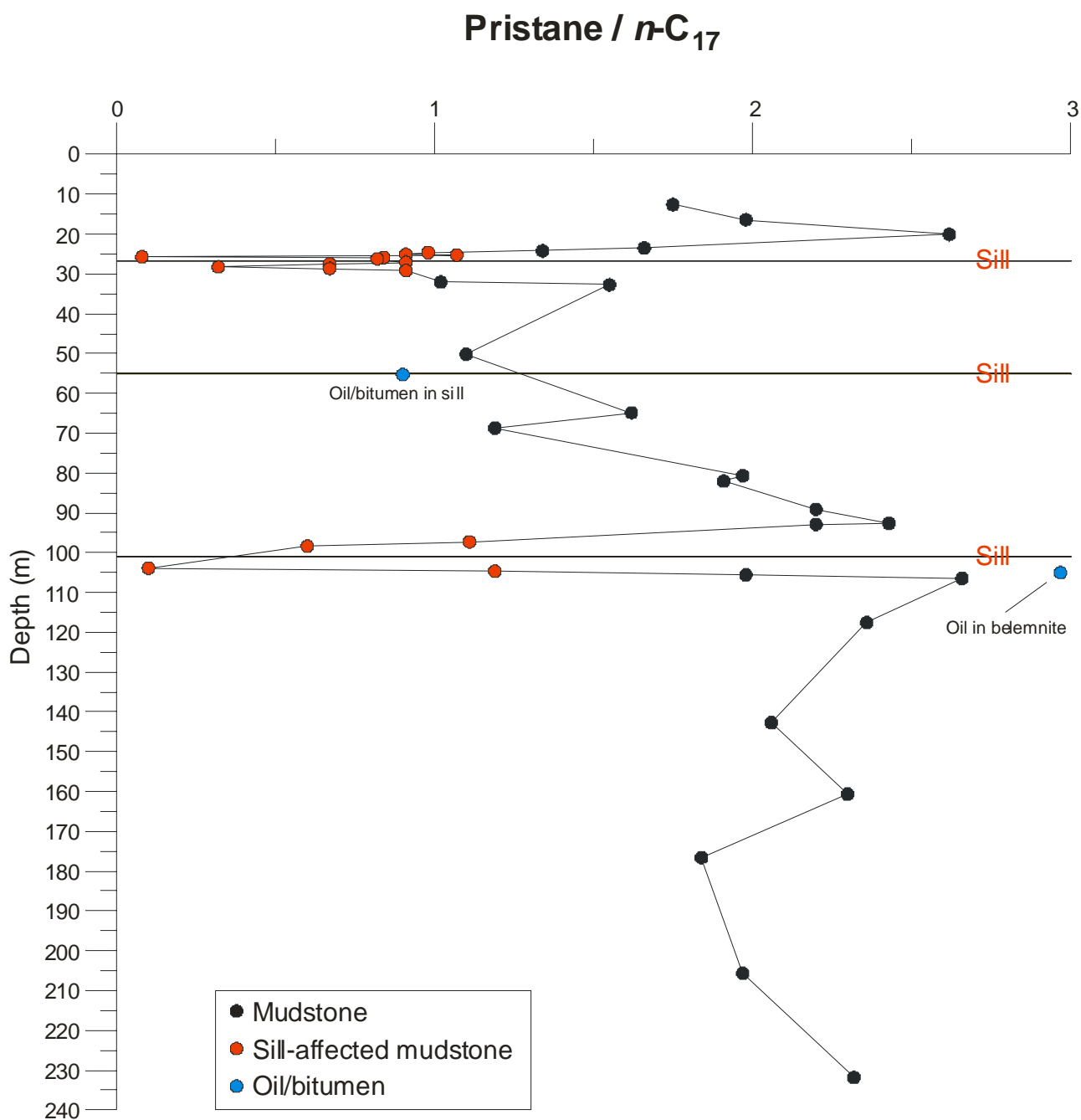


Fig. 7.2.5. Pristane/ $n\text{-C}_{17}$ ratios decrease close to the sills due to preferential generation of n -alkanes and/or lower thermal stability of pristane at high maturities.

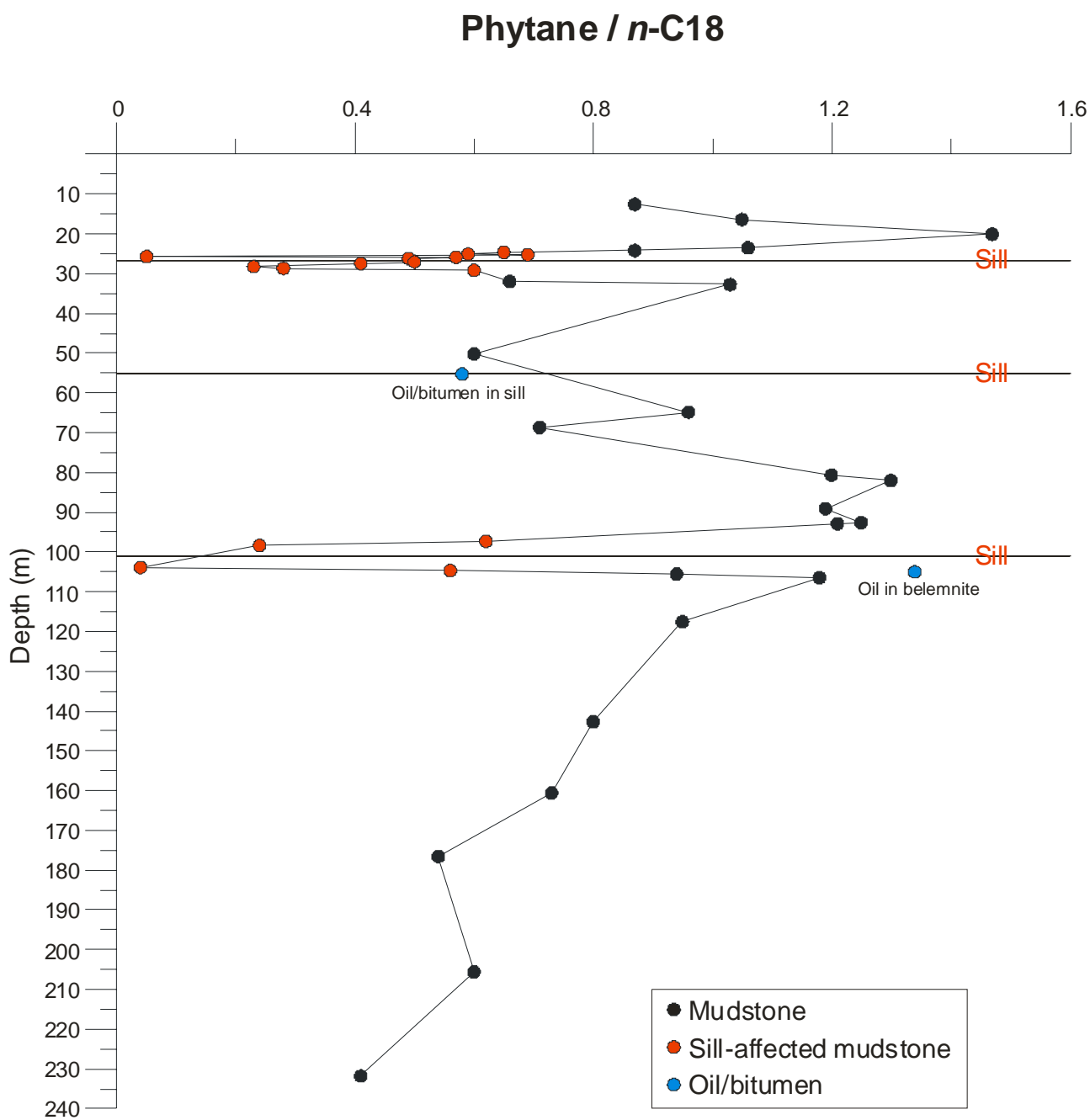


Fig. 7.2.6. Phytane/*n*-C₁₈ ratios decrease close to the sills due to preferential generation of *n*-alkanes and/or lower thermal stability of phytane at high maturities.

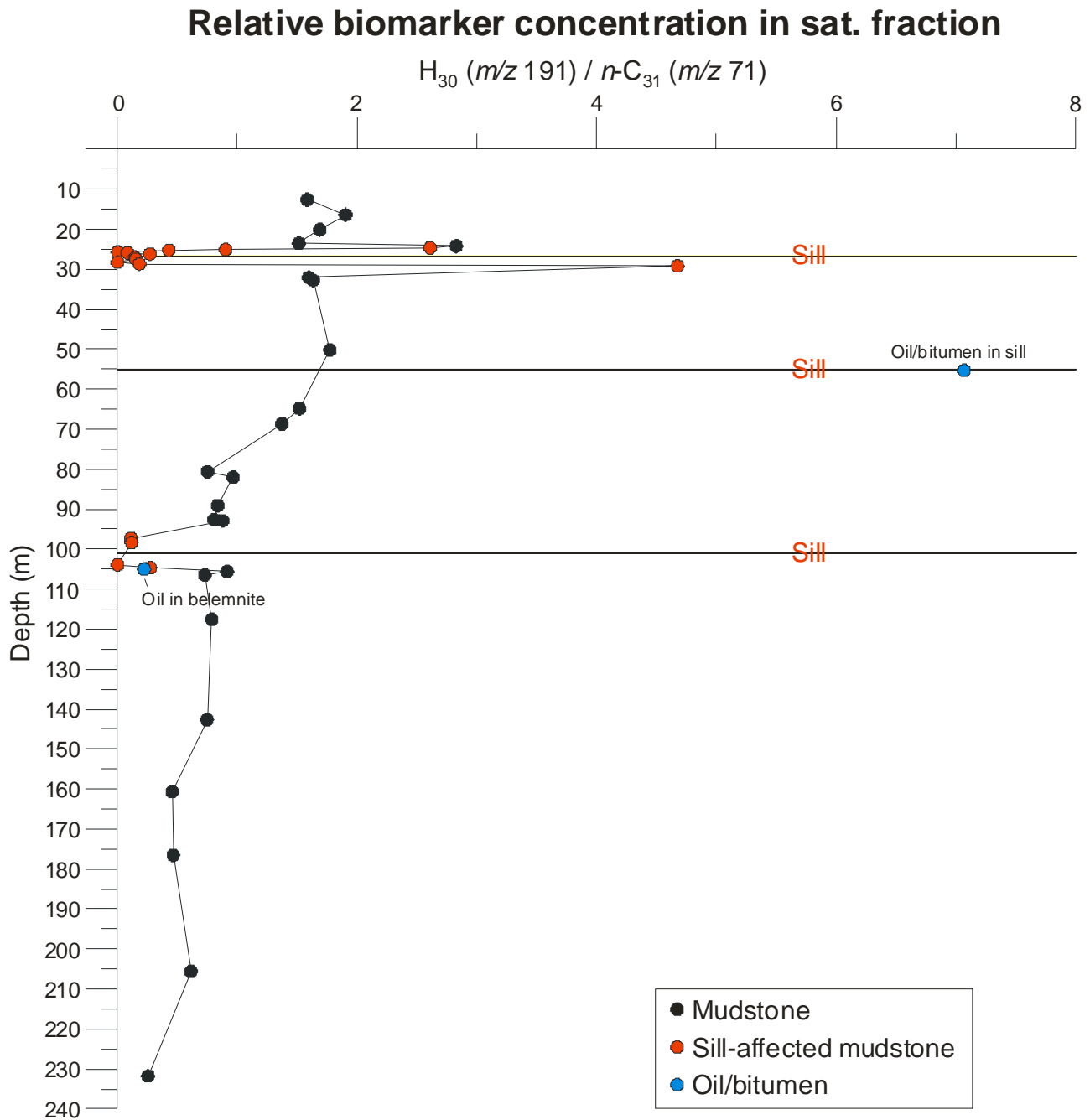


Fig. 7.2.7. The relative concentration of the various cyclic biomarkers (hopanes and steranes) decreases with maturity (depth) and near the sills due to preferential generation of *n*-alkanes and cracking of the less stable hopanes and steranes. Three samples from sill-affected parts of the mudstones were almost devoid of hopanes and steranes. Shown here: peak area of $17\alpha,21\beta(H)$ -hopane (m/z 191) versus $n-C_{31}$ (m/z 71).

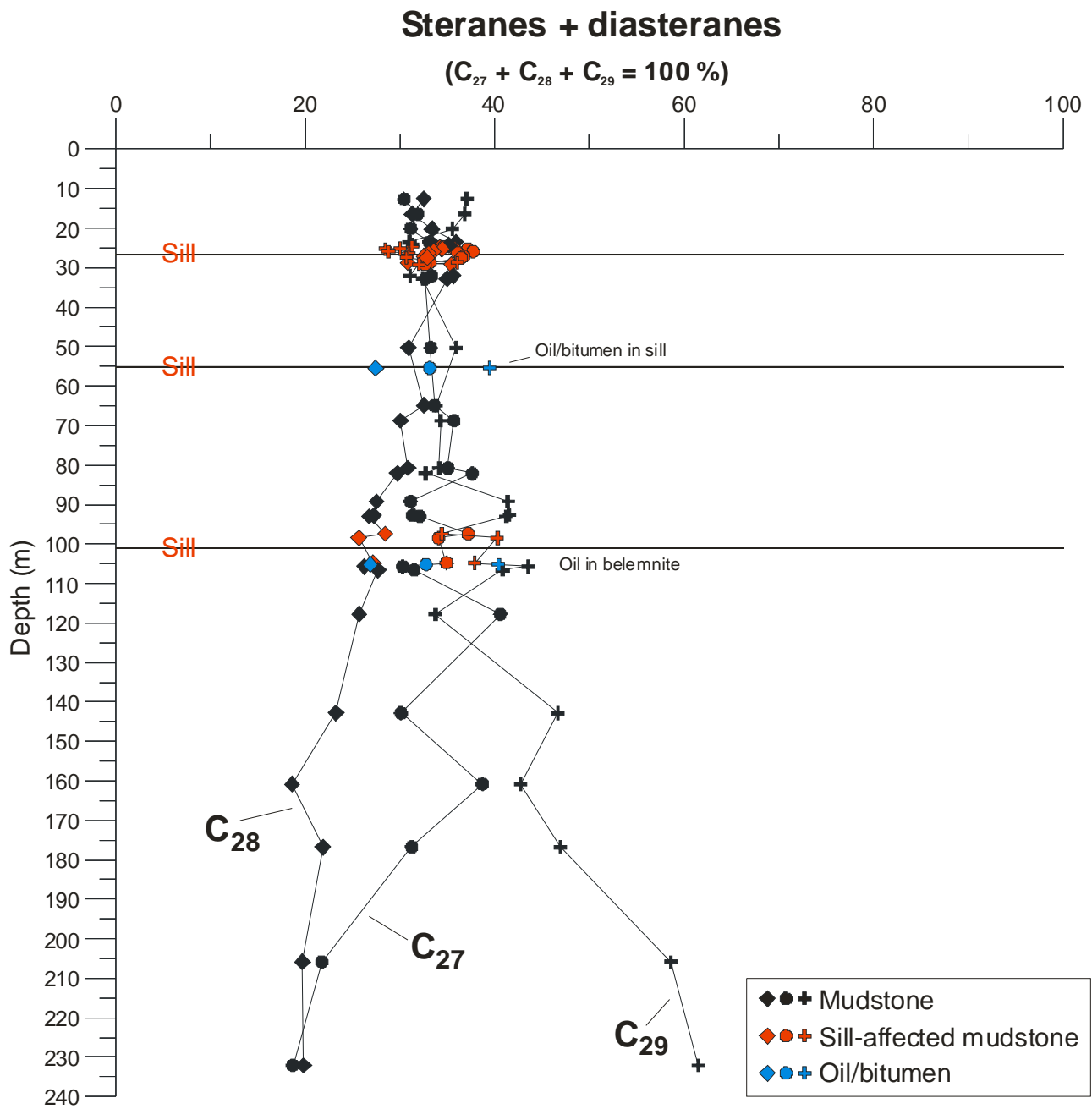


Fig. 7.2.8. Distribution of C_{27} , C_{28} and C_{29} diasteranes + steranes. The proportion of C_{29} steranes increases below 120 m indicating a more terrestrial-influenced kerogen.

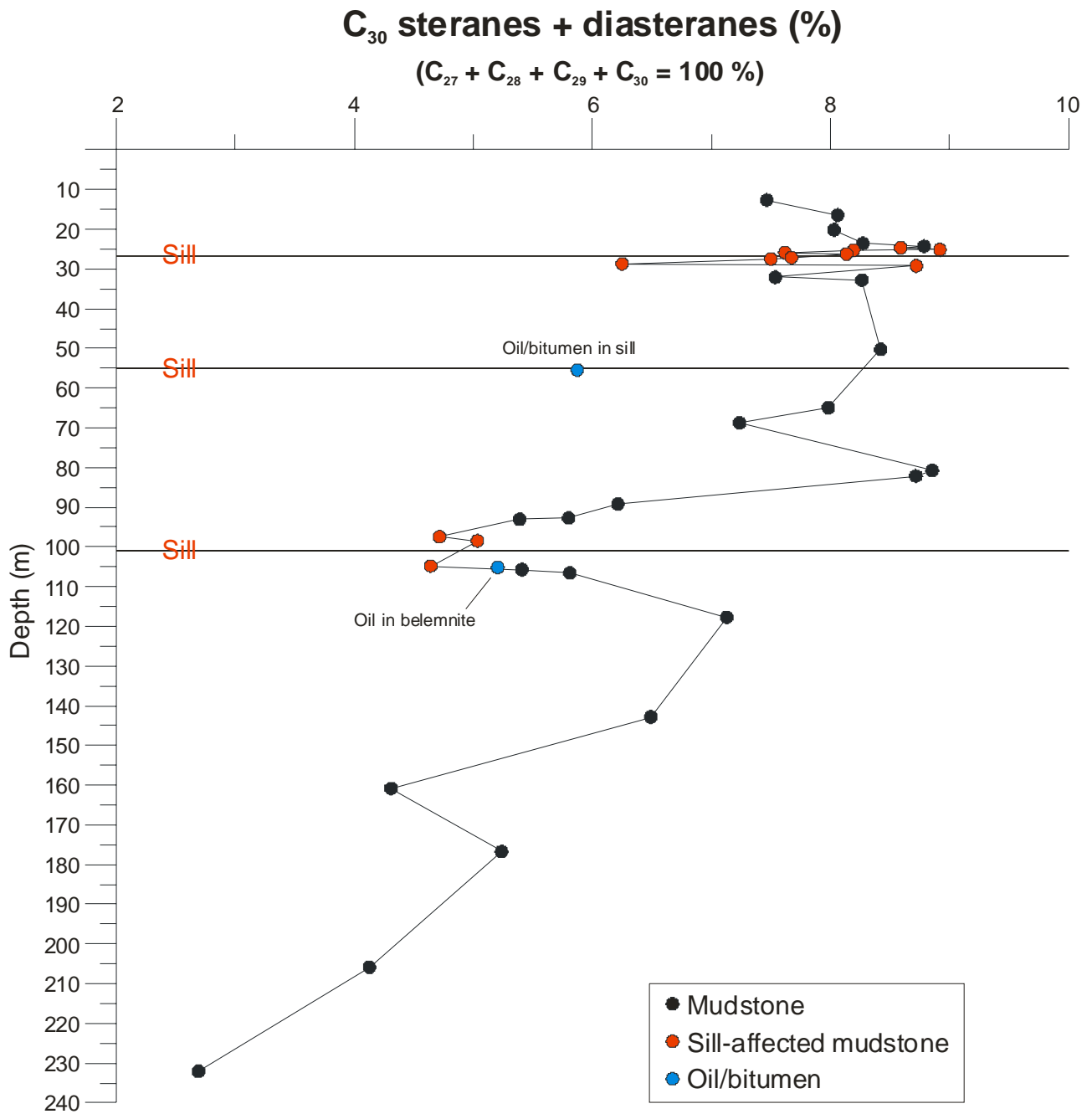


Fig. 7.2.9. The relative proportion of C₃₀ steranes decreases below ~100m = less marine input. C₃₀ steranes (24-*n*-propylcholestanes) is the most powerful means in order to identify input of marine organic matter to the source rock (Peters et al., 2005).

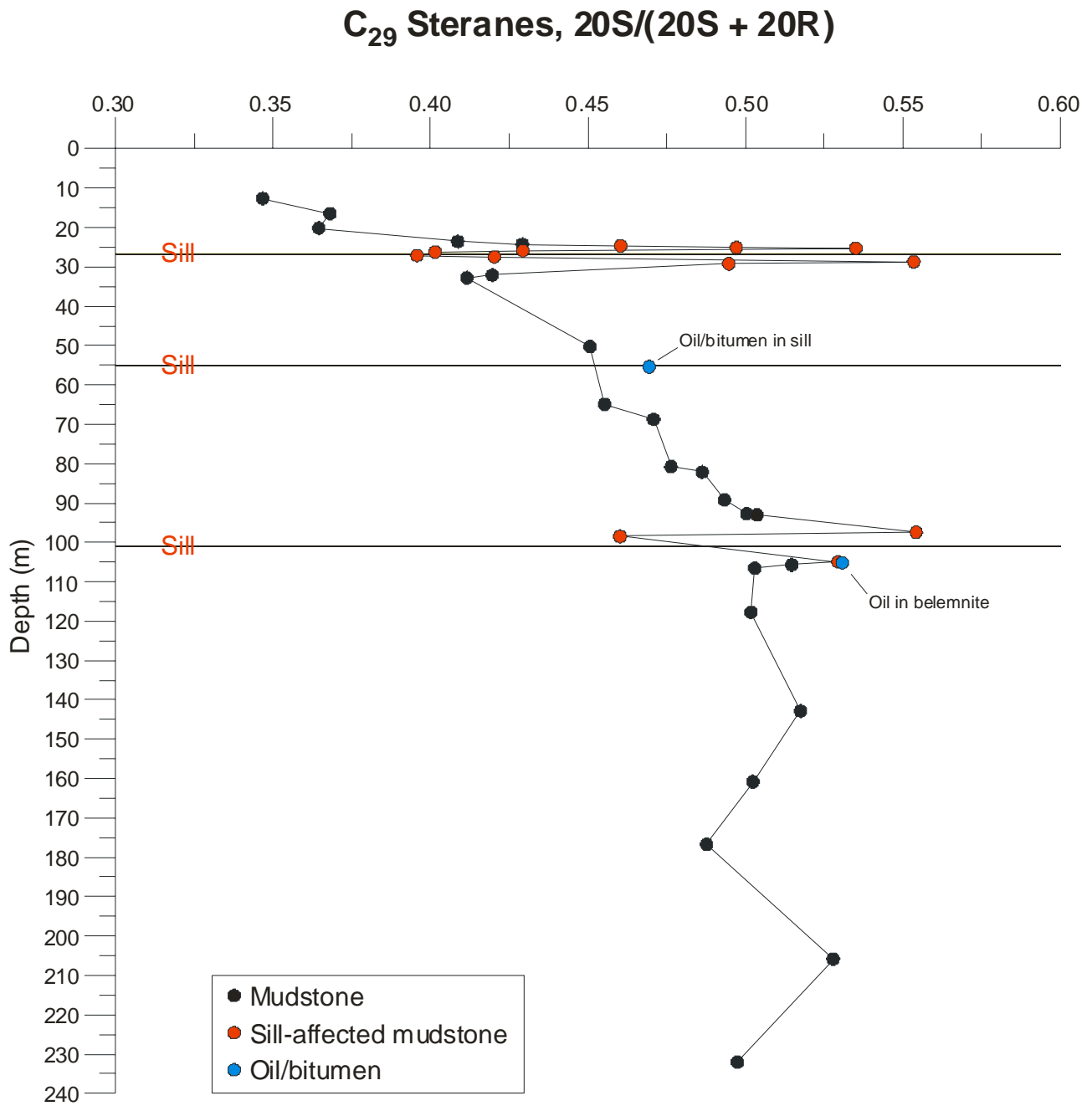


Fig. 7.2.10. 20S/(20S + 20R) ratio for C₂₉ steranes (400 → 217). The steranes are close to equilibrium (0.52-0.55) below 100m and near the sills. Some sill-affected samples with a low sterane concentration show low 20S/(20S + 20R) ratios.

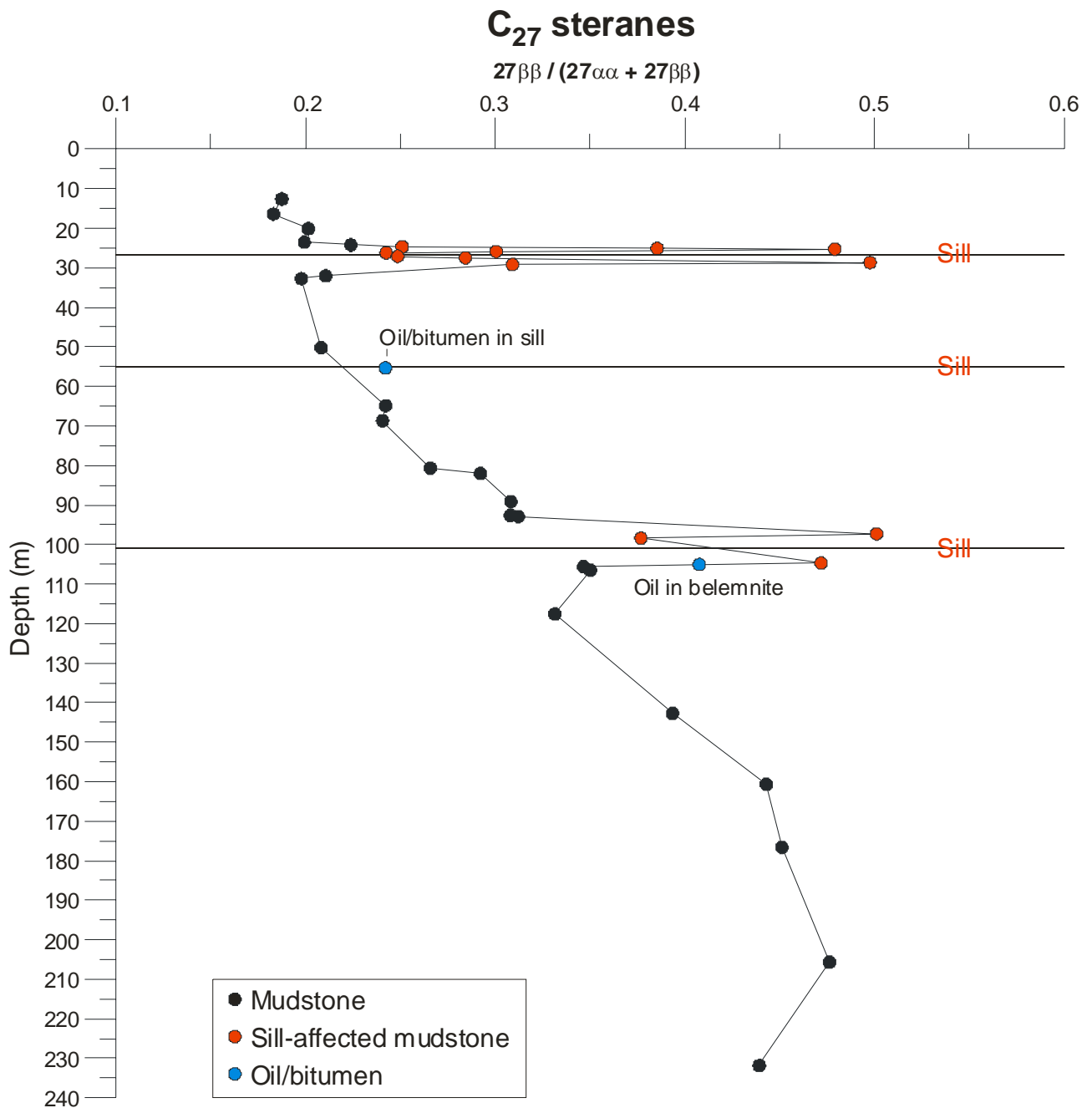


Fig. 7.2.11. Variation in the relative proportion of C₂₇ ββ steranes through the Blokely-1 well.

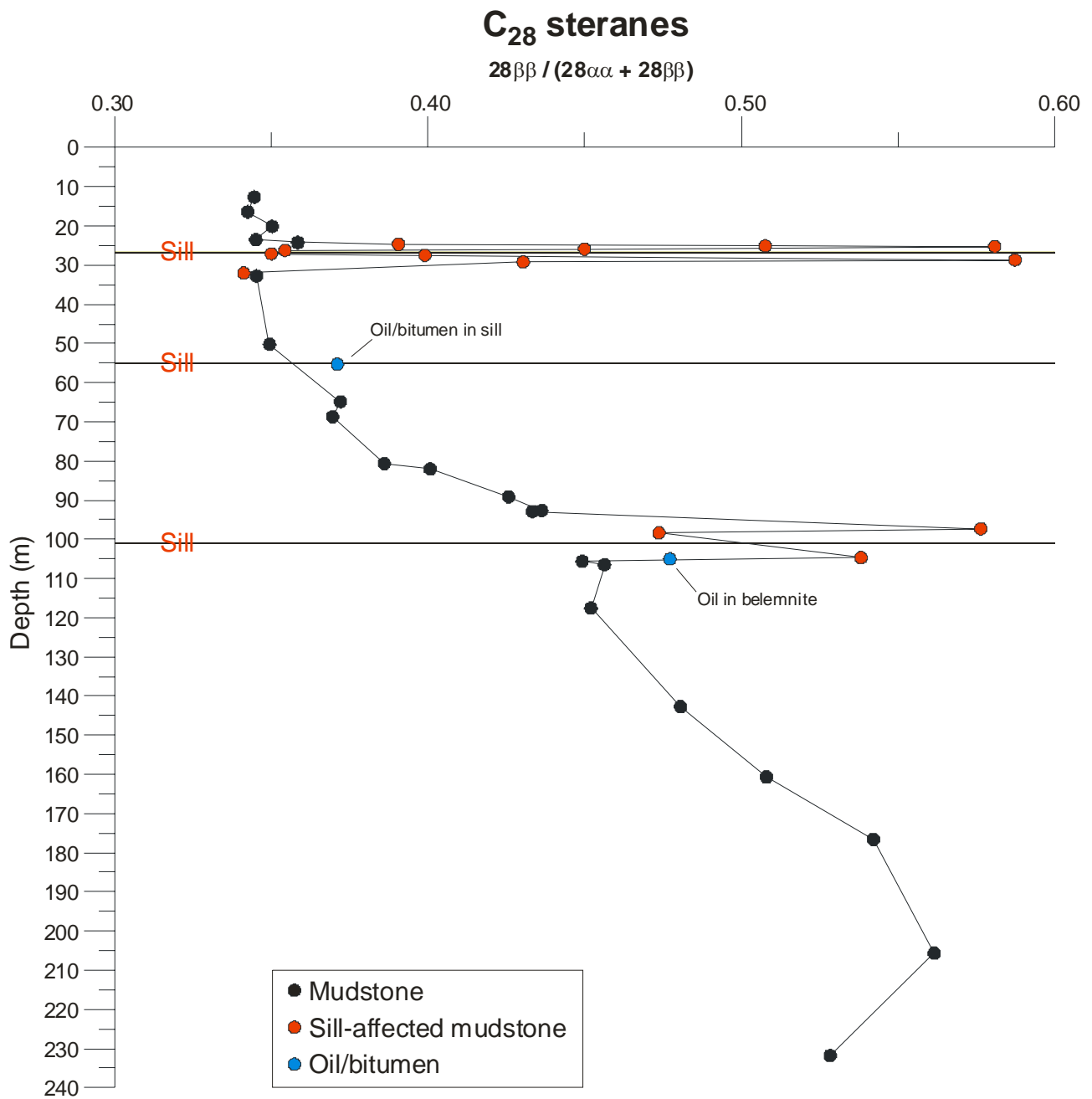


Fig. 7.2.12. Variation in the relative proportion of C₂₈ ββ steranes through the Blokely-1 well.

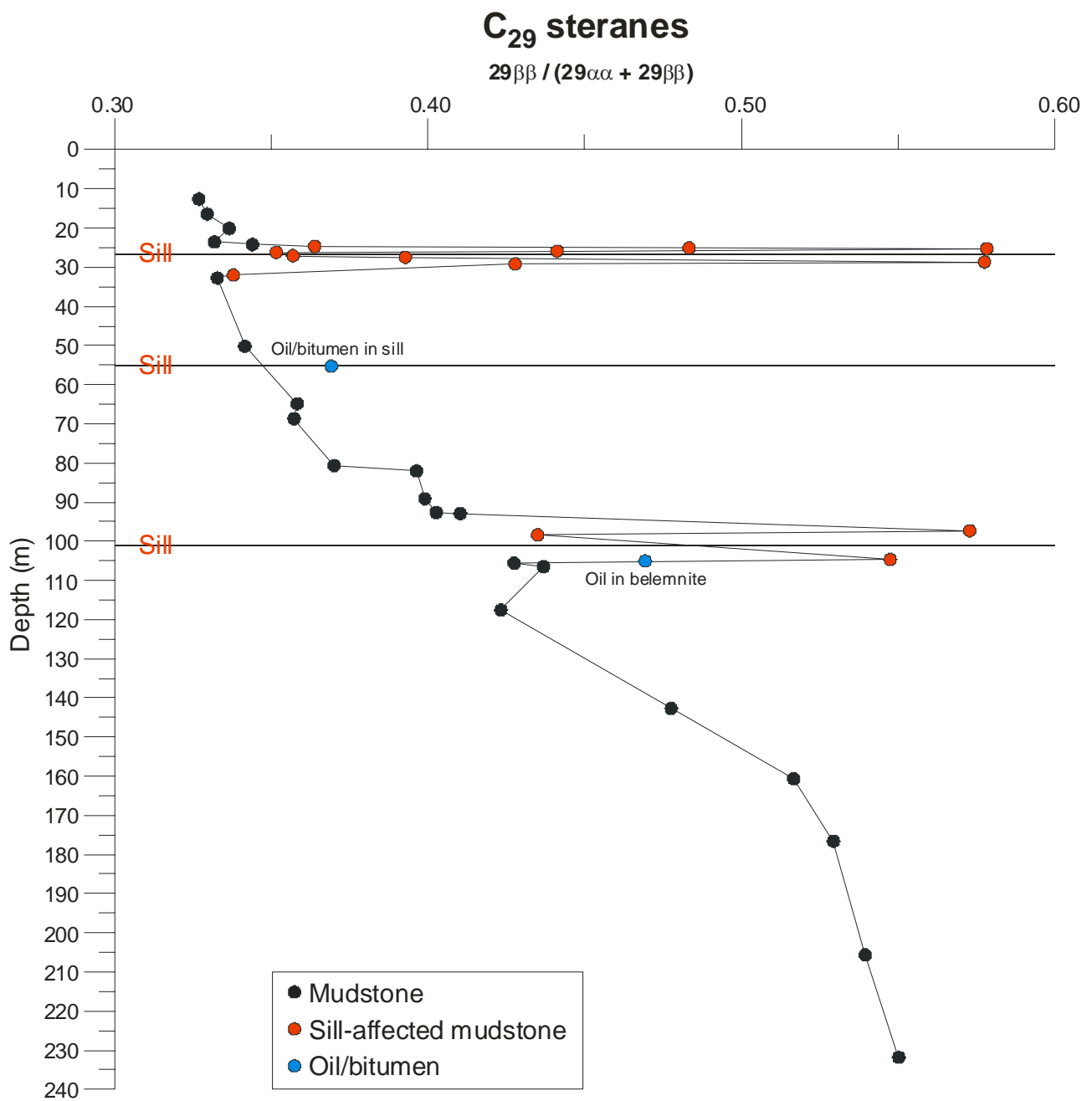


Fig. 7.2.13. Variation in the relative proportion of C₂₉ ββ steranes through the Blokely-1 well.

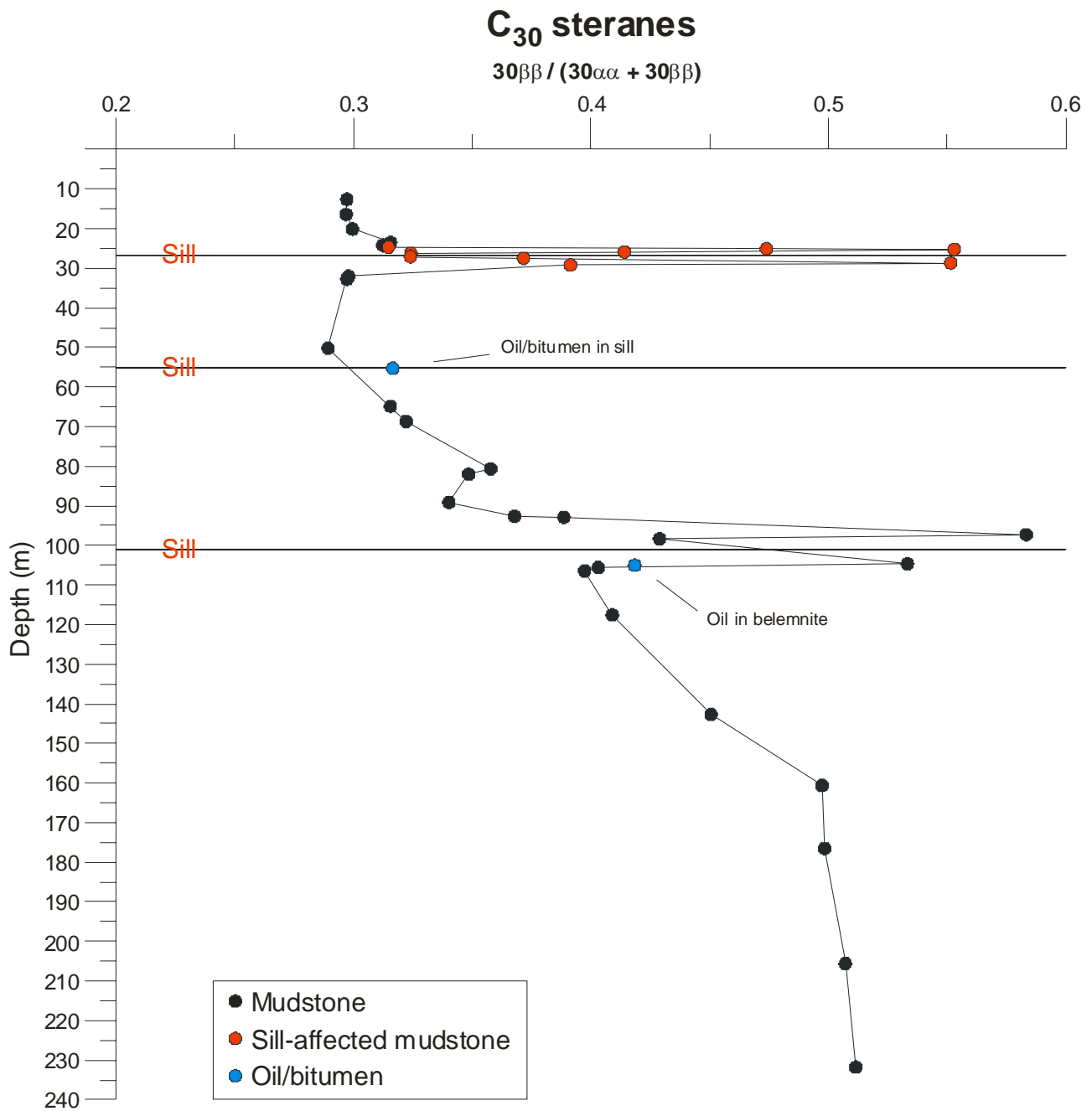


Fig. 7.2.14. Variation in the relative proportion of C₃₀ ββ steranes through the Blokely-1 well.

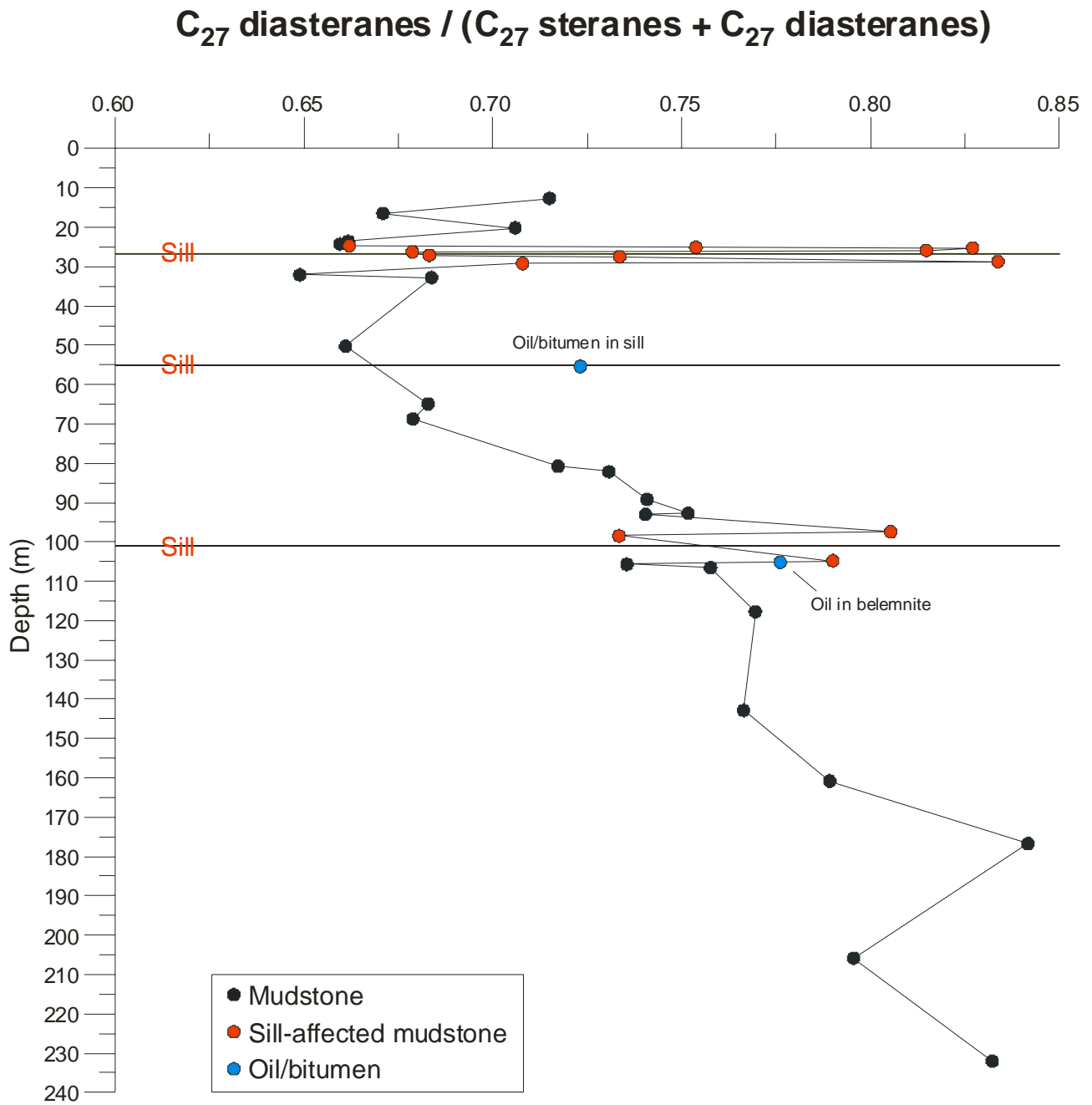


Fig. 7.2.15. Variation in the C_{27} diasteranes/(diasteranes + regular steranes) ratio through the Blokely-1 well. The relative proportion of C_{27} diasteranes is influenced by both thermal maturity and the depositional environment.

C_{28} diasteranes / (C_{28} steranes + C_{28} diasteranes)

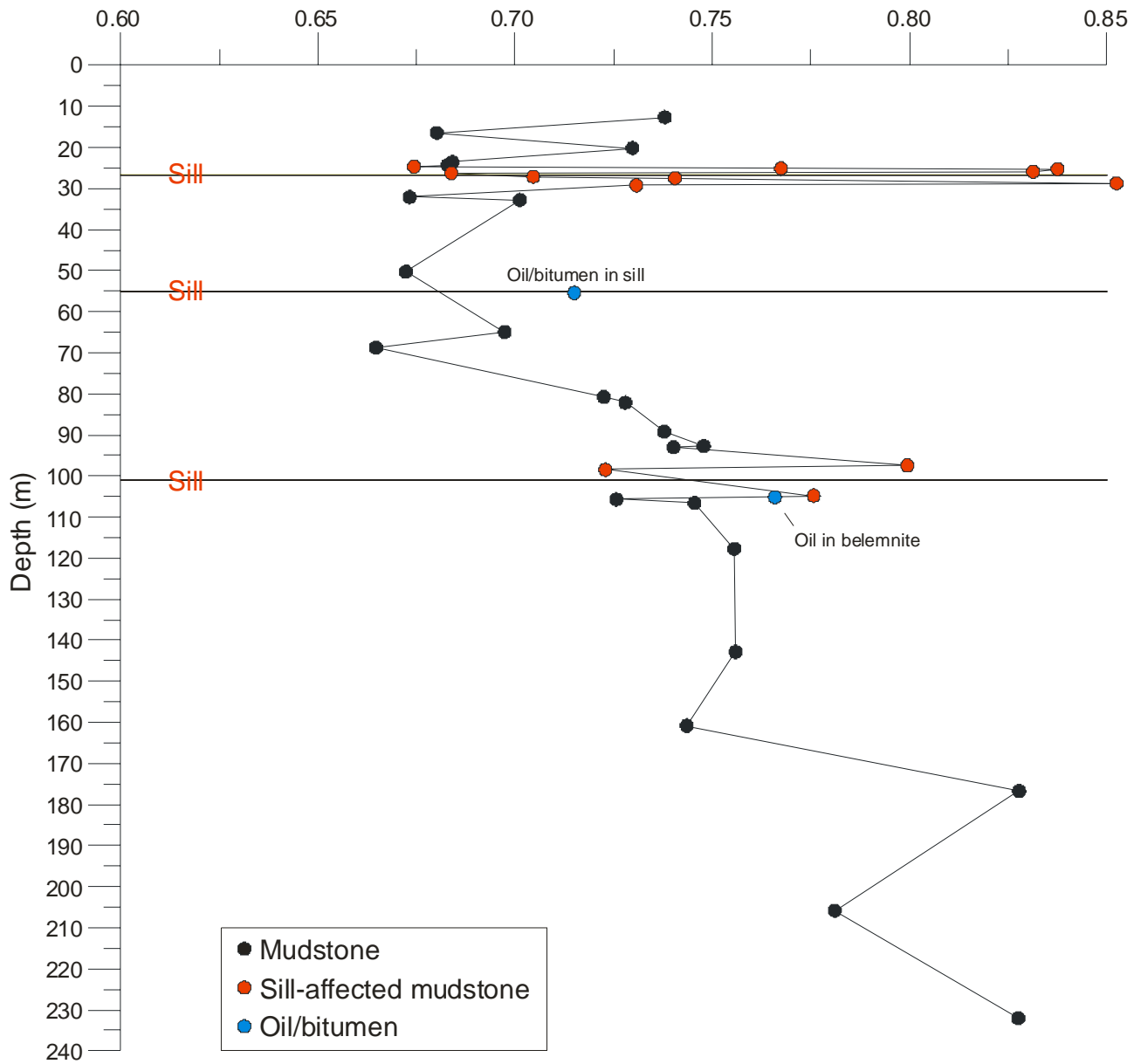


Fig. 7.2.16. Variation in the C_{28} diasteranes/(diasteranes + regular steranes) ratio through the Blokely-1 well. The relative proportion of C_{28} diasteranes is influenced by both thermal maturity and the depositional environment.

C_{29} diasteranes / (C_{29} steranes + C_{29} diasteranes)

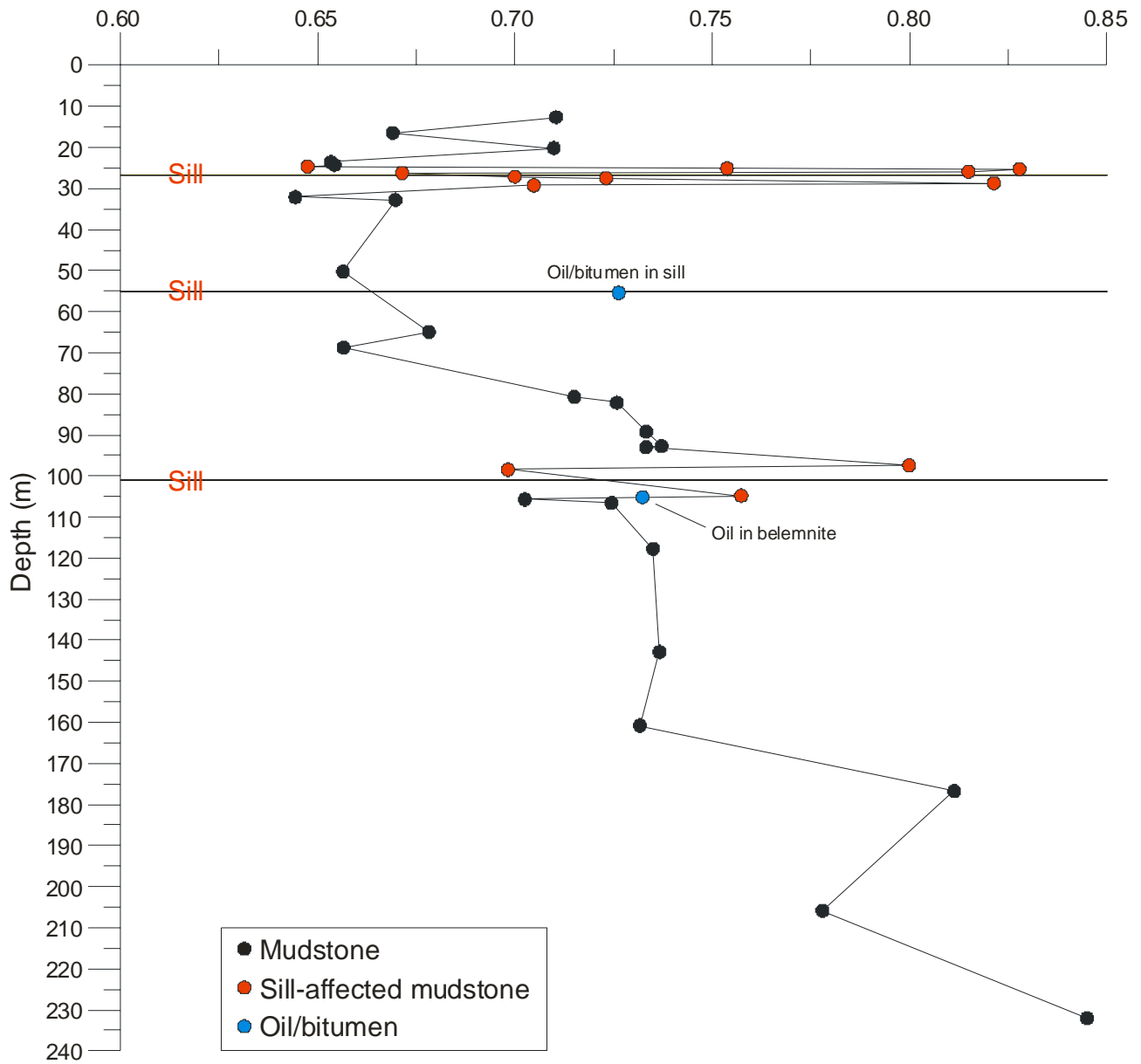


Fig. 7.2.17. Variation in the C_{29} diasteranes/(diasteranes + regular steranes) ratio through the Blokely-1 well. The relative proportion of C_{29} diasteranes is influenced by both thermal maturity and the depositional environment.

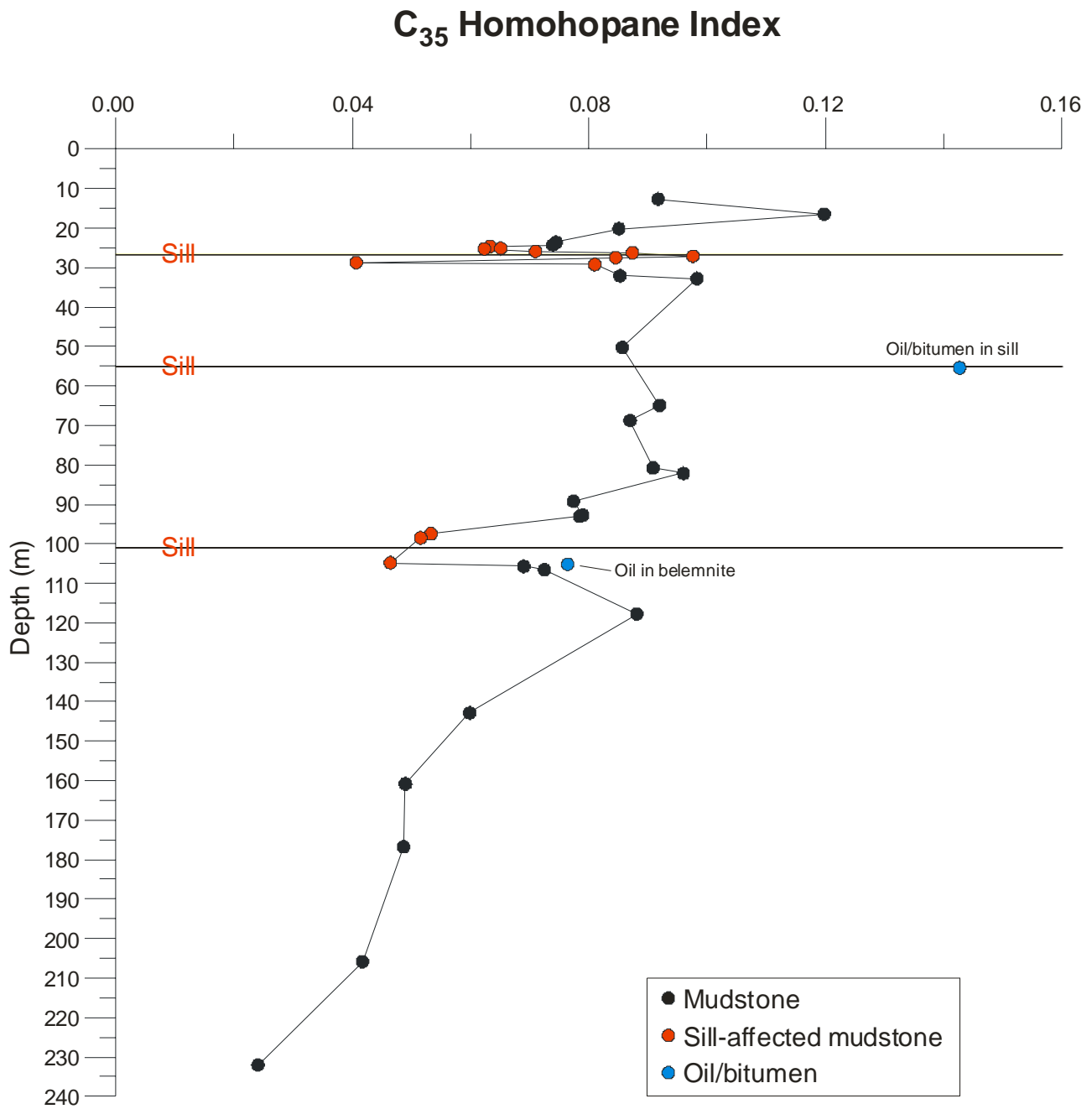


Fig. 7.2.18. Variation in the C₃₅ homohopane index = $C_{35}/(C_{31}-C_{35})$ through the Blokely-1 well. The C₃₅ homohopane index is an indicator of redox potential in marine sediments. High values indicate anoxia, but also affected by thermal maturity (Peters et al., 2005).

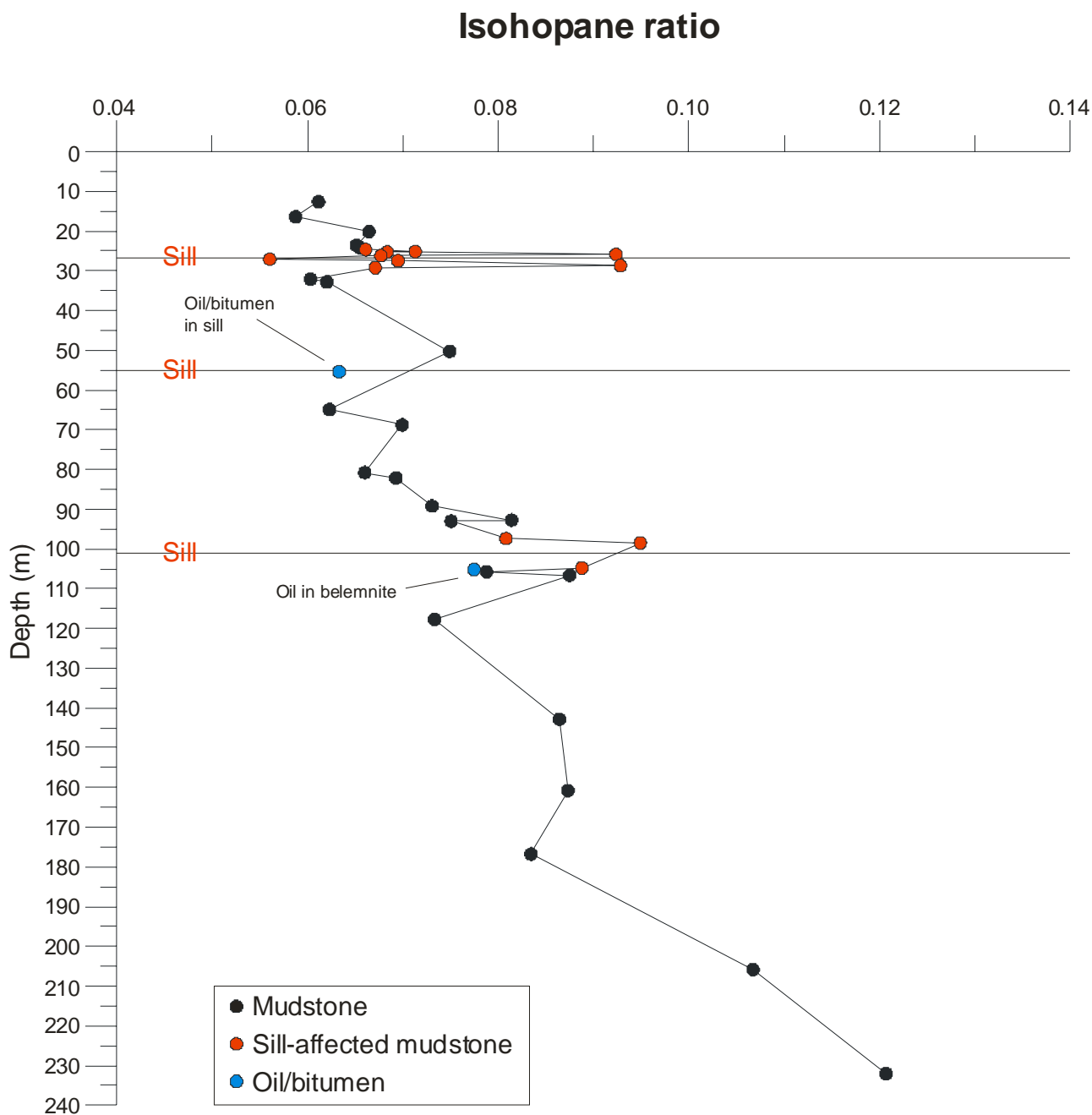


Fig. 7.2.19. Variation in the $C_{33} + C_{34}$ isohopane ratio through the Blokely-1 well. Isohopanes are extended hopanes having a side chain with an additional methyl branch (C_{33} and higher, Nytoft 2007, 2009). Their relative abundance is low in oils sourced from marine organic matter deposited under anoxic condition and high in oils having a coaly source.

28,30-Bisnorhopane / $17\alpha,21\beta$ (H)-hopane

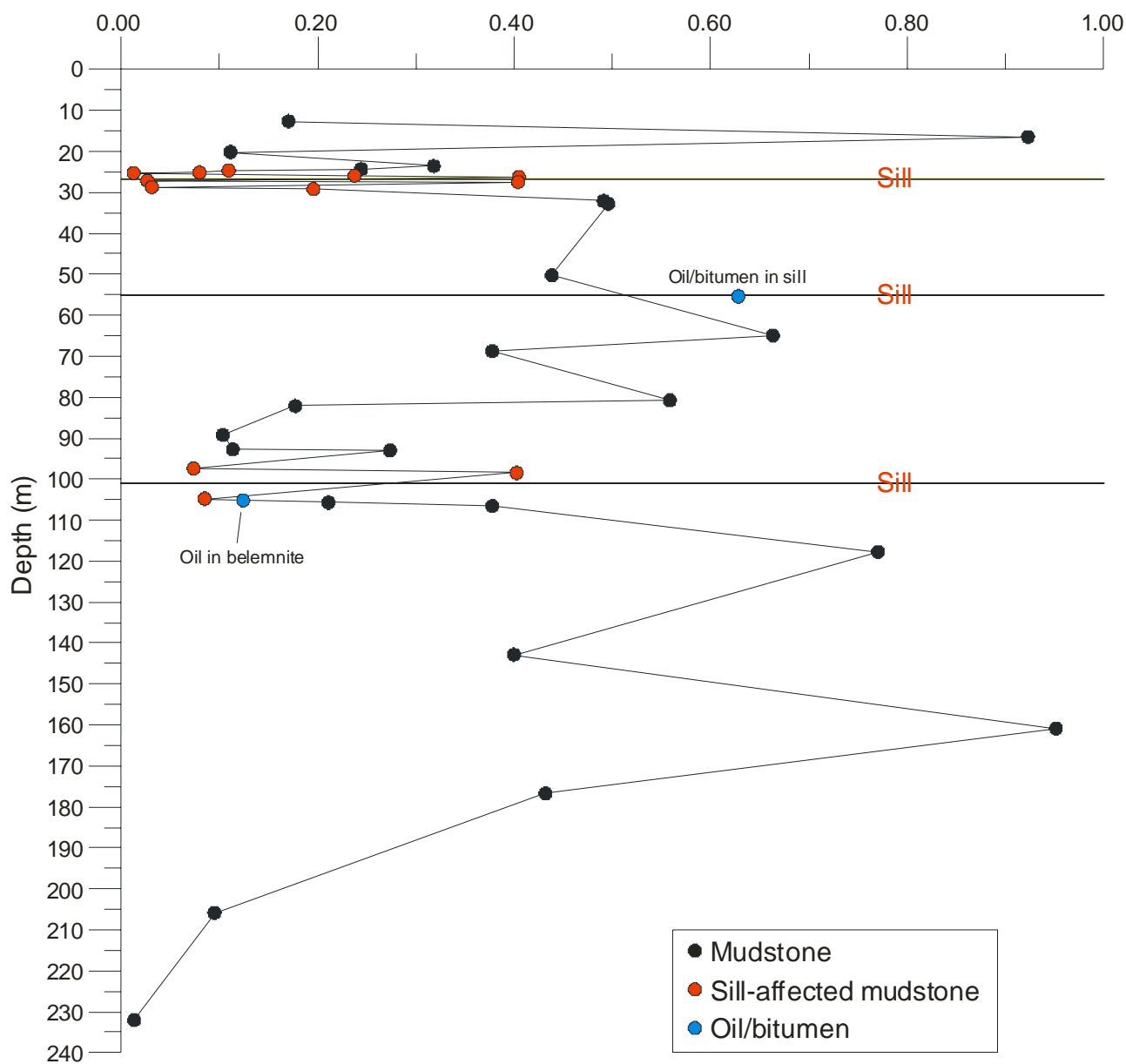


Fig. 7.2.20. Variation in the 28,30-bisnorhopane/ $17\alpha,21\beta$ (H)-hopane ratio (BNH/H30) through the Blokely-1 well.

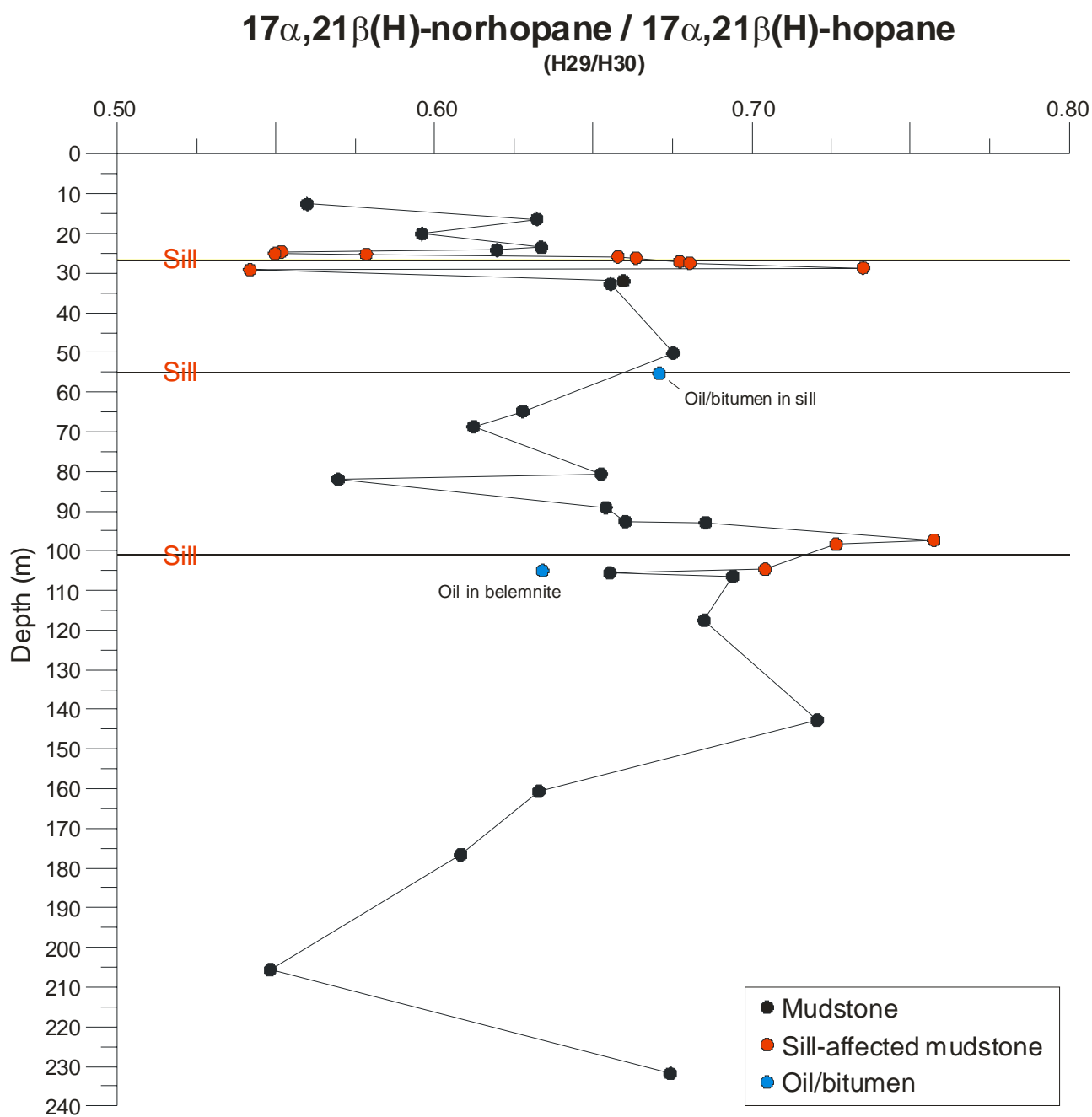


Fig. 7.2.21. Variation in the $17\alpha,21\beta(\text{H})$ -norhopane/ $17\alpha,21\beta(\text{H})$ -hopane ratio through the Blokely-1 well.

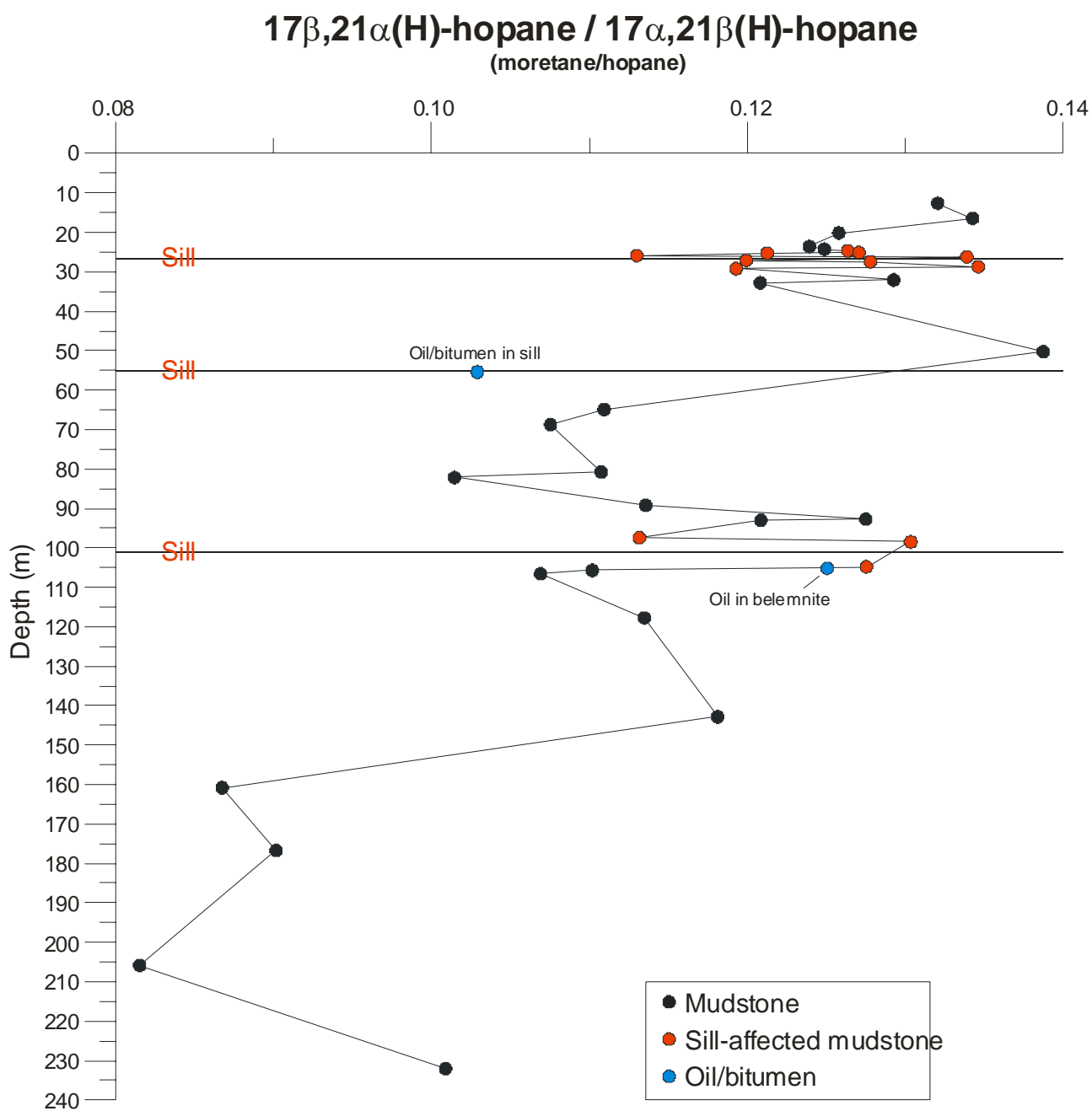


Fig. 7.2.22. Variation in the $17\beta,21\alpha(\text{H})\text{-hopane}/17\alpha,21\beta(\text{H})\text{-hopane}$ ratio through the Blokely-1 well.

Ts/(Ts + Tm) and 29Ts/(29Ts + H29)

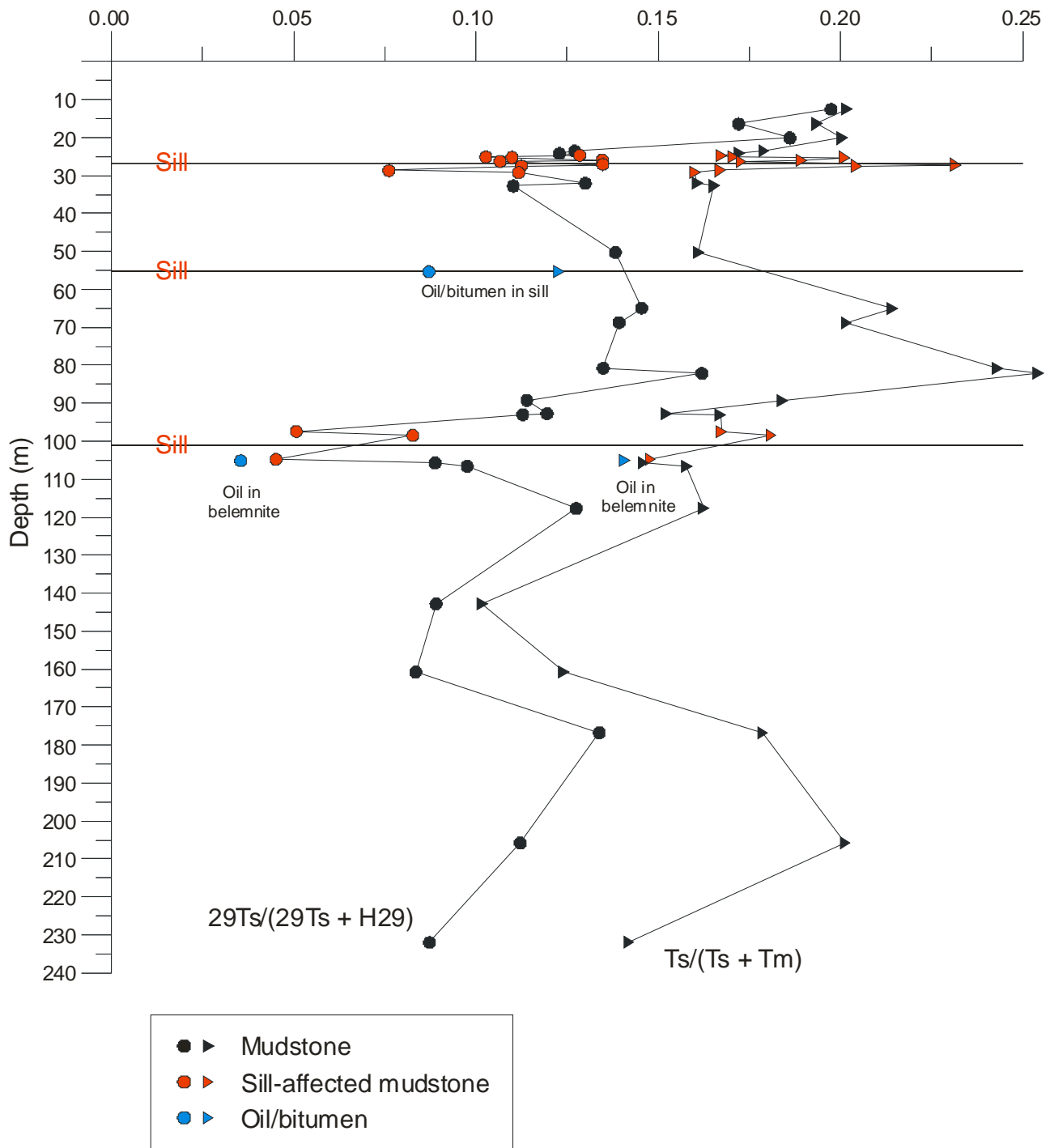


Fig. 7.2.23. Variation in the relative proportion of 18 α -neohopanes ($Ts/(Ts+Tm)$ & $29Ts/(29Ts+H29)$) through the Blokely-1 well.

7.3 Stable Carbon isotope analyses

Stable carbon isotope analyses of saturated, aromatic polar and asphaltene fractions of 20 solvent extracts and 2 oil/bitumen samples from the Blokely well were carried out by APT, Kjeller, Norway. The results are shown in Table 7.3.1 and Appendix 11.5.

Galimov-type plots of data from all samples are shown in Fig. 7.3.1. Except for one extract sample (2009003-16740) and one oil/bitumen sample (2009003-16764) that both show remarkable low (numerically large negative number) $\delta^{13}\text{C}_{(\text{asphaltenes})}$ values, all samples show rather similar trends with respect to the relative $\delta^{13}\text{C}$ -values of saturated, aromatic, polar, and asphaltene fractions. With few exceptions the relative $\delta^{13}\text{C}$ values show:

$$\delta^{13}\text{C}_{(\text{saturates})} \leq \delta^{13}\text{C}_{(\text{aromatics})} \leq \delta^{13}\text{C}_{(\text{polars})} \leq \delta^{13}\text{C}_{(\text{asphaltenes})}$$

Sample-to-sample variation is primarily manifest in shifts of 1–3 permil of the $\delta^{13}\text{C}$ values of all fractions in a sample while maintaining the same internal fraction-to-fraction trend, probably reflecting variation in the relative proportions of terrestrially and marine derived material to the parent kerogen.

A crossplot of $\delta^{13}\text{C}_{(\text{saturates})}$ versus $\delta^{13}\text{C}_{(\text{aromatics})}$ is shown in Fig. 7.3.2. Extract samples (blue symbols) generally plot very close to the broken line that indicates the empirically defined (by Sofer 1984) best separation between “waxy” (*i.e.* terrestrially dominated, above line) and “non-waxy” (*i.e.* marine, below line) oils or extracts. Both oil/bitumen samples (red symbols) plot well within the “non-waxy” field.

A crossplot of the “canonical variable”, as defined by Sofer (1984) versus pristane/phytane ratio for solvent extracts (blue symbols) and oil/bitumen samples (red symbols) from the Blokely well is shown in Fig. 7.3.3. The broken line indicates the empirically defined (by Sofer 1984) best separation between “waxy” (*i.e.* “terrestrial”, above line) and non-waxy (*i.e.* marine, below line) oils/extracts. No correlation is observed between the “canonical variable” and the pristane/phytane ratio. Both oil/bitumen samples plot well within the “marine” field, whereas extract samples are evenly distributed on either side of the separation line.

7.3.1 References

Sofer, Z. 1984: Stable carbon isotope compositions of crude oils; application to source depositional environments and petroleum alteration. AAPG Bulletin **68**, 31-49.

Sample number	Depth (m)	$\delta^{13}\text{C}$ -Saturates	$\delta^{13}\text{C}$ -Aromatics	$\delta^{13}\text{C}$ -Polars	$\delta^{13}\text{C}$ -Asphaltenes	Canonical variable	Comment
2009003-16707	12,62	-30,5	-29	-28,8	-27,9	1,135	
2009003-16713	20,15	-30,6	-29,6	-29,1	-28,5	0,056	
2009003-16822	23,59	-30,2	-29,6	-29,2	-28,9	-0,956	
2009003-16718	25,15	-29,4	-28,5	-28,3	-28,3	-0,538	
2009003-16736	25,24	-29,1	-28,4	-28,1	-28,7	-1,075	
2009003-16721	26,23	-29	-28,2	-28,3	-28,7	-0,884	
2009003-16740	27,46	-32,3	-29	-27,8	-31,4	5,689	
2009003-16743	28,69	-28,9	-27,4	-27,4	-27,5	0,639	
2009003-16725	32,1	-30,1	-28,5	-28,5	-28,3	1,233	
2009003-16823	32,78	-30,4	-29,2	-28,5	-28,1	0,438	
2009003-16749	64,91	-30	-28,6	-28,4	-27,9	0,758	
2009003-16827	80,77	-29,7	-29	-28,7	-28,3	-0,889	
2009003-16773	89,22	-29,3	-28,3	-28	-27,5	-0,347	
2009003-16777	93,02	-29,1	-27,5	-27,7	-27,1	0,923	
2009003-16778	97,42	-28,5	-26,8	-27,2	-27,1	0,959	
2009003-16829	104,79	-28,1	-26,6	-26,2	-25,6	0,391	
2009003-16781	105,75	-28,6	-26,8	-26,4	-25,5	1,212	
2009003-16782	106,59	-28,7	-27	-26,4	-25,5	1,021	
2009003-16812	160,8	-27,1	-25,7	-25,4	-24,7	-0,141	
2009003-16850	205,84	-27,3	-25,4	-25	-24,5	1,031	
2009003-16764	105,18	-28,5	-27,6	-28,2	-35,3	-0,817	Asph tested twice
2008007-16053	55,4	-28,5	-27,3	-27,7	-27,4	-0,151	

Table 7.3.1. Stable Carbon isotope data on solvent extracts and oils from the Blokely well, grey shading: oil/bitumen. Canonical variable according to Sofer (1984).

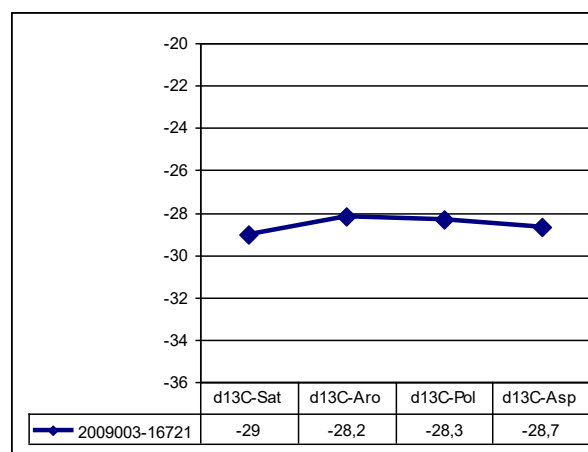
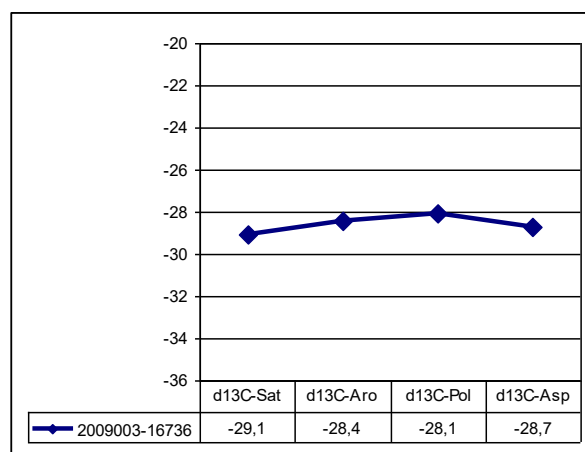
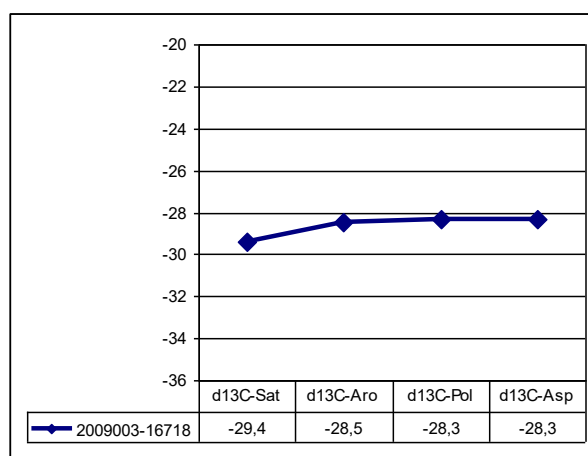
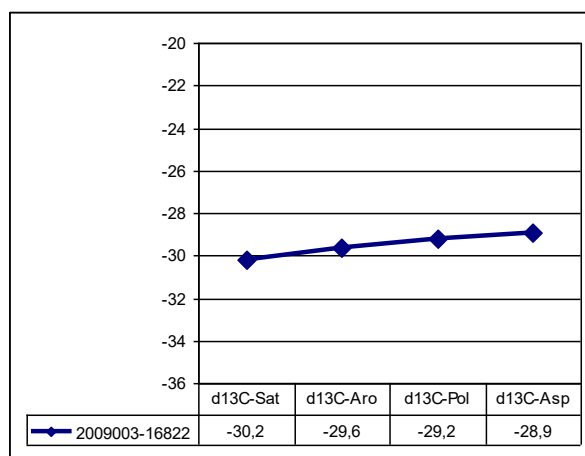
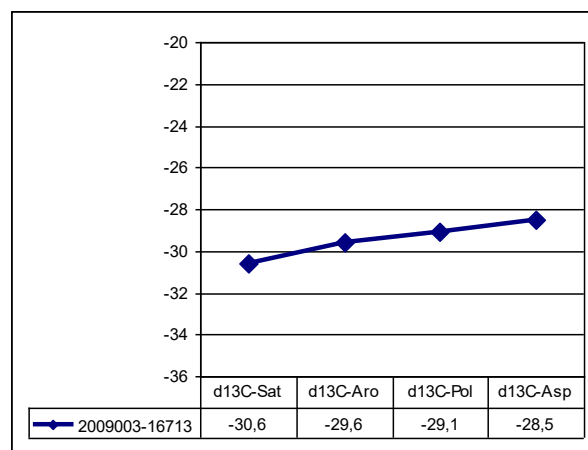
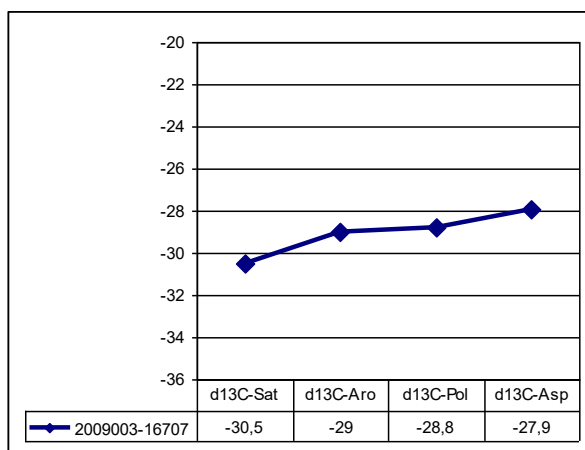


Fig. 7.3.1 Galimov-type plots of stable carbon isotope data from the Blokely well. Horizontal axis: extract fraction, vertical axis $\delta^{13}\text{C}$. Sample identification: lower left corner of each plot.

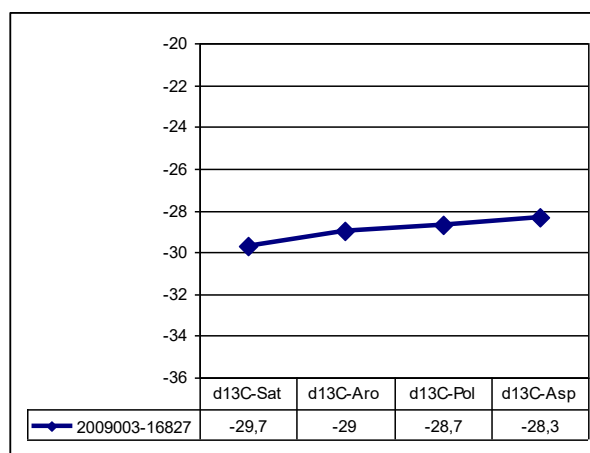
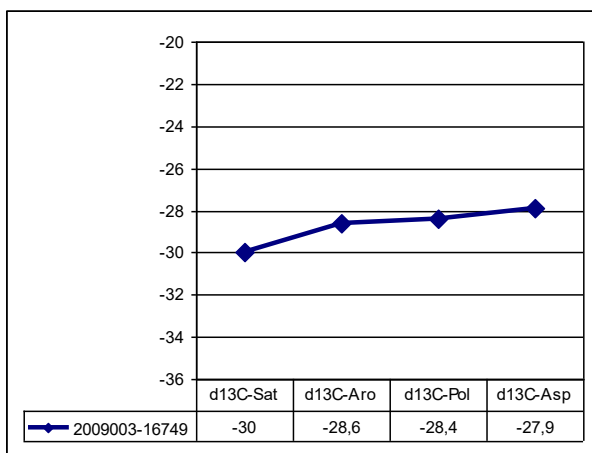
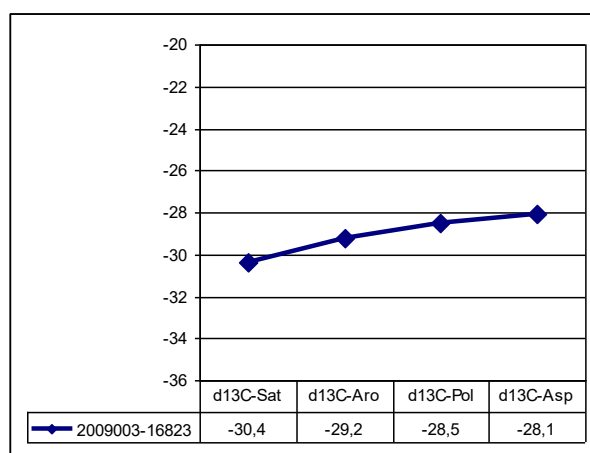
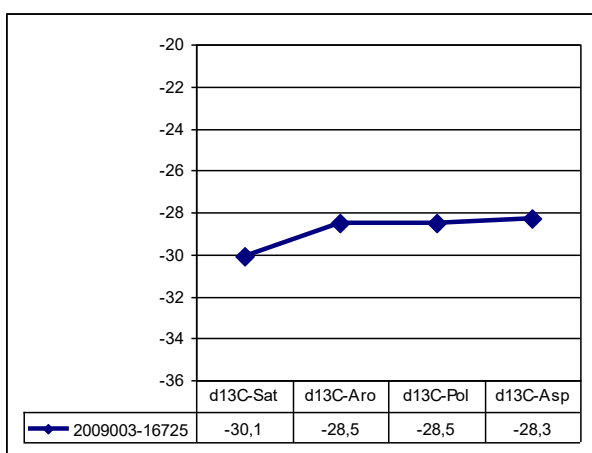
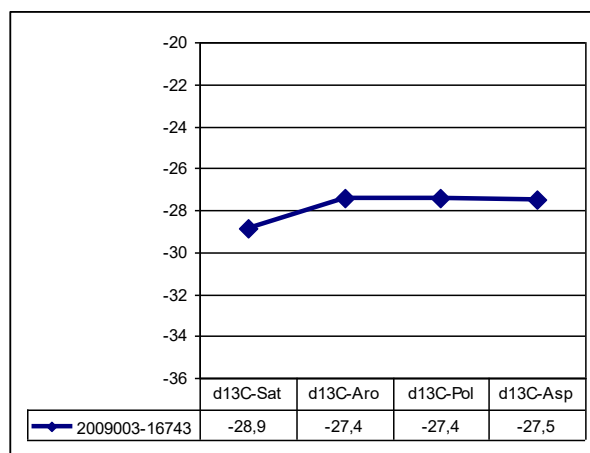
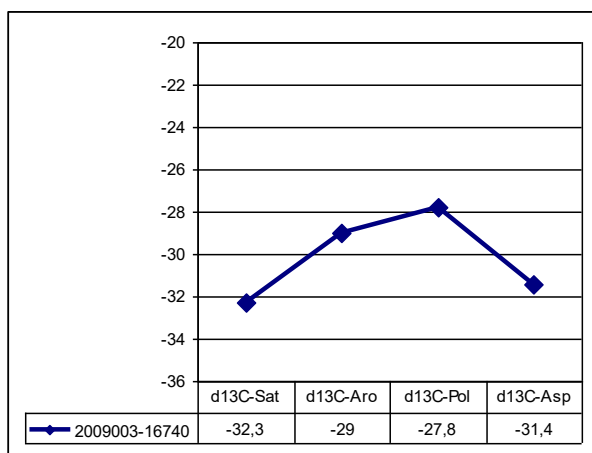


Fig. 7.3.1 continued. Galimov-type plots of stable carbon isotope data from the Blokely well. Horizontal axis: extract fraction, vertical axis $\delta^{13}\text{C}$. Sample identification: lower left corner of each plot.

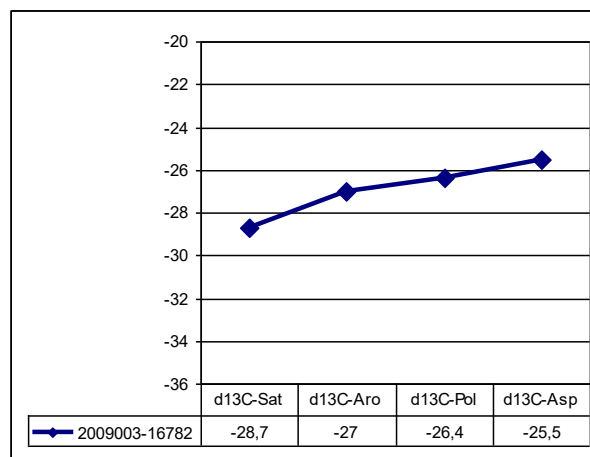
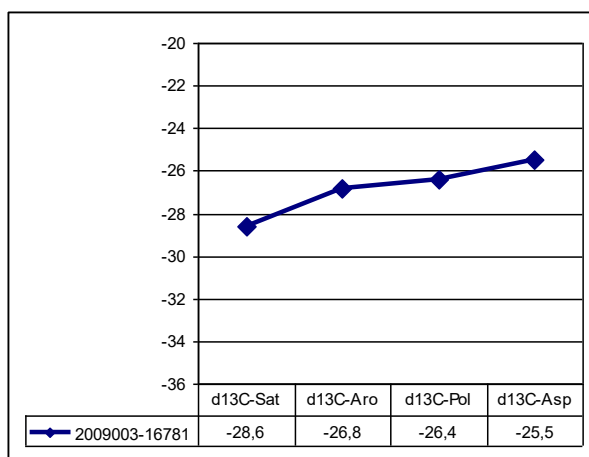
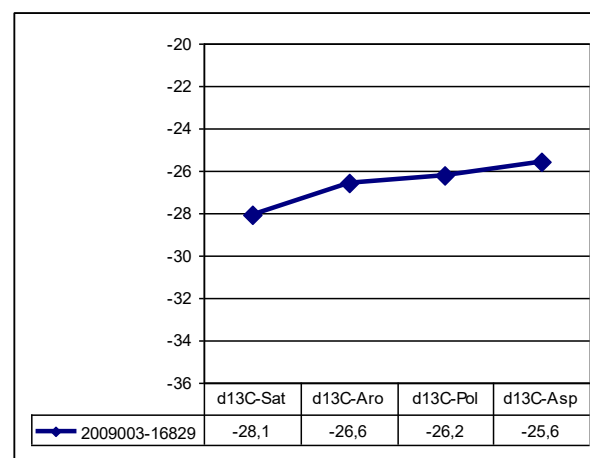
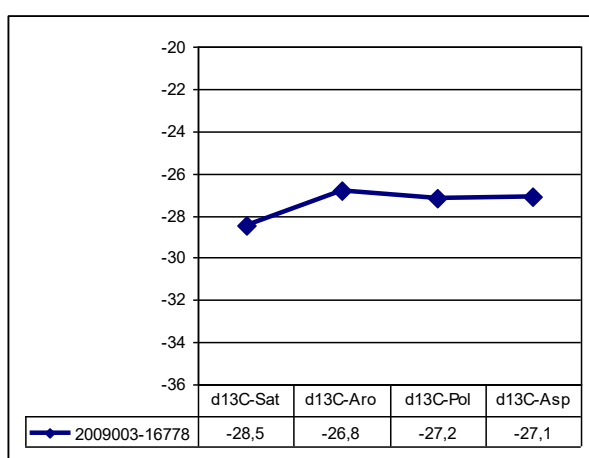
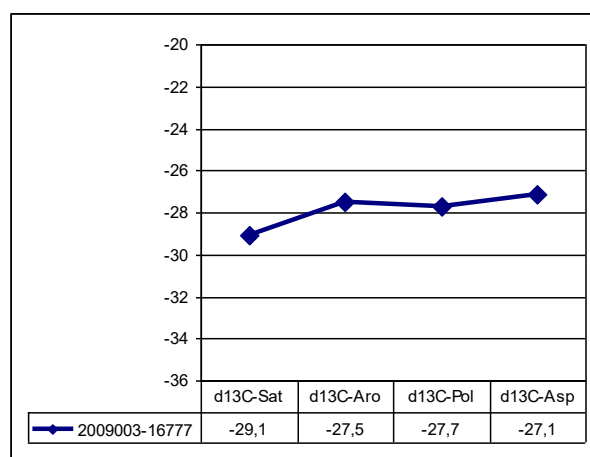
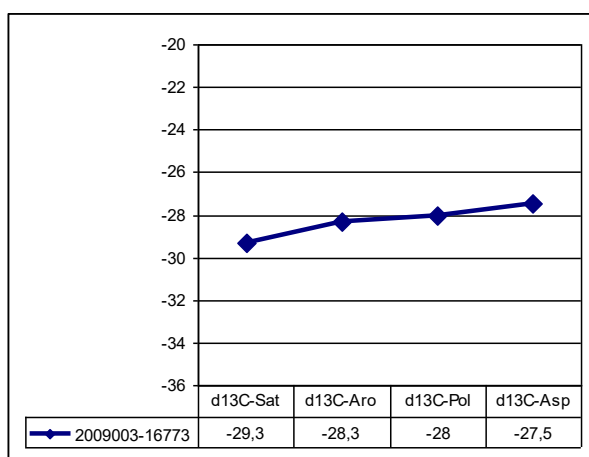


Fig. 7.3.1 continued. Galimov-type plots of stable carbon isotope data from the Blokely well. Horizontal axis: extract fraction, vertical axis $\delta^{13}\text{C}$. Sample identification: lower left corner of each plot.

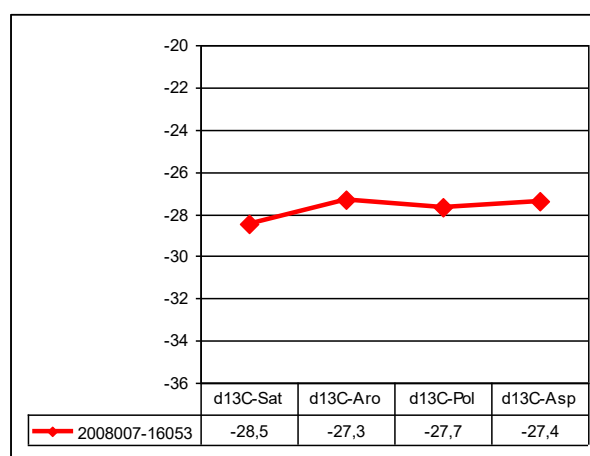
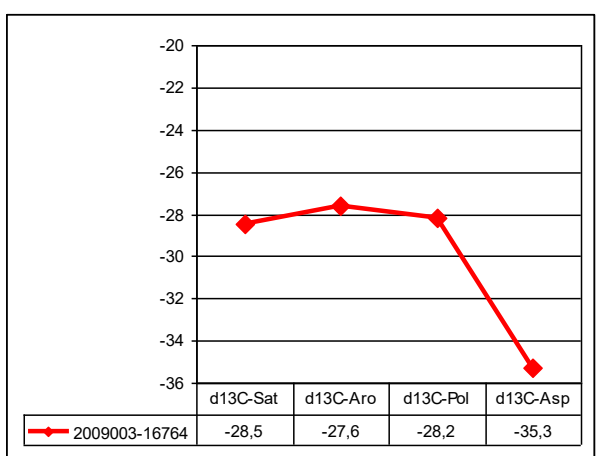
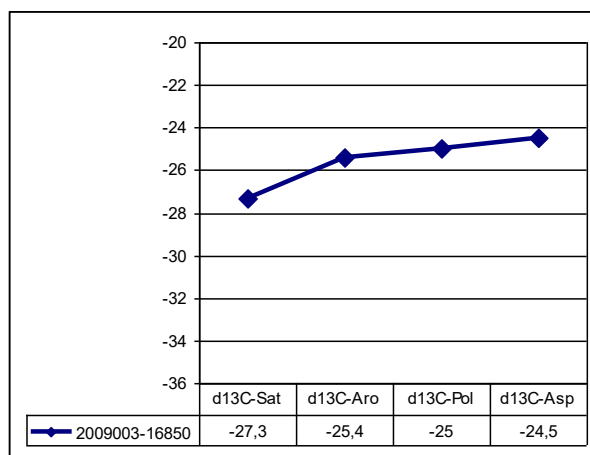
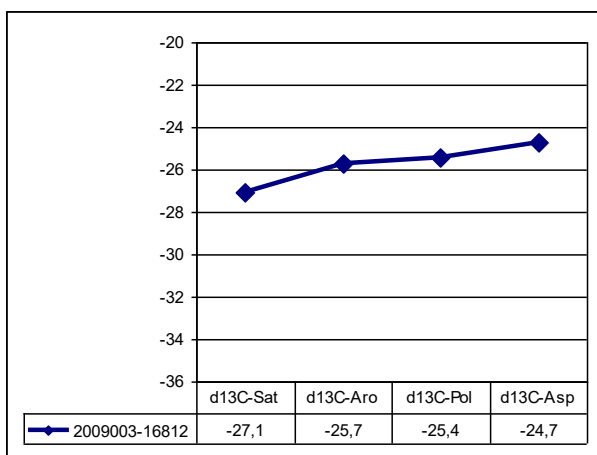


Fig. 7.3.1 continued. Galimov-type plots of stable carbon isotope data from the Blokely well. Horizontal axis: extract fraction, vertical axis $\delta^{13}\text{C}$. Sample identification: lower left corner of each plot.

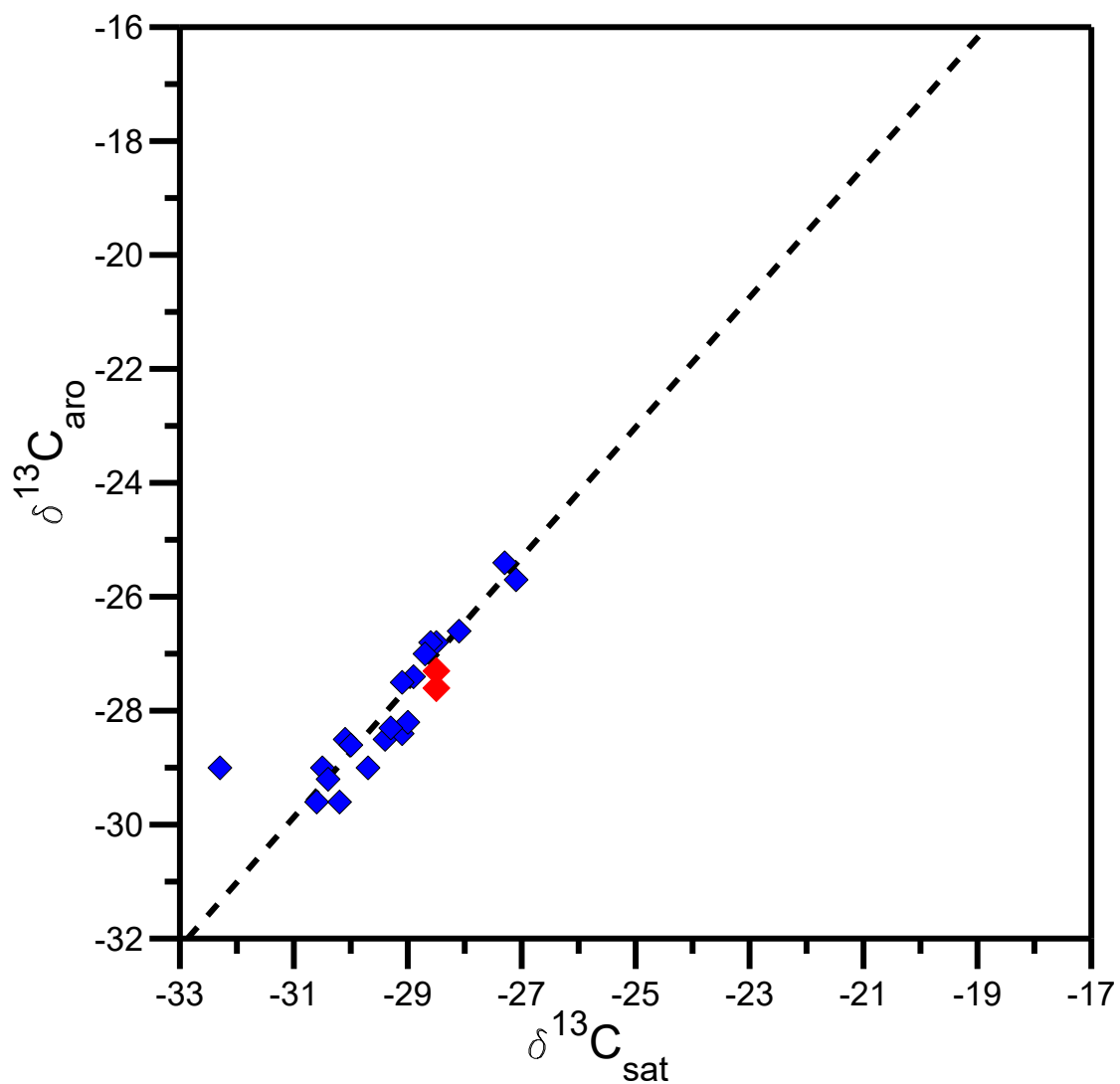


Fig. 7.3.2. $\delta^{13}\text{C}_{\text{(saturates)}}$ *versus* $\delta^{13}\text{C}_{\text{(aromatics)}}$ for solvent extracts (blue symbols) and oils (red symbols) from the Blokely well. Broken line indicates the empirically defined best separation between “waxy” (above line) and non-waxy (below line) oils/extracts. From Sofer (1984)

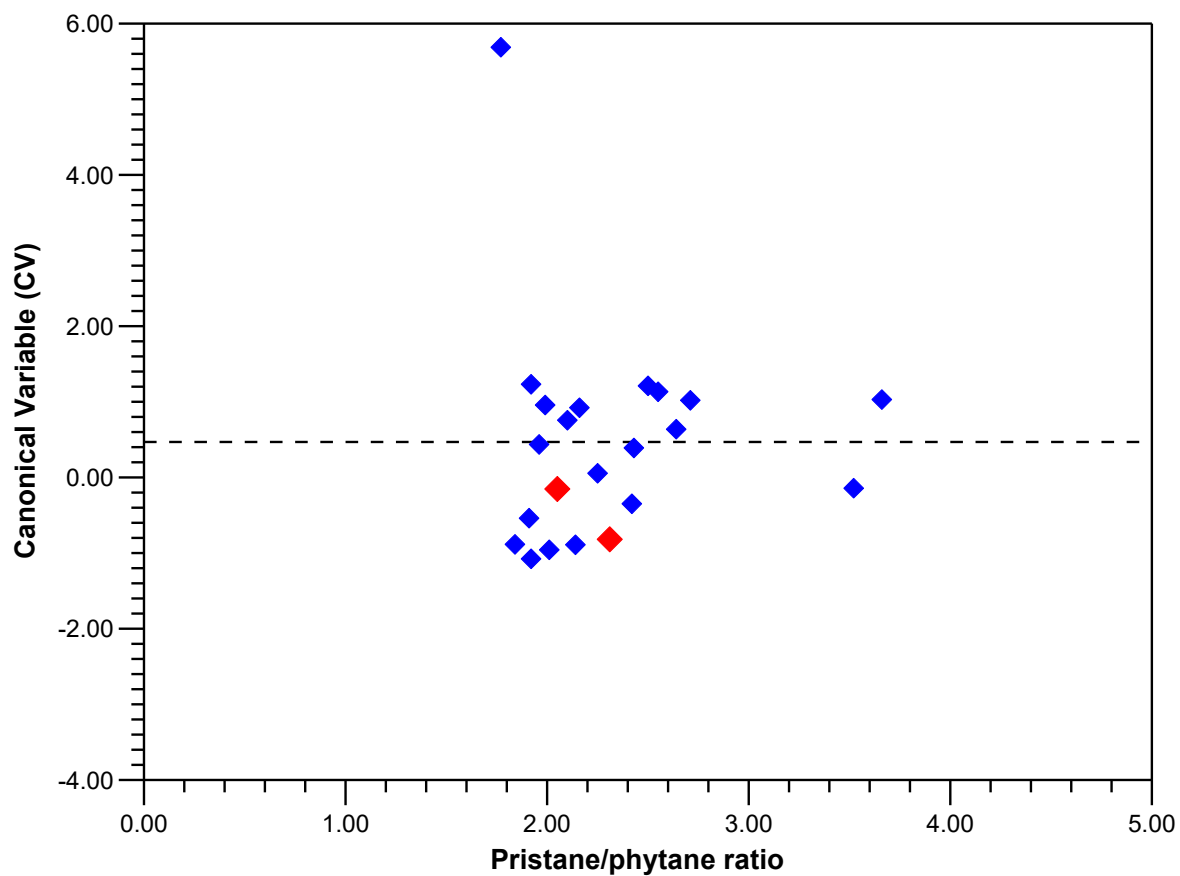


Fig. 7.3.3. Canonical variable, as defined by Sofer (1984) *versus* pristane/phytane ratio for solvent extracts (blue symbols) and oils (red symbols) from the Blokely-1 well. Broken line indicates the empirically defined best separation between “waxy” (above line) and non-waxy (below line) oils/extracts. From Sofer (1984)

7.4 Headspace gas analysis

Samples for head space gas analyses included 21 core pieces, evenly spaced throughout the drilled section. Core pieces were canned in airtight containers at well site immediately after retrieval of each core section. Compositional and isotopic analysis of headspace gas was carried out by APT, Kjeller, Norway (Appendix 11.5)

Hydrocarbon gas concentrations are very variable but generally low, dominated by methane (Table 7.4.1).

C1+ hydrocarbon gases are only detected in 10 samples (Table 7.4.1).

Only six samples allowed carbon and hydrogen isotope analysis to be carried out. Out of these five show compositions conformable with a thermogenic origin, whereas one dataset is probably spurious (Table 7.4.2).

Sample info	Depth (m)	C1%	C2%	C3%	iC4%	nC4%	iC5%	nC5%	C6+%	CO2%	Sum C1-C5	Wetness	iC4/nC4	ppm
511101-01	3,51	26,2								73,8	26,2	0		97
511101-04	11,73									100				8000
511101-08	23,59					0,08	0,14	0,07		99,7	0,29	100		19450
511101-12	32,78	0,97								99	0,97	0		2611
511101-16	44,80	1,2								98,8	1,2	0		2985
511101-20	56,66	0								100	0	-1,5		821
511101-24	68,77	23,4	0,84				0,31			75,4	24,6	3,5		5652
511101-28	80,77	27,1		0,2	0,2	0,4	0,23			71,9	28,1	2,9	0,51	5137
511101-32	92,74	6,4								93,6	6,4	0		1386
511101-36	104,79	94,2	0,04	0	0,07	0,18	0,27	0,28	0,77	4,2	95	0,31	0,41	60779
511101-40	116,82	99,7	0,04							0,23	99,8	0,04		158873
511101-44	128,77	3								97	3	0		29170
511101-48 (punctured)	140,75									100				801
511101-52	152,75	3,7								96,3	3,7	0		915
511101-56	164,82	59,9	0,68	4	0,14	0,57	0,05	0,05	0	34,6	65,4	8,3	0,25	65112
511101-60	176,77	75,4		2		0,67				22	78	3,4		3999
511101-64	188,77	98,1	0,01	0						1,9	98,1	0,01		471389
511101-68	200,76	68,9	0	0,46		0,38		0,24		30	70	1,2		4253
511101-72	212,77	6,5								93,5	6,5	0		646
511101-76	224,74	28,9								71,1	28,9	0		1608
511101-79	233,71	96,6	0,01							3,4	96,6	0,01		106863

Table 7.4.1 Compositional data of head space gas.

Sample info	Depth (m)	C1 d13C	C2 d13C	C3 d13C	i-C4 d13C	n-C4 d13C	i-C5 d13C	n-C5 d13C	CO2 d13C	C1 dD
511101-01	3,51									
511101-04	11,73								-3,5	
511101-08	23,59								-6,2	
511101-12	32,78									
511101-16	44,80									
511101-20	56,66									
511101-24	68,77								-5,9	
511101-28	80,77								-6,4	
511101-32	92,74									
511101-36	104,79	-39,7							-8	-279
511101-40	116,82	-48,9								-289
511101-44	128,77								-6,5	
511101-48 (punctured)	140,75									
511101-52	152,75									
511101-56	164,82	-14,6		-24,8					-2,7	-282
511101-60	176,77									
511101-64	188,77	-42,5							-3,1	-273
511101-68	200,76	-43,4							-7,9	
511101-72	212,77									
511101-76	224,74									
511101-79	233,71	-35,4								-262

Table 7.4.2 Isotope data of head space gas.

8. Sandstone Provenance

The provenance of the sandstones of the Blokely core is evaluated in order to support the reconstruction of the Late Jurassic depositional setting in the Jameson Land Basin, where the direction of sediment supply is essential. The heavy mineral chemistry makes comparison with basement provinces and drainage sediments possible, whereas the zircon ages inform about the formation ages of the source rocks. Furthermore, the degree of sorting and weathering of the heavy mineral assemblages are crucial in order to interpret transport processes and depositional velocities. The provenance signal will be moderated according to the length of transport and number of temporary depositions along the transport pathway, which can make comparison with specific source rocks complex. A special complication of establishing the provenance of the sedimentary rocks of East Greenland is that much of the source area possibly is located under the Greenland ice sheet at present.

8.1 Data

Heavy mineral CCSEM (Computer Controlled Scanning Electron Microscopy) analyses and zircon LA-ICP-MS (Laser Ablation - Inductively Coupled Plasma - Mass Spectroscopy) age datings were made in six sandstones at 7.41, 43.16, 69.78, 139.27, 181.53 and 221.18 m depth. The sampling was made in thick sandstone sequences in which also geochemical and mineralogical analyses were made (Fig. 3.3.11). The sampling was carried out in sandstones of both layered and homogeneous character.

8.2 Methods

8.2.1 Heavy mineral analysis

Samples were crushed and the grain size interval 45–710 μm were collected by wet and dry sieving. The upper limit was chosen to exclude most of the rock fragments, and the

lower limit excluded the material that was too small for the measurements. Heavy liquid separation was made by bromoform with a specific density of 2.82 g/cm³, and the total heavy mineral wt% (weight percentage) of the chosen grain size interval was measured (Table 8.1). The heavy mineral concentrates were dried and 0.9 grams were embedded in epoxy and polished (Fig. 8.1A) after shaking the samples to get a representative cut. Heavy mineral chemistry was determined by CCSEM (Computer Controlled Scanning Electron Microscopy) by GEUS on a Philips XL40SEM equipped with a ThermoNoran EDX (Energy Dispersive X-ray spectrometry) detector (Keulen *et al.* 2008), where about 1200 grains were analysed per sample. A few grains of quartz and feldspar were present in each sample, so their compositions have also been measured. The category named amp/pyr/tour contains amphiboles, pyroxenes and tourmalines. The major element compositions of the minerals were measured as oxides, along with the trace elements Cr, Ni, Cu, Y, Zr, Nb, Sn and Ce. The grain-size and grain-shape parameters were measured at the cut surface in the polished section.

8.2.2 Zircon age dating

Samples were crushed to below 500 µm. Heavy mineral concentrates with discharge of grains below 45 µm were produced on a Wilfley water shaking table (Söderlund & Johansson 2002). Zircon grains were handpicked randomly including all sizes, shapes and colours and then mounted in epoxy (Fig. 8.1B). U-Pb ages were obtained by LA-ICP-MS (Laser Ablation - Inductively Coupled Plasma - Mass Spectroscopy) (Frei & Gerdes 2009) of 162 zircon grains per sample by GEUS as well as the absolute concentration of U and Th. An uncertainty of +/- 2σ was used for the crystallization ages of zircon. The program Zirchron was used for age data reduction. ²⁰⁷Pb/²⁰⁶Pb ages were used for the ages above 1 Ga, and ²⁰⁶Pb/²³⁸U were used for those with a ²⁰⁷Pb/²⁰⁶Pb age below 1 Ga, as the ²⁰⁶Pb/²³⁸U ages are more accurate below this age. K-S (Kolmogorov-Smirnov) tests have been made for the age probability distributions by extracting the p-values (Table 8.2). This was done by calculating the distance between the curves to discover if significant differences exist (Fig. 8.2). Uncertainty was included as the 2σ errors of the measured ages in the construction of the CDF (Cumulative Distribution Function). Several standards were measured as references inside the data sequence in order to maintain a constant beam level.

8.3 Results and Discussion

8.3.1 Heavy mineral assemblage

All the measured heavy minerals are included in Table 8.3 of which the most important and those present in large amounts are included in Fig. 8.3, excluding the authigenic minerals pyrite and ankerite in order to highlight the detrital signature. No chromite, spinel, cassiterite, sphene, sillimanite, kyanite and staurolite were present in any of the analysed sandstone samples. An example of the elemental differentiation between the minerals is shown in Fig. 8.4 as binary Si-Fe diagrams. The backscatter images show that some rock fragments have not been hammered down (Fig. 8.1A), so they are causing a high fraction of unclassified grains in the CCSEM results (Fig. 8.4). The number of mica grains is presumably a little overestimated, as some of the grains probably were parted along their cleavage when the sandstones were crushed.

The garnet compositions of the samples are very similar (Fig. 8.5) with domination of Fe-rich garnets. The diagrams have been omitted for two levels as too few garnets were present. The garnets have average Mn contents of <2 wt% in all samples. Garnet compositions from East Greenland are largely unknown, but other parts of the pre-Laurentian craton can be used to give an indication of what chemistry the garnets of East Greenland might have. The lack of Ca-rich garnets means that the sampled sandstones have no resemblance to the Norwegian basement lithologies (Morton *et al.* 2004), but some of these garnets might be missing in the results due to the chosen mineral differentiation of the CCSEM results. A group of garnets with chemical similarity to those of the Blokelyv core have been reported from the Middle Jurassic sandstones of the northern North Sea, which presumably have a Shetland Platform provenance (Morton 1985). East Greenland and north-western Britain once formed the eastern margin of the Laurentia craton (Higgins *et al.* 2001), which might explain the similarity in garnet chemistry. However, the measured garnet composition is quite normal in many basement areas, but it can at least be said with certainty that the provenance does not contain any amphibolites.

The Ti-mineral distribution is very mature, as exemplified by the sample at 139.27 m depth, where almost none primary immature ilmenite with TiO₂ content of 52 wt% is present in the sample (Fig. 8.6A). This means that much Fe has been leached from ilmenite to form leu-

coxene, rutile/anatase and also a more mature variant of ilmenite. The same sample contains much ankerite (Table 8.3) showing that both minerals are favoured by weathering. The small amount of Ti-magnetite confirms the high maturity, as Ti-magnetite is instable in the same environmental settings as ilmenite. Leucoxene grains are porous because of their partly dissolved nature, so those that have been cemented with ankerite are included in the unclassified fraction in the CCSEM results of the ankerite-rich samples. This means that the true Ti-mineral maturity is even higher than the results indicate.

The pyrite content is largest when only a small amount of ankerite has precipitated (Table 8.3) indicating that the degradation of bioclasts associated with the ankerite precipitation has prevented some of the framboidal pyrite formation within bioclasts. Furthermore, the extensive cementation has limited the nucleation of single pyrite crystals within clay minerals. The ankerite composition is changing up through the core (Table 8.4), which is shown in the ternary diagram in Fig. 8.7. The compositional evolution might not look large, but it actually is when the chemical structure of the mineral is taken into consideration, which limits the number of possible cation exchanges.

Large quartz grains are hydraulic equivalent with smaller denser mineral grains, so the most coarse-grained sandstones has as expected the largest heavy mineral content in the 45-710 μm interval (Table 8.1). A fairly short transport distance is indicated by the poor sorting between the different weight fractions of the heavy mineral assemblage, including many grains of high-density minerals like zircon, garnet, Fe-oxides and Ti-oxides, along with a large number of well-preserved mica grains. The proportion between the heavy minerals varies much between the samples in an apparently random way, except for large chlorite content in the deepest sample (Fig. 8.3). A limited distance from provenance to place of deposition is indicated by the heavy mineral assemblage according to the increasing influence of hydraulic equivalence of grains with travel distance.

8.3.2 Age distributions

All the p-values of the comparisons between the different age distributions are far above 0.050 (Table 8.2) meaning that the confidence is 95% of the populations being largely statistically similar. The cumulative age distributions illustrate the similar outlines (Fig. 8.2). Some of the youngest age datings have large probabilities shown as high peaks (Fig. 8.8), whereas the uncertainty of the datings increases back in time resulting in wider peaks. His-

tograms of 50 Ma intervals show the age distributions of the individual grains (Fig. 8.9). Between 134 and 140 concordant datings were produced from each of the samples, which is an almost constant ratio to the 162 measurements made in each sample. This confirms a common origin of the age dated sandstones. 11.4% of the 829 concordant grains of the six age datings were adjusted for common lead.

The main characteristics are shown in Fig. 8.10 as a merge of all concordant ages of the six age datings. Some variation is found between the six age distributions, although the overall outlines are quite alike. A few Caledonian ages are present in all samples, but most are found in the two deepest samples (Fig. 8.9). Some of these are even post-Caledonian zircons of Carboniferous-Permian age, which is quite extraordinary as no granites of this age are known from Northeast Greenland. Only few Neoproterozoic ages are found in the samples, except for the deepest one. Far most of the dated zircon grains have ages from the late Paleoproterozoic to the Mesoproterozoic. The ages fall into three major peaks of 1.0-1.3, 1.3-1.6 and 1.6-2.2 Ga, in which intervals the number of ages have been counted (Table 8.5) and normalised to the same number for each age distribution. Clear trends are found by plotting these age intervals in a ternary diagram (Fig. 8.11), where a decrease in the oldest peak correlates with increase in the youngest peak for the three deepest samples. A continued decrease is found for the oldest peak in the three uppermost samples, but the increase has changed to the middle peak. All samples have their major peak around 1.65 Ga (Fig. 8.8), and also a peak around 1.10 Ga is quite prominent in all samples. The peak around 1.98 Ga becomes progressively less pronounced upwards. Only few zircon grains of early Paleoproterozoic ages are found. Quite many Mesoarchean and Neoarchean ages are present, whereas a few older grains are found in four of the samples. Especially the uppermost sample contains many Archean zircon grains.

Resetting of zircon ages is a rare phenomenon in the rocks affected by the Caledonian orogeny (Peucat *et al.* 1985), and only few new grains were formed during the Caledonian metamorphism. Nine grains were laser ablated both in the core and in the rim in this study, of which zonation with a younger rim was found in three of the grains. However, none of them were Caledonian, but a single Caledonian zonation was found by chance during the Zirchron data reduction.

The point counts at 7.41 m and 61.96 m depth (Table 5.3) contains more rock fragments and polycrystalline quartz grains than the deeper samples. This suggests that the sediments of the upper part of the core have travelled a shorter distance, which also partly accounts for the point count at 98.92 m depth. The negative Eu-anomaly of all the rocks (Fig.

3.3.10) is indicative of depleted source rocks and of feldspar breakdown along the transport pathway implying a minimum of transport distance.

Studies of the East Greenland basement terrains are scarce, so the well-known geology of Norway is here used for comparison with the Blokelyv sandstones, as western Norway also once formed part of the Laurentia craton. The Upper and Uppermost Allochthon of north-western Norway is characterised by Morton *et al.* (2008) through sampling in the rivers Salteelva and Vefsna draining the area today. Both zircon age distributions have marked similarities with the ages of the Blokelyv core, in opposition to the other Norwegian age datings of river sediments where only that of Vindelälven show some similarities. This is caused by the origination of its drainage area in the Upper Allochthon, but it is dominated by late Early Proterozoic ages as it primarily runs through the Svecofennian area. The Middle to Lower Allochthon represented by Ljungan cannot be neglected entirely, as this age distribution have some overlap with the Blokelyv sandstones, but its influence cannot be large as major peaks are found in the river where only minor are found in the core. The age distributions of Salteelva and Vefsna can account for most of the Blokelyv ages, but not much of those older than 2.2 Ga which are widely present in the core.

The age distributions of the Blokelyv sandstones have the same characteristics as the East Greenland source interpreted by Morton *et al.* (2009) via Jurassic rocks in the Norwegian Sea. Especially the Archean signature is important, as it is not much found in Norway. However, the heavy mineral characteristics of the Blokelyv core neither contain the high-Mg garnet assemblage nor the mineral ratios found in the Norwegian Sea. This confirms that the sediments of the Blokelyv core have travelled a shorter distance before deposition than those in the Norwegian Sea. The hydraulic sorting of the heavy mineral assemblage has therefore been minimal for the Blokelyv sediments. This process does not affect the obtained zircon age datings, which explains the similarities between the proximal and distal setting. The garnet composition of north-eastern East Greenland defined by Morton *et al.* (2005) fits very well with especially the upper part of the measured intervals (Fig. 8.5).

The measured broad age spectrum of the Blokelyv sandstones (Fig. 8.8) must necessarily be sourced by a provenance spanning over more than just the immediate area, as expected from the relatively deep water deposition. This is also the conclusion of Whitham *et al.* (2004), where the rocks of Maastrichtian from East Greenland have a very good correlation with the ages of the Blokelyv core. Furthermore, the garnet compositions of the Blokelyv sandstones fits well with the all the measured Cretaceous compositions included in that study, whereas the Eocene garnets and ages fits poorly.

8.4 Conclusions

The provenance of the Blokølv sandstones is assumed to have been located in the hinterland close to the Jurassic coast of East Greenland, where the complex geology accounts for the diverse age distributions. The upland of the supplying rivers has primarily been local, as seen by the poorly sorted heavy mineral assemblages, but with some contributions from more distant sources. Demarcation of the provenance area is as good as impossible because of the limited knowledge of the diverse basement, but the corresponding Caledonian allochthons from other areas resembles the Blokølv sandstones well. The provenance area has changed steadily but slowly during the deposition, except for an interruption in the middle of the core resulting in changing dominance of the major age peaks. The size of the provenance area has presumably grown more restricted with time, which might have resulted from a rise in relative sea level and associated increasing coarse-grained sediment supply from the prograding shelf margin (see chapter 4). The varying Ti-mineral maturity and amount of ankerite precipitation could be caused either by the number of redepositions or by changes in the activity of mass flow events.

8.5 References

- Frei, D. & Gerdes, A. 2009: Precise and accurate in situ U-Pb dating of zircon with high sample throughput by automated LA-SF-ICP-MS. *Chemical Geology* **261**, 261-270.
- Higgins, A.K., Leslie, A.G. & Smith, M.P. 2001: Neoproterozoic-Lower Palaeozoic stratigraphical relationships in the marginal thin-skinned thrust belt of the East Greenland Caledonides: comparisons with the foreland in Scotland. *Geological Magazine* **138**, 143-160.
- Keulen, N., Frei, D., Bernstein, S., Hutchison, M.T., Knudsen, C. & Jensen, L. 2008: Fully automated analysis of grain chemistry, size and morphology by CCSEM: examples from cement production and diamond exploration. *Bulletin Geological Survey of Denmark and Greenland* **15**, 93-96.
- Morton, A. 1985: A new approach to provenance studies: electron microprobe analysis of detrital garnets from Middle Jurassic sandstones of the northern North Sea. *Sedimentology* **32**, 553-566.
- Morton, A., Hallsworth, C. & Chalton, B. 2004: Garnet compositions in Scottish and Norwegian basement terrains: a framework for interpretation of North Sea sandstone provenance. *Marine Petroleum Geology* **21**, 393-410.

- Morton, A., Whitham, A.G. & Fanning, C.M. 2005: Provenance of Late Cretaceous to Paleocene submarine fan sandstones in the Norwegian Sea: Integration of heavy mineral, mineral chemical and zircon age data. *Sedimentary Geology* **182**, 3-28.
- Morton, A., Fanning, M. & Milner, P. 2008: Provenance characteristics of Scandinavian basement terrains: Constraints from detrital zircon ages in modern river sediments. *Sedimentary Geology* **210**, 61-85.
- Morton, A., Hallsworth, C., Strogon, D., Whitham, A. & Fanning, M. 2009: Evolution of provenance in the NE Atlantic rift: The Early-Middle Jurassic succession in the Heidrun Field, Halten Terrace, offshore Mid-Norway. *Marine Petroleum Geology* **26**, 1100-1117.
- Peucat, J.J., Tisserant, D., Caby, R. & Clauer, N. 1985: Resistance of zircons to U-Pb resetting in a prograde metamorphic sequence of Caledonian age in East Greenland. *Canadian Journal of Earth Sciences* **22**, 330-338.
- Söderlund, U. & Johansson, L. 2002: A simple way to extract baddeleyite (ZrO₂). *Geochemistry Geophysics Geosystems* **3**, 1-7.
- Whitham, A.G., Morton, A.C. & Fanning, M. 2004: Insights into Cretaceous-Palaeogene sediment transport paths and basin evolution in the North Atlantic from a heavy mineral study of sandstones from southern East Greenland. *Petroleum Geosciences* **10**, 61-72.

	grain size distribution wt%			heavy mineral wt%	
	>710 μm	710-45 μm	<45 μm	710-45 μm	total
7.41 m	71.44	23.26	5.29	4.74	1.10
43.16 m	0.55	80.99	18.46	0.94	0.76
69.78 m	0.02	89.16	10.82	0.87	0.77
139.27 m	42.44	50.64	6.93	0.47	0.24
181.53 m	57.10	37.50	5.40	1.21	0.45
221.18 m	62.94	30.86	6.21	1.50	0.46

Table 8.1. The grain size distributions of the levels selected for heavy mineral analyses.

	7.41 m	43.16 m	69.78 m	139.27 m	181.53 m	221.18 m
7.41 m		0.990	0.762	0.428	0.496	0.620
43.16 m	0.990		0.962	0.906	0.659	0.660
69.78 m	0.762	0.962		0.778	0.106	0.418
139.27 m	0.428	0.906	0.778		0.467	0.508
181.53 m	0.496	0.659	0.106	0.467		0.889
221.18 m	0.620	0.660	0.418	0.508	0.889	

Table 8.2. p-values of K-S tests comparing the 6 zircon age distributions using error in the cumulative distribution function.

	7.41 m	43.16 m	69.78 m	139.27 m	181.53 m	221.18 m
muscovite	36.09	55.34	47.58	54.46	36.98	59.69
biotite	0.58	1.39	3.74	1.25	2.66	3.56
chlorite	0.00	0.21	1.32	3.29	1.18	19.38
ilmenite	0.00	1.07	2.20	0.78	0.30	1.11
leucoxene	0.29	1.60	5.51	3.91	0.30	2.45
rutile	1.59	7.05	5.29	5.95	3.25	2.45
Ti-magnetite	0.00	0.21	0.00	0.63	0.00	0.00
Fe-oxides	0.29	0.53	2.42	4.69	2.66	1.34
zircon	0.14	9.72	6.61	3.91	0.89	1.78
garnet	0.29	4.17	1.54	0.00	2.37	2.45
corundum	0.14	0.00	0.00	0.31	0.00	0.00
monazite	0.00	0.75	0.00	0.00	0.00	0.00
xenotime	0.00	0.43	0.22	0.00	0.00	0.00
apatite	0.00	1.92	1.32	0.94	1.48	1.11
epidote	0.14	0.00	0.00	0.00	1.18	0.00
olivine	0.29	0.11	0.00	0.00	0.00	0.00
amp/pyr/tour	3.04	9.19	12.33	3.13	4.73	3.34
pyrite	0.00	3.10	4.41	0.78	0.89	0.89
ankerite	57.10	3.21	5.51	15.96	41.12	0.45

Table 8.3. Heavy mineral assemblage listing all measured heavy minerals of the CCSEM analyses. The authigenic minerals pyrite and ankerite are listed lastly.

	distribution in ankerite			
	CaO	Fe ₂ O ₃	MgO	MnO
7.41 m	57.23	18.99	23.36	0.42
43.16 m	60.19	14.79	24.60	0.42
69.78 m	53.29	19.80	25.94	0.97
139.27 m	58.10	20.50	20.76	0.64
181.53 m	55.26	23.32	20.42	1.00
221.18 m	54.83	23.94	20.50	0.73

Table 8.4. The content of Ca, Fe, Mg and Mn in ankerite in the levels where the heavy mineral composition has been measured. An upwards decrease in Fe-content is visible.

	0.2-0.5 Ga	0.5-1.0 Ga	1.0-1.3 Ga	1.3-1.6 Ga	1.6-2.2 Ga	2.2-3.8 Ga
7.41 m	4.0	1.0	32.0	31.0	37.0	35.0
43.16 m	2.0	4.0	34.2	29.2	44.3	26.2
69.78 m	1.0	2.1	41.8	30.3	41.8	23.0
139.27 m	3.0	3.0	41.3	23.2	53.4	16.1
181.53 m	12.1	2.0	26.2	20.1	54.4	25.2
221.18 m	6.1	12.2	21.3	20.3	56.8	23.3

Table 8.5. Number of zircon grains of the 6 age datings divided in 6 age categories. The grain numbers are normalised to 140 grains per analysis.

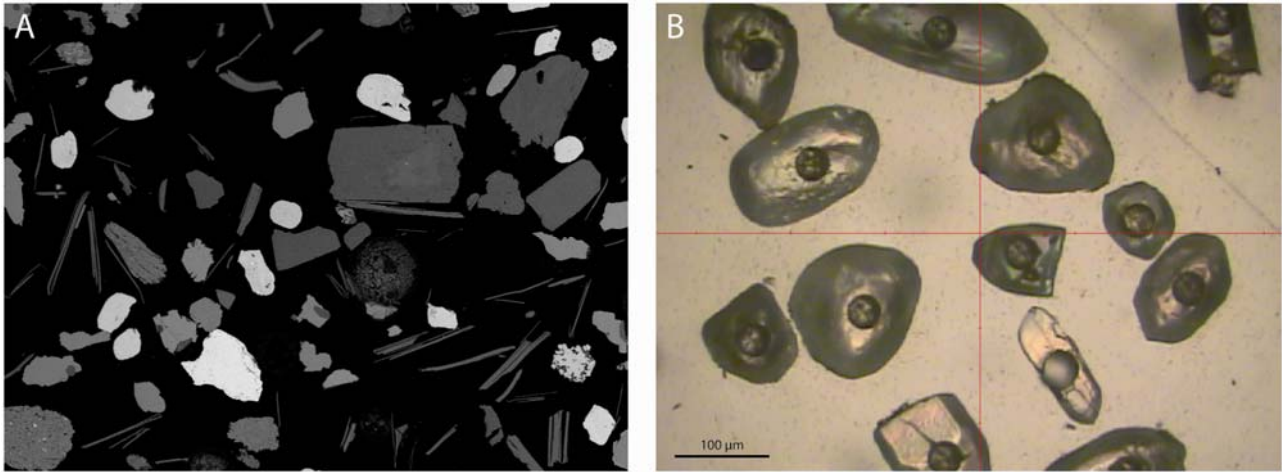


Fig. 8.1. A: Heavy minerals in a CCSEM mount. B: Zircon grains that have been laser ablated.

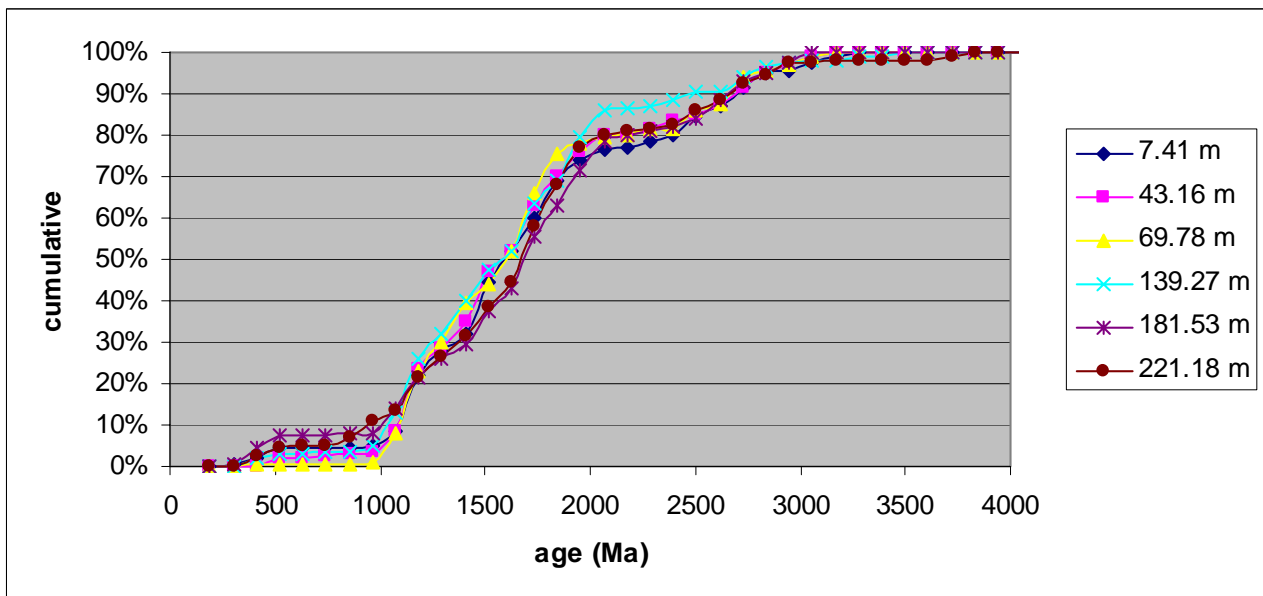


Fig. 8.2. Cumulative age distribution of the 6 age dated samples showing good correlation.

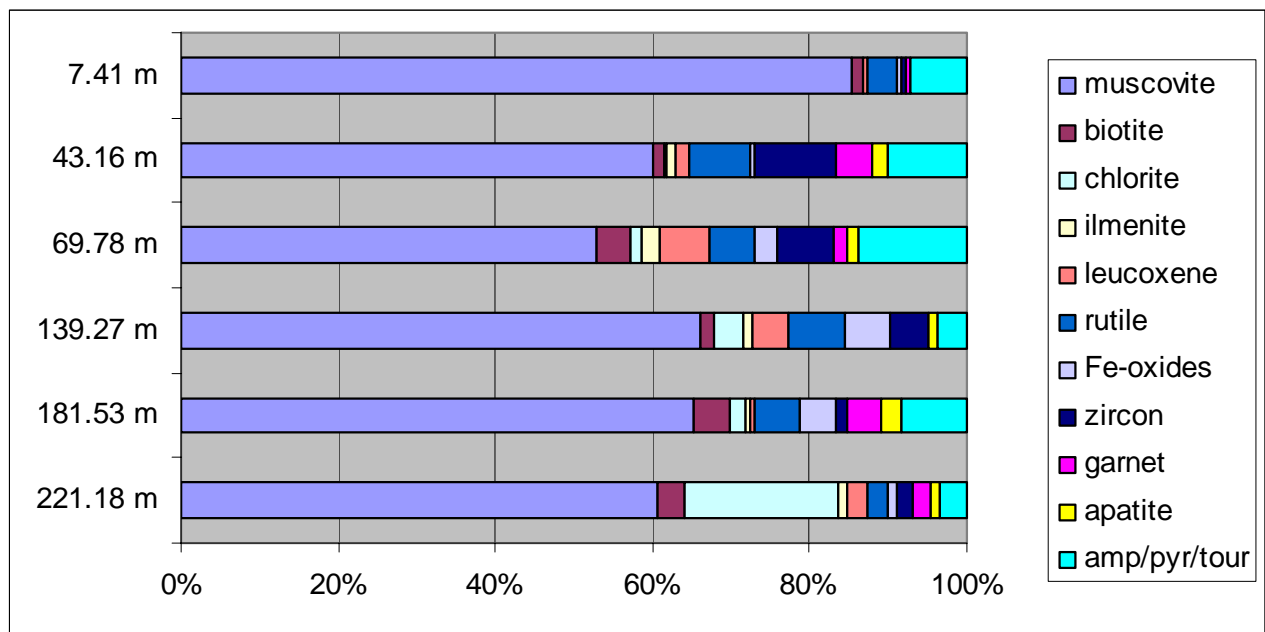


Fig. 8.3. Heavy mineral wt% excluding the authigenic minerals and the irrelevant detrital minerals present in small amounts.

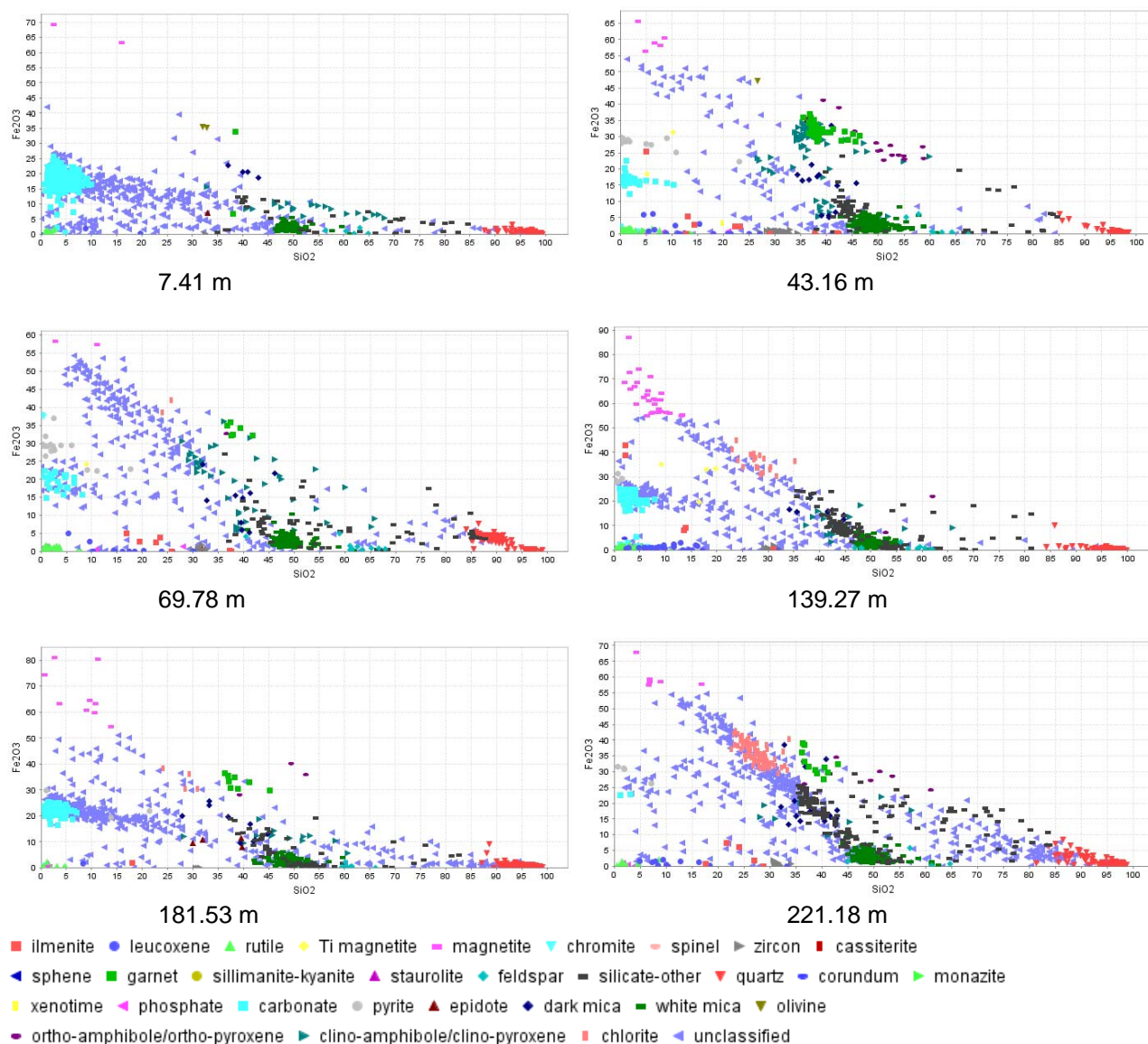


Fig. 8.4. Distribution of the minerals in a Si-Fe plot according to the present classification. The unclassified fraction consists mostly of rock fragments, as shown by their intermediate compositions. Note the different scales for Fe.

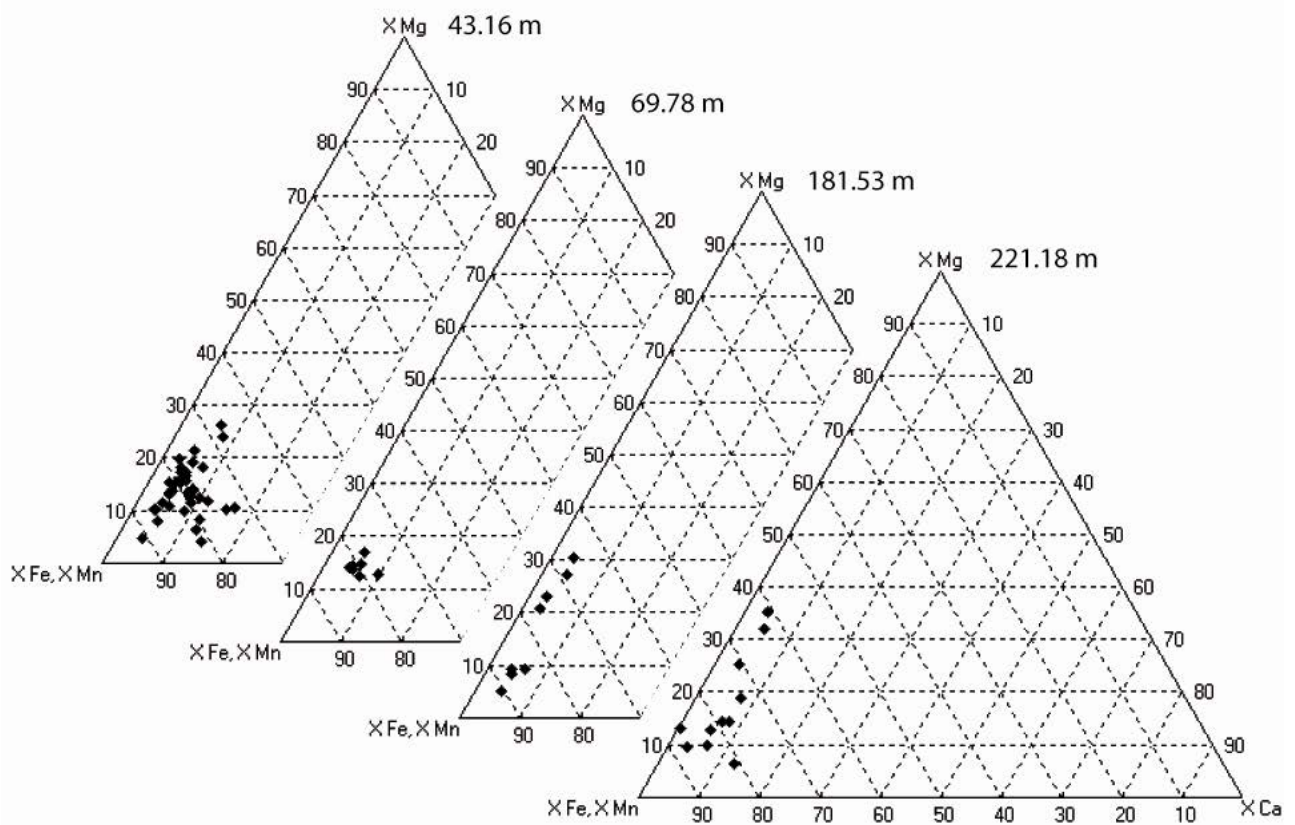


Fig. 8.5. Garnet composition of those samples containing most garnet grains.

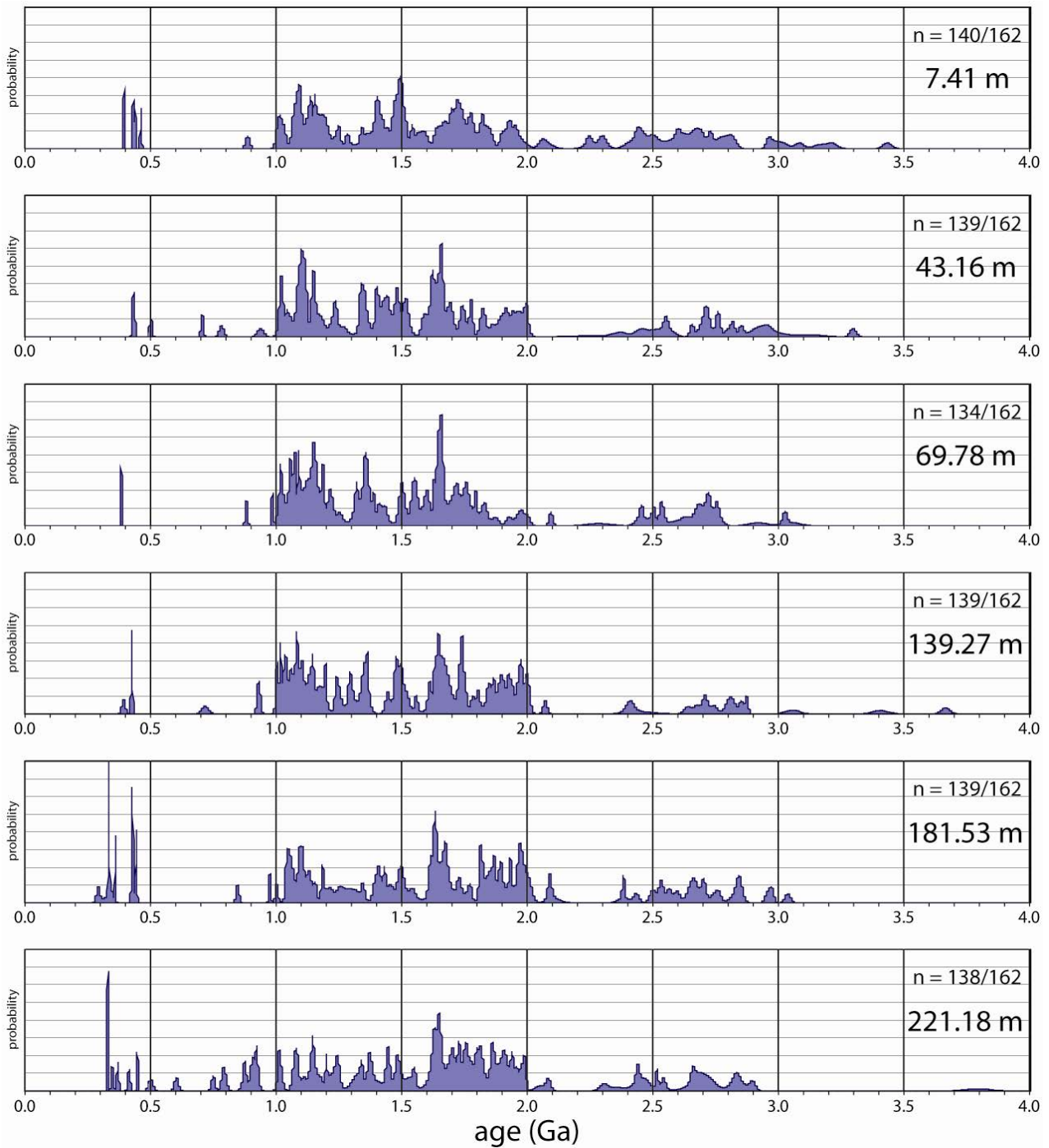


Fig. 8.8. Age distribution of the 6 zircon age dated samples of the Blokely core shown as probability distributions where the height and width of the peaks is controlled by the uncertainty of the age datings.

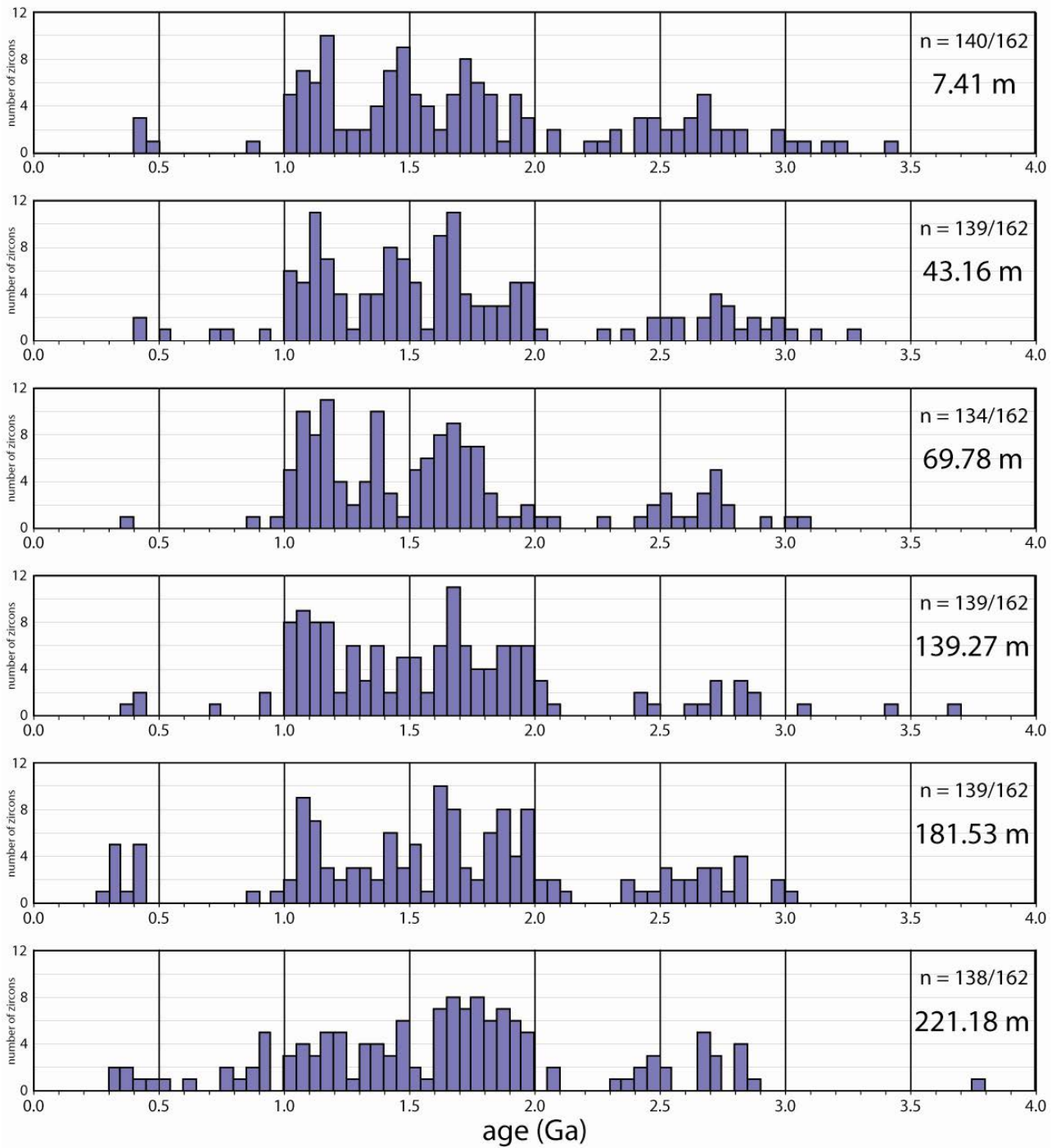


Fig. 8.9. Age distribution of the 6 zircon age dated samples of the Blokely core shown as histograms with 0.05 Ga intervals.

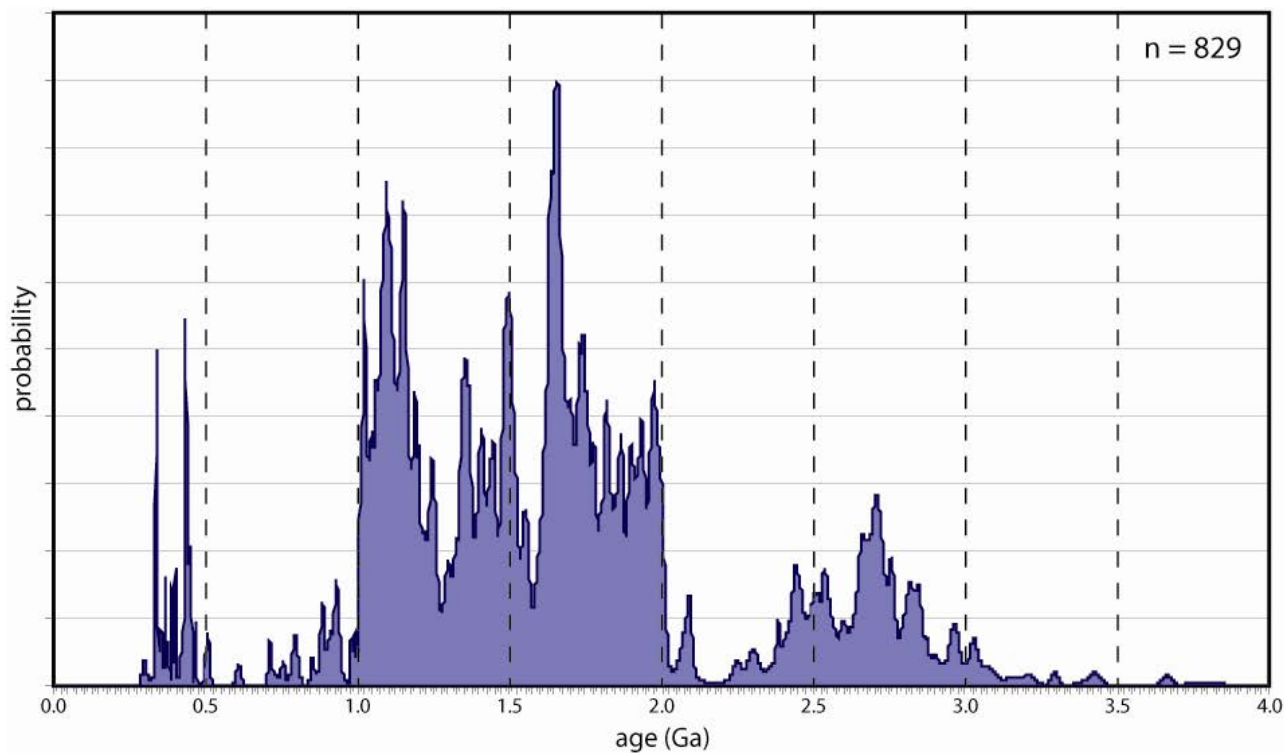


Fig. 8.10. All 829 concordant zircon ages of the 6 age datings have been merged to a common probability distribution in order to give a more homogeneous age distribution of the Jurassic sandstones.

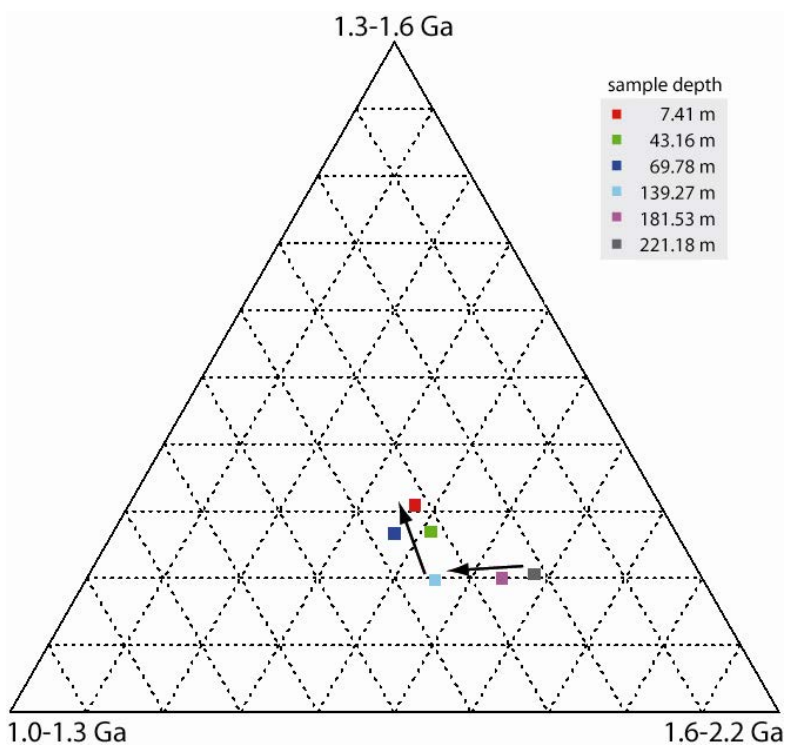


Fig. 8.11. Age trends of the 6 age datings divided into 3 age categories.

9. Igneous Intrusions

The succession in the Blokely drill core is cut by intrusive igneous rocks at four levels: 7.05–7.35 m (thickness 0.3 m), 26.40–27.10 m (thickness 0.70 m), 55.2–56.4 m (thickness 1.2 m) and 100.1–102.04 m (thickness 1.9 m). The three lower intrusions show horizontal boundary contacts to the host rock and thus appear to be sills. The uppermost intrusion shows oblique boundary contacts dipping 60° and is accordingly described as a dyke. The two thickest sills have caused prominent alteration of the surrounding sediments (see also chapter 5).

9.1 Lithology

The dyke and sills are lithologically similar and consist of fine-grained, sparsely plagioclase-olivine-phyric basalt. At the chilled contacts they are very fine-grained to aphanitic, altered, and cut by carbonate veins.

9.2 Petrography

Dyke, 7.05–7.35 m

Thin section 511101-161: Very fine-grained rock with sparse 0.5 mm plagioclase microphenocrysts all altered to secondary minerals. Groundmass intersertal with numerous plagioclase microlites.

Sill, 26.40–27.10 m

Very fine-grained nearly aphyric rock with scattered vugs filled with light minerals. The lower contact is not preserved. The rock becomes slightly finer grained towards the upper contact and there is possibly a thin glass chill at the top. There is no visible influence on the overlying sediments.

No thin sections.

Sill, 55.2–56.4 m

Thin section 511101-240: 55.24 m, upper chilled margin of the sill.

Very fine-grained rock with sparse 0.5 mm plagioclase microphenocrysts and tiny <0.5 mm euhedral olivine crystals all altered to clay. Groundmass intersertal with numerous plagioclase microlites.

Thin section 511101-241: 56.04 m, central part of the sill.

Fine-grained rock with sparse plagioclase phenocrysts <1 mm and sparse fresh olivine microphenocrysts c. 0.5 mm, assembled in glomerocrysts. Groundmass intergranular with plagioclase, clinopyroxene, Fe-Ti oxide, olivine, and abundant mesostasis.

Sill, 100.1–102.04 m

Thin section 511101-245: 102.01 m, lower chilled margin of the sill.

Aphanitic rock with sparse plagioclase microphenocrysts 0.1-0.2 mm. Strongly carbonated groundmass, but plagioclase phenocrysts are fresh. The rock is crosscut by 0.1–0.5 mm wide veins of carbonate and massive oxide.

Thin section 511101-246: 102.04 m, lower contact to sandstone (Fig. 9.3).

Aphanitic rock with many plagioclase microlites. A few plagioclase-olivine glomerocrysts with up to 2 mm plagioclase laths and 0.8 mm olivine crystals. Plagioclase is fresh but olivine completely altered. Groundmass is strongly carbonated. Carbonate veins cross both sill and sandstone. In the sill the veins contain massive oxide. The veins are thickest at the contact. The veins in the sandstone appear to fill tension cracks.

9.3 Chemical compositions

Two samples from the centres of the two lower sills have been analysed for major and trace elements. Major elements were analysed by J.G. Fitton at University of Edinburgh by X-ray fluorescence spectrometry (XRF) and procedures as described by Fitton *et al.* (1998). Trace elements were analysed in GEUS² Rock Geochemical Laboratory using a PerkinElmer Elan 6100 DRC Quadrupole Inductively coupled Plasma Mass Spectrometer (ICP-MS). Sample dissolution followed a modified version of the procedure used by Turner *et al.* (1999) and Ottley *et al.* (2003). Calibration was done using two certified REE solutions and three international reference standards. Results for reference samples processed and run simultaneously with the unknowns are normally within 5% of the reference value for most elements with concentrations > 0.1 ppm. The results are shown in Table 9.1.

The two sills consist of tholeiitic basalt. The lowermost sill has 5.6 ppm Pb which is very high, and it must be contaminated with Pb either during emplacement or from the drilling process; it is not otherwise clearly contaminated.

9.4 Discussion

The two lower sills have closely similar compositions and must be considered to be intruded during the same magmatic event. The tholeiitic basalt represents a magma type that is known from widespread sills and dykes in the Jameson Land Basin (Larsen *et al.* 1989; Hald & Tegner 2000). Hald & Tegner (2000) found five different magma types in sills and dykes, and by far the most common is the one found in the Blokelv sills. Figures 9.1 and 9.2 shows geochemical patterns for the Blokelv sills compared with similar patterns for the Jameson Land sills and dykes. The close similarity of the Blokelv sills with the major group of tholeiitic sills and dykes in Jameson Land is clearly seen.

Hald & Tegner (2000) dated a sill and a dyke from this rock group by the $^{39}\text{Ar}/^{40}\text{Ar}$ method. The sill yielded a 5-point isochron age of 52.0 ± 1.2 Ma, and the dyke yielded a four-point isochron age of 52.6 ± 1.4 Ma. It is therefore most probable that the Blokelv sills were emplaced at 52–53 Ma. Their petrography (alteration, few plagioclase phenocrysts) and chemistry (low K_2O) makes them poorly suited for $^{39}\text{Ar}/^{40}\text{Ar}$ dating.

9.5 Conclusions

The dyke and sills in the Blokelv drill core are compositionally similar to the main type of sills and dykes in the Jameson Land Basin. These are dated at 52–53 Ma, and the Blokelv dyke and sills most probably have the same age.

9.6 References

- Fitton, J.G., Saunders, A.D., Larsen, L.M., Hardarson, B.S. & Norry, M.J. 1998: Volcanic rocks from the Southeast Greenland margin at 63°N: composition, petrogenesis and mantle sources. In Saunders, A. D., Larsen, H. C. & Wise, S. H. (eds): Proceedings of the Ocean Drilling Program, Scientific Results 152: College Station, TX (Ocean Drilling Program), 331–350.
- Hald, N. & Tegner, C. 2000: Composition and age of tertiary sills and dykes, Jameson Land Basin, East Greenland: relation to regional flood volcanism. *Lithos* **54**, 207–233.
- Larsen, L.M., Watt, W.S. & Watt, M. 1989: Geology and petrology of the Lower Tertiary plateau basalts of the Scoresby Sund region, East Greenland. *Bulletin Grønlands Geologiske Undersøgelse* **157**, 164 pp.
- Ottley, C.J., Pearson, D.G. & Irvine, G.J. 2003: A routine method for the dissolution of geological samples for the analysis of REE and trace elements via ICP-MS. In: Holland, J.G. & Tanner, S.D. (eds): *Plasma Source Mass Spectrometry: Applications and Emerging Technologies*, 221–230. Cambridge: Royal Society of Chemistry.

Turner, S.P., Platt, J.P., George, R.M.M., Kelly, S.P., Pearson, D.G. & Nowell, G.M. 1999: Magmatism associated with orogenic collapse of the Beltic–Alboran domain, SE Spain. *Journal of Petrology* **40**, 1011–1036.

Jameson Land From				
Hald & Tegner (2000)				
Blokely				
	Middle sill	Lower sill	Dyke	Sill
Depth	55.2-56.4 m	100.1-102.0 m	0	0
Sample no	511101.230	511101.229	407203	403021
Major elements, wt% (XRF analyses)			Recalculated to 100%	
SiO ₂	47.84	48.43	48.87	48.90
TiO ₂	2.30	2.11	2.37	2.36
Al ₂ O ₃	13.71	12.87	13.94	13.97
Fe ₂ O ₃	14.07	12.95	14.21	14.24
MnO	0.206	0.260	0.20	0.21
MgO	6.85	6.24	7.07	7.04
CaO	11.23	12.08	11.65	11.61
Na ₂ O	2.23	2.03	2.42	2.40
K ₂ O	0.215	0.399	0.29	0.30
P ₂ O ₅	0.203	0.191	0.24	0.24
LOI	0.47	1.84		
Sum	99.33	99.40	100.00	100.00
Trace elements, ppm (ICP-MS analyses)				
Sc	38.37	35.91	39.69	37.69
Ti	1.38	1.28		
V	373.80	345.22	370.72	362.17
Cr	189.94	179.12	258.95	249.02
Mn	0.16	0.19		
Co	54.78	50.28	52.68	52.23
Ni	99.17	89.52	120.97	108.79
Cu	240.20	217.88	256.07	248.51
Zn	108.42	100.28	113.51	115.48
Ga	21.02	19.95		
Rb	3.41	8.70	5.33	6.26
Sr	217.35	230.08	236.91	227.87
Y	31.10	30.51	32.11	31.68
Zr	145.31	134.87	159.12	159.02
Nb	12.06	11.66	12.58	12.81
Cs	0.516	0.202	0.48	0.12
Ba	130.03	109.62	71.62	71.89

La	10.48	11.60	10.71	10.89
Ce	27.18	29.88	28.02	28.02
Pr	4.10	4.27	4.16	4.17
Nd	19.67	20.12	19.05	19.17
Sm	5.09	5.01	5.15	5.27
Eu	1.68	1.64	1.77	1.74
Gd	6.07	5.79	5.42	5.3
Tb	0.989	0.912	0.94	0.93
Dy	5.782	5.452	5.49	5.36
Ho	1.135	1.072	1.13	1.1
Er	3.090	2.954	2.91	2.87
Tm	0.467	0.438	0.43	0.43
Yb	2.767	2.687	2.65	2.61
Lu	0.413	0.387	0.36	0.38
Hf	3.767	3.466	3.6	3.57
Ta	1.123	1.373	0.84	0.84
Pb	0.909	5.609	1.29	1.71
Th	0.843	1.252	0.9	0.89
U	0.260	0.292	0.31	0.31

Table 9.1 Chemical analyses of two sills in the Blokely drill core, with comparisons.

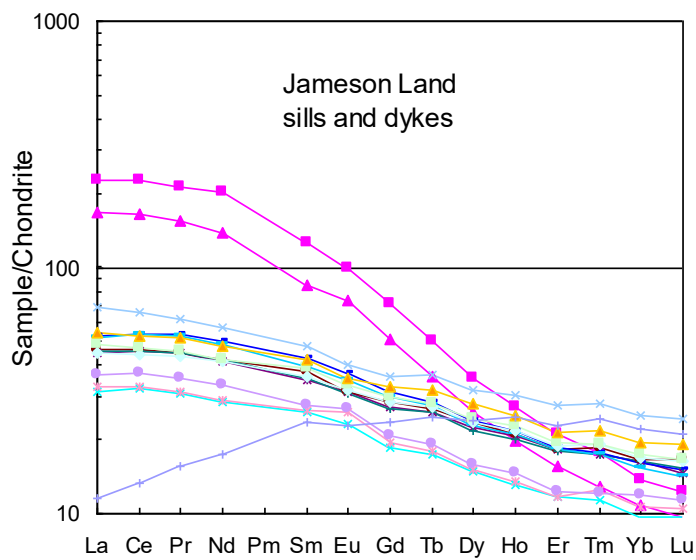
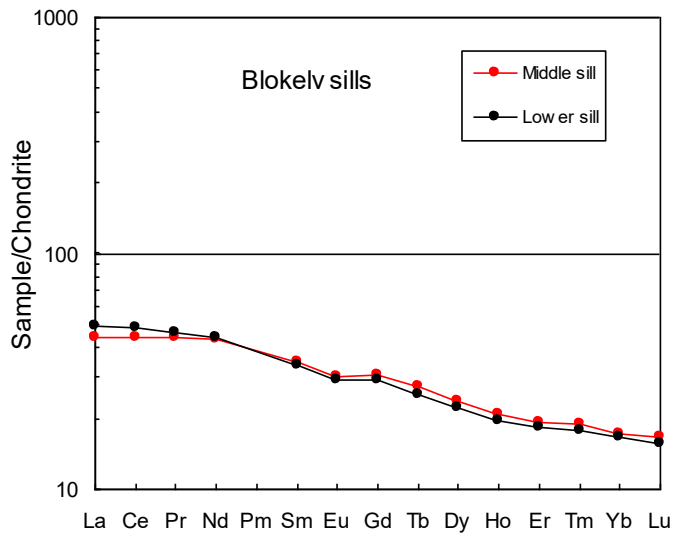


Fig. 9.1 Rare earth element patterns for the Blokelyv sills compared with sills and dykes in the Jameson Land Basin (from Hald & Tegner 2000). The pink patterns are from alkali basaltic sills.

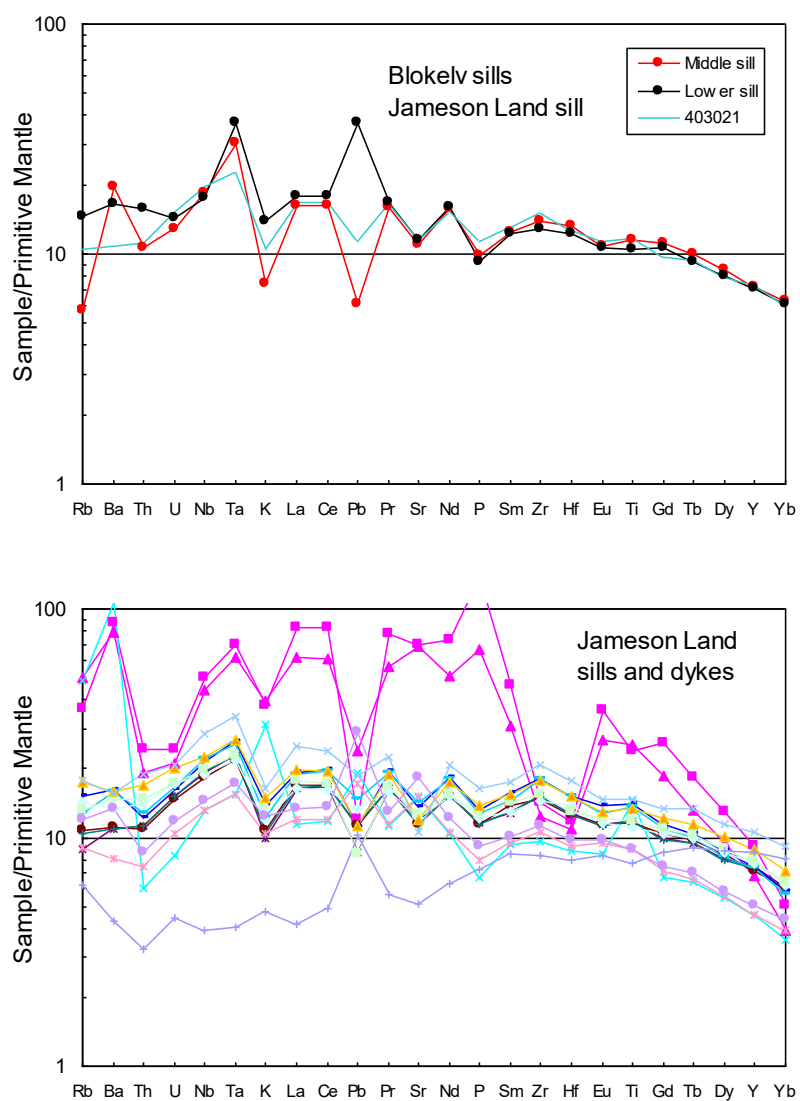


Fig. 9.2. Multi-element patterns for the Blokelyv sills compared with sills and dykes in the Jameson Land Basin (from Hald & Tegner 2000). The pink patterns are from alkali basaltic sills.

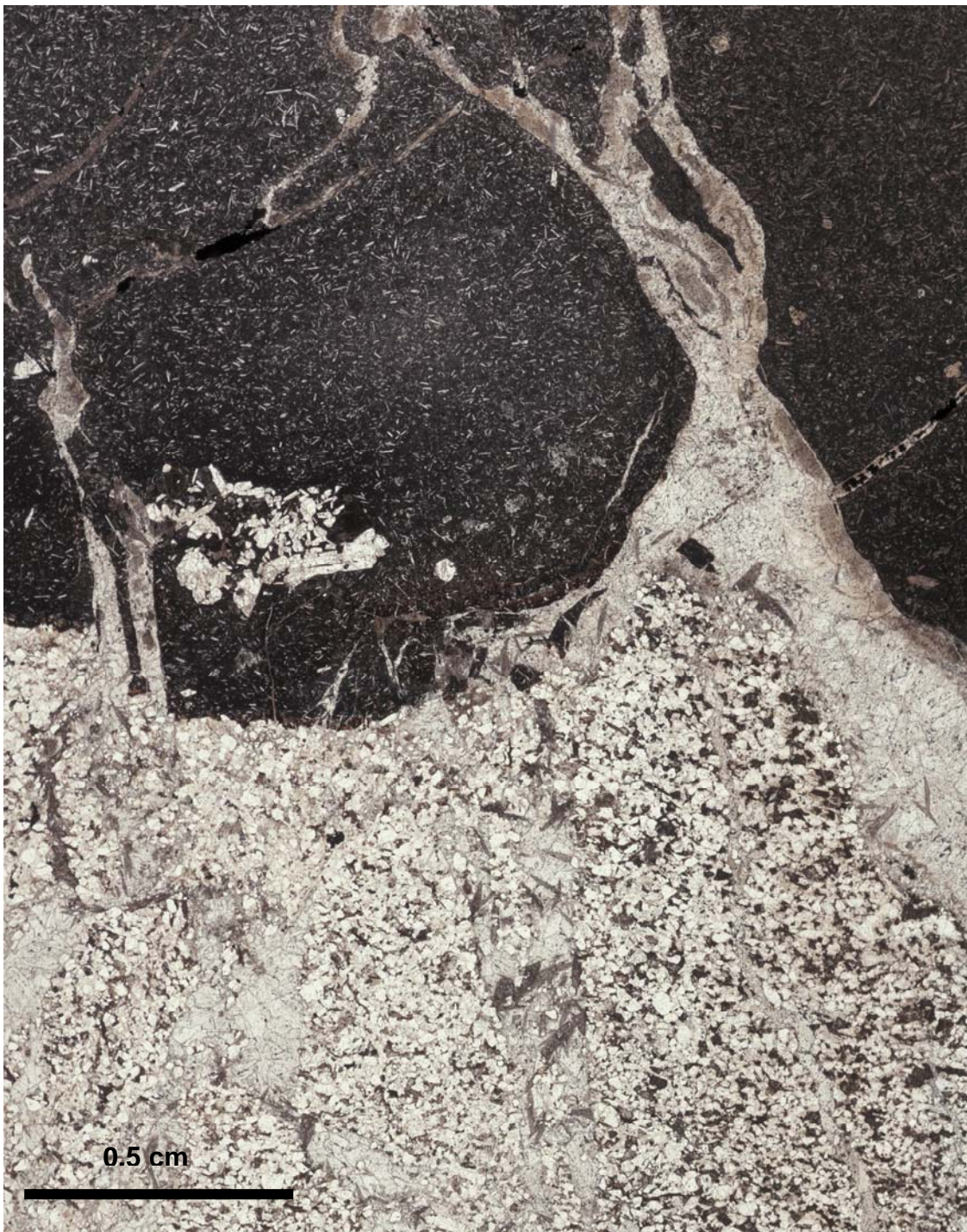


Fig. 9.3. Lower boundary contact of sill at 102.04 m. Note carbonate veins in the sill and in the sandstone. Thin section 511101-246.

10. Apatite Fission Track Analysis (AFTA)

Geotrack Report 1052 describes in detail the Thermal History Reconstruction study of the Blokely borehole based on new Apatite Fission Track Analysis (AFTA®) data in two core samples from the borehole, together with vitrinite reflectance (VR) and other organic maturity data provided by GEUS (Appendix 11.7). Here we summarise the main results and interpretations.

10.1 Thermal history reconstruction

The Blokely borehole intersected a 233.8 m section of Upper Jurassic sedimentary units, with igneous intrusions noted at depths of ~7, ~27, ~56 and ~101 metres. A present-day geothermal gradient of 30°C/km has been assumed for the section intersected in the borehole, although given the shallow depths involved, the thermal history solutions extracted from the AFTA data are not sensitive to this parameter.

10.1.1 Thermal history interpretation of AFTA data

Two samples of core were processed for AFTA from this borehole, with excellent apatite yields in each case. AFTA data from both samples provide highly reliable thermal history constraints. Measured fission track ages in both samples are significantly less than predicted from the Default Thermal History (see Appendix 11.7). This shows that the sampled units have been much hotter than present-day temperatures at some time after deposition (see also vitrinite reflectance data in chapter 7.2). This evidence comes from both the fission track age and track length data, which both display a greater degree of post-depositional annealing than can be explained on the basis of the Default Thermal History alone.

Quantitative interpretation of the AFTA data in each sample is summarised in Geotrack Report 1052 (Appendix 11.7). AFTA data in sample GC1052-1 at 6 m depth clearly require at least two palaeo-thermal episodes, while the AFTA data in sample GC1052-2 at 219 m depth appear to require three palaeo-thermal episodes, although the precise timing of the earliest episode cannot be defined with confidence.

Timing constraints derived from AFTA data in each sample are shown in Figure 10.1, where they are compared with the timing of three regional cooling episodes defined from AFTA in samples from southern Jameson Land and adjacent areas in a regional study of Eastern Greenland north of 70°N (Geotrack Report GC1016 for GEUS; see also Japsen *et al.* 2009). Cooling in these three episodes began in the intervals:

- 56 to 45 Ma (“Early Eocene”)
- 37 to 35 Ma (“Late Eocene”)
- ~12 Ma (“Middle Miocene”)

In the regional uplift study these events were interpreted in the following way (see Japsen *et al.* 2009):

- The Early Eocene event is recognised in AFTA data in samples of Jurassic and older age from Jameson Land and Milne Land. This extent overlaps with that of intensive Palaeogene intrusive activity and the timing correlates with the age of c. 53 Ma for a dyke on Jameson Land (see Chapter 9 in this Report). Paleotemperatures of the Early Eocene event are generally around 100°C or above, and show erratic variation with elevation. On this basis the palaeotemperatures characterising this episode are interpreted to be due either to contact or hydrothermal effects associated with igneous activity. No convincing evidence for any Paleocene to Eocene exhumation has been identified.
- The Late Eocene event is recognised in AFTA data in samples of Palaeogene and older age along most of East Greenland both north and south of 70° N. The event is most strongly expressed in the vicinity of Traill Ø and northwards. The event is, however, not recognised in samples from the remaining part of Jameson Land and from Milne Land, which may be due to the local effects of the Early Eocene and the Early Miocene events. Highest paleotemperatures in excess of 110°C are recognised from locations close to Late Eocene igneous intrusions on Traill Ø. Consequently, this episode is interpreted as representing regional uplift resulting in km-scale exhumation, while results from Traill Ø suggest a significantly higher basal heat flow in that area.
- The Middle Miocene event is recognised across most of East Greenland. The event is not recognised in the western parts of Jameson Land, but that is because of the strong signature of the Early Miocene event there. In most inland regions, Middle Miocene palaeotemperatures estimated for rocks that are now at sea level are typically found to be around 70 to 80°C, decreasing with increasing elevation to 60°C

or less. But around Traill Ø and Jameson Land, Middle Miocene palaeotemperatures are higher. This episode is interpreted as representing regional uplift resulting in km-scale exhumation combined with an elevated heat flow in the vicinity of Traill Ø, representing the diminishing signature of the Late Eocene intrusive activity.

Figure 10.1 illustrates a high degree of consistency between the timing of cooling identified in this study and the dominant regional episodes. On this basis, we interpret the results from sample GC1052-1 as representing the two most recent episodes (i.e. Late Eocene and Middle Miocene episodes), while all three episodes are recognised in sample GC1052-2.

10.1.2 Thermal history interpretation of VR data

Results of vitrinite reflectance analyses provided by GEUS for this report are shown in Fig. 10.2 together with equivalent VR (VReq) values derived from Rock-Eval Tmax values provided by GEUS. Also shown in the figure is the range of equivalent VR values derived from AFTA data in samples GC1052-1 and 2 and the VR profile predicted on the basis of the Default Thermal History. Both VR and VReq data plot well above the profile predicted by the Default Thermal History, confirming the evidence from AFTA that the sampled units have been hotter than their present-day temperatures at some time since deposition

In detail, the VR values tend to be slightly lower than the VReq values derived from the Tmax data throughout the section. In general, Tmax values tend to be sensitive to a range of factors and are not used quantitatively to provide estimates of maximum palaeotemperature in the same way that VR data are. But overall, the agreement between VR and VReq values from Tmax in Fig. 10.2 is sufficient to confirm the general trend of maturity with depth, with the two datasets defining an accurate trend with depth, first decreasing to depths around 30 m and then increasing at greater depths.

Maximum palaeotemperatures derived from the VR values show a general increase from 86 to 125°C through the section intersected in the borehole (see Fig. 10.3).

10.1.3 Integration of AFTA and VR data, palaeotemperature profiles and mechanisms of heating and cooling

Palaeotemperature constraints from AFTA and from the measured VR values are plotted against depth in Fig. 10.3. Comparison of maximum palaeotemperatures indicated by

AFTA and VR data reveals some consistencies and some differences. The range of maximum palaeotemperatures indicated by AFTA data in sample GC1052-1 (100 to 105°C) is higher than the corresponding values indicated by the shallowest VR values, which come from slightly greater depth. In contrast, the two techniques provide more consistent results around the depth interval from which AFTA sample GC1052-2 was collected.

Comparing palaeotemperatures from AFTA and VR data in the uppermost 50 m of the section, the decrease from AFTA in sample GC1052-1 to the VR data at slightly greater depth echoes the variation of VR and VReq with depth in Fig. 10.2. But on the basis of regional AFTA data from our regional AFTA database (Geotrack Report GC1016), we regard the Late Eocene event as pervasive in this region, and therefore we would expect measured VR values at shallow depth to be similar to the range of equivalent values defined from AFTA data in sample GC1052-1. The consistent expression of the Late Eocene episode in both AFTA samples supports this expectation. We therefore regard the measured VR values at shallow depths in this well as being slightly suppressed, as is often observed in Upper Jurassic organic-rich mudstones of the North Atlantic region. Palaeotemperatures from VR data at depths between ~150 and 200 m, together with Late Eocene palaeotemperatures derived from AFTA in samples GC1052-1 and -2 define a linear profile characterised by a palaeogeothermal gradient around 30°C/km, and Middle Miocene palaeotemperatures defined from AFTA in the two samples are interpreted in similar fashion. See Chapters 3 and 7 in this Report for a discussion of the differences between the organic material above (dominated by amorphous marine organic material) and below (marine organic material with a terrigenous component) c. 120 m in the cored interval.

The Early Eocene palaeotemperature revealed by AFTA data in sample GC1052-2 is then interpreted as representing localised heating restricted to the vicinity of this sample, and most likely represented by the VR data in adjacent samples. This interpretation is highly consistent with the explanation of regional palaeo-thermal data from southern Jameson Land and adjacent regions in Geotrack Report GC1016, in which the Middle Miocene and Late Eocene cooling episodes were regarded as representing successive episodes of exhumation, while Early Eocene effects were interpreted as due to local effects associated with igneous intrusions.

10.1.4 Thermal history synthesis

On the basis of the discussion presented above, we interpret the palaeotemperature constraints derived from AFTA and VR data in the Blokelyv borehole as representing the com-

bined effects of deeper burial followed by (at least) two episodes of exhumation, combined with localised heating due either to contact heating or hydrothermal effects associated with intrusive activity. The results provided here are highly consistent with regional data and the interpretation presented here is regarded as reliable.

10.1.5 Thermal history reconstruction

Here we present reconstructed thermal and burial-uplift histories for the section intersected in the Blokelyv borehole, based on the results presented above. It should be emphasised that while the preferred reconstruction illustrated here provides a satisfactory explanation of the AFTA and VR data from this well, the reconstruction is not unique. Therefore, it is important to appreciate those aspects of the histories that are constrained by the data, and those that are not. Factors that can be confidently defined in this study (within the limits of analytical uncertainty) include:

- Magnitude of heating at the palaeo-thermal maximum and the subsequent palaeo-thermal peaks
- Timing of the onset of cooling in each episode

Factors that can be defined when samples are available over a sufficiently large range of depths or elevations, but cannot be constrained in this study include:

- Palaeogeothermal gradients during each episode
- Additional burial during each episode for a specified values of palaeogeothermal gradient

Aspects which cannot be uniquely defined in any situation include:

- Thermal history prior to the palaeo-thermal maximum and/or the subsequent palaeo-thermal peak
- Amounts of re-burial between multiple episodes within a single unconformity
- Detailed style of cooling history from each episode

Figure 10.4 illustrates a possible thermal history reconstruction for the sedimentary units intersected in the Blokelyv borehole, based on the synthesis developed above. Key aspects of this reconstruction are:

- Surface temperature of 20°C at 30 Ma and earlier, decreasing to 10°C at 12 Ma and to the present-day value of 4°C over the last 12 Myr.
- Palaeogeothermal gradient of 30°C/km, constant to the present day.
- Localised heating within the vicinity of sample GC1052-2 to a palaeotemperature around 120°C, shown at ~53 Ma but any time between 56 and 45 Ma is allowed by the regional timing constraints on this episode.

- An additional 2750 metres of section deposited above the Late Jurassic section intersected in the borehole, between 146 and 36 Ma.
- Subsequent removal of 1150 metres of section between 36 and 30 Ma, followed by deposition of a further 600 metres of section between 30 and 12 Ma.
- Removal of the remaining 2200 metres of additional section between 12 Ma and the present day.

Note that the amount of re-burial between the two episodes of exhumation is not controlled by the data, and therefore also the exact amount of section removed in the initial episode beginning at 36 Ma is also not constrained. In this reconstruction, for the purposes of illustration the localised heating around sample GC1052-2 at ~53 Ma is shown as taking place over a duration of 2 Myr, as is the subsequent cooling. This reconstruction is considered to provide a reliable depiction of the history of the Upper Jurassic section intersected in the Blokølv borehole.

10.2 References

- Geotrack Report GC1016: *Thermal history of outcrop samples from East Greenland north of 70°N based on AFTA*. Green, P.F. 2009. Geotrack International, Victoria, Australia, 195 pp and appendices.
- Geotrack Report 1052: Thermal history reconstruction in the Blokølv borehole, East Greenland, based on AFTA and VR data. Green, P.F. 2009. Geotrack International, Victoria, Australia, 32 pp and appendices.
- Japsen, P., Bonow, J.M. & Green, P.F. 2009. Burial, uplift and exhumation history of East Greenland (70° to 75° N) based on AFTA data, the geological record and preliminary landscape analysis. Special study of uplift history. GEUS Report 2009/53, 135 pp.

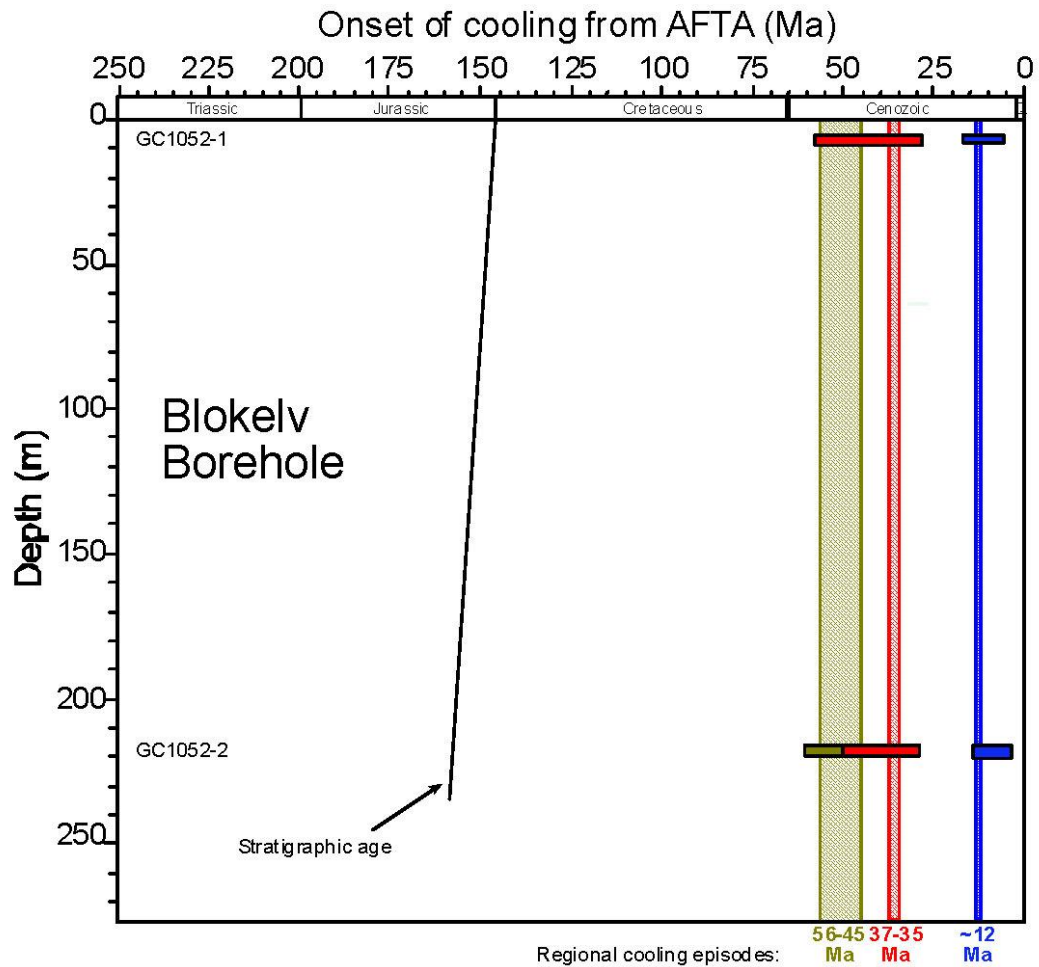


Figure 10.1 Timing constraints on cooling episodes derived from AFTA data in two samples from the Blokely Borehole. The timing of cooling in three regional palaeo-thermal episodes identified from AFTA data in a regional study of outcrop samples across Jameson Land and adjacent regions are also shown. The three episodes identified in samples from this study show good agreement with the timing of the regional episodes and the results presented in this report are interpreted on this basis.

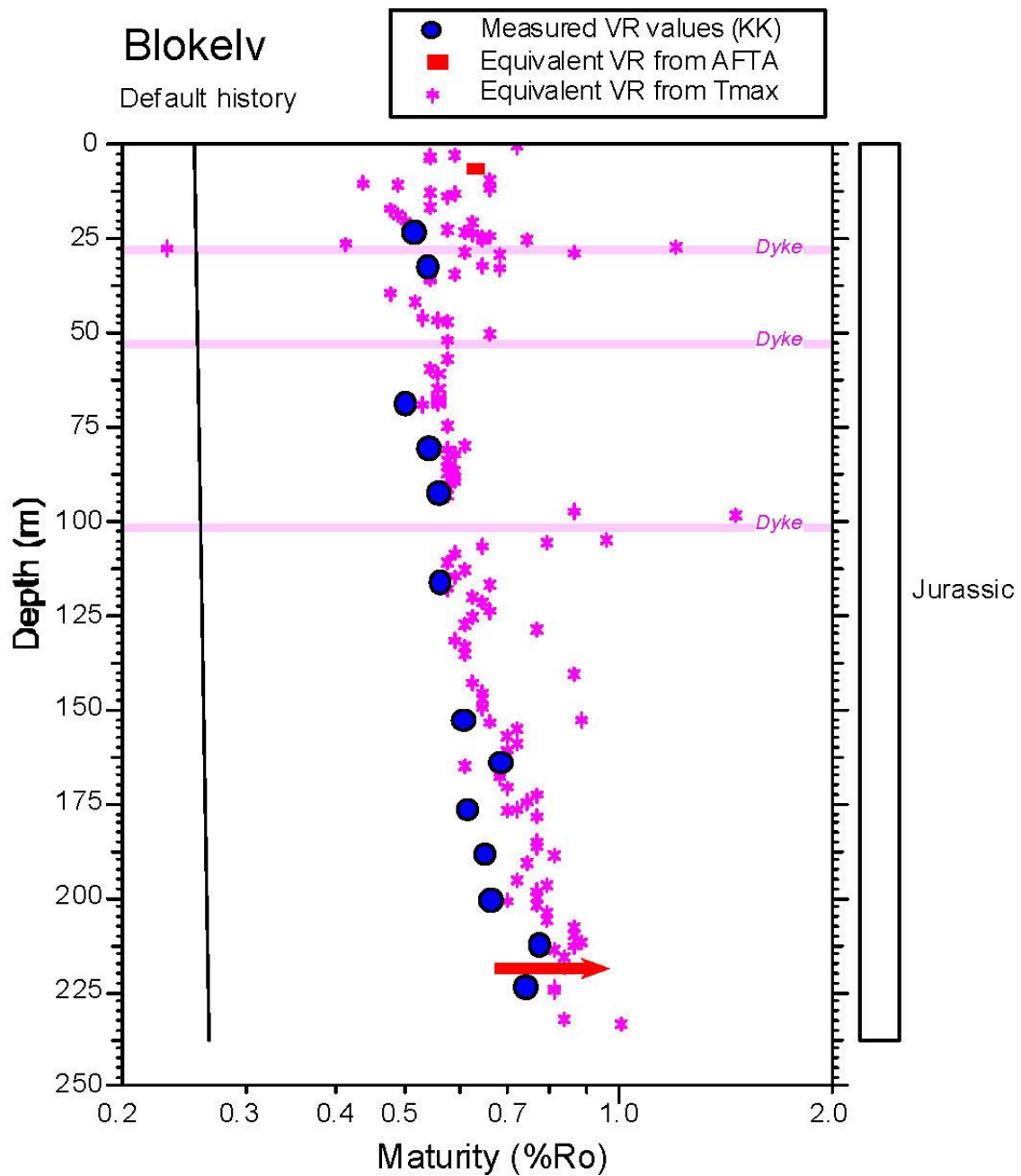


Figure 10.2 Vitrinite reflectance values in samples from the Blokely Borehole, plotted against depth (TVD rkb), together with equivalent VR values (VReq) derived from Rock-Eval Tmax data, and equivalent ranges of VR defined from the AFTA data. The solid line shows the profile predicted from the “Default Thermal History”, i.e., the history calculated from the assumption that all units throughout the well are currently at their maximum temperatures since deposition.

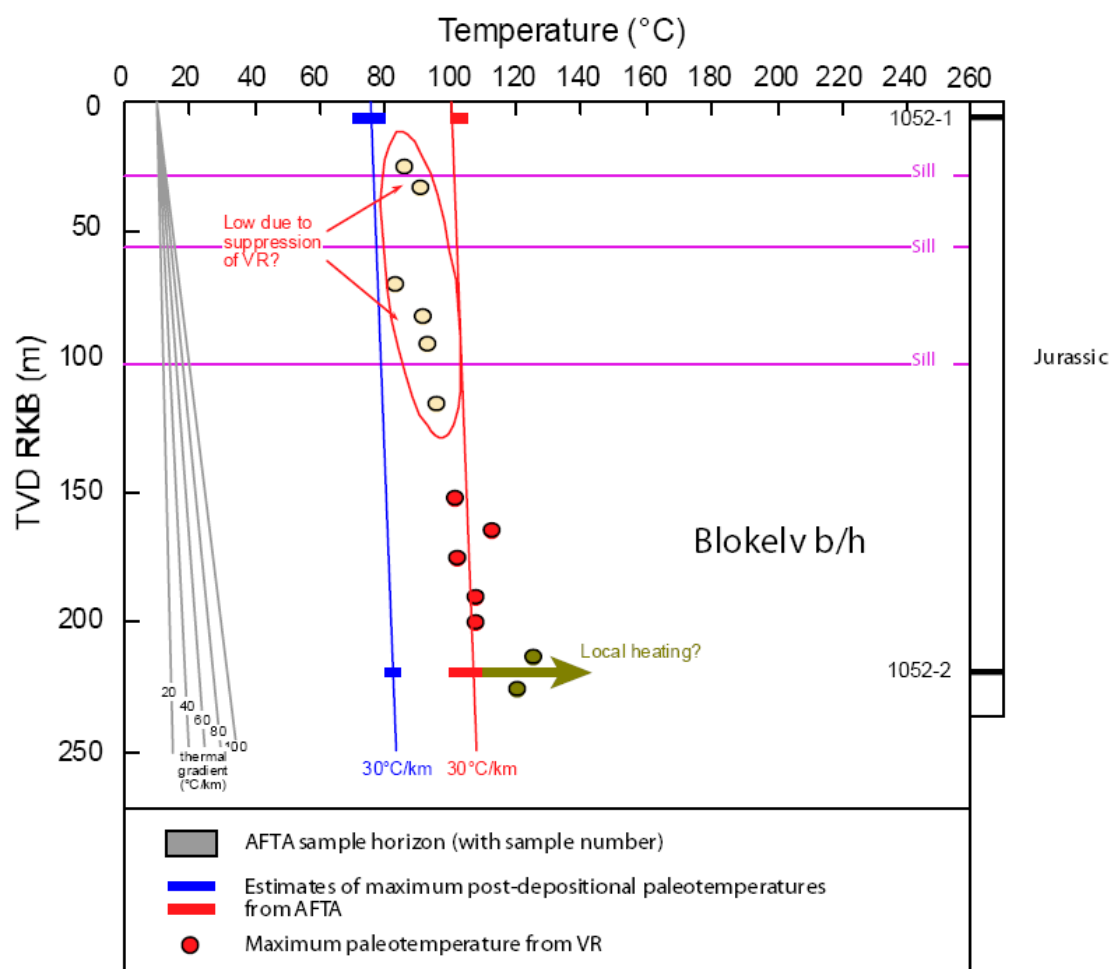


Fig. 10.3 Interpreted palaeotemperature profiles describing the palaeotemperatures in three episodes derived from AFTA and VR data in the Blokely Borehole. Based on evidence from an extensive regional study of East Greenland, we interpret the maximum palaeotemperature revealed by AFTA data in sample GC1052-2 as representing localised heating due to intrusive activity. The end-Eocene (37-35 Ma) and Miocene (~12 Ma) palaeotemperatures revealed by AFTA are interpreted as representing the effects of regional burial, with end-Eocene cooling representing the onset of regional exhumation, and Miocene cooling representing the final phase. On this basis, the VR values shallower than 120 m are interpreted as anomalously low, most likely due to suppression of reflectance in source-rock facies organic rich mudstones. VR values deeper than 120 m are regarded as providing reliable indications of the degree of post-depositional heating. Linear profiles representing various thermal gradients are shown, for reference, together two profiles representing with our preferred interpretation, based on regional data, involving palaeogeothermal gradients of ~30°C for the end-Eocene and Miocene episodes.

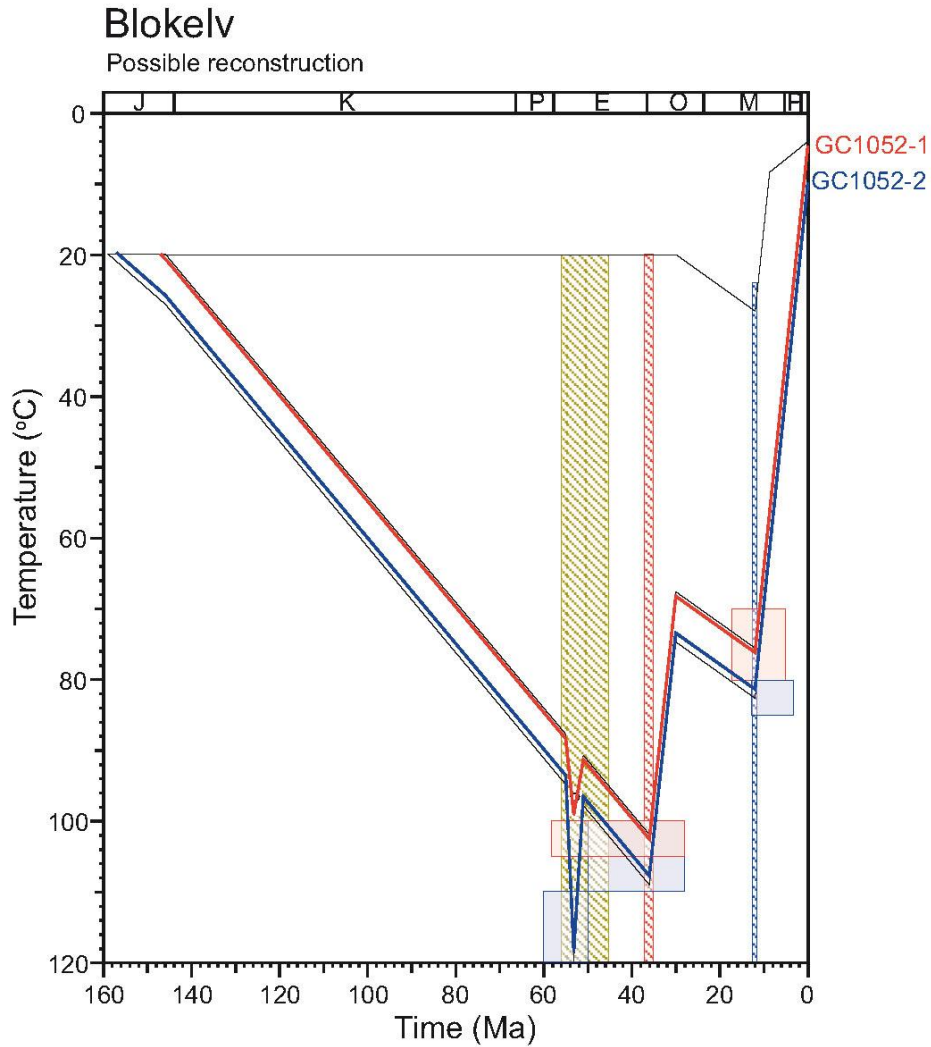


Fig. 10.4 Schematic illustration of the preferred thermal history reconstruction for the section intersected in the Blokelv Borehole, based on the AFTA and VR data presented in Geotrack Report 1052. The illustration compares palaeothermal constraints from AFTA in selected samples with thermal histories of the corresponding sample horizons, coded by colour. The vertical columns show the preferred timing of three dominant palaeo-thermal episodes identified in the region.

11. Appendix

11.1 Sedimentological profiles

11.2 Core photographs

11.3 Thin sections

11.4 Geochemistry data

11.5 Headspace gas analysis

11.6 Biomarker data

11.7 Thermal History reconstruction in the Blokely Borehole, East Greenland, based on AFTA® and VR data, GEOTRACK report.

11.8 Spectral Core Gamma Log for Blokely Well GGU 511101, data report

11.1 Appendix

Sedimentological logs of Blokely core 511101

Legend

Lithology



Mudstone



Siltstone



Heterolithic sandstone-mudstone



Muddy sandstone



Sandstone



Mudstone conglomerate



Igneous intrusion

Depositional environment



Sandstone, low density turbidite



Sandstone, intrusive



Sandstone, high density turbidite



Mudstone, basinal



Igneous intrusion

Bed contacts



Sharp/erosional or irregular



Irregular

Structures, biota and accessories



Planar lamination/bedding



Cross-lamination



Wavy bedding



Slump



Veins



Sandstone intrusion



Burrow



Mudstone intra clast



Bentonite



Quartz



Pyrite



Large mudstone clast



Coal



Belemnite



Bitumen



Ammonite



Bivalve



Brachiopod



Vertebrate



Base unit dip



Water escape structures



Concretion

Sjællandselv Mb/Hareelv Fm

Sjællandselv Mb/Hareelv Fm

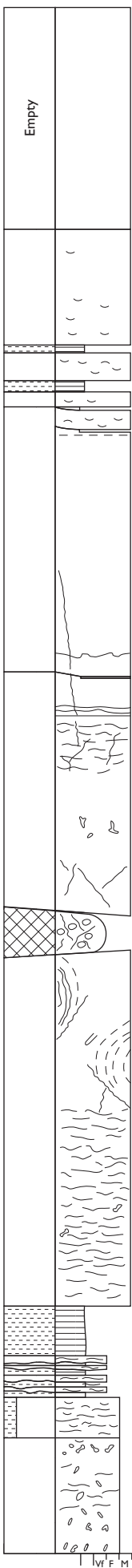
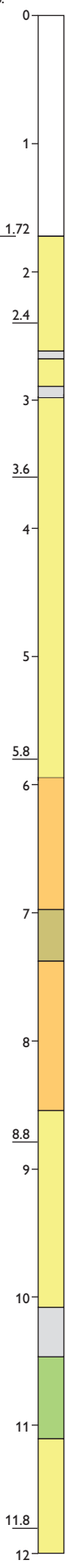
Katedralen Mb/Hareelv Fm

Box No.

Box 1

Box 2

Box 3

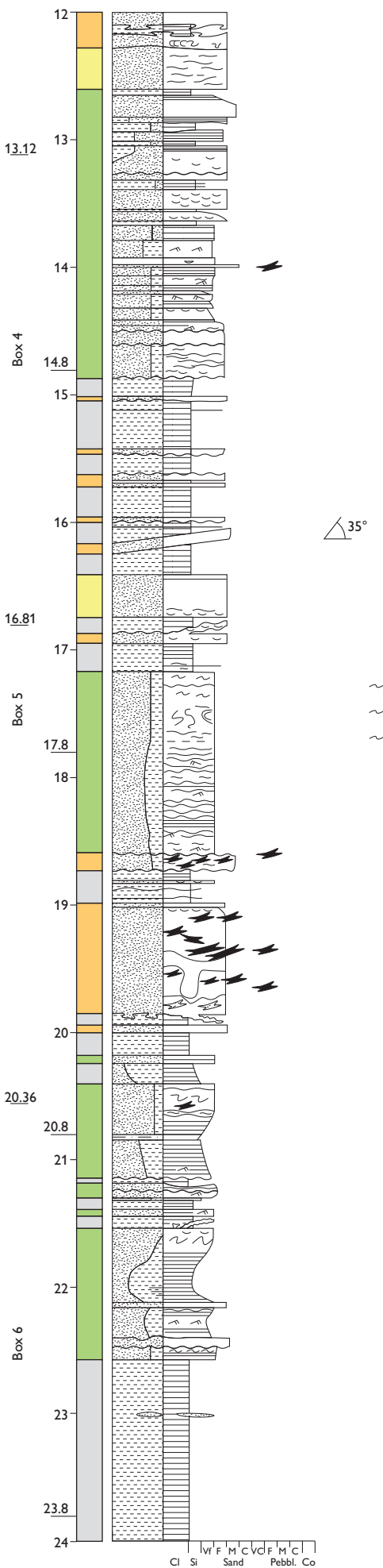


60°

Cl Si W F M C V F M C Pebbl. Co

Katedralen Mb/Hareelv Fm

Box No.



Cl Si Sand Pebbl. Co

Katedralen Mb/Hareelv Fm

Box No.

6
24.23

Box 7

Box 8

Box 9

Box 10

24-

25-

26-

26.4

27-

27.8

28-

29-

5.51

29.8

30-

31-

31.66

32-

32.8

33-

34-

35-

35.31

36-

Py

Qz

Py

40°

Py

Py

Py

Cl Si Ivf F M C V C F M C Pebbl. Co

Katedralen Mb/Hareelv Fm

Katedralen Mb/Hareelv Fm

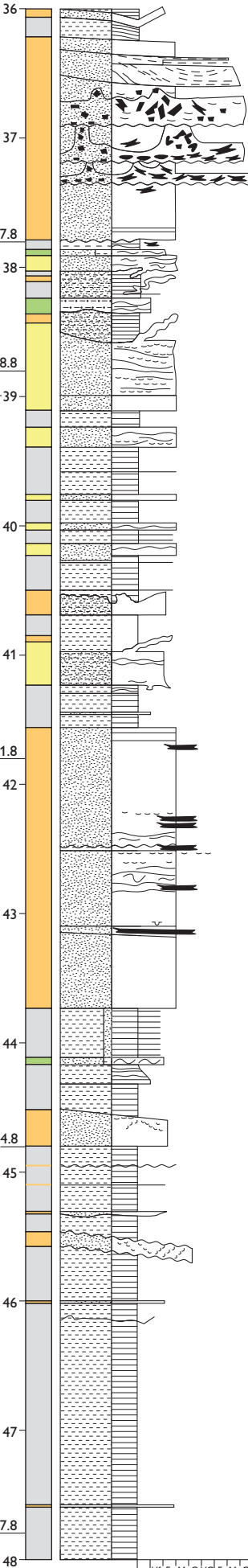
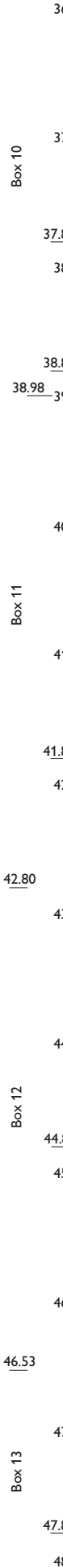
Box No.

Box 10

Box 11

Box 12

Box 13



20°

50°

25°

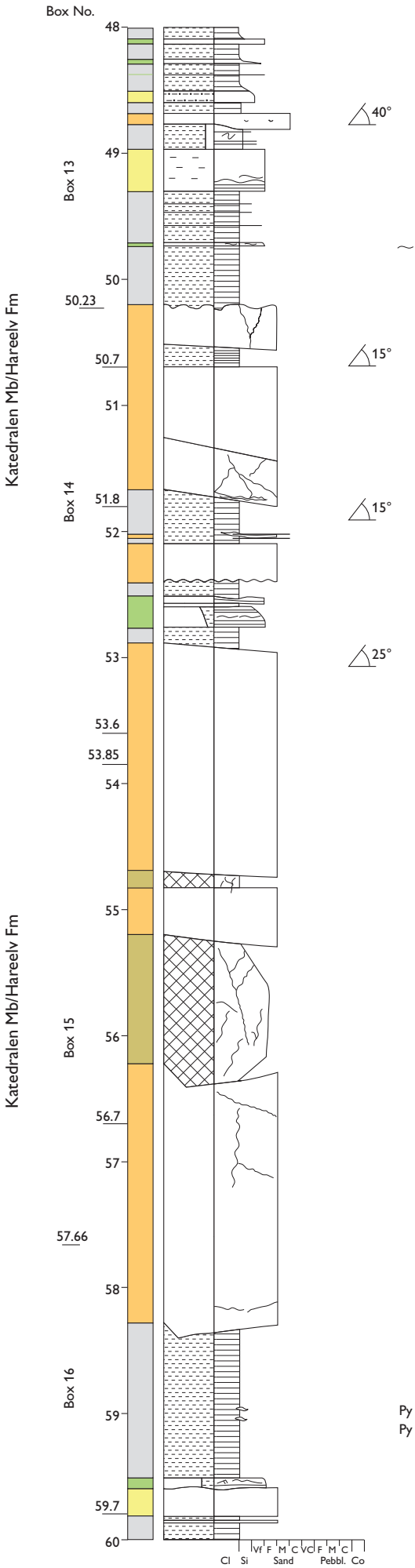
25°

30°

Py

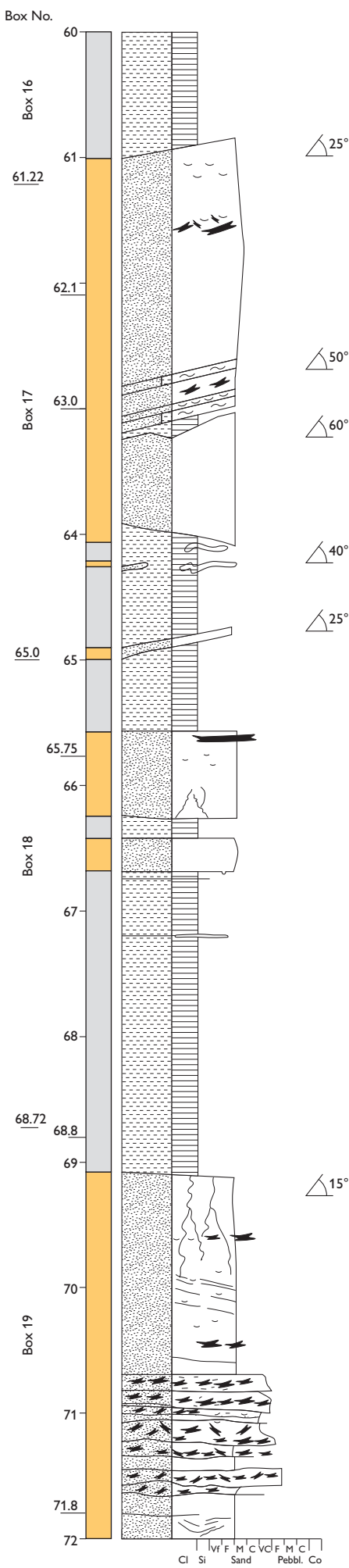
~

Cl Si V F M C V C F M C Pebbl. Co



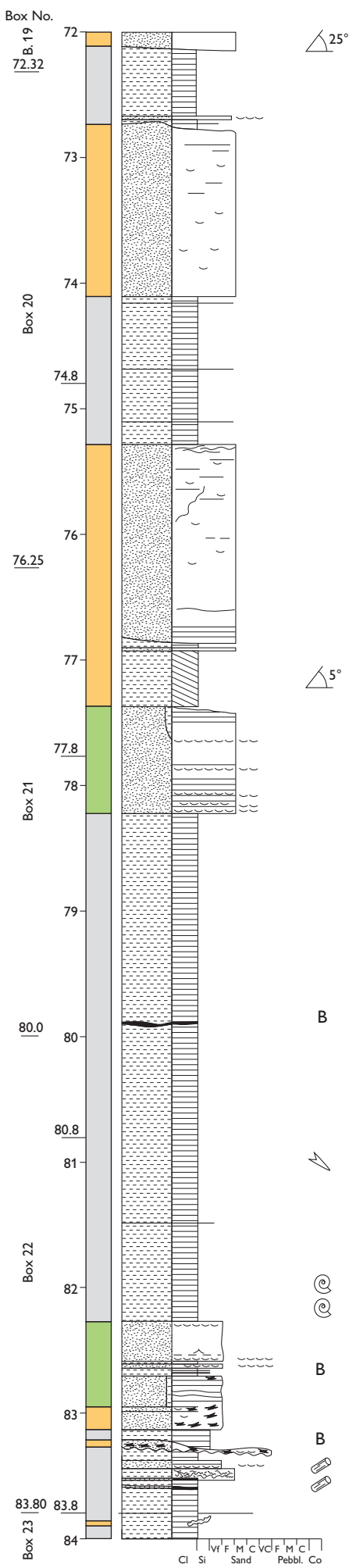
Katedralen Mb/Hareelv Fm

Katedralen Mb/Hareelv Fm



Katedralen Mb/Hareelv Fm

Katedralen Mb/Hareelv Fm



Katedralen Mb/Hareelv Fm

Katedralen Mb/Hareelv Fm

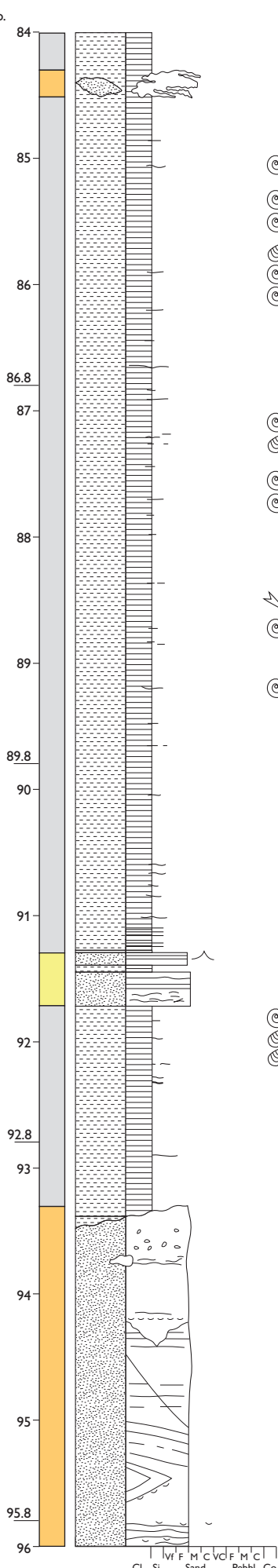
Box No.

Box 23

Box 24

Box 25

Box 26



Py

Py

Py

Py

Py

Py

Py

Py

Py

Py

Py

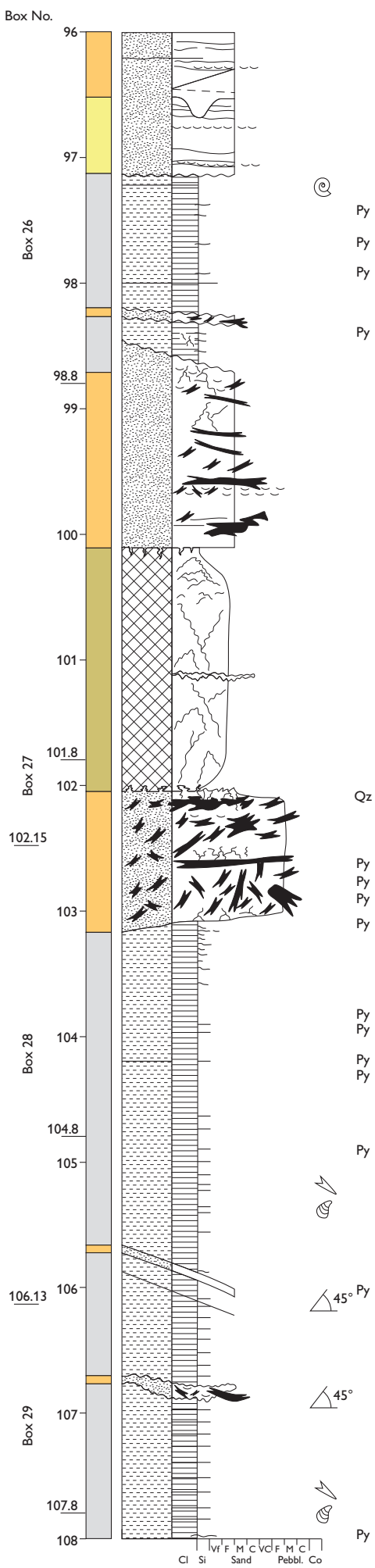
Py

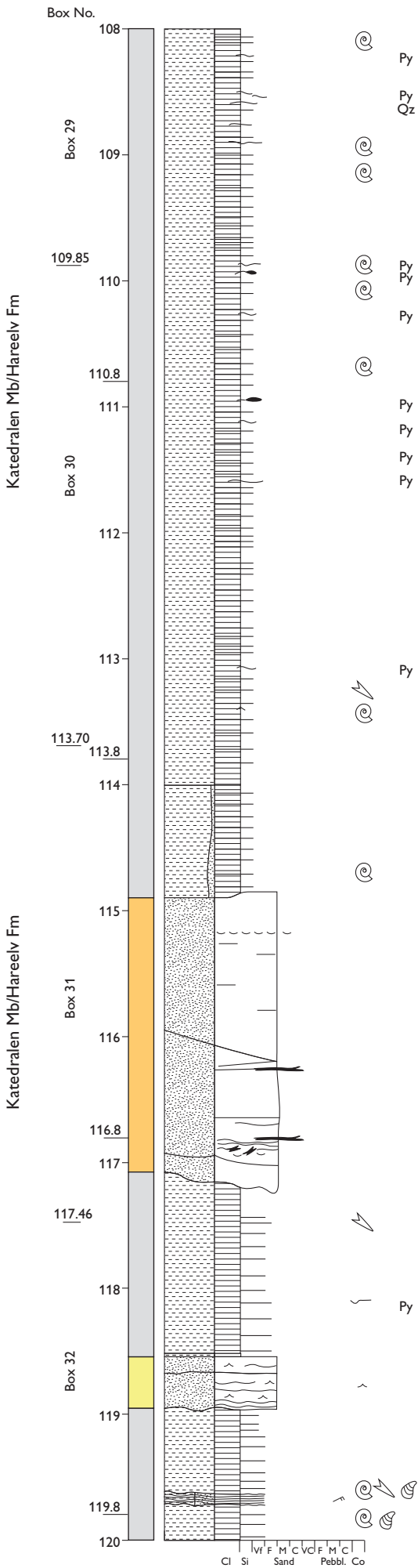
Py

Py

Katedralen Mb/Hareelv Fm

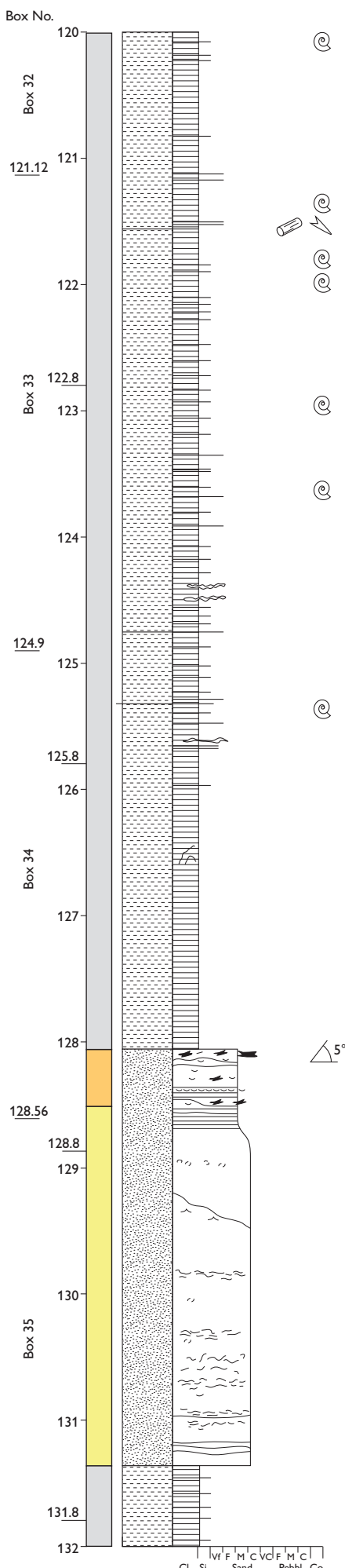
Katedralen Mb/Hareelv Fm





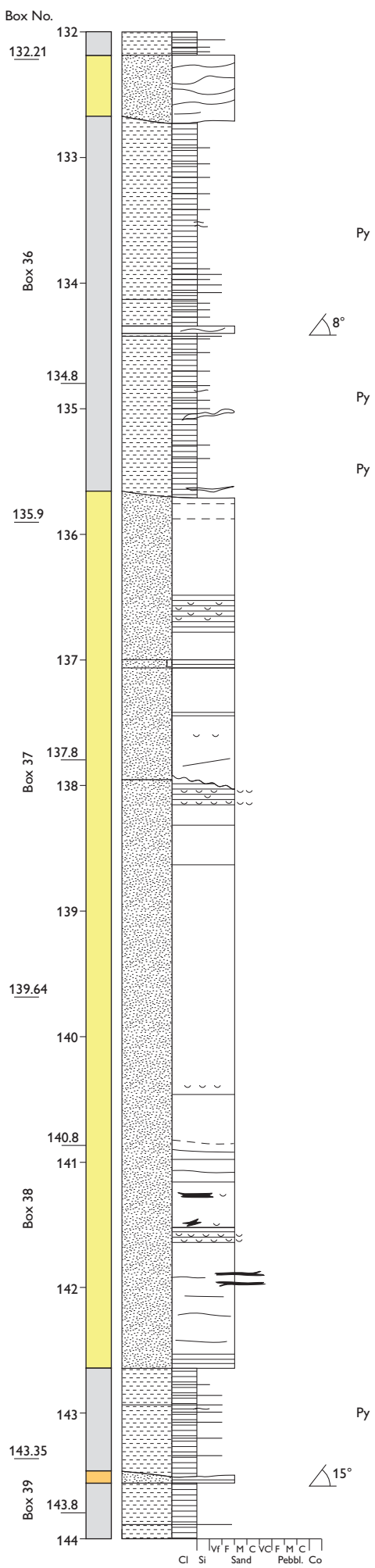
Katedralen Mb/Hareelv Fm

Katedralen Mb/Hareelv Fm



Katedralen Mb/Hareelv Fm

Katedralen Mb/Hareelv Fm



Katedralen Mb/Hareelv Fm

Katedralen Mb/Hareelv Fm

Box No.

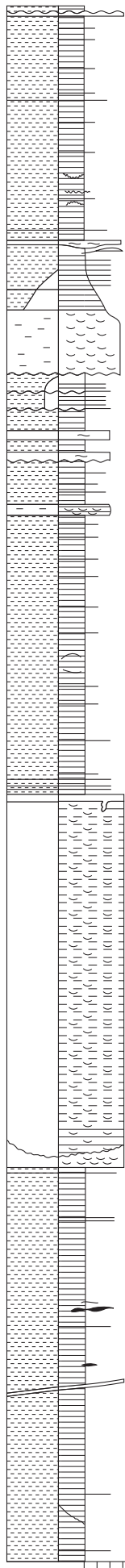
Box 39

Box 40

Box 41

Box 42

144
145
146
146.8
146.9
147
148
149
149.8
150
150.79
151
152
152.8
153
154
154.56
155
155.9
156



Qz
Qz
Qz

Qz

Py

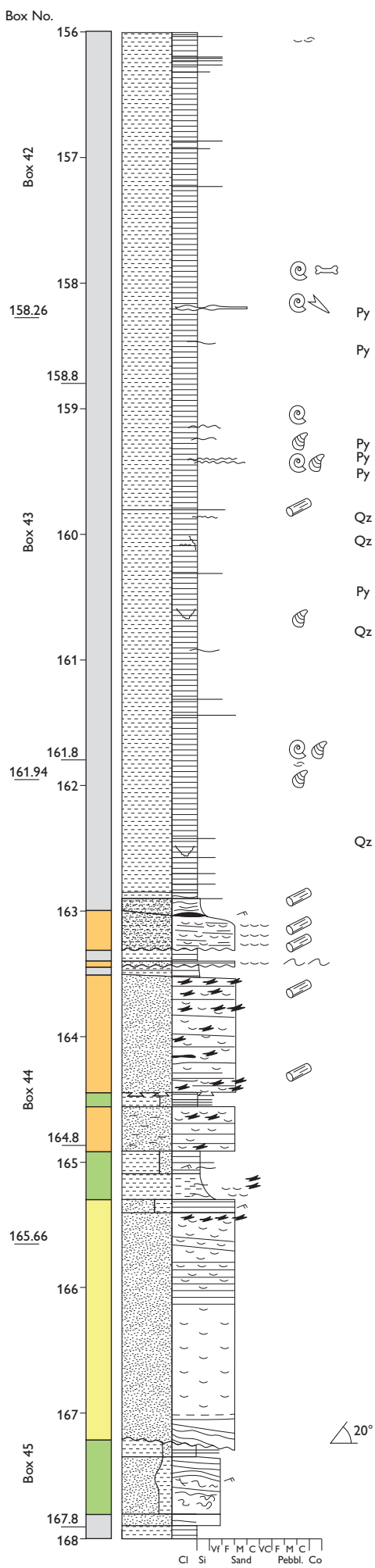
Py
Py
Qz

Py
Qz

Cl Si Ivf F M C Vd F M C Pebbl. Co

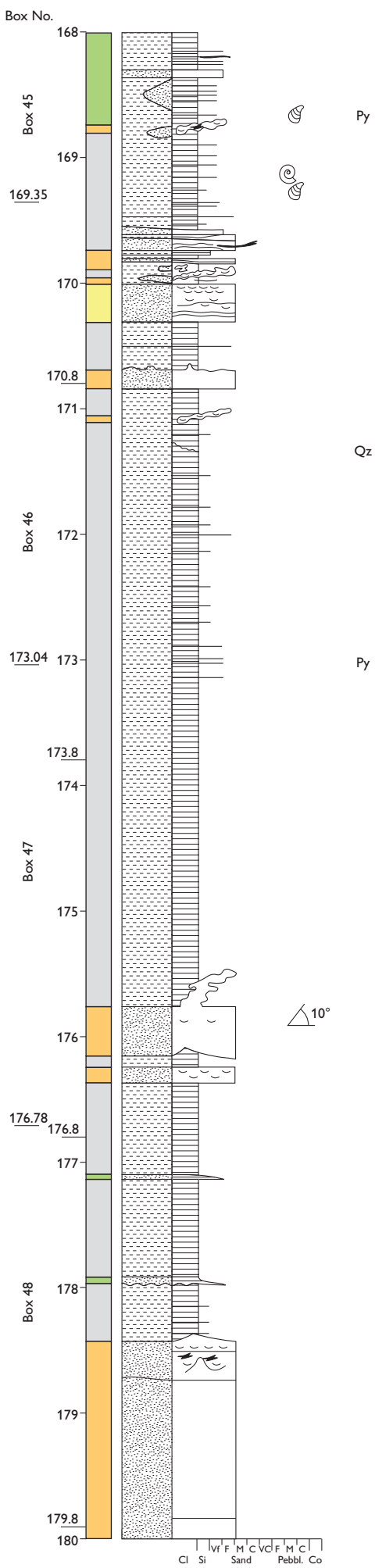
Katedralen Mb/Hareelv Fm

Katedralen Mb/Hareelv Fm



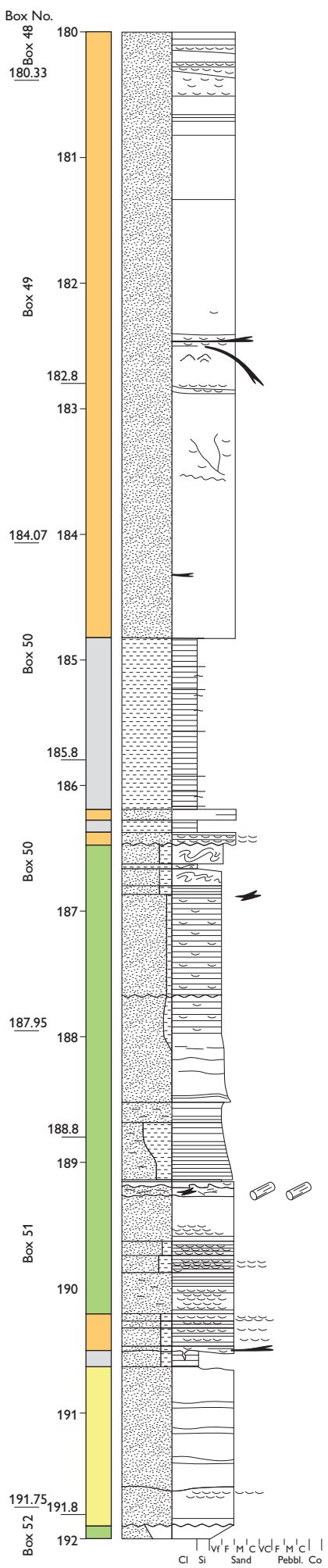
Katedralen Mb/Hareelv Fm

Katedralen Mb/Hareelv Fm



Katedralen Mb/Hareelv Fm

Katedralen Mb/Hareelv Fm



Py
Py

Py

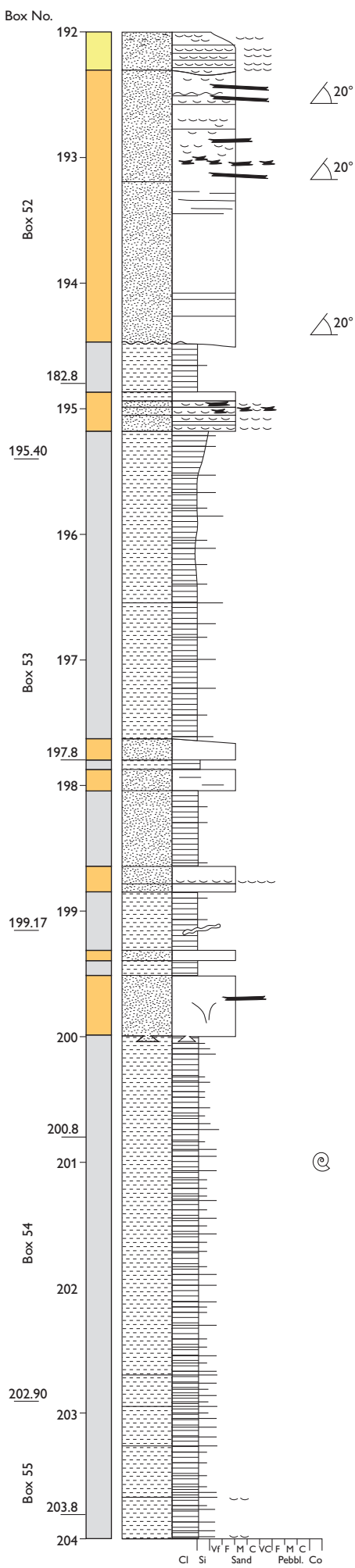
Z

Py

Cl Si Sand Pebbl. Co

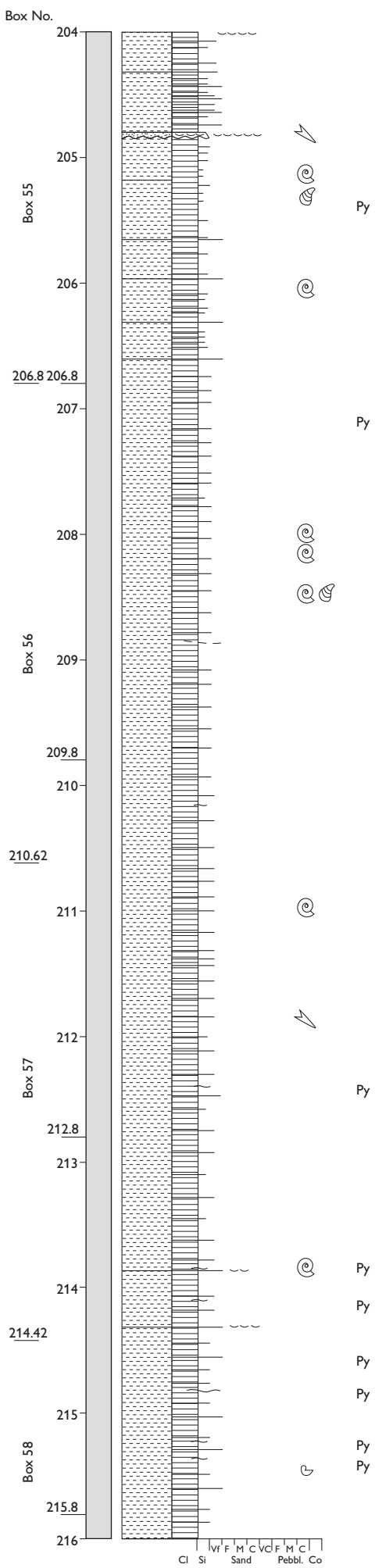
Katedralen Mb/Hareelv Fm

Katedralen Mb/Hareelv Fm



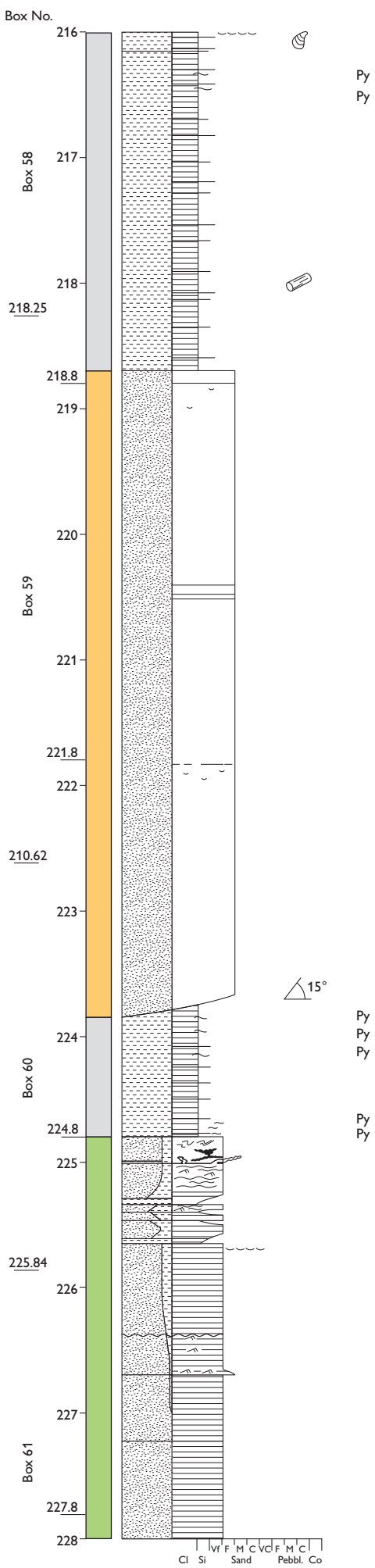
Katedralen Mb/Hareelv Fm

Katedralen Mb/Hareelv Fm

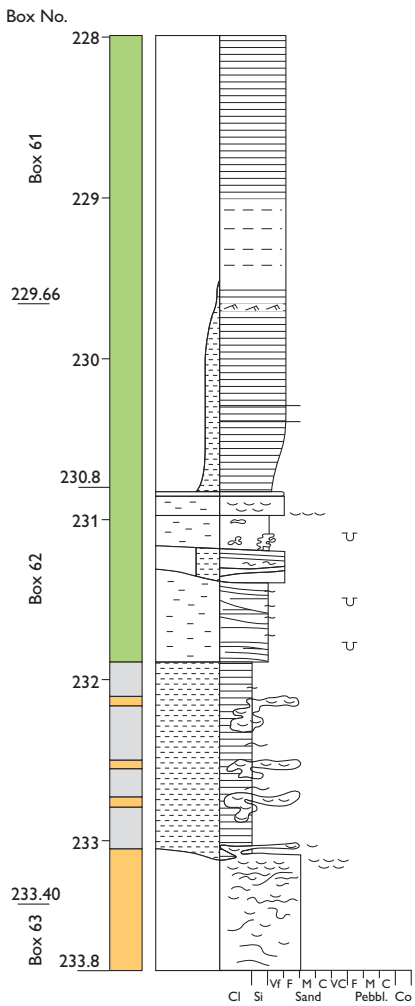


Katedralen Mb/Hareelv Fm

Katedralen Mb/Hareelv Fm



Katedralen Mb/Hareelv Fm



11.2 Appendix

Core photos of Blokely 511101

Images of cores recorded at drill site.

The cores are placed in 63 core boxes.

Filename include box number and depth interval in cm.

Upper left marks the top of each core box and lower right marks the bottom.

Core diameter is 5.6 cm, and individual core sections are up to 1 m in length.

Table: Blokely GGU 511101 Core Box Depths.

Box	Top	Bottom	Core length	Box	Top	Bottom	Core length
Box 1	1.72	5.51	3.79	Box 32	117.46	121.12	3.66
Box 2	5.51	9.33	3.82	Box 33	121.12	124.90	3.78
Box 3	9.33	13.12	3.79	Box 34	124.90	128.56	3.66
Box 4	13.12	16.81	3.69	Box 35	128.56	132.21	3.65
Box 5	16.81	20.56	3.75	Box 36	132.21	135.90	3.69
Box 6	20.56	24.23	3.67	Box 37	135.90	139.64	3.74
Box 7	24.23	27.80	3.57	Box 38	139.64	143.35	3.71
Box 8	27.80	31.66	3.86	Box 39	143.35	146.97	3.62
Box 9	31.66	35.31	3.65	Box 40	146.97	150.79	3.82
Box 10	35.31	38.98	3.67	Box 41	150.79	154.56	3.77
Box 11	38.98	42.80	3.82	Box 42	154.56	158.26	3.70
Box 12	42.80	46.53	3.73	Box 43	158.26	161.94	3.68
Box 13	46.53	50.23	3.70	Box 44	161.94	165.66	3.72
Box 14	50.23	53.85	3.62	Box 45	165.66	169.35	3.69
Box 15	53.85	57.66	3.81	Box 46	169.35	173.04	3.69
Box 16	57.66	61.22	3.56	Box 47	173.04	176.72	3.68
Box 17	61.22	65.00	3.78	Box 48	176.72	180.33	3.61
Box 18	65.00	68.77	3.77	Box 49	180.33	184.07	3.74
Box 19	68.77	72.32	3.55	Box 50	184.07	187.95	3.88
Box 20	72.32	76.25	3.93	Box 51	187.95	191.75	3.80
Box 21	76.25	80.00	3.75	Box 52	191.75	195.40	3.65
Box 22	80.00	83.80	3.80	Box 53	195.40	199.17	3.77
Box 23	83.80	87.60	3.80	Box 54	199.17	202.90	3.73
Box 24	87.60	91.35	3.75	Box 55	202.90	206.80	3.90
Box 25	91.35	95.20	3.85	Box 56	206.80	210.62	3.82
Box 26	95.20	98.80	3.60	Box 57	210.62	214.42	3.80
Box 27	98.80	102.45	3.65	Box 58	214.42	218.25	3.83
Box 28	102.45	106.13	3.68	Box 59	218.25	222.07	3.82
Box 29	106.13	109.85	3.72	Box 60	222.07	225.84	3.77
Box 30	109.85	113.70	3.85	Box 61	225.84	229.66	3.82
Box 31	113.70	117.46	3.76	Box 62	229.66	233.40	3.74
				Box 63	233.40	233.80	0.40



Box01 000-551.jpg



Box02 551-933.JPG



Box03 933-1312.JPG



Box04 1312-1681.JPG



Box05 1681-2056.JPG



Box06 2056-2423.JPG



Box07 2423-2780.JPG



Box08 2780-3166.JPG



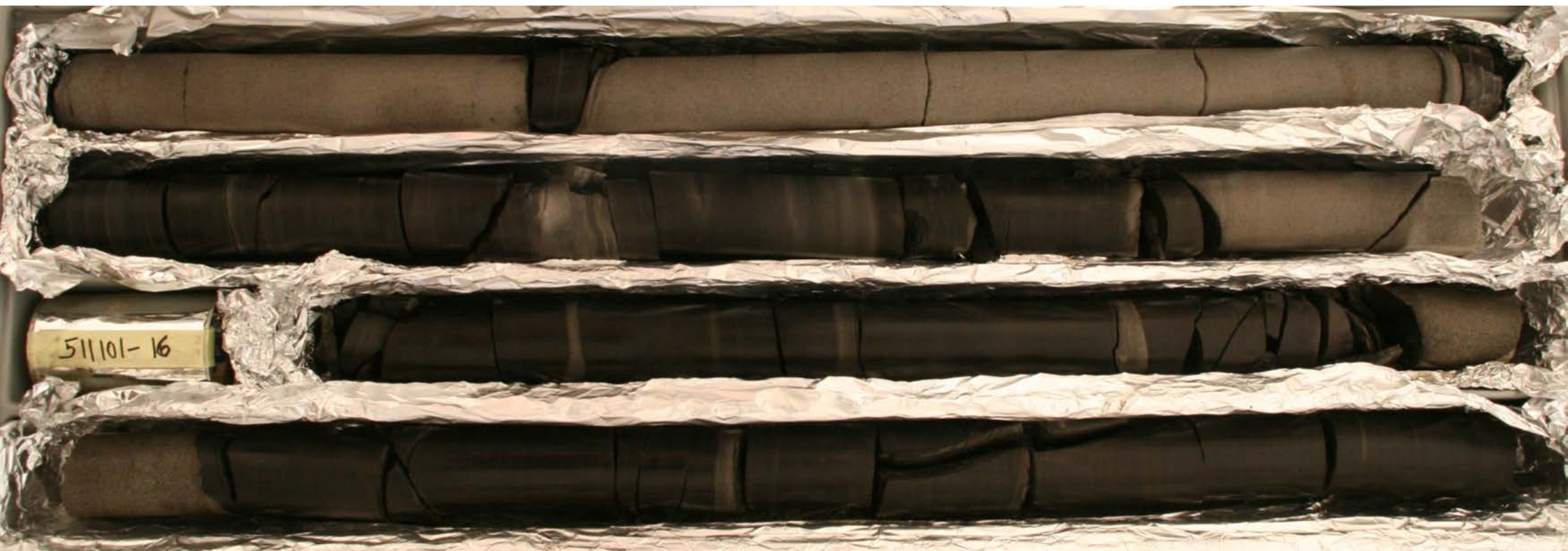
Box09 3166-3531.JPG



Box10 3531-3898.JPG



Box11 3898-4280.JPG



Box12 4280-4653.JPG



Box13 4653-5023.JPG



Box14 5023-5385.JPG



BOX15 5385-5766.JPG



Box16 5766-6122.JPG



Box17 6122-6500.JPG



Box18 6500-6877.JPG



Box19 6877-7232.JPG



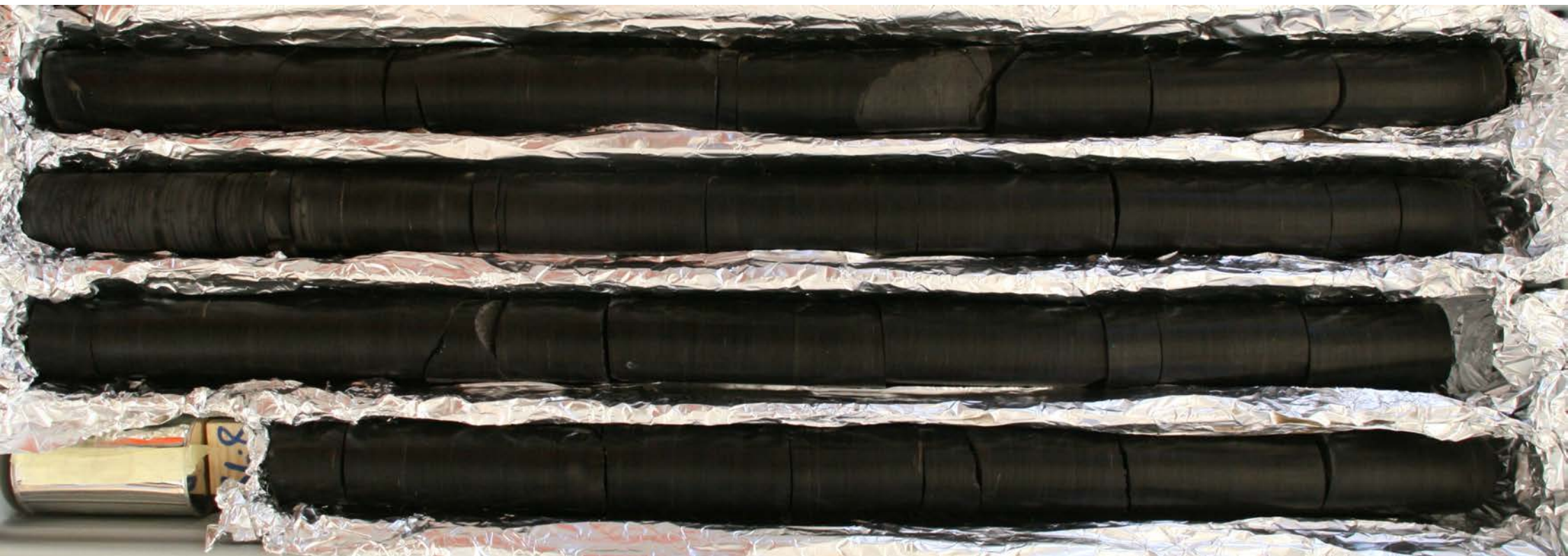
Box20 7232-7625.JPG



Box21 7625-8000.JPG



Box22 8000-8380.JPG



Box23 8380-8760.JPG



Box24 8760-9135.JPG



Box25 9135-9520.JPG



Box26 9520-9880.JPG



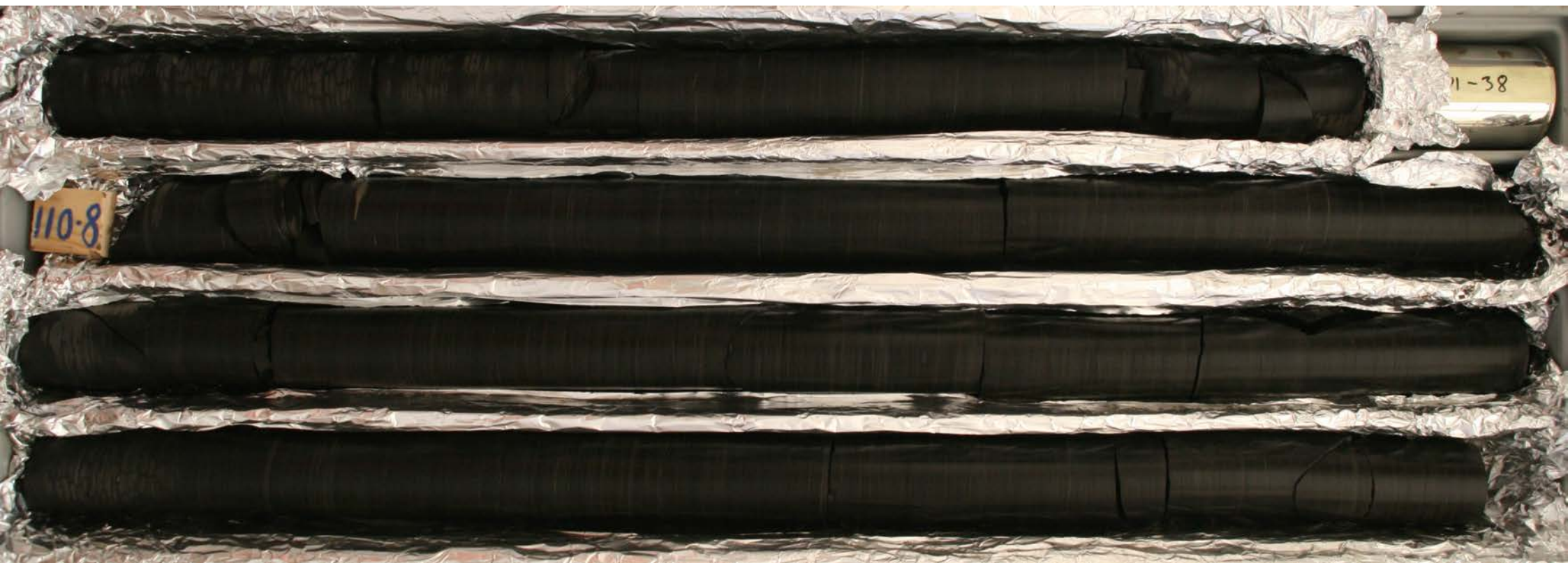
Box27 9880-10245.JPG



Box28 10245-10613.JPG



Box29 10613-10985.JPG



Box30 10985-11370.JPG



Box31 11370-11746.JPG



Box32 11746-12112.JPG



Box33 12112-12490.JPG



Box34 12490-12856.JPG



Box35 12856-13221.JPG



Box36 13221-13590.JPG



Box37 13590-13964.JPG



Box38 13964-14335.JPG



Box39 14335-14697.JPG



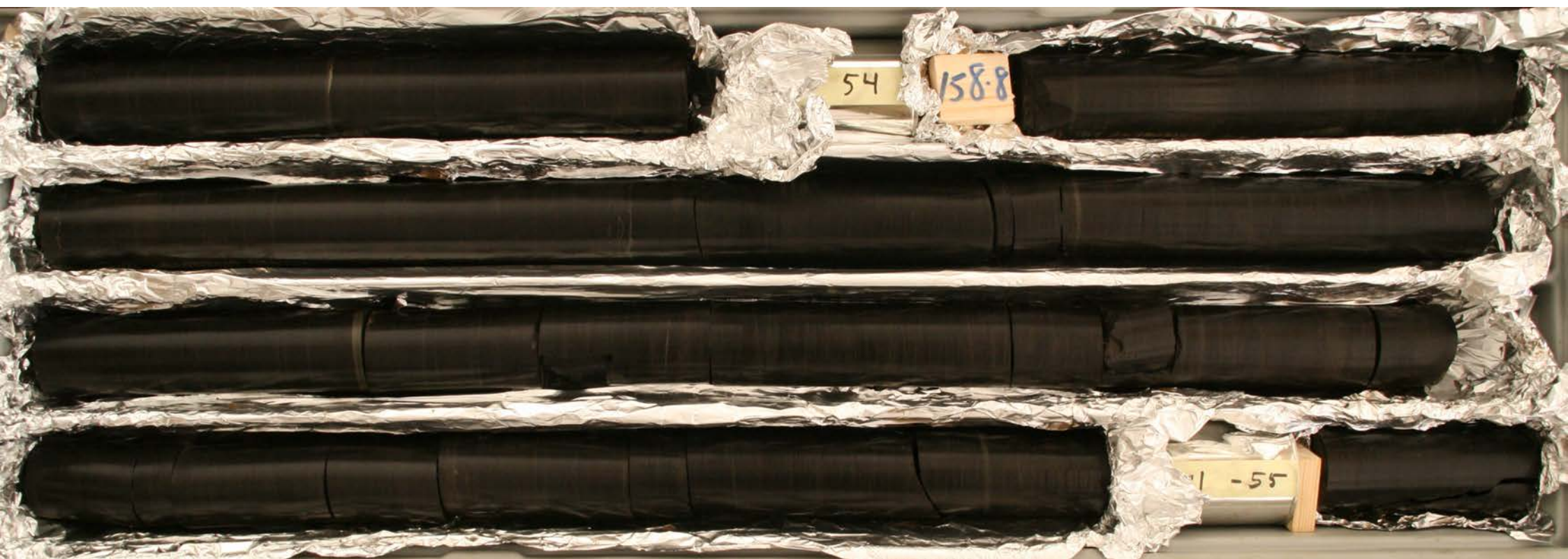
Box40 14697-15079.JPG



Box41 15079-15456.JPG



Box42 15456-15826.JPG



Box43 15826-16194.JPG



Box44 16194-16566.JPG



Box45 16566-16935.JPG



Box46 16935-17304.JPG



Box47 17304-17672.JPG



Box48 17672-18033.JPG



Box49 18033-18407.JPG



Box50 18407-18795.JPG



Box51 18795-19175.JPG



Box52 19175-19540.JPG



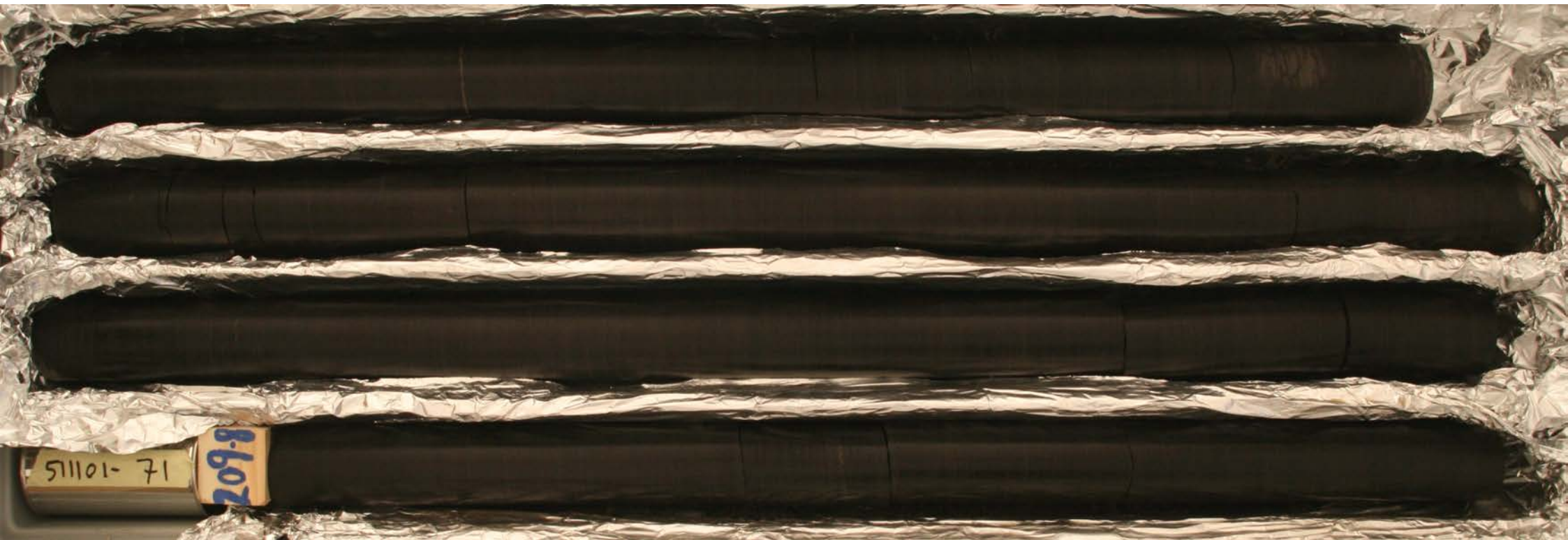
Box53 19540-19917.JPG



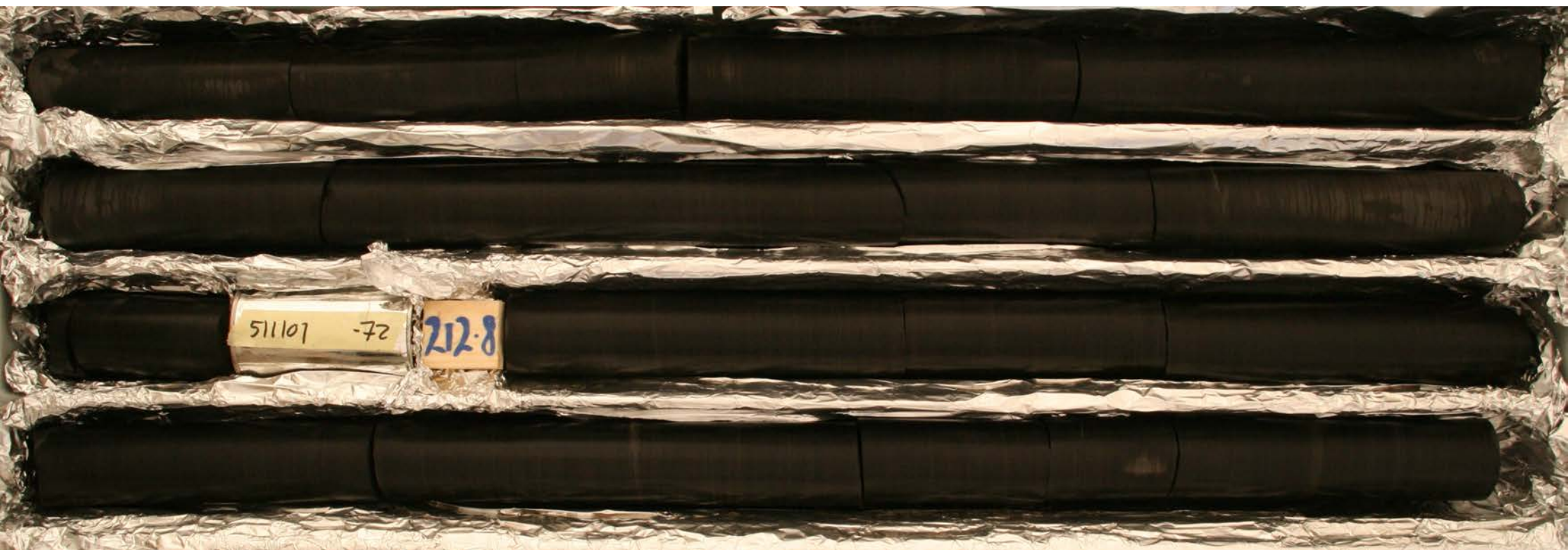
Box54 19917-20290.JPG



Box55 20290-20680.JPG



Box56 20680-21062.JPG



Box57 21062-21442.JPG



Box58 21442-21825.JPG



Box59 21825-22207.JPG



Box60 22207-22584.JPG



Box61 22584-22966.JPG



Box62 22966-23340.JPG



Box63 23340-23380.JPG

11.3 Appendix

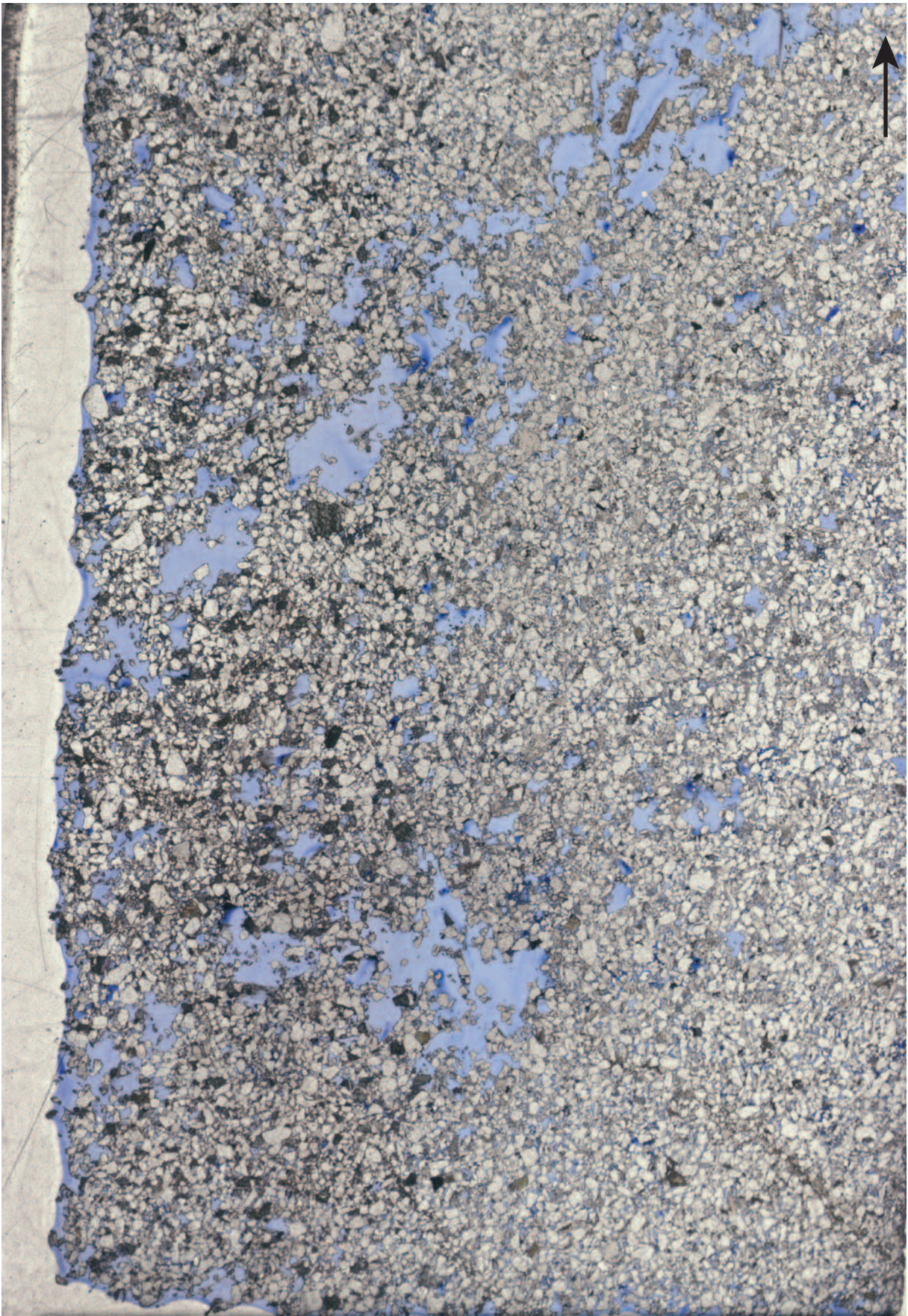
Thin sections of Blokely 511101 core

Scan images of thin sections.

Sample name of thin section is inserted and includes top depth in cm.

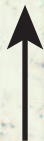
Arrow show upward direction.

Thin sections are impregnated with blue epoxy and ~1/2 of each thin section was etched and stained with sodium cobaltnitrite.



0.5 cm

511101-157 446 cm.tif



0.5 cm

511101-239 557cm.ai

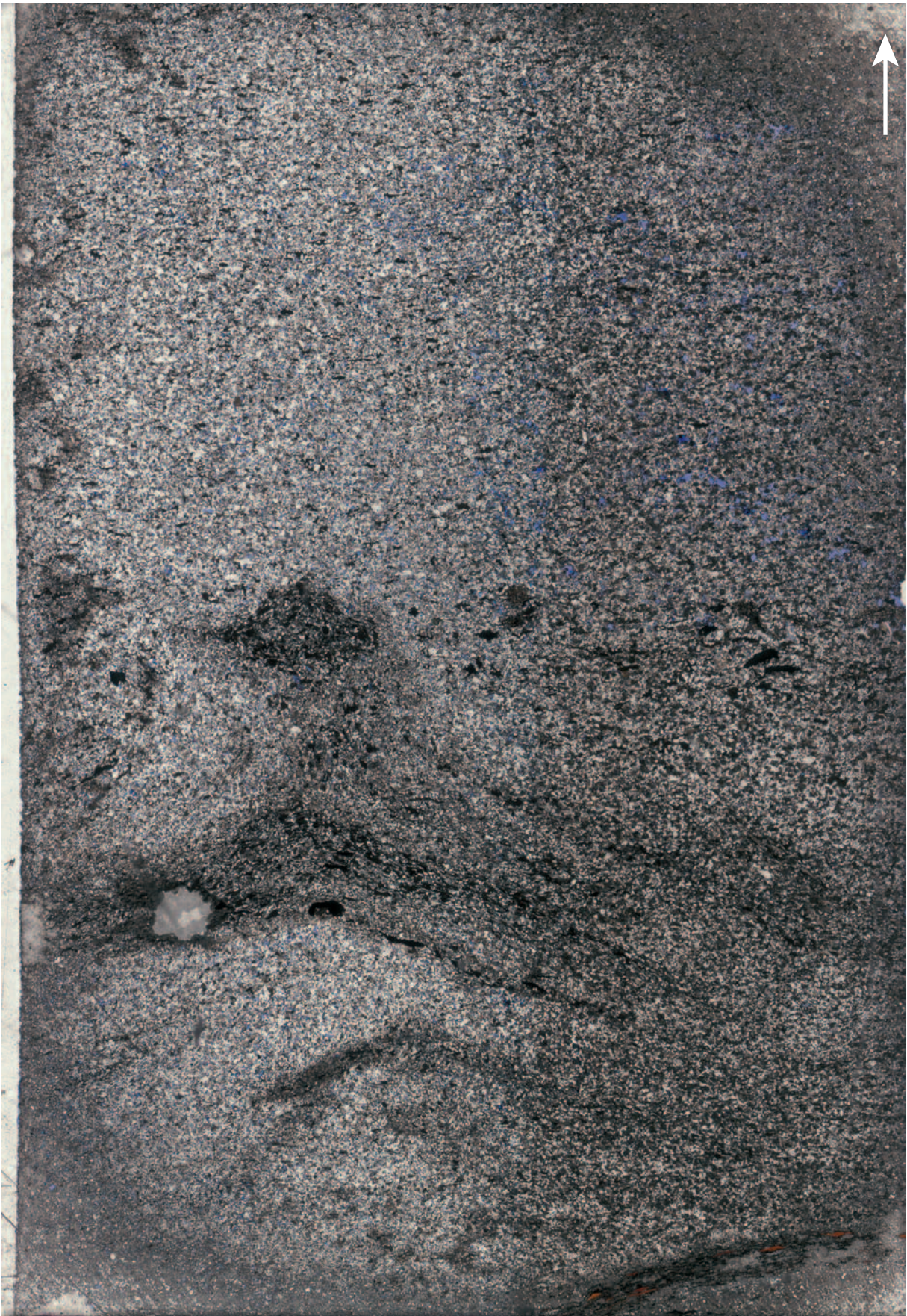


0.5 cm

511101-161 711cm.ai



0.5 cm



0.5 cm

511101-159 1466cm.ai



0.5 cm

511101-158 1455cm.ai



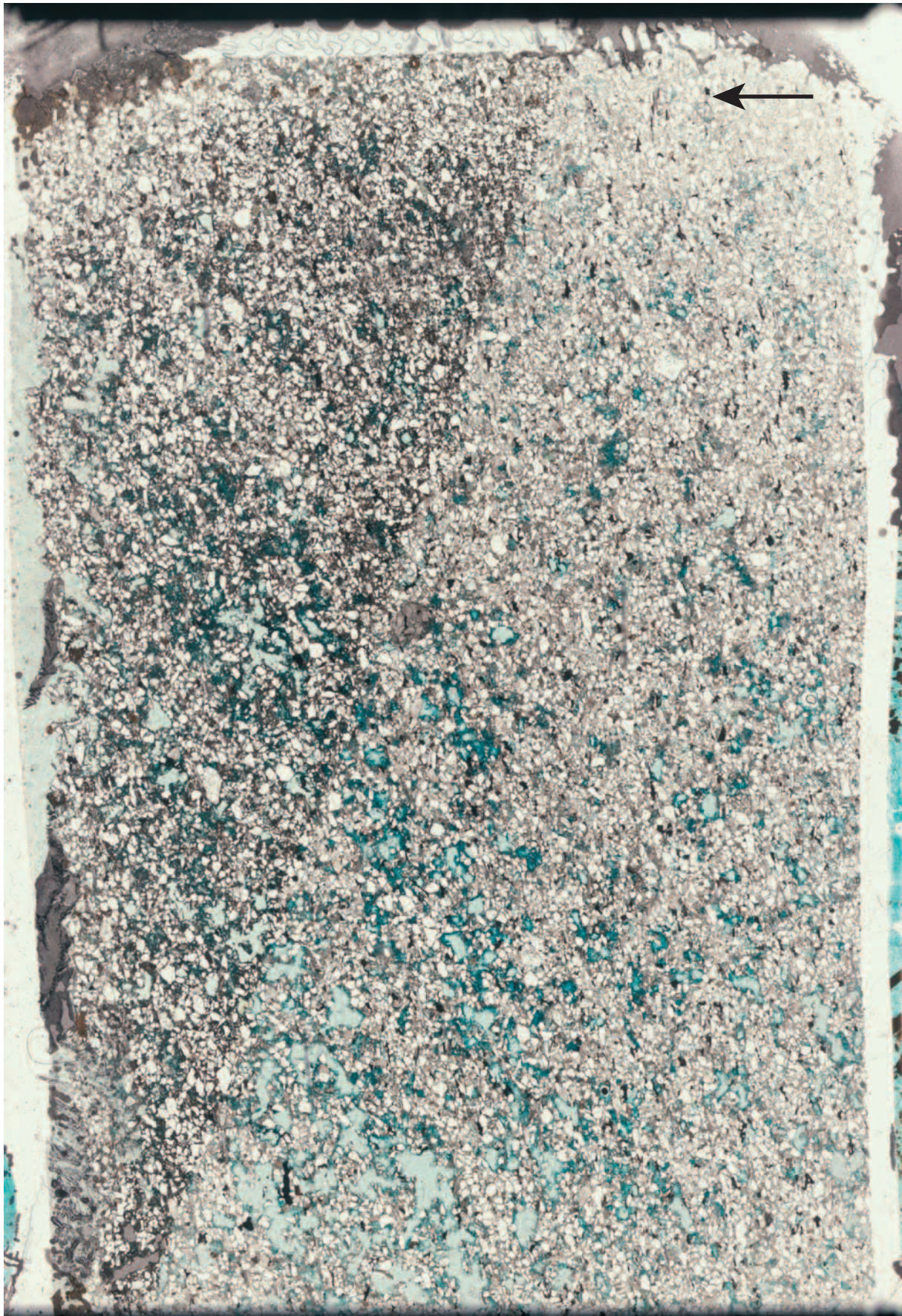
0.5 cm

511101-155 2942cm.tif



0.5 cm

511101-156 3097cm.tif



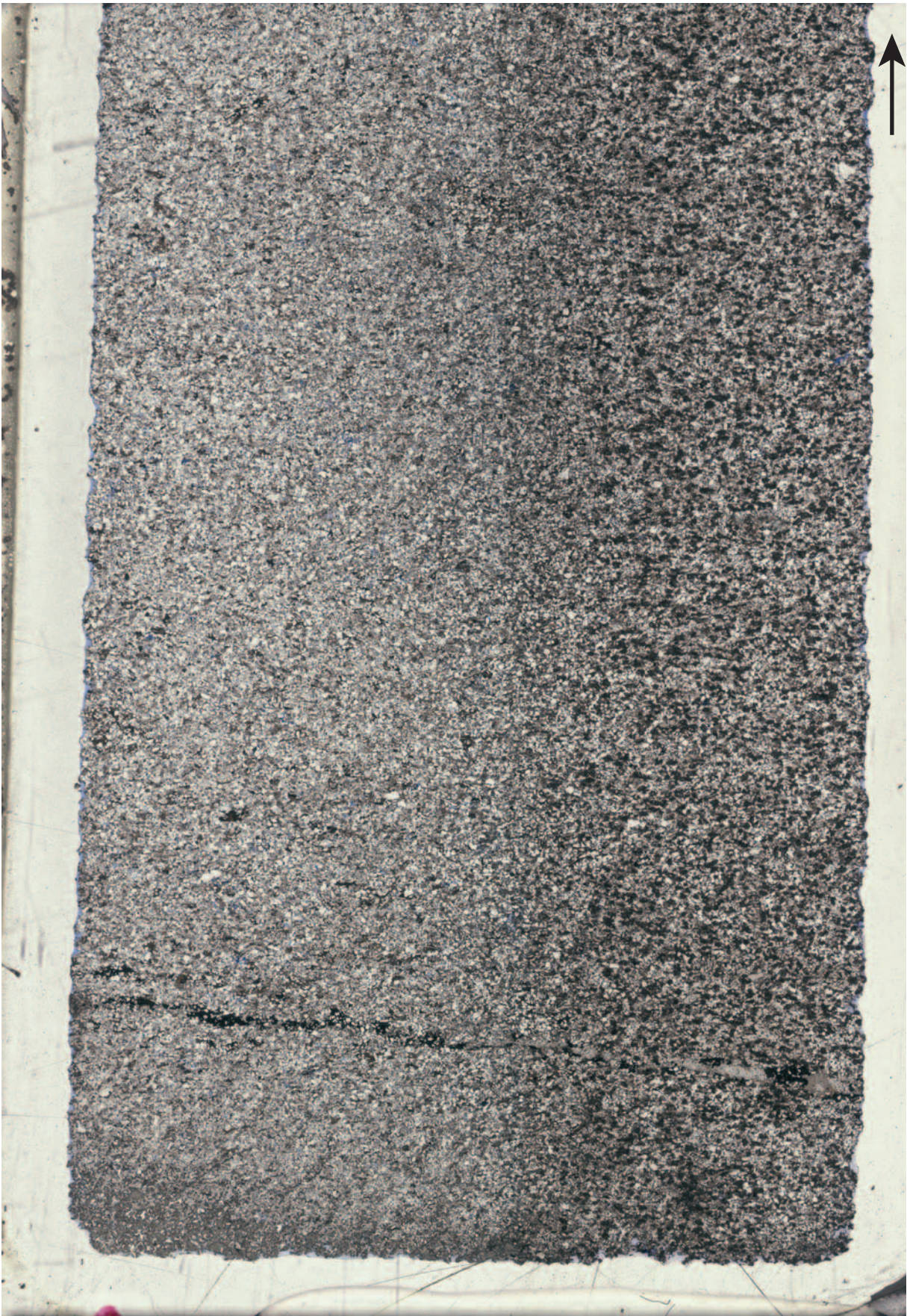
0.5 cm

511101-4316cm.ai



0.5 cm

511101-235 5368cm.ai



0.5 cm

511101-236 5406.ai



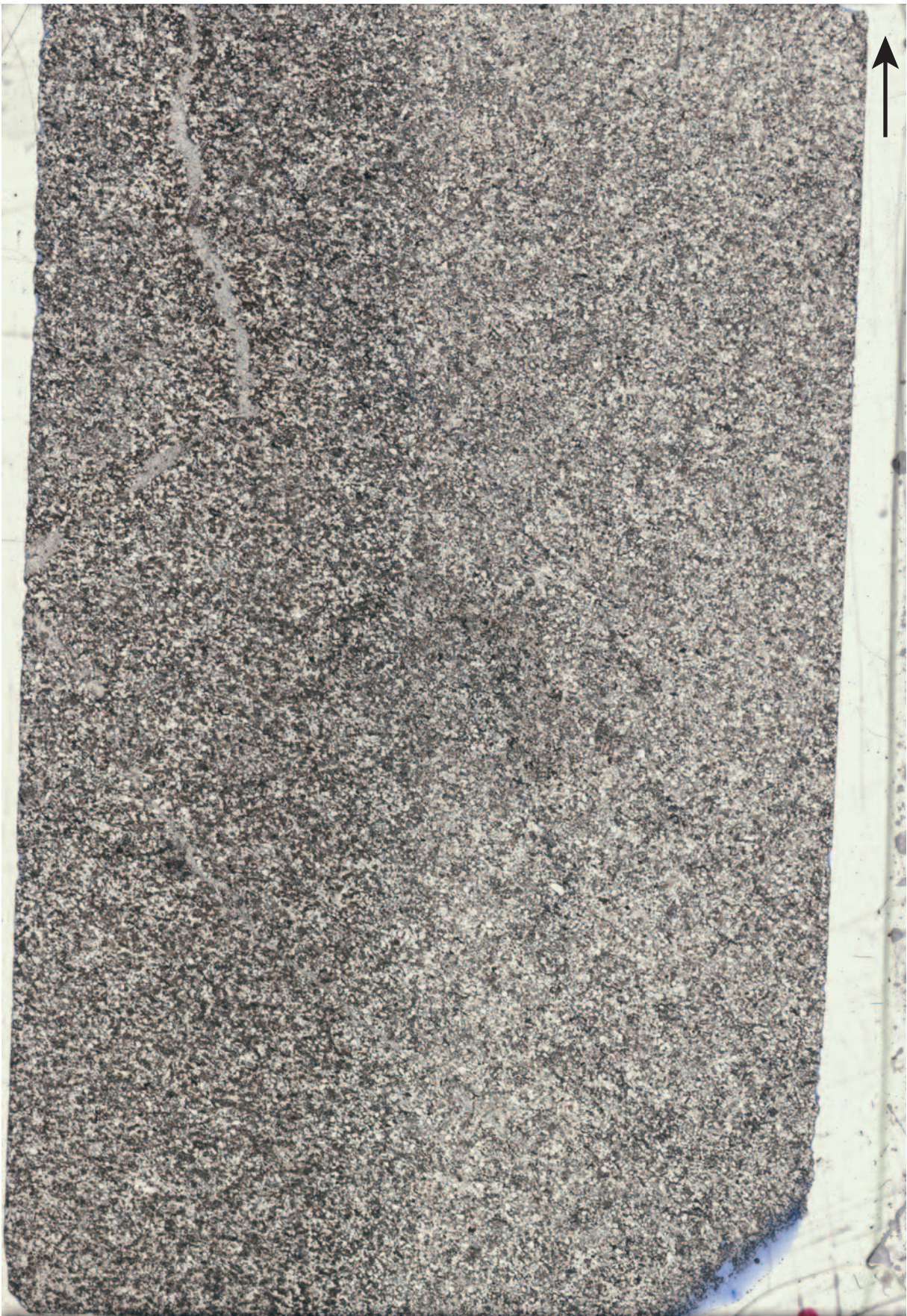
0.5 cm

511101-05455cm.ai



0.5 cm

511101-237 5471cm.ai



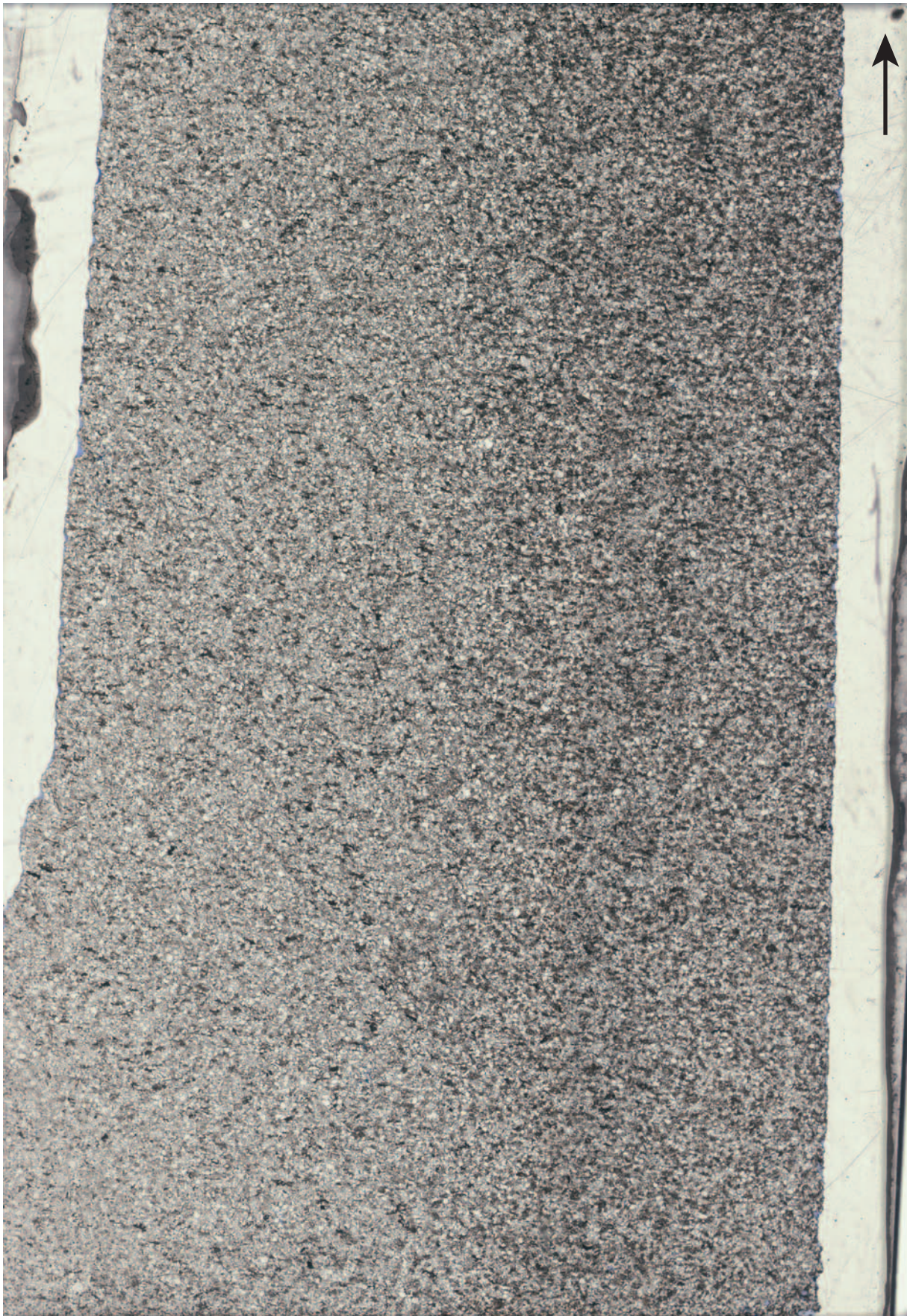
0.5 cm

511101-238 5493cm.ai



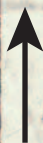
0.5 cm

511101-240 5524cm.ai



0.5 cm

511101-242 5559cm.ai



0.5 cm

511101-241 5604cm.ai



0.5 cm

511101-243 5672cm.ai



0.5 cm

511101-244 5810 cm.ai



0.5 cm

511101-06196cm.ai



0.5 cm

511101-07084cm.ai





0.5 cm

511101-184 8350cm.ai



0.5 cm

511101-09420cm.ai



0.5 cm

511101-09892cm.ai



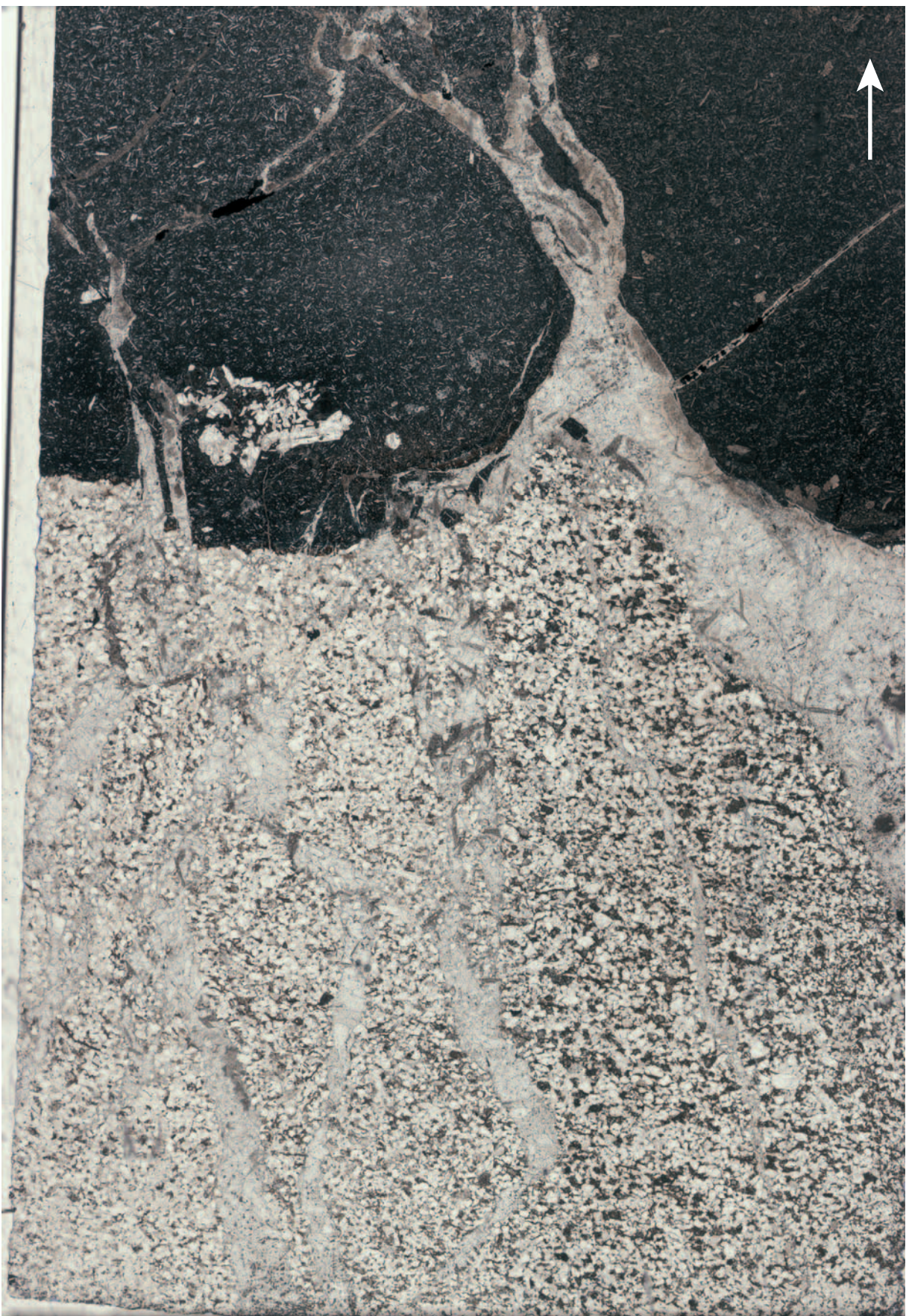
0.5 cm

511101-09998cm.ai



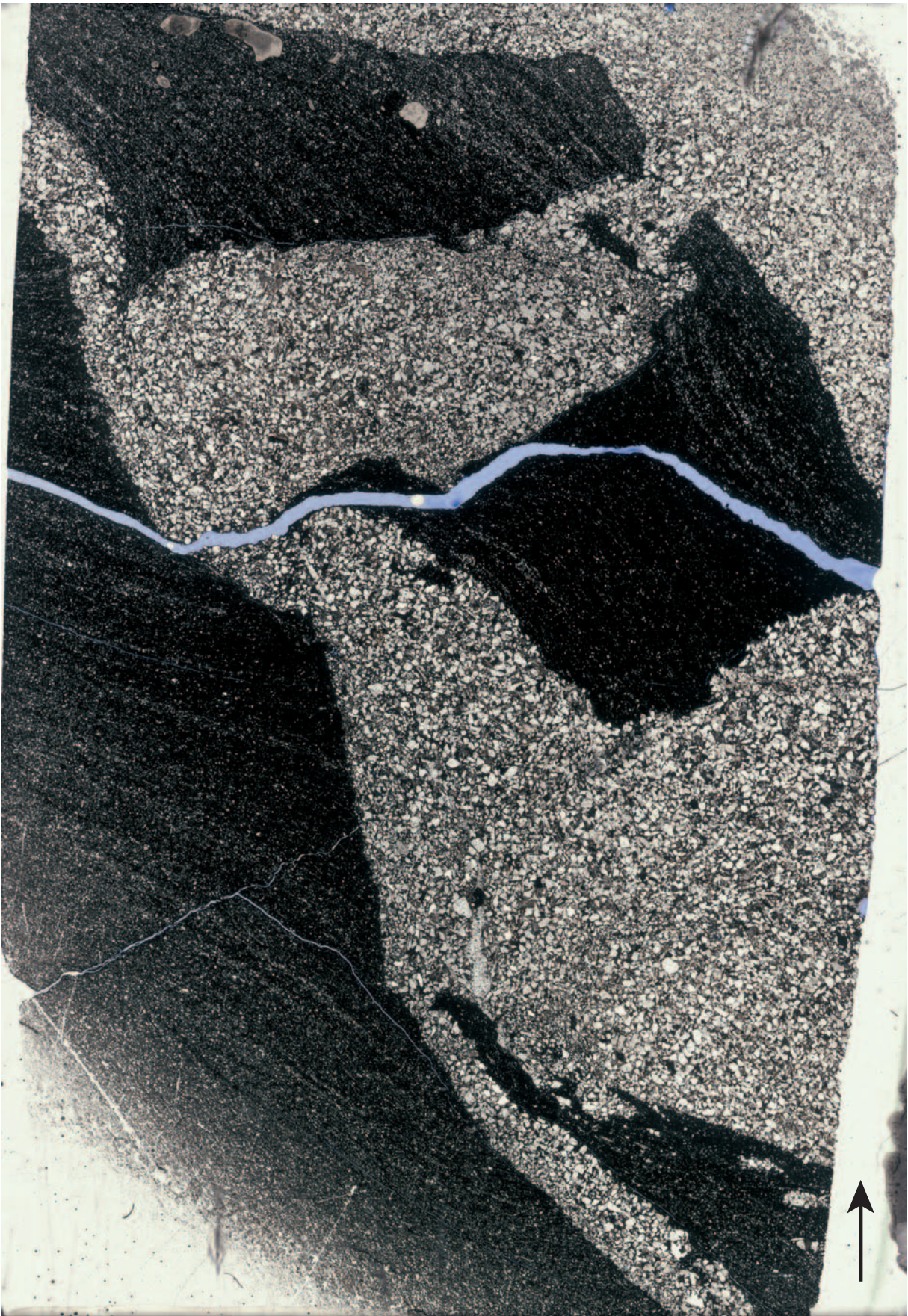
0.5 cm

5511101-245 10201cm.ai



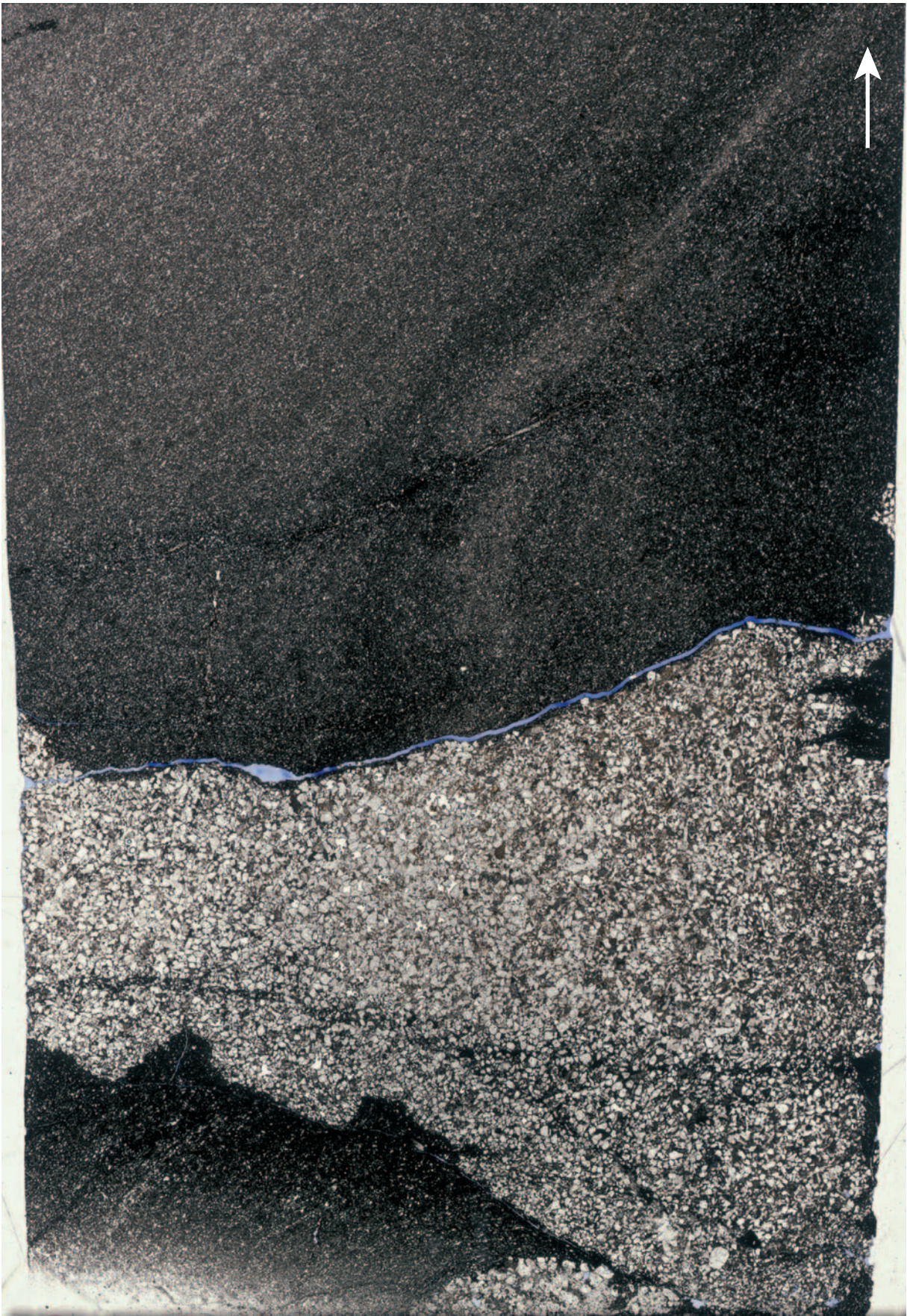
0.5 cm

511101-246 10204cm.ai



0.5 cm

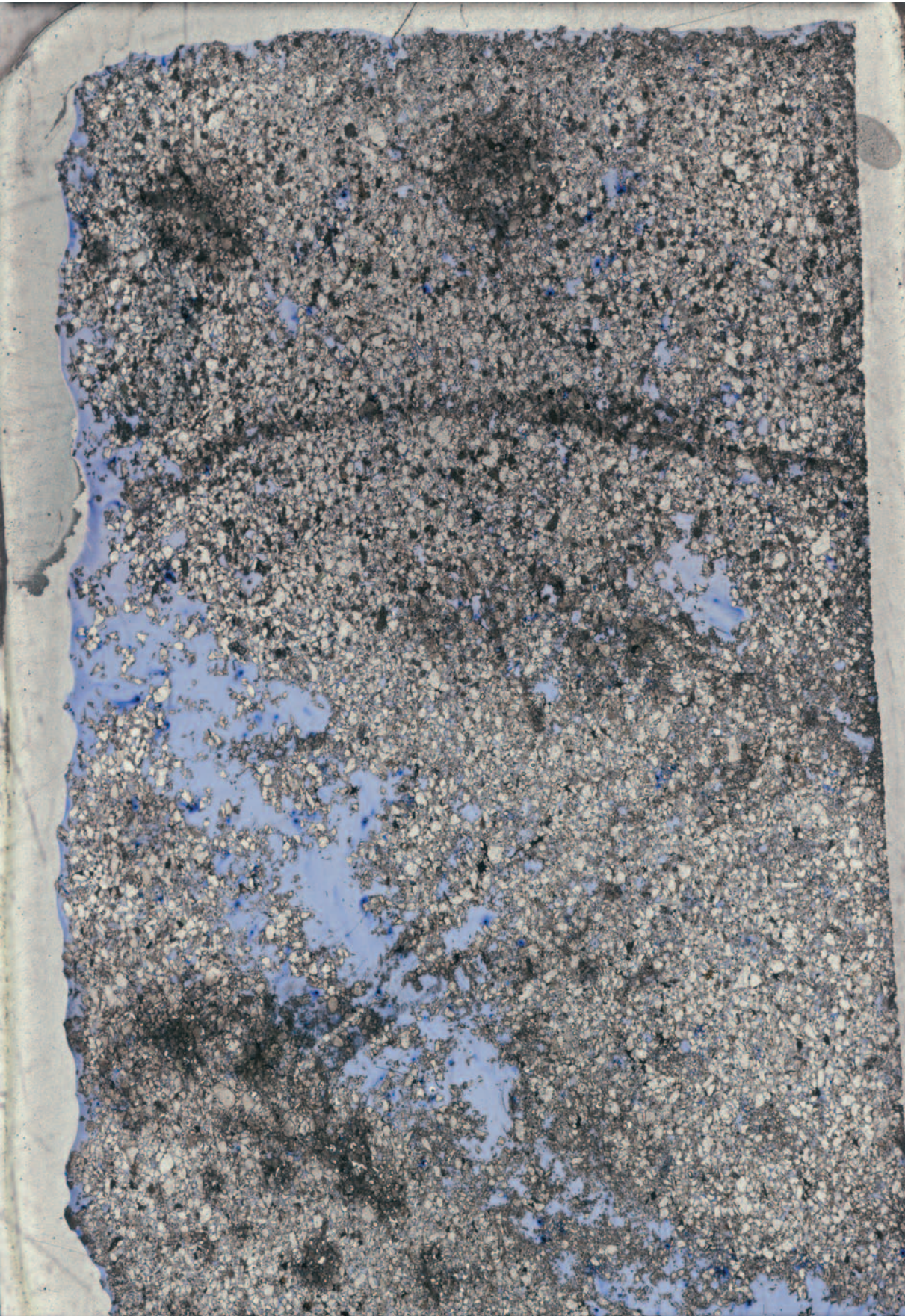
511101-248 10239cm.ai





0.5 cm

511101-11872cm.ai



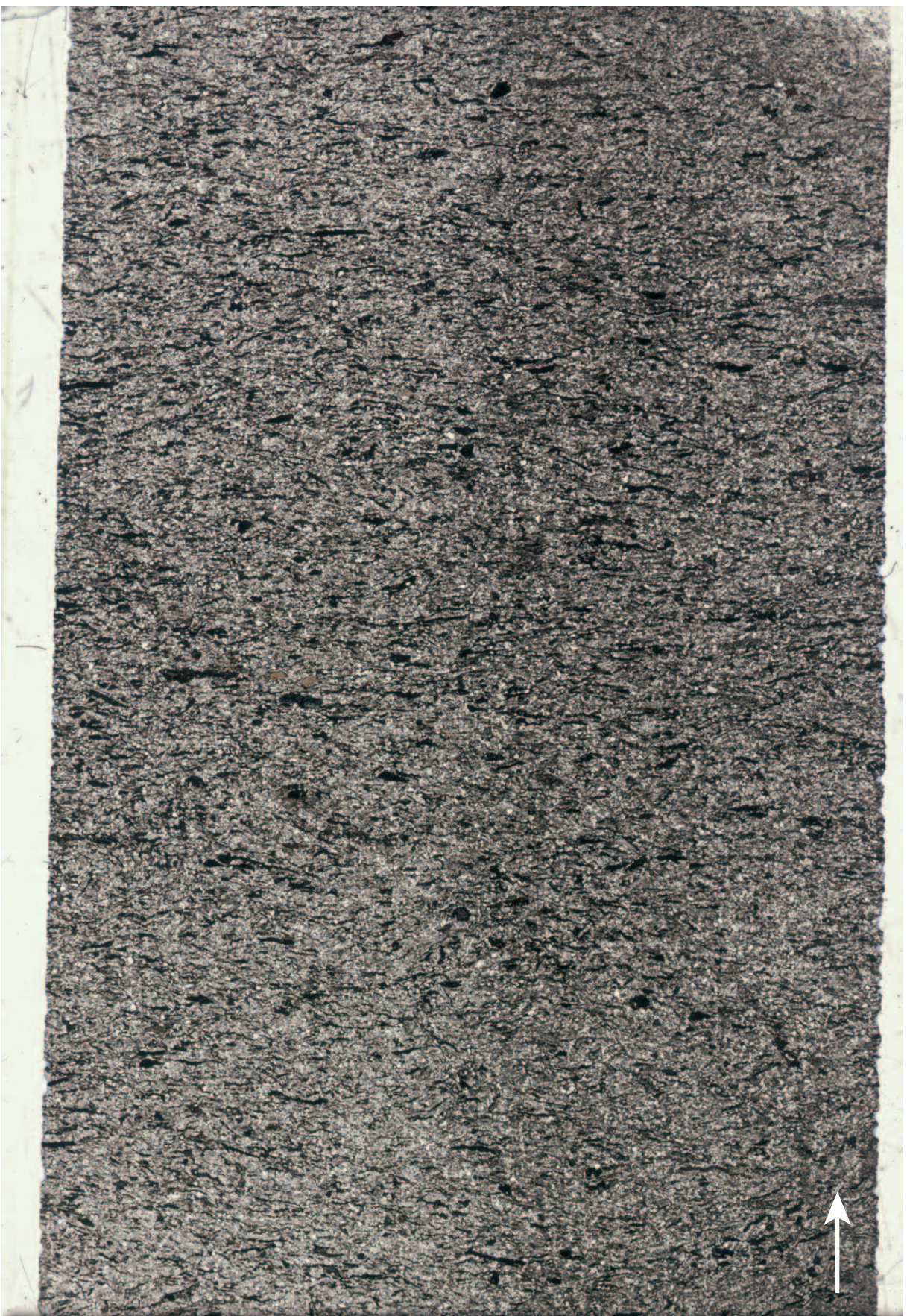
0.5 cm

511101-12880cm.ai



0.5 cm

511101-15171cm.ai



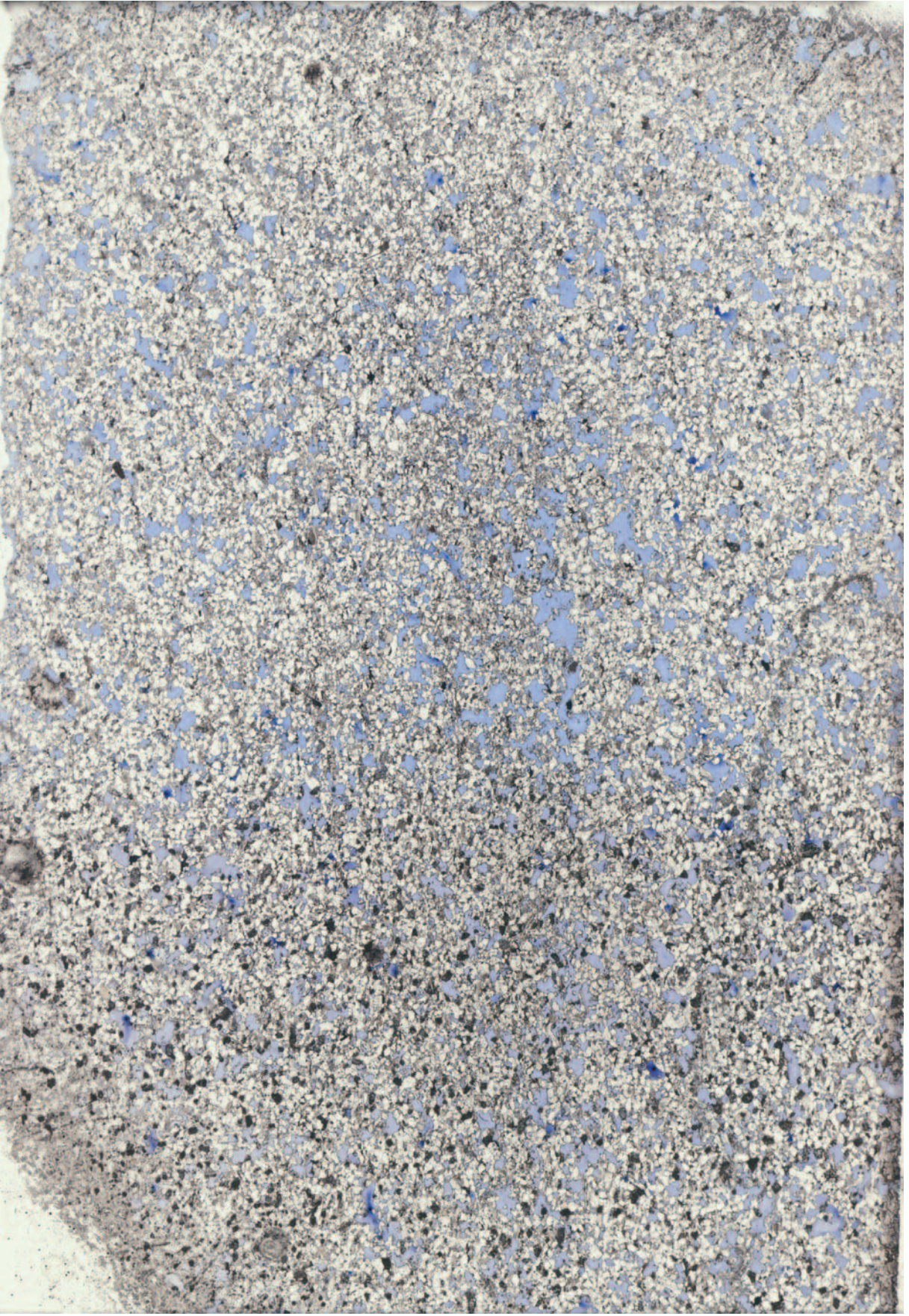
0.5 cm

511101-234 14674cm.ai



0.5 cm

511101-17848cm.ai



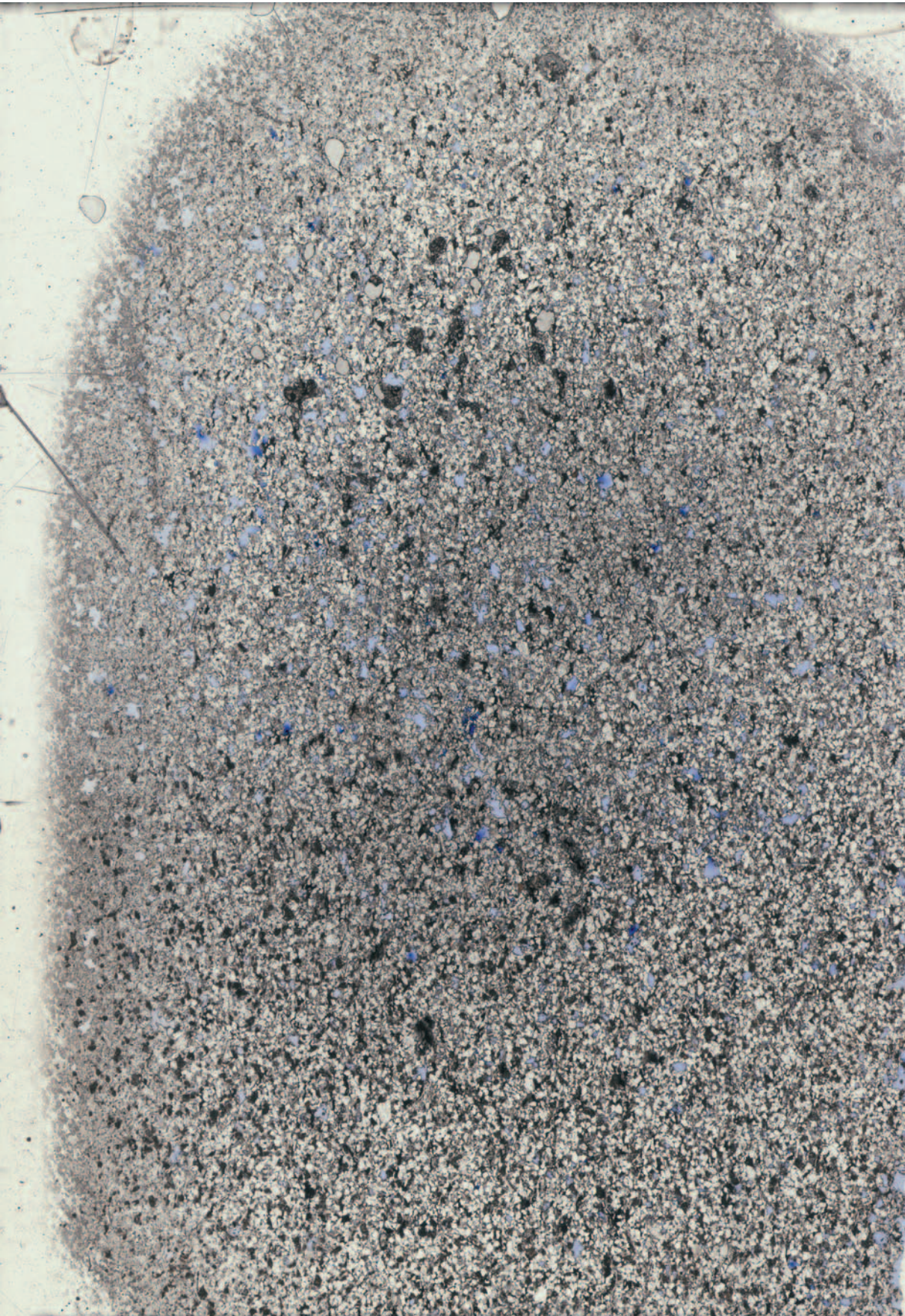
0.5 cm

511101-18153cm.ai



0.5 cm

511101-21880cm.ai



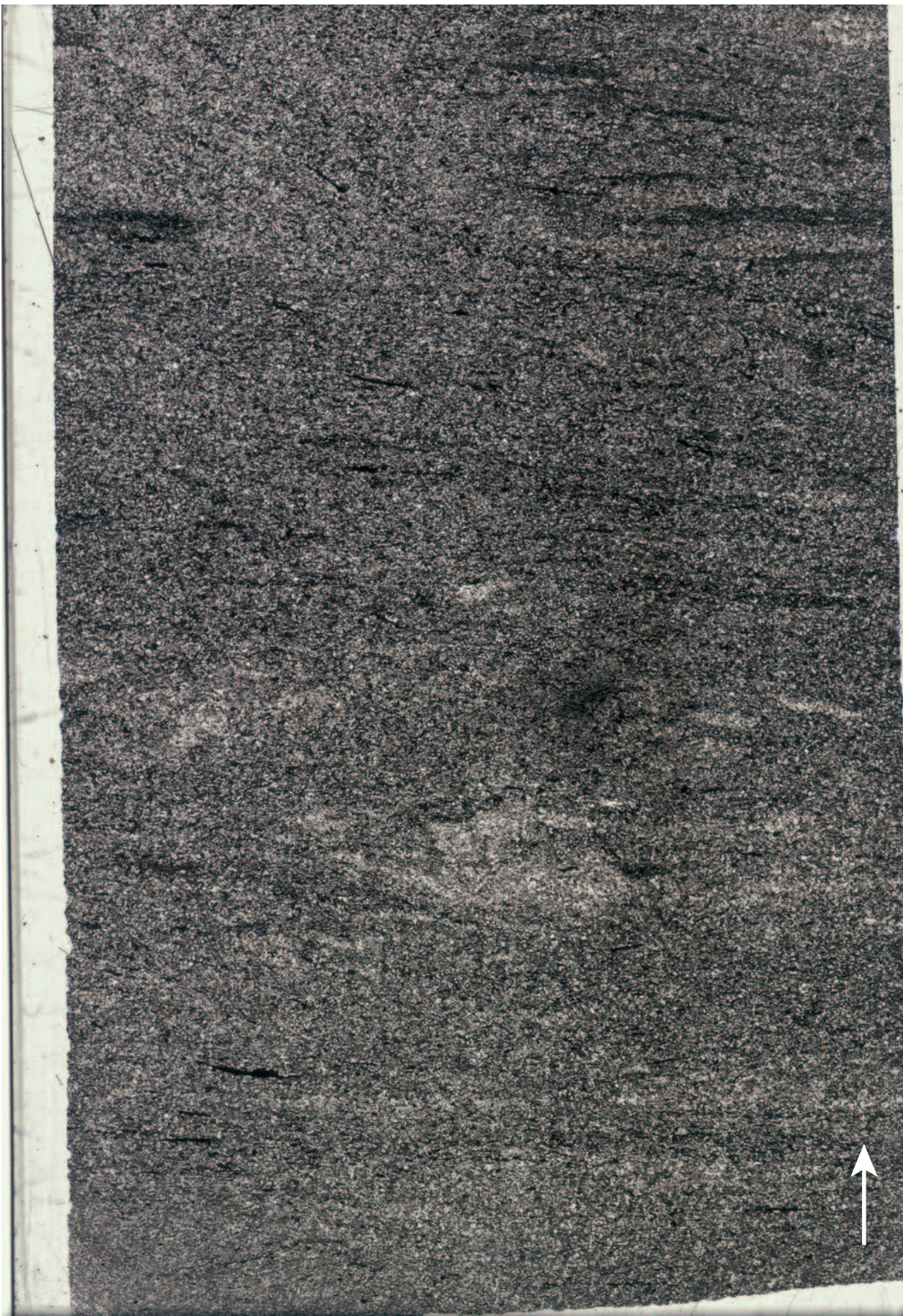
0.5 cm

511101-22118ccm.ai



0.5 cm

511101-22353cm.ai



0.5 cm

511101-233 23175cm.ai



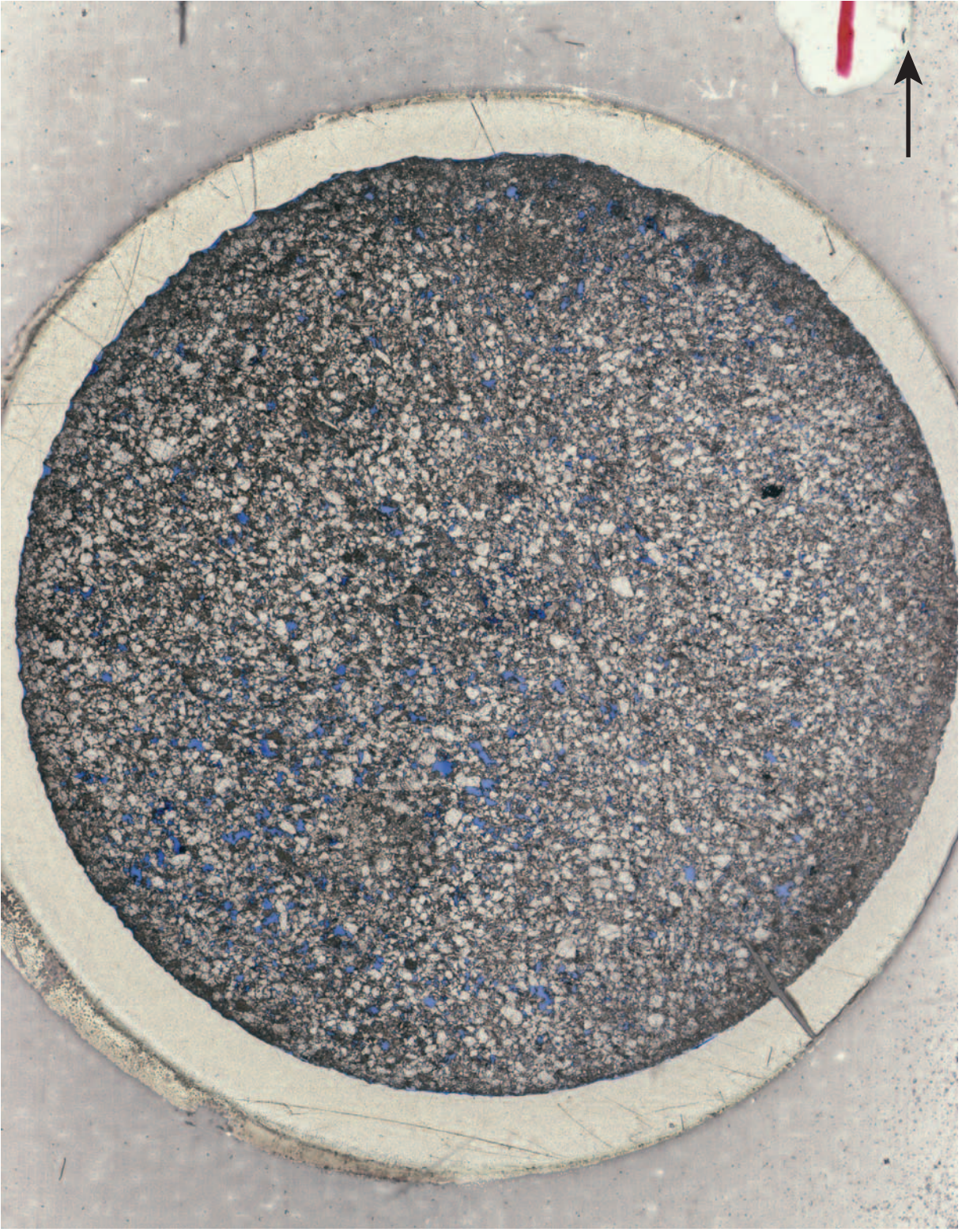
0.5 cm

511101-612 5710cm.ai



0.5 cm

511101-604 2210cm.ai



0.5 cm

511101-602 980cm.ai



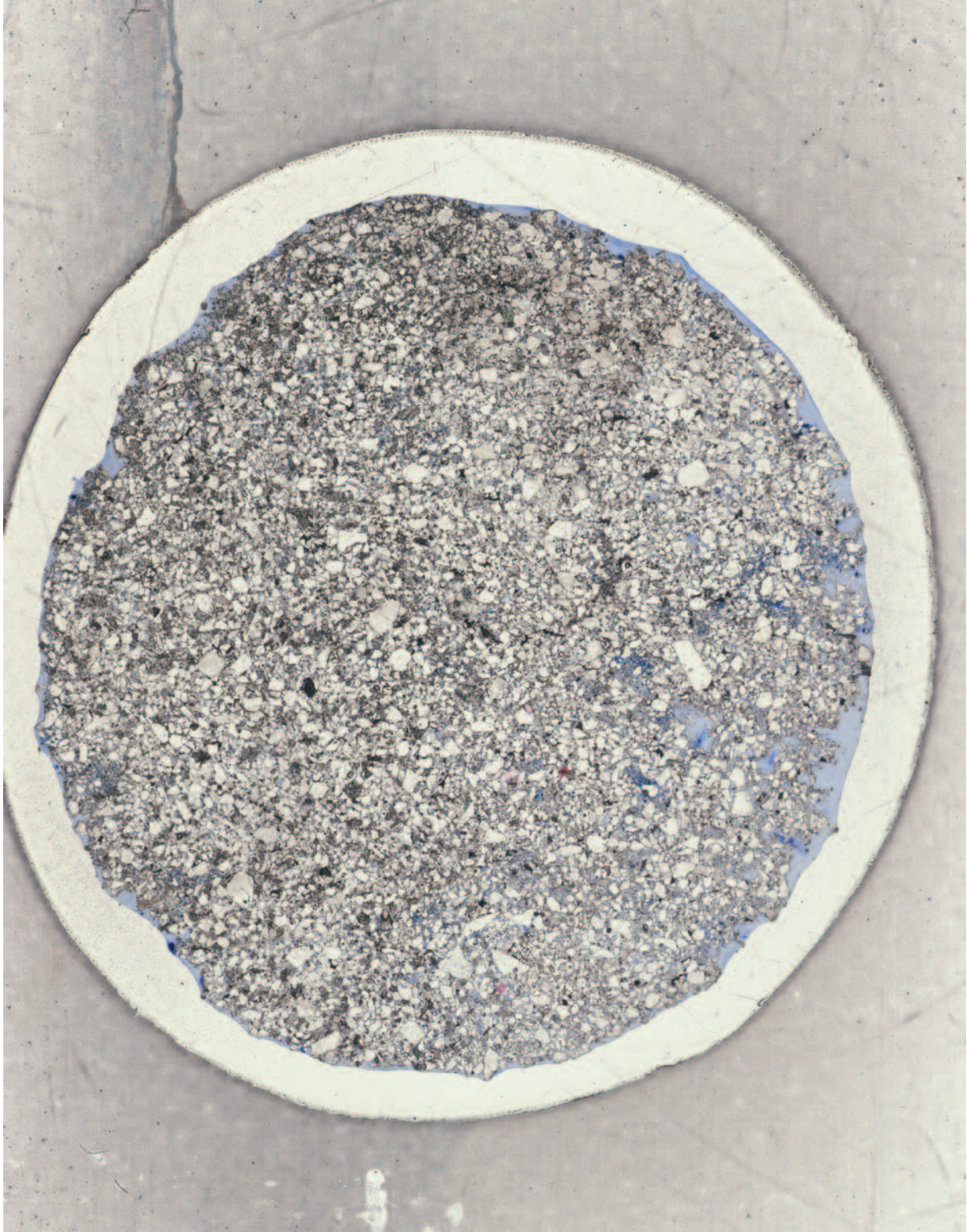
0.5 cm

511101-614 7075cm.ai



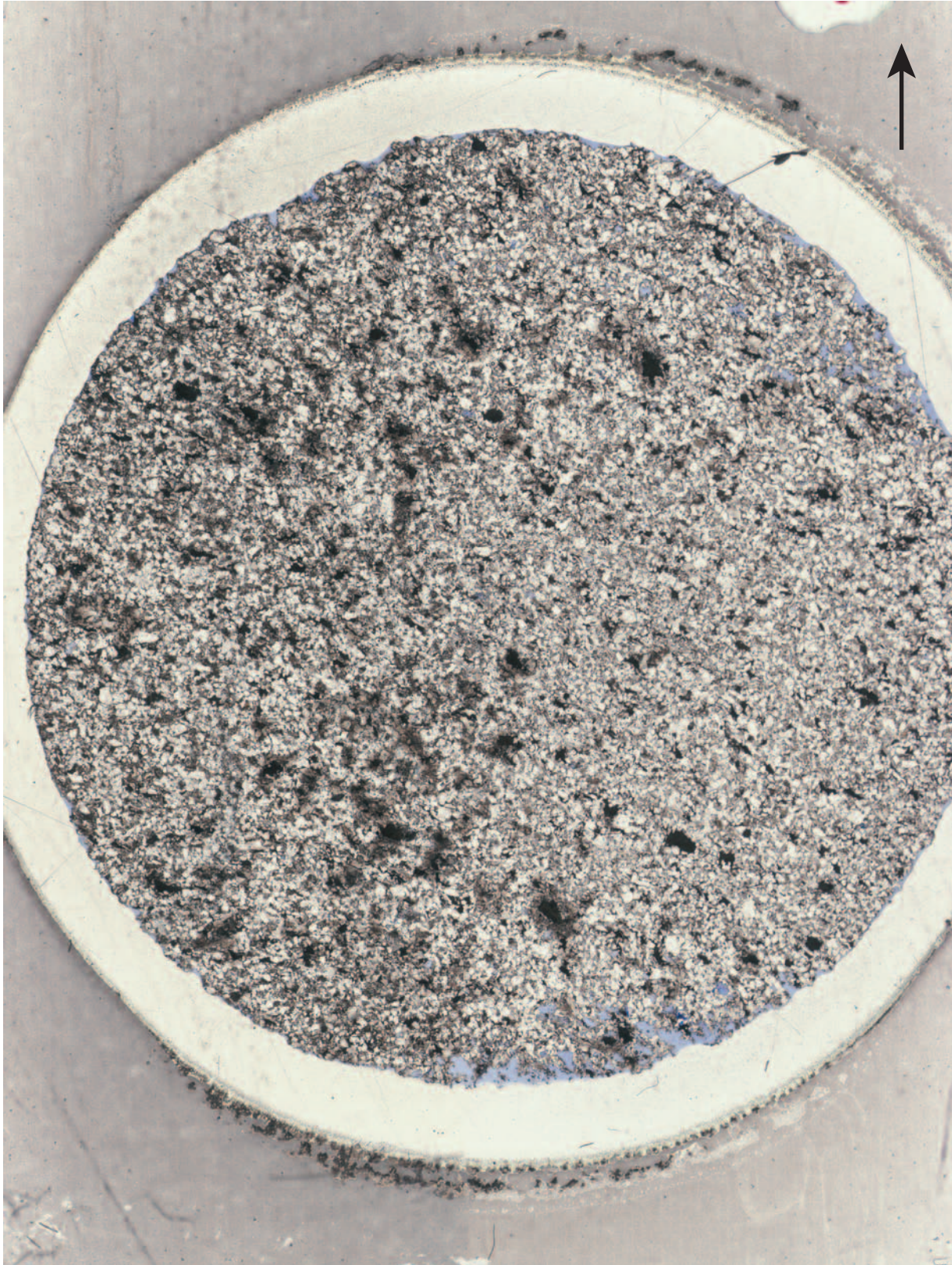
0.5 cm

511101-618 9950cm.ai



0.5 cm

511101-622 13030cm.ai



0.5 cm

511101-634 23335cm.ai



0.5 cm

511101-09420cm.ai

11.4 Appendix

Geochemistry data of Blokely core 511101

11.4 Appendix Geochemistry data

Bulk geochemistry of samples of 29 sandstones, 4 heteroliths and 9 mudstones from the Blokely core. Blue and green indicate the mudstone and heterolith levels, respectively. The amounts are given in wt%, ppm and ppb.

	SiO ₂	Al ₂ O ₃	Fe ₂ O ₃	MgO	CaO	Na ₂ O	K ₂ O	TiO ₂	P ₂ O ₅	MnO	Cr ₂ O ₃	LOI
m	%	%	%	%	%	%	%	%	%	%	%	%
3.60	89.83	4.88	1.03	0.10	0.06	0.49	1.49	0.22	0.07	<0.01	0.003	1.7
7.41	75.53	4.49	2.25	2.37	5.23	0.45	1.39	0.21	0.05	0.04	0.003	7.9
14.56	78.34	9.16	3.10	0.80	0.54	1.07	2.07	0.48	0.12	0.03	0.005	4.1
27.38	56.63	17.99	7.77	1.27	0.51	0.63	2.75	0.74	0.23	0.02	0.015	11.0
29.80	82.87	7.89	1.69	0.57	0.40	0.88	2.07	0.39	0.08	0.02	0.005	2.9
37.72	56.92	4.64	4.83	5.11	10.06	0.53	1.32	0.27	0.05	0.09	0.003	15.9
43.16	88.46	5.61	0.84	0.27	0.29	0.69	1.66	0.35	0.06	<0.01	0.003	1.6
51.02	60.60	7.82	5.88	3.56	6.50	0.84	1.76	0.43	0.12	0.14	0.005	12.1
51.61	74.30	12.33	2.61	0.61	0.33	1.10	2.72	0.49	0.10	0.01	0.005	5.1
56.43	57.19	6.55	3.91	4.72	9.42	0.93	1.71	0.42	0.08	0.12	0.004	14.7
56.91	70.65	8.26	3.22	2.29	3.97	0.96	2.01	0.51	0.10	0.10	0.006	7.7
60.54	52.46	18.92	6.08	1.07	0.35	0.57	2.64	0.75	0.10	0.02	0.015	16.7
61.96	90.06	4.64	0.67	0.24	0.27	0.59	1.31	0.24	0.06	<0.01	0.003	1.8
69.78	86.35	6.46	1.06	0.34	0.39	0.78	1.73	0.35	0.08	0.02	0.004	2.3
74.99	48.24	18.31	8.11	1.00	0.40	0.50	2.38	0.71	0.18	0.02	0.016	19.8
93.42	87.12	4.84	0.90	0.46	1.32	0.49	1.28	0.28	0.02	0.01	0.003	3.1
94.20	82.08	9.50	1.54	0.34	0.21	1.13	2.20	0.46	0.10	<0.01	0.005	2.2
98.92	76.20	8.32	2.43	1.55	2.48	0.77	2.04	0.34	0.08	0.04	0.004	5.6
114.69	57.59	15.40	4.80	0.72	0.74	0.83	2.64	0.73	0.13	0.02	0.014	16.1
116.32	87.80	5.35	0.68	0.40	0.90	0.60	1.40	0.33	0.07	0.01	0.003	2.3
118.72	77.25	6.17	1.62	1.57	4.00	0.66	1.51	0.29	0.19	0.04	0.003	6.5
120.20	50.55	17.69	5.98	1.21	1.33	0.78	2.73	0.78	0.18	0.03	0.017	18.4
128.80	89.07	5.56	0.61	0.15	0.11	0.55	1.62	0.30	0.06	<0.01	0.003	1.8
139.27	88.33	5.91	0.68	0.26	0.26	0.40	1.61	0.31	0.06	<0.01	0.004	2.0
142.83	50.56	18.07	5.41	0.95	0.25	0.67	3.00	0.84	0.12	0.02	0.020	19.8
151.71	48.39	9.47	3.82	5.41	10.81	0.75	1.96	0.51	0.16	0.07	0.007	18.3
163.85	57.57	14.53	5.85	1.60	2.69	0.83	2.93	0.74	0.18	0.03	0.014	12.8
166.95	49.68	8.24	4.15	5.54	11.65	0.58	1.86	0.40	0.07	0.08	0.006	17.5
178.32	44.94	22.09	7.10	0.89	0.17	0.59	3.29	1.11	0.09	0.03	0.023	19.4
178.48	87.65	6.67	0.64	0.16	0.06	0.30	1.49	0.22	0.04	<0.01	0.003	2.6
181.53	86.70	6.16	0.85	0.47	0.85	0.24	1.48	0.26	0.06	0.02	0.003	2.8
185.23	53.17	17.68	5.62	0.98	0.24	0.48	2.84	0.89	0.14	0.03	0.016	17.7
187.12	65.17	13.66	5.43	1.25	0.77	0.56	2.54	0.67	0.17	0.05	0.012	9.5
188.39	72.95	11.35	3.00	1.07	1.68	0.56	2.25	0.56	0.11	0.02	0.008	6.3
193.66	67.34	10.39	5.51	1.93	2.88	0.56	2.11	0.48	0.11	0.08	0.007	8.4
209.88	53.12	17.84	6.36	1.11	1.39	0.70	2.81	0.80	0.30	0.03	0.015	15.3
218.50	51.01	18.54	6.00	0.95	0.72	0.49	3.04	0.93	0.31	0.02	0.017	17.7
218.80	84.93	7.10	0.92	0.41	0.90	0.32	1.87	0.40	0.05	0.02	0.005	2.9
221.18	82.38	7.96	1.94	0.56	0.44	0.31	2.08	0.41	0.03	0.03	0.006	3.7
223.53	83.32	8.16	1.13	0.45	0.61	0.33	2.02	0.58	0.06	0.02	0.006	3.1
230.33	67.39	14.03	4.31	1.08	1.14	0.54	2.80	0.68	0.11	0.03	0.010	7.7
233.30	81.35	9.05	1.99	0.55	0.46	0.33	2.07	0.35	0.05	0.02	0.006	3.6

	Ni	Sc	Ba	Be	Co	Cs	Ga	Hf	Nb	Rb	Sn	Sr
m	ppm	ppm	ppm	ppm	ppm	ppm	ppm	ppm	ppm	ppm	ppm	ppm
3.60	<20	3	317	<1	25.8	1.2	6.1	3.6	4.3	50.1	3	62.9
7.41	<20	3	298	<1	17.1	1.0	6.0	4.1	4.3	46.9	1	91.1
14.56	<20	8	670	1	26.6	1.9	10.9	10.9	9.6	73.2	2	124.6
27.38	149	18	1037	3	33.3	9.7	23.8	5.9	17.0	134.8	3	387.7
29.80	<20	6	569	2	34.6	2.0	10.9	5.7	8.3	75.9	3	103.6
37.72	<20	6	347	1	15.3	1.2	6.5	6.2	6.0	47.1	2	222.6
43.16	<20	4	301	<1	33.9	1.2	6.3	6.3	7.2	52.5	5	75.2
51.02	<20	8	422	<1	14.4	1.5	9.9	9.3	17.0	64.4	2	250.4
51.61	<20	9	674	1	29.5	2.9	16.5	3.3	20.1	102.1	3	204.0
56.43	<20	6	446	1	12.4	1.2	8.8	10.3	8.6	56.0	2	207.3
56.91	<20	9	456	1	18.8	1.6	10.2	10.8	9.6	68.1	2	148.8
60.54	125	17	473	3	24.8	7.3	24.4	5.3	15.8	130.8	4	112.5
61.96	<20	4	279	<1	18.2	1.0	6.3	4.7	5.4	45.4	1	60.9
69.78	<20	5	359	1	27.5	1.5	7.8	5.9	6.7	57.6	4	76.9
74.99	220	19	556	3	27.4	7.5	21.3	3.8	14.3	120.1	3	150.1
93.42	<20	4	310	<1	37.3	1.0	5.6	5.6	6.3	42.7	2	96.4
94.20	<20	7	485	1	24.6	1.7	11.9	7.8	9.0	74.8	4	131.9
98.92	<20	8	453	1	27.7	1.5	11.0	4.6	7.2	69.3	2	115.8
114.69	90	13	581	2	18.5	5.2	19.5	7.8	15.5	104.8	3	201.2
116.32	<20	4	253	<1	36.0	1.1	6.9	6.9	6.7	46.2	3	65.3
118.72	<20	6	305	<1	21.4	1.4	8.2	4.0	6.1	53.8	2	163.0
120.20	73	17	600	2	16.2	7.5	23.0	4.4	15.9	124.3	3	136.2
128.80	<20	4	324	<1	23.1	1.1	6.9	5.6	5.9	52.3	3	89.1
139.27	<20	5	325	1	22.1	1.1	7.5	5.4	6.6	52.3	2	100.3
142.83	79	16	582	3	15.1	7.5	22.5	5.5	16.0	128.1	3	150.6
151.71	27	8	579	2	15.1	2.5	12.1	7.8	9.2	69.1	2	342.9
163.85	47	12	633	2	16.0	4.9	19.2	4.1	13.4	120.9	3	172.6
166.95	<20	7	510	1	13.8	1.8	9.9	5.0	7.5	62.8	2	217.4
178.32	93	18	608	4	18.2	8.5	35.1	8.5	22.7	141.8	4	170.3
178.48	<20	3	287	<1	23.6	0.9	7.0	3.4	4.9	45.3	2	50.1
181.53	<20	4	292	<1	26.0	0.8	6.6	3.1	5.3	44.0	1	59.8
185.23	49	16	526	4	14.4	7.0	23.2	6.4	19.3	122.1	4	171.5
187.12	36	12	529	2	15.7	2.6	17.2	7.8	12.3	88.4	3	121.8
188.39	<20	9	455	<1	13.9	1.8	13.6	9.6	10.7	70.5	2	113.2
193.66	<20	11	402	<1	21.7	1.4	11.9	6.2	8.9	67.3	2	120.3
209.88	56	16	517	2	13.2	7.1	21.8	5.2	16.7	118.5	3	115.0
218.50	63	15	531	3	15.2	5.9	24.4	7.2	20.5	106.3	3	136.7
218.80	<20	5	317	1	24.9	1.0	7.4	7.1	7.9	49.6	1	61.6
221.18	<20	7	340	<1	28.5	1.0	8.6	5.4	8.1	55.8	2	55.1
223.53	<20	6	349	<1	39.4	1.1	8.8	11.3	10.9	55.0	2	75.0
230.33	36	10	554	2	24.1	2.9	16.8	8.6	13.2	90.3	2	96.1
233.30	<20	5	371	<1	30.4	1.3	9.4	3.9	7.3	60.8	1	70.7

	Ta	Th	U	V	W	Zr	Y	La	Ce	Pr	Nd	Sm
m	ppm	ppm	ppm	ppm	ppm	ppm	ppm	ppm	ppm	ppm	ppm	ppm
3.60	1.1	3.6	0.9	25	263.0	139.5	6.6	13.7	30.6	3.51	12.7	1.93
7.41	1.4	3.2	1.0	20	166.4	139.9	8.4	11.9	24.5	2.77	10.4	1.76
14.56	1.3	8.7	2.7	53	218.6	391.0	22.3	31.2	66.6	7.82	28.8	5.17
27.38	1.5	17.4	17.8	388	54.6	224.3	43.5	52.2	125.6	13.70	54.5	9.40
29.80	1.6	5.9	1.7	49	330.2	215.9	13.9	22.2	46.8	5.44	20.2	3.52
37.72	1.2	4.1	1.3	38	150.2	224.6	13.7	15.8	32.0	3.79	14.3	2.51
43.16	5.5	4.3	1.2	28	405.9	230.1	11.1	15.3	31.8	3.76	13.8	2.38
51.02	1.0	6.1	1.9	51	91.0	303.2	22.9	24.3	47.2	5.61	21.3	3.81
51.61	2.7	5.5	3.4	112	214.2	125.2	18.5	25.5	55.5	6.30	21.8	4.32
56.43	1.2	8.1	2.2	36	81.8	375.1	17.8	25.6	52.0	6.22	23.9	3.99
56.91	2.2	9.2	2.4	43	154.3	381.5	19.5	28.8	59.4	7.27	27.0	4.75
60.54	1.2	18.2	13.9	372	41.0	206.0	37.8	45.7	108.8	12.15	46.5	8.63
61.96	1.9	3.5	1.4	42	292.7	165.8	12.8	11.8	26.0	3.09	11.6	2.24
69.78	1.5	5.1	1.7	40	458.4	222.6	13.7	16.8	35.7	4.14	15.8	2.79
74.99	0.9	17.2	16.8	424	32.6	145.8	40.1	44.3	114.1	12.16	48.5	8.90
93.42	2.0	4.2	1.7	35	428.0	202.0	12.5	15.0	31.9	3.57	13.7	2.29
94.20	1.5	6.4	2.2	54	334.5	290.5	17.0	22.1	45.8	5.58	22.1	3.63
98.92	2.1	4.0	1.8	61	284.5	173.5	17.3	14.3	31.5	3.86	15.5	2.83
114.69	1.6	13.9	8.4	204	73.4	265.0	32.4	39.7	85.3	9.69	37.7	6.67
116.32	1.5	4.9	1.6	34	400.5	247.3	13.1	16.0	34.3	4.02	15.1	2.66
118.72	1.0	4.0	1.7	48	182.3	157.1	19.1	16.4	34.8	3.93	15.7	2.74
120.20	1.6	18.9	7.2	348	40.6	155.0	46.8	48.2	116.4	12.32	47.9	8.84
128.80	1.2	4.1	1.3	28	373.9	200.5	11.7	14.4	30.3	3.60	13.3	2.32
139.27	5.3	3.8	1.1	25	390.1	196.5	10.5	13.7	29.3	3.42	12.6	2.18
142.83	1.2	18.1	10.9	375	33.4	218.5	44.4	51.0	112.2	12.93	50.2	9.06
151.71	0.9	7.6	2.0	57	81.8	279.9	17.5	24.4	48.7	6.16	22.9	3.93
163.85	1.1	6.8	1.9	102	37.0	139.7	20.1	25.0	50.3	6.54	25.1	4.29
166.95	0.8	5.0	1.2	45	85.4	172.0	13.0	16.6	32.0	4.11	15.7	2.76
178.32	1.9	22.6	6.2	259	29.3	274.8	33.7	57.9	118.5	13.95	49.2	8.47
178.48	0.9	2.8	0.9	28	237.9	117.7	8.3	9.2	19.1	2.45	9.4	1.69
181.53	1.2	3.1	0.9	23	287.4	110.4	9.3	10.0	21.2	2.59	9.6	1.74
185.23	1.6	17.5	5.0	290	40.7	221.9	42.1	46.1	97.9	11.68	43.5	7.95
187.12	1.3	8.0	2.0	86	74.1	280.8	18.8	25.0	50.0	6.19	23.5	4.27
188.39	1.0	8.3	2.1	53	101.4	332.0	19.4	24.9	50.9	6.29	22.8	4.14
193.66	1.0	5.8	1.6	61	128.9	217.1	17.2	18.8	37.3	4.66	17.9	3.26
209.88	1.2	15.5	4.9	220	31.7	190.1	44.4	38.9	88.5	10.59	41.6	8.51
218.50	1.4	17.1	4.7	229	49.2	236.9	40.9	45.5	99.6	11.57	45.0	8.11
218.80	1.2	5.4	1.4	35	225.1	244.4	12.6	16.3	33.1	3.98	15.5	2.64
221.18	1.3	5.6	1.4	37	228.0	200.7	11.4	16.5	33.8	4.01	15.6	2.55
223.53	1.8	9.8	2.4	44	342.5	416.6	17.4	28.6	60.0	7.11	27.5	4.49
230.33	1.9	8.3	2.2	73	151.2	312.3	19.8	27.3	55.1	6.70	24.9	4.48
233.30	1.5	3.5	1.1	47	282.8	145.5	8.9	11.9	25.8	2.88	10.8	1.89

	Eu	Gd	Tb	Dy	Ho	Er	Tm	Yb	Lu	TOT/C	TOT/S	Mo
m	ppm	ppm	ppm	ppm	ppm	ppm	ppm	ppm	ppm	%	%	ppm
3.60	0.38	1.43	0.21	1.10	0.20	0.63	0.11	0.73	0.11	0.09	0.12	0.3
7.41	0.40	1.51	0.24	1.37	0.27	0.82	0.12	0.80	0.12	2.09	0.07	0.2
14.56	0.95	4.33	0.70	3.69	0.70	2.11	0.34	2.09	0.34	0.55	0.34	0.4
27.38	1.99	8.48	1.30	7.08	1.39	3.92	0.60	3.60	0.55	3.30	3.16	54.7
29.80	0.67	2.95	0.44	2.27	0.43	1.33	0.20	1.32	0.20	0.48	0.04	0.5
37.72	0.49	2.36	0.37	2.09	0.40	1.21	0.19	1.24	0.19	4.35	0.14	0.3
43.16	0.45	2.06	0.31	1.74	0.35	1.07	0.17	1.08	0.18	0.17	0.16	0.4
51.02	0.72	3.29	0.55	2.70	0.64	2.19	0.29	2.22	0.36	3.16	0.12	0.2
51.61	0.93	3.76	0.60	2.87	0.63	1.77	0.27	1.62	0.25	0.84	0.83	1.0
56.43	0.64	3.48	0.52	2.77	0.53	1.69	0.28	1.74	0.27	3.94	0.07	0.2
56.91	0.80	3.87	0.58	3.25	0.63	1.87	0.30	1.92	0.28	1.95	0.06	0.2
60.54	1.77	7.32	1.17	6.47	1.15	3.42	0.54	3.35	0.48	6.37	3.33	31.3
61.96	0.48	2.14	0.35	1.98	0.39	1.15	0.18	1.10	0.17	0.51	0.17	0.4
69.78	0.55	2.36	0.37	2.16	0.43	1.37	0.21	1.38	0.20	0.38	0.18	0.3
74.99	1.90	7.75	1.24	6.82	1.28	3.63	0.55	3.29	0.49	8.10	5.08	85.1
93.42	0.41	1.98	0.33	1.96	0.41	1.32	0.21	1.37	0.20	0.88	0.25	0.7
94.20	0.74	3.22	0.51	2.77	0.55	1.61	0.25	1.65	0.26	0.16	0.58	0.5
98.92	0.64	2.56	0.42	2.43	0.47	1.45	0.23	1.31	0.19	1.26	0.02	0.4
114.69	1.29	5.76	0.92	5.15	0.98	2.94	0.45	2.75	0.42	7.87	2.88	18.9
116.32	0.47	2.37	0.37	2.18	0.42	1.25	0.20	1.31	0.20	0.38	0.10	0.3
118.72	0.60	2.59	0.42	2.51	0.50	1.48	0.23	1.32	0.20	1.51	0.21	1.1
120.20	1.90	7.90	1.28	7.04	1.40	3.99	0.61	3.64	0.52	8.52	3.27	3.0
128.80	0.44	2.04	0.30	1.69	0.35	1.06	0.17	1.10	0.17	0.15	0.11	0.4
139.27	0.43	1.88	0.29	1.60	0.33	1.01	0.16	1.06	0.17	0.20	0.07	0.2
142.83	1.88	8.22	1.26	6.58	1.31	3.94	0.58	3.62	0.52	10.39	3.01	8.6
151.71	0.73	3.36	0.52	2.79	0.55	1.67	0.28	1.81	0.26	5.51	0.44	0.2
163.85	0.94	3.73	0.59	3.18	0.63	1.89	0.30	1.85	0.27	5.41	2.34	0.8
166.95	0.59	2.31	0.36	1.98	0.39	1.18	0.19	1.21	0.18	4.84	0.30	0.2
178.32	1.76	6.77	1.05	5.61	1.11	3.33	0.57	3.64	0.55	8.10	4.21	2.4
178.48	0.36	1.55	0.24	1.40	0.28	0.87	0.13	0.84	0.13	0.13	0.17	<0.1
181.53	0.43	1.51	0.25	1.42	0.28	0.97	0.15	0.95	0.14	0.45	0.09	0.1
185.23	1.62	7.03	1.14	6.33	1.30	3.99	0.64	3.88	0.55	8.45	2.98	1.7
187.12	0.85	3.71	0.57	3.08	0.61	1.83	0.31	1.87	0.28	2.39	1.04	0.3
188.39	0.77	3.61	0.57	3.14	0.64	1.93	0.31	2.00	0.30	0.92	0.64	0.1
193.66	0.74	2.95	0.46	2.56	0.52	1.66	0.26	1.71	0.26	1.99	0.31	0.1
209.88	1.89	8.12	1.31	7.35	1.49	4.38	0.65	3.83	0.55	6.22	3.23	3.0
218.50	1.72	7.07	1.15	6.59	1.27	3.78	0.57	3.52	0.55	7.84	2.98	1.0
218.80	0.48	2.12	0.37	2.04	0.41	1.26	0.20	1.36	0.22	0.42	0.11	0.1
221.18	0.50	2.17	0.35	1.90	0.38	1.17	0.19	1.18	0.19	0.52	0.08	0.2
223.53	0.64	3.53	0.54	2.96	0.56	1.74	0.27	1.89	0.29	0.40	0.09	0.2
230.33	0.85	3.92	0.62	3.40	0.69	1.96	0.31	2.00	0.32	1.60	0.74	0.2
233.30	0.43	1.58	0.27	1.50	0.30	0.92	0.14	0.95	0.15	0.55	0.11	0.2

	Cu	Pb	Zn	Ni	As	Cd	Sb	Bi	Ag	Au	Hg	Tl	Se
m	ppm	ppm	ppm	ppm	ppm	ppm	ppm	ppm	ppm	ppb	ppm	ppm	ppm
3.60	19.6	2.6	27	6.1	2.2	0.2	<0.1	<0.1	<0.1	<0.5	<0.01	<0.1	<0.5
7.41	1.5	1.6	14	3.4	1.2	<0.1	<0.1	<0.1	<0.1	0.6	0.01	<0.1	<0.5
14.56	4.1	2.5	54	9.2	1.7	0.3	<0.1	<0.1	<0.1	<0.5	0.02	<0.1	<0.5
27.38	78.9	24.6	518	158.4	47.4	7.8	0.4	0.4	0.6	<0.5	0.02	0.3	18.4
29.80	10.1	3.2	37	5.0	1.0	<0.1	<0.1	<0.1	<0.1	0.8	0.01	<0.1	<0.5
37.72	2.0	1.8	12	5.2	1.8	<0.1	<0.1	<0.1	<0.1	<0.5	0.02	<0.1	<0.5
43.16	30.0	2.3	20	3.6	0.7	<0.1	<0.1	<0.1	<0.1	0.5	<0.01	<0.1	<0.5
51.02	5.0	3.0	39	6.2	2.2	<0.1	<0.1	<0.1	<0.1	4.9	0.01	<0.1	<0.5
51.61	7.0	6.8	71	15.2	4.0	0.2	0.1	<0.1	<0.1	0.6	<0.01	<0.1	1.0
56.43	3.3	3.5	32	6.0	1.5	<0.1	<0.1	<0.1	<0.1	<0.5	0.02	<0.1	<0.5
56.91	4.6	2.3	38	6.9	1.0	<0.1	<0.1	<0.1	<0.1	0.9	0.01	<0.1	<0.5
60.54	77.3	22.6	508	121.0	44.7	6.7	0.8	0.4	0.6	0.6	0.15	0.2	13.5
61.96	3.4	2.2	23	3.5	1.0	<0.1	<0.1	<0.1	<0.1	<0.5	<0.01	<0.1	<0.5
69.78	15.2	2.8	21	4.5	0.7	<0.1	<0.1	<0.1	<0.1	<0.5	0.01	<0.1	<0.5
74.99	88.3	23.3	744	201.1	59.9	10.8	1.0	0.3	0.9	<0.5	0.28	0.2	25.6
93.42	8.1	2.6	22	6.9	1.4	<0.1	<0.1	<0.1	<0.1	0.6	<0.01	<0.1	<0.5
94.20	14.9	5.5	28	9.9	1.1	<0.1	<0.1	<0.1	<0.1	1.0	<0.01	<0.1	<0.5
98.92	3.9	4.6	59	7.3	0.8	0.3	<0.1	<0.1	<0.1	<0.5	0.01	<0.1	0.7
114.69	37.3	15.5	242	86.1	23.3	3.2	0.4	0.3	0.4	<0.5	0.11	0.2	9.5
116.32	16.2	3.4	19	3.9	0.8	<0.1	<0.1	<0.1	<0.1	3.2	<0.01	<0.1	<0.5
118.72	3.5	3.3	29	7.0	2.1	<0.1	<0.1	<0.1	<0.1	<0.5	0.01	<0.1	<0.5
120.20	60.9	25.2	174	59.4	25.7	0.7	0.4	0.4	0.6	<0.5	0.13	<0.1	11.3
128.80	20.4	3.1	19	3.2	0.7	<0.1	<0.1	<0.1	<0.1	<0.5	<0.01	<0.1	<0.5
139.27	6.3	3.6	20	4.9	<0.5	<0.1	<0.1	<0.1	<0.1	<0.5	0.02	<0.1	<0.5
142.83	58.7	24.2	176	72.0	24.8	2.6	0.6	0.4	0.7	<0.5	0.16	<0.1	16.6
151.71	7.9	5.6	48	19.6	4.5	<0.1	<0.1	<0.1	<0.1	<0.5	0.02	<0.1	<0.5
163.85	17.0	13.8	115	42.4	13.7	0.2	0.1	0.2	0.1	<0.5	0.05	0.2	1.8
166.95	5.0	4.7	36	13.7	4.0	<0.1	<0.1	<0.1	<0.1	<0.5	0.01	<0.1	<0.5
178.32	73.7	45.6	109	85.4	45.6	0.3	0.7	0.6	0.6	<0.5	0.63	<0.1	12.0
178.48	4.6	4.7	23	5.2	<0.5	<0.1	<0.1	<0.1	<0.1	17.9	0.04	<0.1	<0.5
181.53	2.5	5.3	18	5.8	<0.5	<0.1	<0.1	<0.1	<0.1	1.3	*	<0.1	<0.5
185.23	58.3	26.1	133	51.9	32.0	0.3	0.8	0.5	0.6	<0.5	0.22	<0.1	10.1
187.12	11.8	11.0	79	29.1	4.0	<0.1	<0.1	<0.1	<0.1	<0.5	0.02	<0.1	<0.5
188.39	5.5	5.0	56	16.2	1.3	<0.1	<0.1	<0.1	<0.1	<0.5	0.01	<0.1	<0.5
193.66	4.9	6.7	46	13.7	1.6	<0.1	<0.1	<0.1	<0.1	<0.5	0.02	<0.1	<0.5
209.88	45.6	23.4	108	49.4	30.6	0.6	0.7	0.4	0.4	<0.5	0.13	<0.1	8.2
218.50	60.0	27.9	124	56.4	28.4	0.3	0.6	0.5	0.4	<0.5	0.24	<0.1	7.0
218.80	4.0	6.5	29	7.8	<0.5	<0.1	<0.1	<0.1	<0.1	<0.5	0.03	<0.1	<0.5
221.18	4.3	8.4	25	8.3	<0.5	<0.1	<0.1	<0.1	<0.1	<0.5	0.03	<0.1	<0.5
223.53	5.1	5.3	30	7.1	<0.5	<0.1	<0.1	<0.1	<0.1	<0.5	*	<0.1	<0.5
230.33	11.4	10.4	92	28.6	4.5	<0.1	<0.1	<0.1	<0.1	<0.5	0.03	0.1	<0.5
233.30	3.2	6.5	29	9.6	1.4	<0.1	<0.1	<0.1	<0.1	<0.5	*	<0.1	<0.5

11.5 Appendix

Headspace gas analysis of Blokely core 511101



Geochemistry Data Report – Gas Analysis of 21 Canned Core Samples



**Applied Petroleum Technology AS
P. O. Box 123
2027 Kjeller
Norway**

Address: Applied Petroleum Technology AS P.O.Box 123 2027 Kjeller Telephone: +47 63 80 60 00 Telefax: +47 63 80 11 38	
Report number APT09-1836	Classification Confidential
Report Title Geochemistry Data Report - Gas Analysis of 21 Canned Core Samples	Submitted Jan. 2009
Client GEUS	Service Order
Client Reference Jørrgen Bojesen-Koefoed	Number of pages 4
Distribution GEUS(Digital) APT (digital)	

Author
Ingar Johansen

	Name	Date	Signature
Reviewed by	Geir Hansen	2009-01-19	
Approved by	Tore Haaland	2009-01-19	

CONTENTS

Table 1. Number of analyses performed	1
Table 2. Gas Composition (volume-%).....	2
Table 3. Gas Isotopes ($\delta^{13}\text{C}$ (‰ PDB) & δD (‰ SMOW)).....	3
Experimental Procedures.....	4

Table 1. Number of analyses performed

Analysis	Cuttings	Total
Headspace	21	21
Stable isotopes of gas	21	21

Table 2. Gas Composition (volume-%)

Well	Sample type	Sample info	APT ID	C1%	C2%	C3%	iC4%	nC4%	iC5%	nC5%	C6+%	CO2%	Sum C1-C5	Wetness	iC4/nC4	ppm
GEUS	DCG	511101-04	56257									100.0				8000
GEUS	DCG	511101-08	56258					0.08	0.14	0.07		99.7	0.29	100.0		19450
GEUS	DCG	511101-12	56259	0.97								99.0	0.97	0.00		2611
GEUS	DCG	511101-16	56260	1.2								98.8	1.2	0.00		2985
GEUS	DCG	511101-20	56261	0.00								100.0	0.00	-1.5		821
GEUS	DCG	511101-24	56262	23.4	0.84				0.31			75.4	24.6	3.5		5652
GEUS	DCG	511101-28	56263	27.1		0.20	0.20	0.40	0.23			71.9	28.1	2.9	0.51	5137
GEUS	DCG	511101-32	56264	6.4								93.6	6.4	0.00		1386
GEUS	DCG	511101-36	56265	94.2	0.04	0.00	0.07	0.18	0.27	0.28	0.77	4.2	95.0	0.31	0.41	60779
GEUS	DCG	511101-40	56266	99.7	0.04							0.23	99.8	0.04		158873
GEUS	DCG	511101-44	56267	3.0								97.0	3.0	0.00		29170
GEUS	DCG	511101-48 (punctured)	56268									100.0				801
GEUS	DCG	511101-52	56269	3.7								96.3	3.7	0.00		915
GEUS	DCG	511101-56	56270	59.9	0.68	4.0	0.14	0.57	0.05	0.05	0.00	34.6	65.4	8.3	0.25	65112
GEUS	DCG	511101-60	56271	75.4		2.0		0.67				22.0	78.0	3.4		3999
GEUS	DCG	511101-64	56272	98.1	0.01	0.00						1.9	98.1	0.01		471389
GEUS	DCG	511101-68	56273	68.9	0.00	0.46		0.38		0.24		30.0	70.0	1.2		4253
GEUS	DCG	511101-72	56274	6.5								93.5	6.5	0.00		646
GEUS	DCG	511101-76	56275	28.9								71.1	28.9	0.00		1608
GEUS	DCG	511101-79	56276	96.6	0.01							3.4	96.6	0.01		106863
GEUS	DCG	511101-01	56277	26.2								73.8	26.2	0.00		97

Table 3. Gas Isotopes ($\delta^{13}\text{C}$ (‰ PDB) & δD (‰ SMOW))

Well	Sample type	Sample info	APT ID	C1 $\delta^{13}\text{C}$	C2 $\delta^{13}\text{C}$	C3 $\delta^{13}\text{C}$	i-C4 $\delta^{13}\text{C}$	n-C4 $\delta^{13}\text{C}$	i-C5 $\delta^{13}\text{C}$	n-C5 $\delta^{13}\text{C}$	CO2 $\delta^{13}\text{C}$	C1 δD
GEUS	DCG	511101-04	56257								-3.5	
GEUS	DCG	511101-08	56258								-6.2	
GEUS	DCG	511101-12	56259									
GEUS	DCG	511101-16	56260									
GEUS	DCG	511101-20	56261									
GEUS	DCG	511101-24	56262								-5.9	
GEUS	DCG	511101-28	56263								-6.4	
GEUS	DCG	511101-32	56264									
GEUS	DCG	511101-36	56265	-39.7							-8.0	-279.0
GEUS	DCG	511101-40	56266	-48.9								-289.0
GEUS	DCG	511101-44	56267								-6.5	
GEUS	DCG	511101-48 (punctured)	56268									
GEUS	DCG	511101-52	56269									
GEUS	DCG	511101-56	56270	-14.6		-24.8					-2.7	-282.0
GEUS	DCG	511101-60	56271									
GEUS	DCG	511101-64	56272	-42.5							-3.1	-273.0
GEUS	DCG	511101-68	56273	-43.4							-7.9	
GEUS	DCG	511101-72	56274									
GEUS	DCG	511101-76	56275									
GEUS	DCG	511101-79	56276	-35.4								-262.0
GEUS	DCG	511101-01	56277									

Experimental Procedures

All procedures follow NIGOGA, 4th Edition. Below are brief descriptions of procedures/analytical conditions.

GC analysis of gas components

Aliquots of the samples were transferred to exetainers. 0.1-1ml were sampled using a Gerstel MPS2 autosampler and injected into a Agilent 7890 RGA GC equipped with Molsieve and Poraplot Q columns, a flame ionisation detector (FID) and 2 thermal conductivity detector (TCD). Hydrocarbons were measured by FID. H₂, CO₂, N₂ and O₂/Ar by TCD.

Carbon isotope analysis of hydrocarbon compounds and CO₂

The carbon isotopic composition of the hydrocarbon gas components was determined by a GC-C-IRMS system. Aliquots were sampled with a syringe and analysed on a Trace GC2000, equipped with a Poraplot Q column, connected to a Delta plus XP IRMS. The components were burnt to CO₂ and water in a 1000 °C furnace over Cu/Ni/Pt. The water was removed by Nafion membrane separation. Repeated analyses of standards indicate that the reproducibility of $\delta^{13}\text{C}$ values is better than 1 ‰ PDB (2 sigma).

Carbon isotope analysis of low concentration methane using the Precon.

The carbon isotopic composition of methane was determined by a Precon-IRMS system. Aliquots were sampled with a GCPal autosampler. CO₂, CO and water were removed on chemical traps. Other hydrocarbons than CH₄ and remaining traces of CO₂ were removed by cryotrapping. The methane was burnt to CO₂ and water in a 1000 °C furnace over Cu/Ni/Pt. The water was removed by Nafion membrane separation. The sample preparation system described (Precon) was connected to a Delta plus XP IRMS for $\delta^{13}\text{C}$ analysis. Repeated analyses of standards indicate that the reproducibility of $\delta^{13}\text{C}$ values is better than 1 ‰ PDB (2 sigma).

Hydrogen isotope analysis of methane

The hydrogen isotopic composition of methane was determined by a GC-C-IRMS system. Aliquots were sampled with a GCPal and analysed on a Trace GC2000, equipped with a Poraplot Q column, connected to a Delta plus XP IRMS. The components were decomposed to H₂ and coke in a 1400 °C furnace. The international standard NGS-2 and an in-house standard (Std A) were used for testing accuracy and precision. The “true” value of NGS-2 is given to -172.5 ‰ V-SMOW (<http://deuterium.nist.gov/standards.html>). Repeated analyses of standards indicate that the reproducibility of δD values is better than 10 ‰ PDB (2 sigma).